Chapter 11

Data Analysis and Seismogram Interpretation

(Version March 2014; DOI:10.2312/GFZ.NMSOP-2_ch11)

Peter Bormann[1)], Klaus Klinge[2)], and Siegfried Wendt[3)]

[1)] Formerly GFZ German Research Centre for Geosciences, Department 2: Physics of the Earth, Telegrafenberg, 14473 Potsdam, Germany; E-mail: pb65@gmx.net;
[2)] Formerly Bundesanstalt für Geowissenschaften und Rohstoffe, Stilleweg 2, 30655 Hannover Germany; E-Mail: klaus.klinge@gmail.com
[3)] Geophysical Observatory Collm, University of Leipzig, 04779 Wermsdorf, Germany; E-mail: wendt@rz.uni-leipzig.de

Note: When reference is made to figures then the first figure number is the respective Chapter number.

11.1 Introduction

Chapter 11 deals with seismogram analysis and extraction of seismic parameter values for data exchange with national and international data centers, for use in research and last, but not least, for informing the public about seismic events. It is mainly written for training purposes and for use as a reference source for seismologists working at observatories, network and analysis centers or with mobile networks for monitoring and analyzing the seismotectonic activity. Complementary, procedures for volcano-seismic monitoring are treated in detail in Chapter 13. However, this Chapter deliberately refers also to classical analog or simple computer assisted interactive procedures and products of seismogram analysis. They are easier to grasp and educationally often more illustrative and appealing. Accordingly we recall with this Chapter also historical aspects of seismic recording and seismogram analysis and provide information and procedures applicable also in the context of education and outreach programs. Thus we hope to address, as the related IRIS program (http://www.iris.edu/hq/programs/education_and_outreach), at least with some sections a wider than specialist audience, including also grade 6-12 students and teachers involved in

"Seismology and Seismographs at Schools", college students and faculty members, researchers from neighboring disciplines and the public.
Accordingly, the Chapter describes the basic requirements, tools and products of both traditional analog and nowadays almost exclusively digital routine observatory practice, i.e.:

- recognize the occurrence of an earthquake in a record;
- identify and annotate the seismic phases;
- determine onset time and polarity correctly;
- measure the maximum ground amplitude and related period;
- calculate slowness and azimuth;
- determine source parameters such as the hypocenter, origin time, magnitude, etc.

In modern digital observatory practice these procedures are implemented in computer programs. Experience, a basic knowledge of elastic wave propagation (Chapter 2), and the available software can guide a seismologist to analyze large amounts of data and interpret seismograms correctly. Nowadays, in most observatories this work is partially or completely automatized. Earthquake detection, initial P-phase picking, initial localization and magnitude determination are normally carried out by the automatic procedure. Seismologists, using graphical processing and visualization tools, then interactively revise and correct these initial results based on scientific reasoning, ample knowledge and – very important - much practical experience. The aim of this Chapter is to introduce the basic knowledge, data, procedures and tools required for proper seismogram analysis and phase interpretation and to illustrate this with selected seismogram examples. Very rapidly developing new procedures and data products will have to be described in specialized future amendments to this Chapter.

Seismograms reflect the combined influence of the seismic source (Chapter 3), the propagation path (Chapter 2), the frequency response of the recording instrument (Chapter 4, section 4.5 and Chapter 5, section 5.2.8), and the ambient noise at the recording site (Chapter 4, section 4.6). Fig. 11.1 summarizes some essential fields of study and kinds of information which benefit or are largely based on the analysis and interpretation of seismograms. The more completely we interpret the seismograms and the better we quantify the parameters that can be derived therefrom, the better we reveal and understand the structure and properties of the Earth as well as the geometry, kinematics and dynamics of seismic sources and the underlying processes.

Seismograms carry basic information about earthquakes, chemical and nuclear explosions, mining-induced earthquakes, rock bursts and other events generating seismic waves in a very wide range of frequencies from kHz to mHz recorded at distances from a few meters to several 10,000 kilometers from the source (Fig. 11.2).

Seismological data analysis for single stations is nowadays increasingly replaced by network (Chapter 8) and array analysis (Chapter 9). Array-processing techniques have been developed for more than 50 years. Networks and arrays, in contrast to single stations, enable better signal detection and source location. Also, arrays can be used to estimate slowness and azimuth, which allow better phase identification. Further, more accurate magnitude values can be expected by averaging single station magnitudes and for distant sources the signal coherency can be used to determine onset times more reliably. Tab. 11.1 summarizes basic characteristics of single stations, station networks and arrays. In principle, an array can be used as a network and in special cases a network can be used as an array. The most important

differences between networks and arrays are in the degree of signal coherence and the data analysis techniques used.

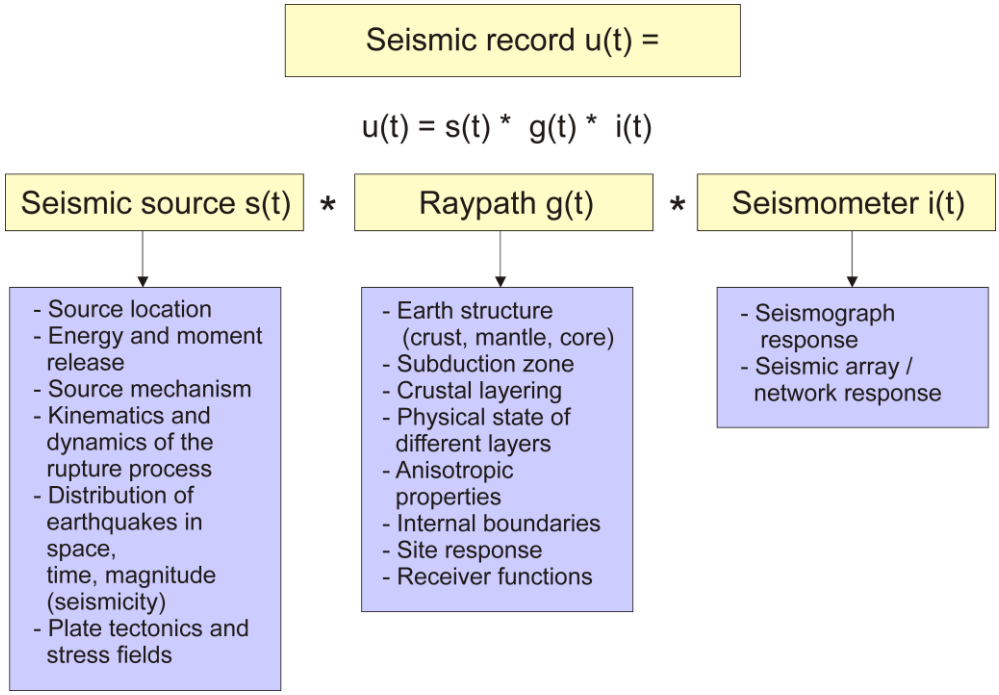

Fig. 11.1 Different sub-systems (without seismic noise) which influence a seismic record (yellow boxes) and the information that can be derived from the analysis of seismic records (blue boxes). The '*' represents the convolution operator.

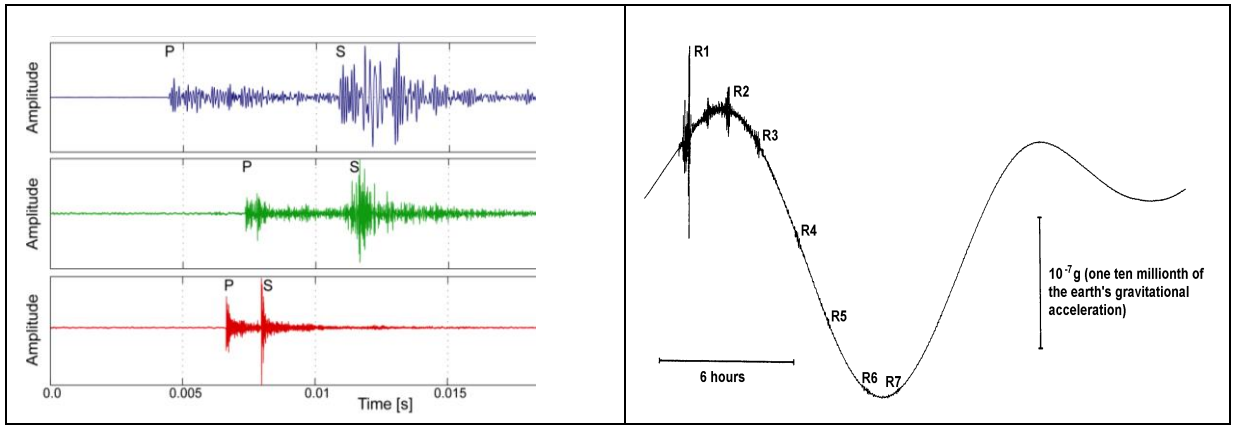

Fig. 11.2 Left: Very weak mining induced seismo-acoustic events with frequencies between about 1 and 100 kHz recorded at distances from meters to decameters in a South African goldmine (cut-out from Figure 2A of Plenkers et al. (2010), Seism. Res. Lett., vol. 81, no. 3, p. 470; © Seismological Society of America**; Right:** Very broadband STS1 record with seismic wave groups from a magnitude 8.2 earthquake in the Kermadec Islands (October 20, 1986) that are superimposed to solid Earth's tides. The mantle Rayleigh wave R7 has traveled almost 130000 km before it was recorded at the station of Nagoya University, Japan (modified from a pamphlet of the Japanese Global Seismology Subcommittee for the POSEIDON project).

Tab. 11.1 Short characteristic of single stations, station networks and arrays.

Single station	Classical type of seismic station with its own data processing. Event location only possible by means of three-component records.
Seismic network	Local, regional or global distribution of stations, physical or ad hoc virtuell, that are as identical as possible, with a common data center and time reference (Chapter 8). Event source parameter estimation (hypocenter, magnitude, mechanism…) is one of the main tasks.
Seismic array	Cluster of seismic stations with a common time reference and uniform instrumentation. The stations are located close enough to each other in space for the signal waveforms to be correlated between adjacent sensors (Chapter 9). Benefits are: • extraction of coherent signals from random noise; • determination of directional information of approaching wavefronts (determination of backazimuth of the source); • determination of slowness and thus of epicentral distance of the source; • event localization by using backazimuth and distance

Like single stations, also narrow band-limited seismometer systems loose nowadays increasingly in importance for global monitoring. However, the much easier to handle and cheaper short-period seismographs, which are particularly suitable for local monitoring of weaker events, still outnumber by far the more costly and with respect to environmental effects much more sensitive broadband systems (see http://www.iris.edu/data/DCProfiles.htm as well as Chapter 5 and IS 5.4). In any event, bandwidth limitation filters the ground motion, thus distorting the signal shape, the more the narrower the bandwidth. In the extreme it may even shift the apparent onset time and reverse the apparent first-motion polarity (Chapter 4, section 4.5). Most seismological observatories, and especially regional and global networks, are now equipped with broadband seismometers that are able to record signal frequencies between about 0.001 Hz and 50 Hz. The frequency and dynamic range covered by broadband recordings are shown in Figs. 1.9, 4.7 and 11.38 in comparison with classical band-limited analog recordings of the Worldwide Standard Seismograph Network (WWSSN).

A number of classical analog seismograph systems are still in operation at autonomous single stations in some countries. Also, archives are filled with analog recordings of these systems, which were collected over many decades. These data constitute a wealth of information most of which has yet to be fully analyzed and scientifically exploited. Although digital data are superior in many respects, both for advanced routine analysis and even more for scientific research, it will be many years or even decades of digital data acquisition before one may consider the bulk of these old data as no longer needed. However, for the rare big and thus unique earthquakes, and for earthquakes in areas with low seismicity rates, the preservation and comprehensive analysis of these classical and historic seismograms will remain of utmost importance for many years. Around 300,000 paper seismograms, especially those containing large earthquakes, were already scanned and digitized in the IASPEI SeismoArchives Project (http://www.iaspei.org/downloads/IASPEI_SeismoArchives_Project_summary_2011.pdf,

http://www.iris.edu/seismo/) but this is still a small fraction of the total amount of analog recordings.

More and more old analog data will be reanalyzed only after being digitized and by using similar procedures and analysis programs as for recent original digital data. Nevertheless, station operators and analysts should still be in a position to handle, understand and properly analyze analog seismograms or plotted digital recordings without computer support and with only modest auxiliary means. Digital seismograms are analyzed in much the same way as classical seismograms, except that the digital analysis uses interactive software which makes the analysis quicker and easier, allows comfortable modification of the time and amplitude resolution of the record plots, modification of the record response and component representation (filtering, record simulation, axes rotation) and to use many other useful operations. But the correct seismogram interpretation requires much of the same knowledge of the appearance of seismic records and of individual seismic phases as the interpretation of classical analog records. The analyst needs to know the typical features in seismic records as a function of distance, depth and source process of the seismic events, their dependence on the polarization of the different types of seismic waves and thus on the azimuth of the source and the orientation of sensor components with respect to it. He/she also needs to be aware of the influence of the seismograph response on the appearance of the record. Without this solid background knowledge, phase identifications and parameter readings may be rather incomplete, systematically biased or even wrong, no matter what kind of sophisticated computer programs for seismogram analysis are used.

Therefore, in this Chapter we will deal first with an introduction to the fundamentals of seismogram analysis at single stations and seismic networks, based on waveform data. Although many decision makers in seismology see nowadays less operational need for this kind of instruction and training, from an educational point of view its importance cannot be overemphasized. An analyst trained in comprehensive and competent analysis of traditional analog seismic recordings, when given access to advanced tools of computer-assisted analysis, will by far outperform any computer specialist with only limited seismological background knowledge.

Automated phase identification and parameter determination have advanced significantly in recent years (Chapter 16) and enjoy massive application at seismological observatories, physical and virtual network centers (Chapter 8) and for seismic arrays (Chapter 9). Only with automation the data from a steadily increasing number of seismic stations can be processed, especially during seismic swarms and aftershock activities. Still, the quality of automatic results might be inferior to those achievable by well-trained analysts (section 11.4). Therefore, an adequate combination of automatic and manual data processing should be assured. Both processing phases and their interaction must be optimized. In many observatories the automatic procedures are only used for fast information to the authorities and the public and run simply in parallel to the manual data processing which intends to produce high quality results for later scientific applications. Therefore, this Manual focusses on providing competent guidance and advice to station operators and seismologists with limited experience on the complexity of seismic waveforms, their comprehensive analysis and interpretation. Moreover, specialists in program development and the automation of algorithms usually also lack the required seismological background knowledge and own rich experience in seismogram analysis. This, however, is an indispensable requirement for further qualification of currently available computer procedures for interactive and automatic data analysis, parameter determination and source location. They have to be in tune both with

older data and established standards to assure long-term data continuity and compatibility and at the same time also assure a broader range of quality observatory products which meet modern research requirements. In this sense, the chapter also addresses the needs of this advanced user community.

Digital recording has the big advantage that the seismic recordings can be reprocessed easily when new processing methods are available. It should also be noted that the falling prices of digital storage media make continuous recording and backup economically feasible. So, new detection algorithms can be applied to the recordings, or the parameters of the algorithms can be tuned by comparing their results with those of human interpretation.

Accordingly, we first give a general introduction to "classical" routine seismogram interpretation which was developed using analog records, respectively waveform plots of digital records at single stations and local or regional seismic networks. Then we discuss both similarities and differences when processing analog or digital data. The basic requirements for parameter extraction, bulletin production as well as parameter and waveform data exchange are also outlined. In the sub-Chapter on digital seismogram analysis we discuss in more detail problems of signal coherence, the related different procedures of data processing and analysis as well as available software for it. The majority of record examples from Germany have been processed with the program Seismic Handler (SHM) developed by K. Stammler which is used for seismic waveform retrieval and data analysis. This program and descriptions are available via http://www,seismic-handler.org. Reference is made and examples are given, however, also to/from other analysis software that is widely used internationally, e.g. SEISAN, SeisComP3, Earthworm, SAC and many others (see 11.4). Typical examples of seismic records from different single stations, networks and arrays in different distance ranges (local, regional and teleseismic) and at different source depth are presented, mostly broadband data or filtered records derived therefrom. Special sections are dedicated to the interpretation of seismic core phases (see 11.5.3.3 and 11.5.4).

The treatment of the detailed analysis of teleseismic recordings might provide an interesting, even "exotic" view for readers working at observatories with a high local seismicity where the work is often uniquely focused on the processing of near seismic events. At many networks in areas with complicated crustal structures (e.g., in subduction environments) the locations are normally only carried out with the first P- and S-waves and the high workload due to a strong seismicity does not permit to look for secondary or teleseismic arrivals. But, it should be noted that an understanding of teleseismic records is sometimes very beneficial for local network seismologist too. It happens, for instance, that strong relatively high-frequency teleseismic P or PKP arrivals, under the bad luck of low residuals due to some casual station geometry, are misinterpreted by automatic location procedure as phases from a local or regional event and then a "ghost" earthquake is reported. Another difficulty for automatic and even human interpretation is the recording of two or more seismic events at nearly the same time. This is not so seldom, especially for extended regional networks, and during aftershock or swarm activities in the monitored area. The automatic procedures, which assign the detected phases to earthquake origins, fail occasionally in this situation and then human interaction is necessary.

Since all authors of Chapter 11 come from Germany, the majority of records shown have been collected at stations of the German Regional Seismic Network (GRSN), the Gräfenberg array (GRF) or at other local station networks (Fig. 11.3a). Fig. 11.3b depicts the global distribution of epicenters of seismic events from which record examples are presented.

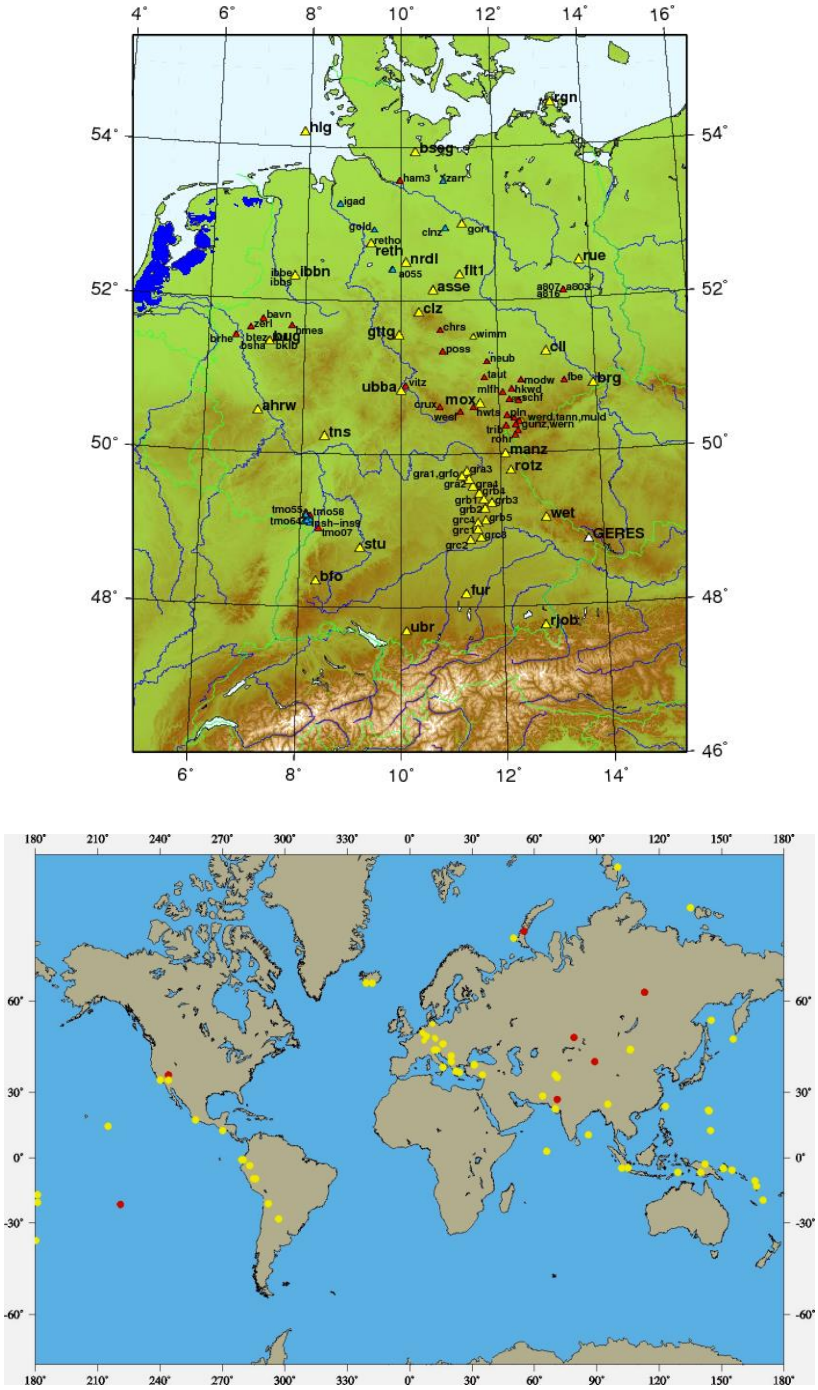

Fig. 11.3 **a)** Broadband stations in Germany. Yellow triangles: stations of the German Regional Seismic Network (GRSN) and of the Gräfenberg-Array (GRF). Other triangles: other stations (for details Chapter 8, section 8.7.5). **b)** Global distribution of epicenters of seismic events (red dots: underground nuclear explosions; yellow dots: earthquakes) for which records from the above stations will be presented in Chapter 11 and DS 11.1-11.4.

All GRSN/GRF stations record originally velocity-broadband (BB-velocity) data. All record examples from these stations of short-period (SP), long-period (LP) or BB-displacement seismograms are digitally simulated ones, corresponding to those which would have been

recorded by classical Wood-Anderson, WWSSN-SP, WWSSN-LP, SRO-LP or Kirnos SKD seismographs. Users of this Chapter may feel that the seismograms presented are too much biased towards Europe. Indeed, we may have overlooked some important aspects or typical seismic phases which are well observed in other parts of the world. Therefore, we invite anybody to send valuable complementary data and information to the Editor for integration into revised or amended editions of this electronic Manual.

For routine analysis and international data exchange a standard nomenclature of seismic phases is required. The latest version of the IASPEI Standard Nomenclature of Seismic Phases is given in IS 2.1, together with ray diagrams for most phases. This nomenclature (published earlier in Storchak et al., 2002, 2003 and 2011) partially modifies and complements earlier ones, e.g., that in the last edition of the Willmore (1979) Manual of Seismological Observatory Practice (and in pre-2010 issues of the seismic Bulletins of the International Seismological Centre (ISC). It is more in tune than the earlier versions with the phase definitions of modern Earth and travel-time models (Chapter 2, section 2.7).

The scientific fundamentals of some essential subroutines in seismological analysis software, e.g., on event location and travel-time calculations, are separately treated in annexed material such as IS 11.1, IS 11.3, PD 11.1 and PD 11.2. Complementary tutorials, exercises and information sheets, also suitable for demonstration and practicals in undergraduate courses and "Seismology in Schools" explain in detail basic steps in the interpretation process (e.g., EX 11.1-11.3 and IS 11.6). More related information may be added in the course of future upgrading of this electronic Manual.

11.2 Criteria and parameters for routine seismogram analysis

11.2.1 Record duration and dispersion

The first thing an experienced seismologist looks for when assessing a seismic record is the duration of the signal. Due to the different nature and propagation velocity of seismic waves and the different propagation paths taken by them to a station, travel-time differences between the main wave groups usually grow with distance. Accordingly, the record spreads out in time. The various body-wave groups show no dispersion, so their individual duration remains more or less constant, only the time difference between them changes with distance. The time difference between the main body-wave onsets is roughly < 3 minutes for events at distances $D < 10°$, < 16 min for $D < 60°$, < 30 min for $D < 100°$ and < 45 min for $D < 180°$ (Figs. 1.4b, 1.6 and 2.60).

In contrast to body waves, the velocity of surface waves is frequency dependent and thus surface waves are dispersed. Accordingly, depending on the crustal/mantle structure along the propagation path, the duration of Love- and Rayleigh-wave trains increases with distance. At $D > 100°$ surface wave seismograms may last for an hour or more (Fig. 1.6), and for really strong events, when surface waves may circle the Earth several times, their oscillations on sensitive long-period (LP) or broadband (BB) records may be recognizable over 6 to 12 hours (Fig. 11.2 right). Even for reasonably strong regional earthquakes, e.g., $Ms \approx 6$ and $D \approx 10°$, the oscillations may be recognizable above the noise level for about an hour although the time difference between the P and S onset is only about 2 min and between P and the maximum amplitude in the surface wave group only 5-6 min. The magnitude dependence of the total earthquake signal duration led the Hungarian seismologist Bisztricsany (1958) to propose a

simple teleseismic procedure for estimating the magnitude of earthquakes that is independent on the knowledge of the distance-dependent amplitude attenuation of different seismic phases and the risk of amplitude clipping of analog records in the case of very strong events.

Finally, besides proper dispersion, scattering may also spread wave energy. This is particularly true for the more high-frequency waves traveling in the usually heterogeneous crust. This gives rise to signal-generated noise and coda waves. Coda waves follow the main generating phases with exponentially decaying amplitudes. The coda duration depends mainly on the event magnitude (Figure 1b in DS 11.1) and only weakly on epicentral distance (Figure 2 in EX 11.1). Thus, record duration can be used for calculating also local coda or duration magnitudes Mc or Md (Chapter 3, section 3.2.4.5).

In summary, signal duration, the time difference between the Rayleigh-wave maximum and the first body-wave arrival (Table 5 in DS 3.1) and in particular the time span between the first and the last recognized body-wave onsets before the arrival of surface waves allow a first rough estimate, whether the earthquake is a local, regional or teleseismic one. This rough classification is a great help in choosing the proper approach, criteria and tools for further more detailed seismogram analysis, source location, and magnitude determination.

11.2.2 Key parameters to be measured

11.2.2.1 Phase onset time

Onset times of seismic wave groups, first and foremost of the P-wave first arrival, when determined at many seismic stations at different azimuth and at different distance, but also of later arriving phases, are the key input parameter for the location of seismic events (IS 11.1). Travel times published in travel-time tables (such as Jeffreys and Bullen, 1940; Herrin, 1968; Kennett, 1991) and travel-time curves, such as those shown in Figs. 2.48, 2.56 or 2.60 have been derived either from observations or Earth models. They give, as a function of epicentral distance D and hypocentral depth h, the differences between *onset times* t_{ox} (also called *arrival times*) of the respective seismic phases x and the *origin time* OT of the seismic source. This time difference is called *travel time*. Onset times mark the first energy arrival of a seismic wave group. The process of recognizing and marking a wave onset and of measuring its onset time is termed *onset time picking*. IS 11.4 provides an elaborated tutorial for both manual and computer assisted consistent picking of phases at local and teleseismic distances and IS 11.5 looks into the problem of picking errors of local phases depending on the signal-to-noise ratio (SNR) as well as on the training and years of experience of analysts and provides a training data set to check analyst performance and the effect of training and gained experience.

The recognition of a wave onset largely depends on the SNR at various frequencies for the given waveform as a whole and the steepness and amplitude of its leading edge. Both are modulated by the shape and bandwidth of the recording seismograph or filter (Figs. 4.9 to 4.13). It is a classical convention in seismological practice to classify onsets, as a qualitative measure for the reliability of their time-picking, as either impulsive (i) or emergent (e). These lower case letters i or e are put in front of the phase symbol. Nowadays, however, with the time resolution and amplitudes and thus the steepness of the waveform flanks being manipulated at will with modern analysis systems, it has become more common to attribute instead a different weight to the picked onset time and polarity readings (see also IS 11.4).

Generally, it is easier to recognize and precisely pick the very first arrival (usually a P wave) on a seismogram than later phases that arrive within the signal-generated coda of earlier waves, often termed “signal-generated noise”.

The relative precision with which an onset can be picked largely depends on the factors discussed above, but the absolute accuracy of onset-time measurement is controlled by the available time reference. Seismic body-wave phases travel rather fast. Their apparent velocities at the surface typically range between about 3 km/s and over 100 km/s (at the antipode the apparent velocity is effectively infinite). Therefore, an absolute accuracy of onset-time picking of less than a second and ideally less than 0.1 s is needed for estimating reliable epicenters (IS 11.1) and determining good Earth models from travel-time data. This was difficult to achieve in earlier decades when only mechanical pendulum clocks or marine chronometers were available at most stations. They have unavoidable drifts and could rarely be checked by comparison with radio time signals more frequently than twice a day. Also, the time resolution of classical paper or film records is usually between 0.25 to 2 mm per second, thus hardly permitting an accuracy of time-picking better than parts of a second. In combination with the limited timing accuracy, the reading errors at many stations of the classical world-wide network, depending also on distance and region, were often two to three seconds (Hwang and Clayton, 1991). However, this improved since the late 1970s with the availability of very-low frequency and widely received time signals, e.g., from the DCF and Omega time services, and recorders driven with exactly 50 Hz stabilized alternating current.

Yet, onset-time reading by human eye from analog records with minute marks led to sometimes even larger errors, a common one being the ± 1 min for the P-wave first arrival. This is clearly seen in Fig. 2.56 (left), which shows the travel-time picks collected by the ISC from the world-wide seismic station reports between 1964 and 1987. Nowadays, atomic clock time from the satellite-borne Global Positioning System (GPS) is readily available in nearly every corner of the globe. Low-cost GPS receivers are easy to install at both permanent and temporary seismic stations and generally affordable. Therefore the problem of unreliable absolute timing should no longer exist. However, technical problems do occur and one needs to be aware of potential timing problems. In fact, there still are many GPS driven digitizers with wrong timing. Nevertheless, also with high resolution digital data and exact timing now being available it is difficult to decide on the real signal onset, even for sharp P from explosions. Douglas et al. (1997) showed that the reading errors have at best a standard deviation between 0.1 and 0.2 s. However, human reading errors no longer play a major role when digital data are evaluated by means of seismogram analysis software which automatically records with high precision the time at the positions where onsets have been marked with a cursor. Moreover, the recognition of signal onsets and the precision of time picks can be modified easily in the case of digital records within the limits set by the sampling rate and the dynamic range of recording. Both the time and amplitude scales of a record can be compressed or expanded as needed, and task-dependent optimal filters for best phase recognition can be applied as well.

Fig. 11.4 shows such a digital record with the time scale expanded to 12 mm/s. The onset time can be reliably picked with an accuracy of a few tenths of a second. This P-wave first arrival has been classified as an impulsive (i) onset, although it looks emergent in this time-stretched plot. But by expanding the amplitude scale also, the leading edge of the wave arrival becomes steeper and so the onset appears impulsive. This ease with which digital records can be manipulated reduces the representativeness and thus the value of qualitative characterization of onset sharpness by either i or e although there are in fact “e” type of phases where no

change in scaling allows a clear characterization. Alternatively, it has been proposed, therefore, to quantify the *onset-time reliability*. This could be done by reporting, besides the most probable or interpreter-preferred onset time, the estimated range of uncertainty by picking the earliest (t_{ox-}) and latest possible onset time (t_{ox+}) for each reported phase x, and of the first arrival in particular (Fig. 11.6).

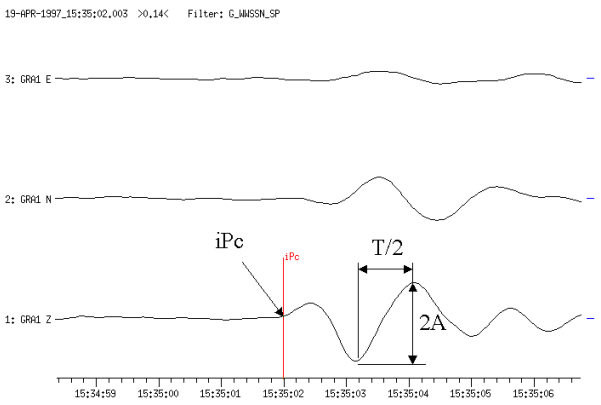

Fig. 11.4 First motion onset times, phase and polarity readings (c – compression; d – dilatation), maximum amplitude A and period T measurements for a sharp (i - impulsive) onset of a P wave from a Severnaya Zemlya event of April 19, 1997, recorded by a broadband three-component single station of the Gräfenberg Array (GRF), Germany but filtered so as to simulate a short-period record of the World-Wide Standard Seismograph Network (WWSSN_SP).

11.2.2.2 Amplitude and period

Whereas the quality, quantity and spatial distribution of reported arrival-time picks largely controls the precision of *source locations* (see IS 11.1), the quality and quantity of amplitude readings for identified specific seismic phases determine the representativeness of amplitude-based event *magnitudes*. The latter are usually based on readings of maximum ground-displacement amplitudes A_{max} and related periods for body- and surface-wave groups but for the newly proposed IASPEI broadband magnitude standards mB_BB and Ms_BB on direct measurement of the maximum ground motion velocity amplitudes V_{max} (Chapter 3, sections 3.2.4 and 3.2.5 and IS 3.3). For symmetric oscillations and as general IASPEI measurement standard amplitudes should be given as half peak-to-trough (double) amplitudes. Some computer programs mark the record cycle from which the maximum amplitude A_{max} and the related T have been measured (Figures 3 and 4 in EX 3.1).

However, some algorithms for automatic amplitude measurement prefer maximum zero-to-peak (or trough) measurements instead. In the case of strongly asymmetric phase wavelets the difference may be significant (Fig. 3.19b) but remains always less than 0.3 magnitude units. The related periods were in analog records with limited time resolution traditionally measured as the time between the largest neighboring peaks or troughs, respectively (Fig. 3.19). However, digital data with high time resolution and the use of precise vertical line cursors for time picking in modern analysis tools make it preferable to measure as period twice the time difference between the adjacent maximum peak and maximum trough amplitude, as in Fig. 11.4. This is now the IASPEI recommended measurement standard for

periods (see IASPEI 2013). However, some automatic digital procedures measure zero-to-peak (or trough) amplitude instead and associate with it as period the double time difference between the two adjacent zero crossings related to the maximum positive or negative swing. For a comparison of $\log(A/T)_{max}$ and $\log(V_{max}/2\pi)$ measurements according to IASPEI standards or to modified automatic procedures see Chapter 3, section 3.2.3.2 and the discussion therein on possible discrepancies.

Note that the measured maximum trace amplitudes in a seismic record have to be corrected for the frequency-dependent magnification of the seismograph to find the "true" ground-motion amplitude at the given period. According to the new IASPEI standards amplitudes should nowadays be measured and reported in nanometers (1 nm = 10^{-9} m), in contrast to the traditional units of micrometers (1 μm = 10^{-6} m), as in the original amplitude-based magnitude formulas defined in analog days when the seismographs recorded with relatively low magnification. Fig. 3.20 shows a few typical displacement amplification curves of standard analog seismographs used with paper or film records. For digital seismographs, instead of displacement or velocity magnification, the frequency dependent *nominal resolution* is usually given in units of nm/counts, or in nm s^{-1}/count for ground velocity measurements.

Both record amplitudes and related dominating periods do not only depend on the spectrum of the arriving waves but are mainly modulated by the shape, peak magnification and bandwidth of the seismograph or record filter response (e.g., Fig. 4.14). Moreover, the magnifications given in the seismograph response curves are strictly valid only for steady-state harmonic oscillations without any *transient response* (Chapter 4, section 4.5.2). The latter, however, might be significant when narrow-band seismographs record short wavelets of body waves. Signal shape, amplitudes and signal duration are then heavily distorted (Figs. 4.9-4.14 and 4.16-4.19). Therefore, we have written "true" ground motion in quotation marks. Scherbaum (2001 and 2007) gives a detailed discussion of signal distortion which is not taken into account in standard magnitude determinations from band-limited records. However, signal distortion must be corrected for in more advanced digital signal analysis for source parameter estimation by taking into account the full *transfer function* which comprises both the amplitude and the phase response of the seismograph (Chapter 5 and IS 5.2). The distortions are largest for the very first oscillation(s) and they are stronger and longer lasting the narrower the recording bandwidth (Chapter 4, sections 4.5.1 and 4.5.2). Transient response decays with time, depending also on the damping of the seismometer. It is usually negligible for amplitude measurements on dispersed teleseismic surface wave trains.

To calculate real ground motion amplitudes from recorded amplitudes, the frequency-dependent seismometer phase and amplitude response as well as the instrument gain, have to be known from careful calibration (Chapter 5, section 5.6 and IS 5.2). Analog seismograms should be clearly annotated and relate each record to a seismometer with known amplitude response. For digital data, the instrument response is usually included in the header information of each seismogram file or has to be inserted, e.g. in the case of SEED data, by the user or to be given in a separate file that is automatically linked when analyzing data files. As soon as amplitudes and associated periods are picked in digital records, most software tools for seismogram analysis calculate instantaneously the ground displacement or ground velocity amplitudes and write them in related parameter files.

11.2.2.3 First-motion polarity

Another parameter which has to be determined (if the SNR permits) and reported routinely is the polarity of the P-wave first motion in vertical component records. Reliable observations of the first motion polarity at stations surrounding the seismic source in different directions allow deriving seismic fault-plane solutions (Chapter 3, section 3.4 and EX 3.2). The wiring of seismometer components has to be carefully checked to assure that compressional (c) first arrivals appear on vertical-component records as an upward motion (+ or U) while dilatational (d) first arrivals are recorded as a downward first half-cycle (- or D). The conventions for horizontal component recordings are + (U) for first motions towards N and E, and – (D) for motions towards S and W, respectively. These need to be taken into account when determining the *backazimuth* of the seismic source from amplitude and polarity readings on 3-component records (see EX 11.2, Figure 1). However, horizontal component polarities are usually not considered in polarity-based fault-plane solutions and therefore not routinely reported to data centers. Fig. 11.4 shows a compressional first arrival.

One should be aware, however, that narrow-band signal filtering may reduce the first-motion amplitude by such a degree that its polarity may no longer be reliably recognized or may even get lost completely in the noise (Figs. 4.9 - 4.11). This may result in wrong polarity reporting and hence erroneous fault-plane solutions. Since short-period (SP) records usually have a narrower bandwidth than medium- to long-period or even broadband records, one should differentiate between first-motion polarity readings from SP and LP/BB records. Also, long-period waves integrate over much of the detailed rupture process and so should show more clearly the overall direction of motion which may not be the same as the first-motion arrival in SP records which may be very small. Therefore, according to recommendations in 1985 of the WG on Telegrafic Formats of the IASPEI Commission on Practice, polarities reported to international data centers should unambiguously differentiate between readings on SP (c and d) and those on LP and BB records (u for “up” = compression and r for “rarefaction” = dilatation). Although event-size and SNR-dependent, polarity readings on BB records tend to be more reliable (Chapter 4, Figs. 4.10 and 4.11). Fig. 11.5 shows short-period P-wave onsets from a Severnaya Zemlya event of April 19, 1997, as recorded in WWSSN_SP filtered broadband stations of the German Regional Seismic Network (GRSN). The P-wave amplitudes vary significantly within the network, the first-motion polarity remains the same.

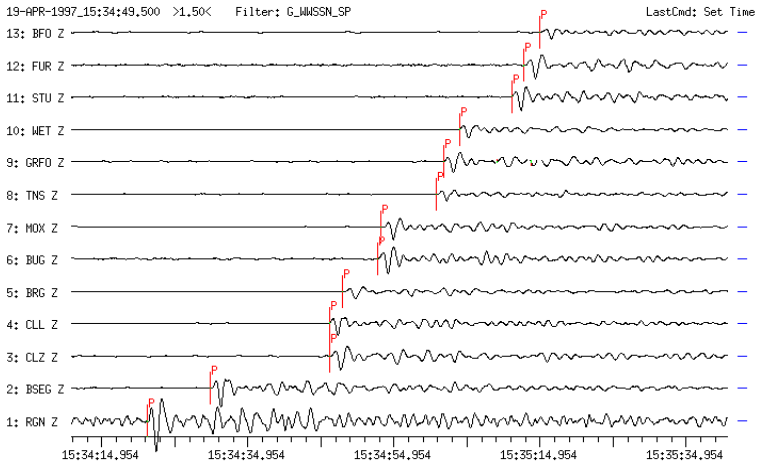

Fig. 11.5 WWSSN_SP filtered vertical-component broadband records at GRSN stations for the same event as in Fig. 11.4.

11.2.3 Advanced wavelet parameter reporting from digital records

The parameters discussed in 11.2.2 have been routinely reported over the decades of analog recording. Digital records, however, allow versatile signal processing so that additional wavelet parameters can be measured routinely. Such parameters may provide a much deeper insight into the seismic source processes and the seismic moment release. Not only can onset times be picked but their range of uncertainty can also be marked. Further, for a given wave group, several amplitudes and related times may be quickly measured and these allow inferences to be drawn on how the rupture process may have developed in space and time. Moreover, the duration of a true ground displacement pulse t_w and the rise time t_r to its maximum amplitude contain information about size of the source, the stress drop and the attenuation of the pulse while propagating through the Earth. Integrating over the area underneath a displacement pulse allows to determine its signal moment m_s which is, depending on the bandwidth and corner period of the recording, related to the seismic moment M_0 (Seidl and Hellweg, 1988). Finally, inferences on the attenuation and scattering properties along the wave path can be drawn from the analysis of wavelet envelopes.

Fig. 11.6 depicts various parameters in relation to different seismic waveforms. One has to be aware, however, that each of these parameters can be severely affected by the properties of the seismic recording system (Fig. 4.17 and Scherbaum 2001). Additionally, one may analyze the SNR and report it as a quantitative parameter for characterizing signal strength and thus of the reliability of phase and parameter readings. This is routinely done when producing the Reviewed Event Bulletin (REB) of the International Data Centre (IDC) in the framework of the CTBTO (Chapter 15). The SNR may be either given as the ratio between the maximum amplitude of a considered seismic phase to that of the preceding ambient noise or signal-generated coda without taking differences in the frequencies into account, by the respective STA/LTA or rms ratio (see IS 8.1) or by determining the spectral SNR (Fig. 11.60). Regrettably, no standard procedure is yet available for best assessment of the quality of phase amplitude and onset-time readings (see also IS 11.4 and section 11.6).

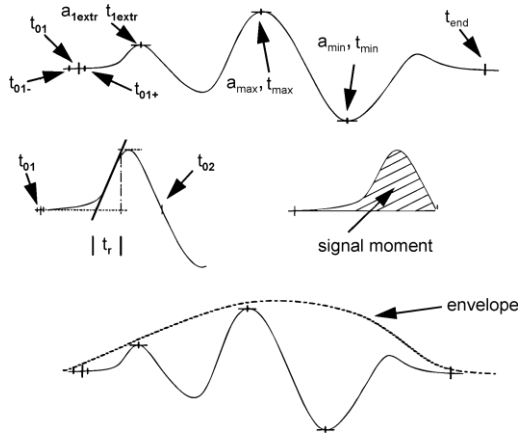

Fig. 11.6 Complementary signal parameters such as multiple wavelet amplitudes and related times, rise-time t_r of the displacement pulse, signal moment m_s and wavelet envelope (with modification from Scherbaum, Of Poles and Zeros, Fig. 1.9, p. 10, © 2001; with permission of Kluwer Academic Publishers).

Although these complementary signal parameters could be determined rather easily and quickly by using appropriate software for signal processing and seismogram analysis, their measurement and reporting to data centers is not yet common practice. It is expected, however, that the recently introduced more flexible formats such as the IASPEI Seismic Format for parameter reporting and storage (see ISF, Chapter 10.2.5), or QuakeML (section 2 in IS 3.2), in conjunction with e-mail and internet data transfer, will pave the way for their routine reporting.

11.2.4 Criteria to be used for phase identification

11.2.4.1 Travel time and slowness

As outlined in Chapter 2, travel times of identified seismic waves are not only the key information for event location but also for the identification of seismic wave arrivals and the determination of the velocity structure of the Earth along the paths which these waves have traveled. The same applies to the horizontal component s_x of the slowness vector s. The following relations hold:

$$s_x = dt/dD = p = 1/v_{app}$$

were v_{app} is the apparent horizontal velocity of wave propagation, dt/dD the gradient of the travel-time curve t(D) in the point of observation at distance D, and p is the ray parameter. $v_{app} = \infty$ for vertical incidence at the surface (i = 0°) and $v_{app} = v$ = true wave propagation velocity for i = 90°, i.e., when the seismic ray runs along the Earth's surface. The animation linked to section 2.1 of IS 1.1 (New Zealand earthquake 2001) is an excellent example for the slowness differences of the different seismic phases traveling through the GRSN.

Due to the given structure of the Earth, the absolute as well as relative travel-time and slowness differences between various types of seismic waves vary with distance in a systematic way. Therefore, differential travel-time curves with respect to the first P-wave arrival (Figure 4 in EX 11.2) or absolute travel-time curves with respect to known origin time OT (Figs. 2.48 and 2.60) or known slowness-distance relationships (e.g., Fig. 11.7) are very suitable for identifying seismic waves in seismic records. This may be done by matching as many of the recognizable wave onsets in the record as possible with theoretical travel-time or slowness curves for various theoretically expected phases at epicentral distance D, depending also on source depth h.

When using analog records with fixed time resolution one should make sure that the plotted t(D)-curves have the same time-resolution as your record and investigate the match between the theoretical phase travel-times and phase onsets on the records at different distances. Relative travel-time curves thus allow not only the identification of best matching phases but also the distance of the station from the epicenter of the source to be estimated (Fig. 11.8). Note, however, that in certain distance ranges the travel-time curves of different types of seismic waves (Figure 4 in EX 11.2) are close to each other, or even overlap, for example for PP and PcP between about 40° and 50° (see also Figure 6a in DS 11.2) and for S, SKS and ScS between 75° and 90° (Fig. 11.9). Proper phase identification then requires to take besides travel-time differences also additional criteria such as slowness, amplitude, polarity and dominating period into account (sections 11.2.4.2 to 11.2.4.4). The most probable distance should agree best also with those complementary criteria. If absolute travel-time curves or tables are available also the origin time can be estimated (EX 11.1 and EX 11.2).

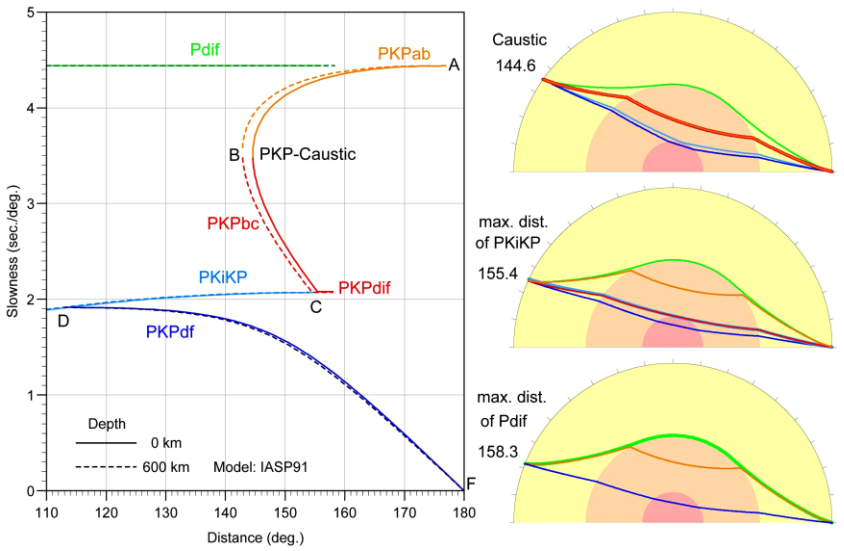

Fig. 11.7 The distance-variable horizontal component ray parameter (slowness) of different seismic core phases and the constant slowness of the Pdif phase that is diffracted around the core-mantle boundary (CMB).

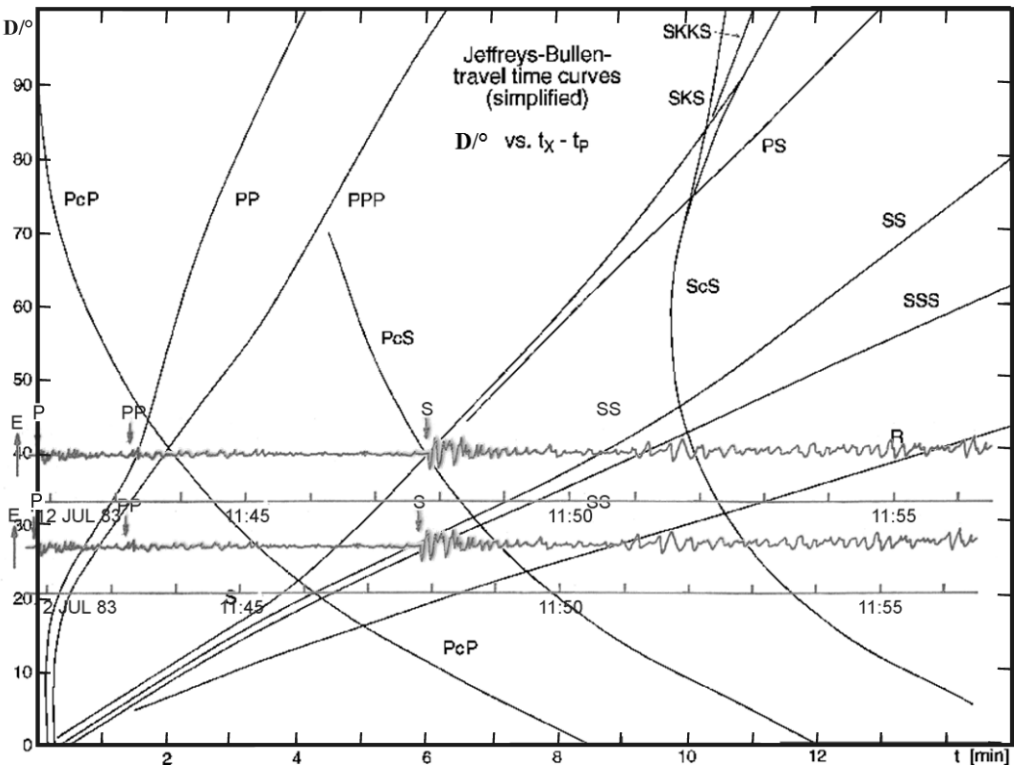

Fig. 11.8 Determination of epicentral distance by **s**earching for the best fit when moving a seismic record from below upward over a differential travel-time curve until one reaches the best possible match of the dominating wave onsets with the travel-time branches of major seismic phases. In the given case the best match was achieved at about 40° distance (1° = 111.2 km).

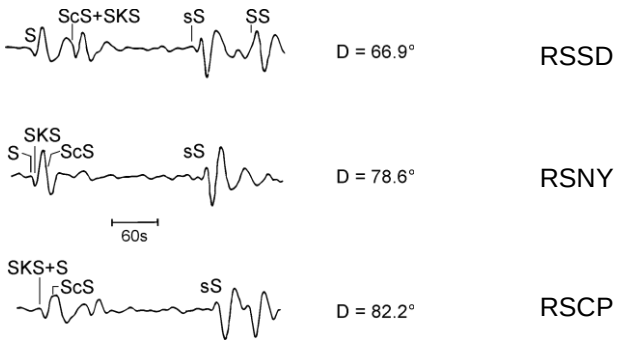

Fig. 11.9 Example of long-period horizontal component seismogram sections from a deep-focus earthquake in the Sea of Okhotsk (20.04.1984, mb = 5.9, h = 588 km), recorded at the stations RSSD, RSNY, and RSCP, respectively, in the critical distance range of overlapping travel-time branches of S, SKS and ScS. Because of the large focal depth the depth phase sS is clearly separated in time. Modified cut-out of Plate 40 in Kulhánek (1990), Anatomy of Seismograms, p.137-138; © 1990; with permission from Elsevier Science.

Note that the travel-time curves shown in Figs. 11.8 and 2.60 or those given in EX 11.1 and EX 11.2 are valid for near-surface sources only. Both absolute and (to a lesser extent) relative travel times between different phases change with source depth (see IASPEI 1991 Seismological Tables, Kennett, 1991) and, in addition, also depth phases may appear, as in Fig. 11.9 (see also section 2.6.3 in Chapter 2 and Table 1 in EX 11.2). Note also that far-regional travel-time curves (D > (17-20°) vary little from region to region. Typically, the theoretical travel times of the main phases deviate less than 2 s from those observed (compare Figs. 2.57-2.60 in Chapter 2). In contrast, local/regional travel-time curves for crustal and uppermost mantle phases may differ much more from region to region. This is due to the pronounced lateral variations of crust and lithosphere thickness, structure, composition, age and related propagation velocities in continental and oceanic areas. For variations in crustal thickness see Fig. 2.11 in Chapter 2. Therefore, local/regional travel-time curves should be derived for each region in order to improve phase identification and estimates of source distance and depth and thus event location.

Nowadays, rapid epicenter and/or source depth estimates are normally already available at the data center prior to detailed record analysis. Then seismogram analysis software (section 11.4) such as SEISAN (Ottemöller, Voss and Havskov, 2013; Havskov and Ottemöller, 1999; http://www.ifjf.uib.no/seismo/software/seisan/seisan.html), Seismic Handler (SHM) (author: Klaus Stammler, recent developments: Marcus Walther; http://www.seismic-handler.org) or SeisComp3 (http://www.seiscomp3.org/) allow the theoretically expected travel times for all main seismic phases to be marked on the record. This eases phase identification. An example is shown in Fig. 11.17 for a record analyzed with Seismic Handler. One should be aware, however, that arrival times calculated via ray theory and the appearance of the real wave onsets may differ. Therefore, onset-times of phases, calculated on the basis of a homogeneous 1D global average Earth model via ray theory can only guide the phase identification but should not be used for onset picking! A striking example of possible differences in the order of a few seconds between theoretically expected and really observed phase onsets is shown in Figure 9b of DS 11.3. Realizing this discrepancy led to the improvement of the velocity model for the Earth core in IASP91 (Kennett and Engdahl, 1991) which was taken into account in the AK135 model (Kennett et al., 1995).

Be aware that one of the major challenges for modern global seismology is 3-D tomography of the Earth. We need to know better the location and size of deviations in wave velocity with respect to the global 1-D reference model. Only then will material flows in the mantle and core (which drive plate tectonics, the generation of the Earth's magnetic field and other processes) be better understood. Station analysts should never trust the computer generated theoretical onset times more than the ones that they can recognize in the record itself. For Hilbert transformed phases (see 2.5.4.3) onset times are best read after filtering to correct for the transformation. Without unbiased analyst readings we will never be able to derive improved models of the inhomogeneous Earth. Moreover, the first rapid epicenters, depths and origin-times published by the data centers are only preliminary estimates and are usually based on first arrivals only. Their improvement, especially with respect to source depth, requires more reliable onset-time picks, and the identification of secondary (later) arrivals (Figure 7 in IS 11.1).

At a local array or regional seismic network center both the task of phase identification and of source location of teleseismic events is easier than at a single station because local or regional slowness can be measured from the time differences of the respective wave arrivals at the various stations (Chapter 9 and sections 11.3.4 and 11.3.5 below). But even then, determining D from travel-time differences between P or PKP and later arrivals can significantly improve the location accuracy. This is best done by using three-component broadband recordings from at least one station in the array or network center. The reason is that travel-time differences between first and later arrivals vary more rapidly with distance than the slowness of first arrivals. But large arrays and regional networks usually give better control of the backazimuth of the source than 3-component recordings (compare 11.2.6 and 11.2.7), especially for low-magnitude events recorded at low SNR and thus uncertain first-motion polarity readings.

11.2.4.2 Amplitude-distance relations, dominating periods and waveforms

Amplitudes of seismic waves vary with distance due to geometric spreading, focusing and defocusing caused by variations of wave speed and attenuation in the Earth. To correctly identify body-wave phases one has first to be able to differentiate between body- and surface-wave groups and then estimate at least roughly, whether the source is at shallow, intermediate or rather large depth. At large distance, surface waves are only seen on LP and BB seismograms. Because of their 2D propagation, geometrical spreading for surface waves is less than for body waves that propagate 3-D. Also, because of their usually longer wavelength, surface waves are less attenuated and less affected by small-scale structural inhomogeneities than body waves. Therefore, on records of shallow seismic events, surface-wave amplitudes dominate over body-wave amplitudes and show less variability with distance (Figs. 11.10 to 11.12). This is also obvious when comparing the magnitude calibration functions for body and surface waves (Figures and tables in DS 3.1).

However, as source depth increases, surface-wave amplitudes decrease relative to those of body waves. The decrease is the larger the shorter the wavelengths. Thus, the surface waves from earthquakes at depth > about 70-100 km may have amplitudes smaller than those of body waves or may not even be detected at all on seismic records (Figure 2 in EX 11.2). This should alert seismogram analysts to look for depth phases, which are then usually well separated from their primary waves and more easily recognizable (Fig. 11.9 above and Figures 6a and b in DS 11.2).

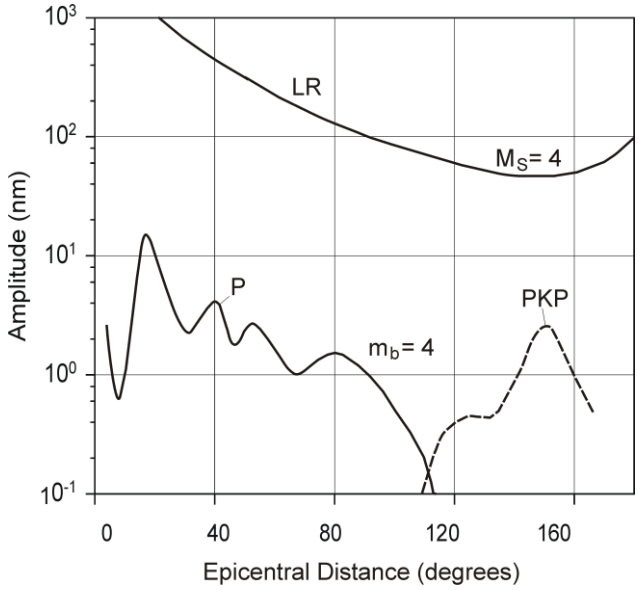

Fig. 11.10 Approximate smoothed amplitude-distance functions for P and PKP body waves (at about 1 Hz) and of long-period Rayleigh surface waves (LR, T ≈ 20 s) for an event of magnitude 4.

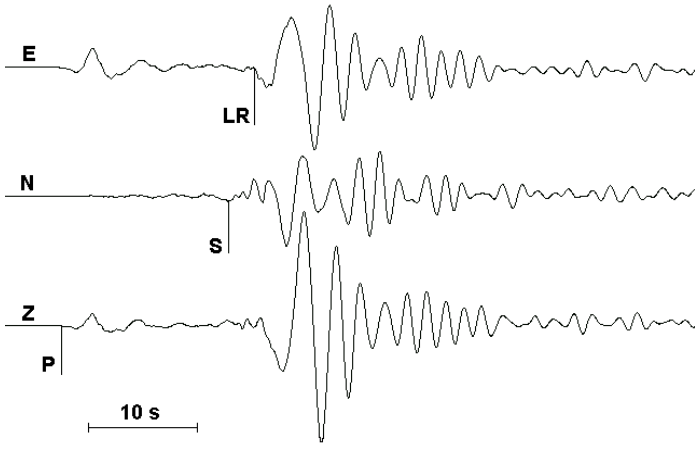

Fig. 11.11 Three-component BB-velocity record at station MOX of a mine collapse in Germany; (13 March 1989; Ml = 5.5) at a distance of 112 km and with a backazimuth of 273°. Note the Rayleigh surface-wave arrival LR with subsequent normal dispersion.

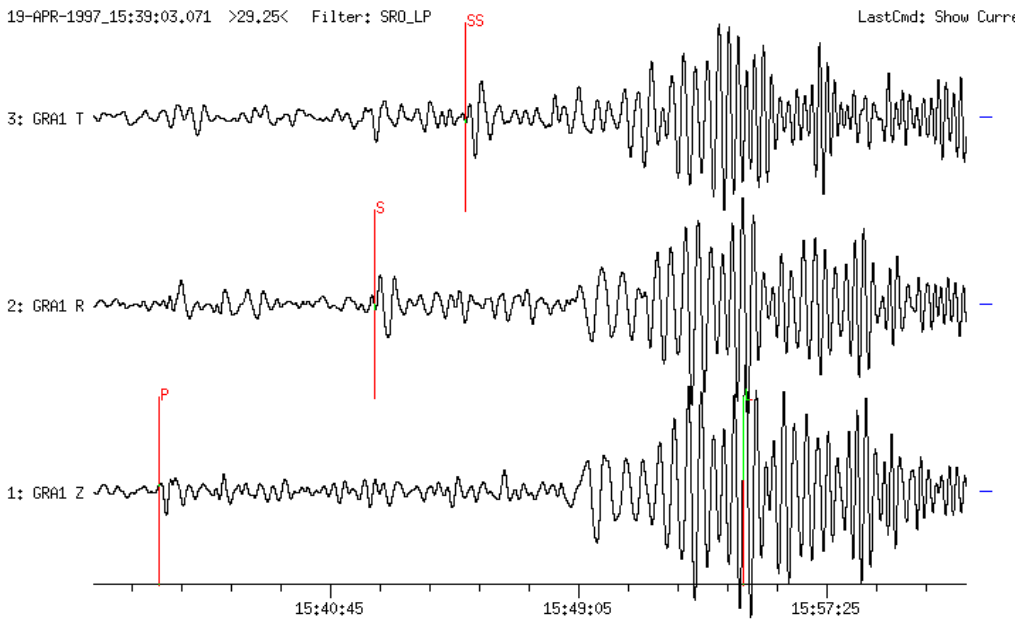

Fig. 11.12 T-R-Z rotated three-component seismogram (SRO-LP filter) from an earthquake east of Severnaya Zemlya (19 April 1997, D = 46.4°, mb = 5.8, Ms = 5.0). The record shows P, S, SS and strong Rayleigh surface waves with clear normal dispersion. The surface wave maximum has periods of about 20 s. It is called an Airy-phase and corresponds to a minimum in the dispersion curve for continental Rayleigh waves (Fig. 2.10).

Another feature that helps in phase identification is the waveform. Most striking is the difference in waveforms between body and surface waves. Dispersion in surface waves results in long wave trains of slowly increasing and then decreasing amplitudes, whereas non-dispersive body waves form short duration wavelets. Usually, the more long-period surface waves arrive first ("normal" or "positive" dispersion) (as in Figs. 11.11 and 11.12). However, very long-period waves (T > 60 s to about 200 s), that penetrate into the upper mantle down to the asthenosphere (a zone of low wave speeds), may show inverse dispersion. The longest waves then arrive later in the wave train (Figs. 2.20 and 11.15).

For an earthquake of a given seismic moment, the maximum amplitude of the S wave is about five-times larger at source than that of the P waves (Fig. 11.13 left and Figs. 2.4, 2.25, and 2.50). This is a consequence of the different propagation velocities of P and S waves [see Eq. (3.2) in Chapter 3]. Also the spectrum is different for each wave type. Thus, P-wave source spectra have corner frequencies about $\sqrt{3}$ times higher than those of S. In high-frequency filtered records this may increase P-wave amplitudes with respect to S-wave amplitudes (Fig. 11.13 right). Additionally, the frequency-dependent attenuation of S waves is significantly larger than for P waves (Chapter 2, section 2.5.4.2). Due to both effects, S waves and their multiple reflections and conversions are – within the teleseismic distance range – mainly observed on LP or BB records. On the other hand, the different P-wave phases, such as P, PcP, PKP, and PKKP, are well recorded, up to the largest epicentral distances, by SP seismographs with maximum magnification typically around 1 Hz.

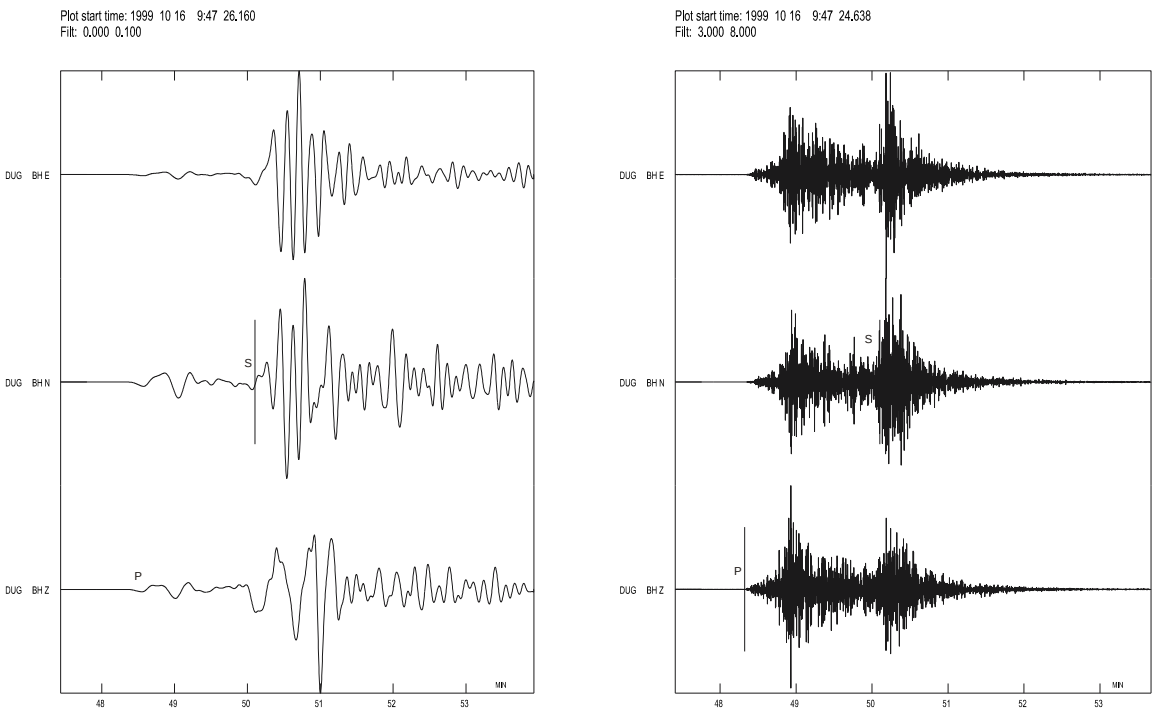

Fig. 11.13 Left: Low-pass filtered (< 0.1 Hz) and right: band-pass filtered (3.0-8.0 Hz) seismograms of the Oct. 16, 1999, earthquake in California (mb = 6.6, Ms = 7.9) as recorded at the broadband station DUG at D = 6° (courtesy of L. Ottemöller).

Generally, the rupture duration of earthquakes is much longer than the source process of explosions (milliseconds). It ranges from less than a second for small micro-earthquakes up to several minutes for the largest earthquakes with a source which is usually a complex multiple rupture process (e.g., Figs. 11.14, 3.9 and 3.23 and the animations in sections 2.6 of IS 1.1).

As compared to shallow crustal earthquakes, deep earthquakes of comparable magnitude are often associated with higher stress drop and smaller source dimension. This results in the strong excitation of higher frequencies and thus more simple and impulse-like waveforms (e.g. Figs. 11.15, 2.64, 4.14 and Figures 6a and b in DS 11.2). Therefore, S waves from deep earthquakes may be recognizable even in short-period records at teleseismic distances.

The waveforms of first arriving P waves from underground nuclear explosions (UNE) are in many cases rather impulsive too but associated with comparably small S waves. As compared to shallow earthquakes and when scaled to the same magnitude, the source dimension of an UNE is usually much smaller, their source process simpler and their source duration much shorter (typically in the range of milliseconds). Accordingly, explosions generate significantly more high-frequency energy than earthquakes and usually produce shorter and simpler waveforms of the P first arrivals. However, since their source depths is rather small, typically ranging between several hundred to less than 2000 m, these high frequency waves are prone to scattering and multi-pathing at upper crustal heterogeneities and the near-surface topography, thus producing strong signal-generated coda in local and regional records. Examples of regionally and (less complicated) teleseismically recorded waveforms of underground nuclear explosions are given in Fig. 2.17 and Figures 1 to 5 of DS 11.4, respectively.

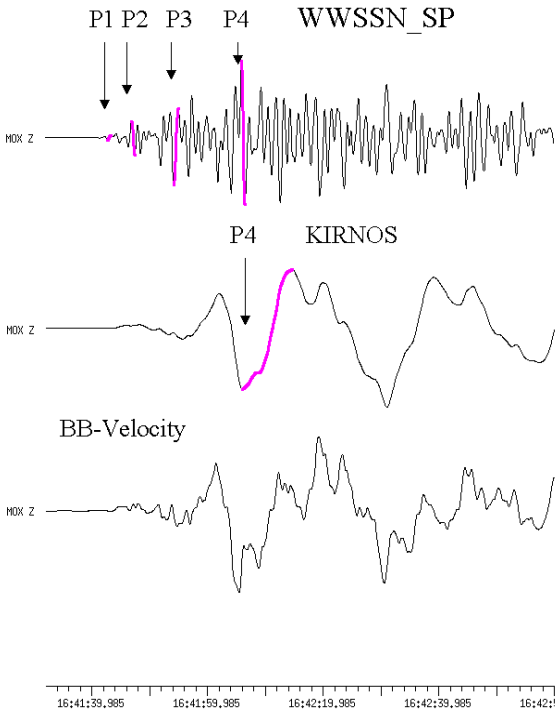

Fig. 11.14 Vertical component records of the P-wave group from a crustal earthquake in Sumatra (04 June 2000; mb = 6.8, Ms = 8.0) at the GRSN station MOX at D = 93.8°. **Top:** WWSSN-SP (type A); **middle:** medium-period Kirnos SKD BB-displacement record (type C), and **bottom:** original BB-velocity record. Clearly recognizable is the multiple rupture process with P4 = P_{max} arriving 25 s after the first arrival P1. The short-period magnitude mb determined from P1 would be only 5.4, mb = 6.3 from P2 and mb = 6.9 when calculated from P4. When determining the medium-period broadband body-wave magnitude from P4 on the Kirnos record then one gets mB = 7.4.

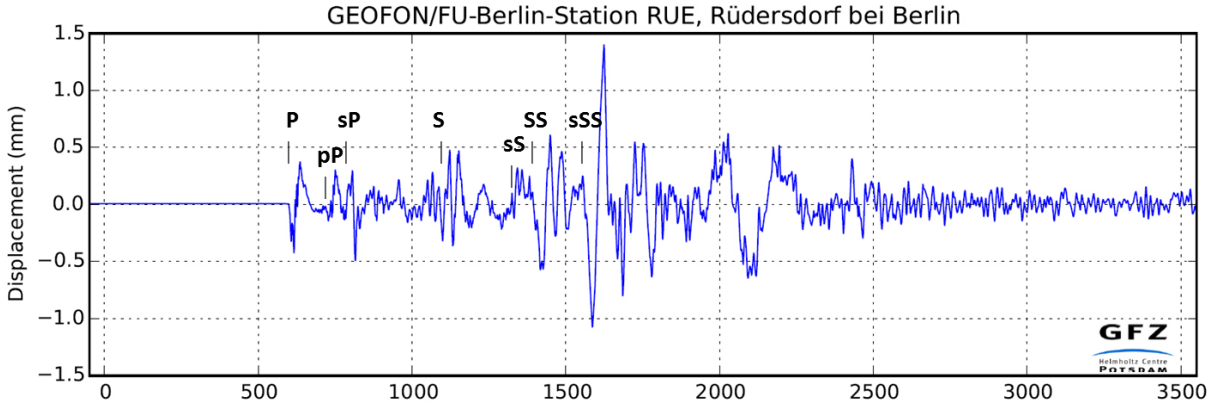

Fig. 11.15 Very broadband vertical component record of the great Mw = 8.2 deep earthquake (h = 609 km) on 24 May 2013 underneath the Okhotsk Sea at station RUE (D = 67.9°), Germany. Note the rather impulsive broadband waveforms of the primary P and S waves and their related depth phases as well as the inverse dispersion of the very long-period mantle surface waves following sSS.

Note, however, that production explosions in large quarries or open cast mines, with yields ranging from several hundred to more than one kiloton TNT, are usually fired in sequences of time-delayed sub-explosions that are spread out over a larger area. Such explosions may generate rather complex wave fields, waveforms and unusual spectra, sometimes further complicated by the local geology and topography, and thus not easy to discriminate from local earthquakes. For discrimination criteria see section 11.2.5.2.

At some particular distances, body waves may have relatively large amplitudes (Fig. 11.10), especially near *caustics* (Figs. 2.30 to 2.33), e.g. for P waves in the distance range between 15° and 30° or around D = 145° for PKP phases (Figs. 11.10 and 11.72). Due to the caustic around 145° PKP amplitudes are about as large as P-wave amplitudes around 50° epicentral distance (Fig. 11.10). The double triplication of the P-wave travel-time curve between 15° and 30° results in closely spaced successive onsets and consequently rather complex waveforms (Fig. 11.63). In contrast, amplitudes decay rapidly in *shadow zones* due to low-velocity layers (Fig. 2.33). In the teleseismic range this applies to direct P for distances beyond 100° in the so-called *core shadow* due to the drastic decay in P-wave velocity in the outer core as compared to the lower mantle (Fig. 2.79). P is then recorded only as diffracted wave Pdif (Figs. 11.7, 11.10, 2.55, 3.34 and example 2 in DS 11.3). At distances between about 30° and 100°, however, long-period waveforms of P and later phases may look rather simple and well separated (Figs. 11.12, 11.17, 11.20, 11.48. 11.52, and 11.63 as well as Figures 8a, 9c, 10c and 11b in DS 11.2). Beyond the PKP caustic, between 145° < D < 160°, longitudinal core phases split into three travel-time branches with typical amplitude-distance patterns. This, together with their systematic relative travel-time differences, permits rather reliable phase identification and distance estimates, often better than 1° (Figs. 11.73 and 11.74 as well as exercise EX 11.3).

Fig. 11.16 is a simplified diagram showing the relative frequency of later body-wave arrivals with respect to the first P-wave arrival or the number n of analyzed earthquakes, as a function of epicentral distance D between 36° and 166°. They are based on observations in standard records (Fig. 3.20 left) of types A4 (SP - T < 1.5 s), B3 (LP – T between 20 s and 80 s) and C (BB displacement for T = 0.1 s - 20 s) at station MOX, Germany (Bormann, 1972a).

These diagrams show that in the teleseismic distance range one can mainly expect to observe in SP records the following longitudinal phases: P, PcP, ScP, PP, PKP (of branches ab, bc and df), P'P' (= PKPPKP), PKKP, PcPPKP, SKP and the depth phases of P, PP and PKP. In LP and BB records, however, additionally S, ScS, SS, SSS, SKS, SKSP, SKKS, SKKP, SKKKS, PS, PPS, SSP and their depth phases are frequently recorded. This early finding based on the visual analysis of traditional analog film recordings has been confirmed by stacking SP and LP filtered broadband records of the Global Digital Seismic Network (GDSN) (Astiz et al., 1996; Figs. 2.57 to 2.60) and most recently by a refined automatic near real-time envelop stacking procedure developed at the IRIS Data Management Center (DMC) (Trabant et al., 2012) (see Fig.11.83).

Since these diagrams or stacked seismogram sections reflect, in a condensed form, some systematic differences in waveforms, amplitudes, dominating periods and relative frequency of occurrence of seismic waves in different distance ranges, they may, when used in addition to travel-time curves and polarization criteria, give some guidance to seismogram analysts as to what kind of phases they may expect at which epicentral distances and in what kind of seismic records or band-pass filter range. Note, however, that the appearance of these phases is not “obligatory” in records of any station. Rather, it may vary from region to region,

depending also on the source mechanisms and the radiation pattern with respect to the recording station, the source depth, the area of reflection (e.g., underneath oceans, continental shield regions, young mountain ranges), and the distance of the given station from zones with frequent deep earthquakes. Therefore, no rigid and globally valid rules for phase identification can be given.

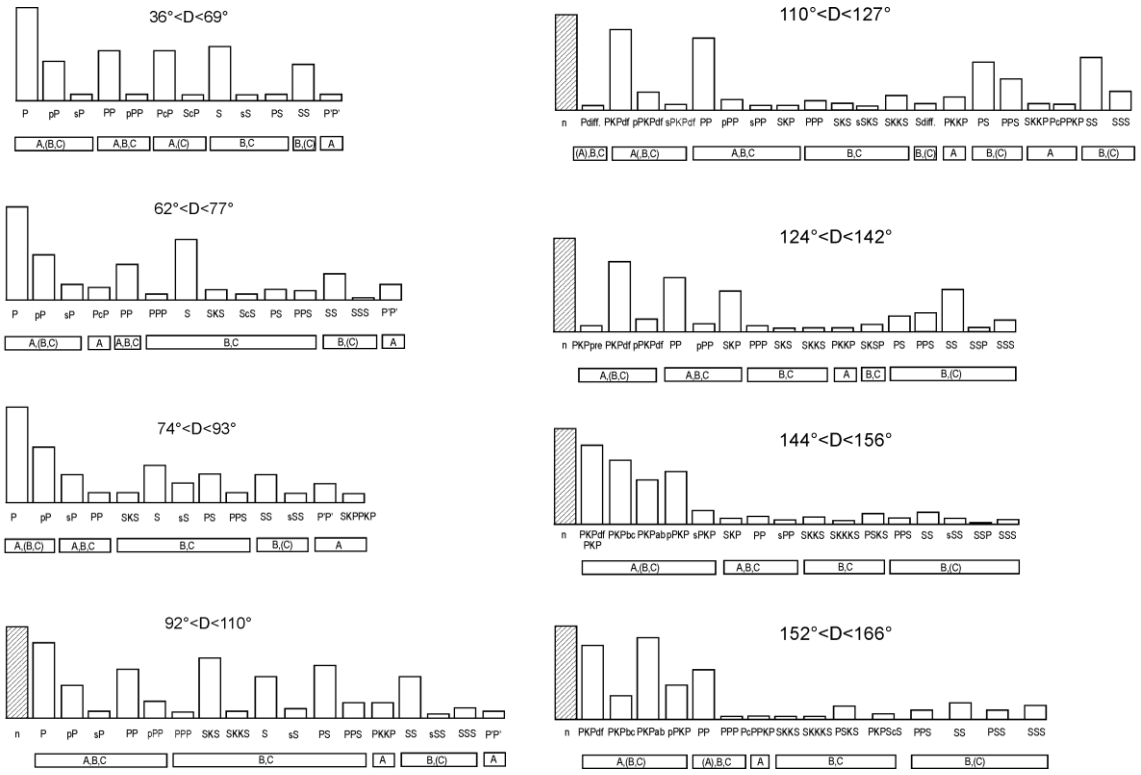

Fig. 11.16 Relative frequency of occurrence of secondary phases in standard analog records at station MOX, Germany, within the teleseismic distance range 36° to 166°. The first column relates to 100% of analyzed P-wave first arrivals or of analyzed events (hatched column), respectively. In the boxes beneath the phase columns the type of standard records is indicated in which these phases have been observed best or less frequently/clear (then record symbols in brackets). A – short-period; B – long-period LP, C – Kirnos SKD BB-displacement according to the respective standard seismograph types in the Willmore (1979) Manual of Seismological Observatory Practice.

Moreover, Fig. 11.16 considers only teleseismic earthquakes. Local and regional earthquakes, however, are mainly recorded by SP seismographs or those with Wood-Anderson response. There are several reasons for this. Firstly, SP seismographs have usually the largest amplification and so are able to record (at distances smaller than a few hundred kilometers) sources with magnitudes of zero or even less. Secondly, as follows from Fig. 3.5, the corner frequency of source displacement spectra for events with magnitudes < 4 is usually > 1 Hz, i.e., small events radiate relatively more high-frequency energy. Thirdly, in the near range the high frequencies have not yet been reduced so much by attenuation and scattering, as they usually are for f > 1 Hz in the teleseismic range. Most local recordings of smaller seismic events (M < 4) show no waves with periods longer than 2 s. However, for Ml > 4, more and

more long-period waves with large amplitudes are generated as well which then dominate also in BB records of local events, as illustrated in Figs. 11.11 and 11.13.

11.2.4.3 Polarization

As outlined in sections 2.2 and 2.3 of Chapter 2, P and S waves are linearly polarized, with slight deviations from this ideal in the inhomogeneous and partially anisotropic real Earth (Figs. 2.7 and 2.8). In contrast, surface waves may either be linearly polarized in the horizontal plane perpendicular to the direction of wave propagation (transverse polarization; T direction; e.g., Love waves) or elliptically polarized in the vertical plane oriented in the radial (R) direction of wave propagation (Rayleigh waves; Figs. 2.9, 2.12, 2.15 and 2.16). P-wave particle motion is dominatingly back and forth in the direction of wave propagation, whereas S-wave motion is perpendicular to it (Fig. 2.6). Accordingly, a P-wave motion can be split into two main components, one vertical (Z) and one horizontal (R) component (Fig. 2.7). The same applies to Rayleigh waves, but with a 90° phase shift between the Z and R components of motion. S waves, on the other hand, may show purely transverse motion, oscillating in the horizontal plane (SH; i.e., pure T component, as Love waves) or motion in the vertical propagation plane, at right angles to the ray direction (SV), or in any other combination of the two components SH and SV, depending on the source mechanisms and the related radiation pattern (Fig. 3.102). In the latter case S-wave particle motion has Z, R and T components, with SV wave split into a Z and an R component. But depending on the incidence angle and the v_P/v_S ratio at the station SV may even show elliptical polarization.

Fig. 11.17 shows the good separation of several main seismic phases on a Z-R-T-component plot. At such a large epicentral distance (D = 86.5°) the incidence angle (between the seismic ray and the vertical: Fig. 2.7) of P is small (about 15°; see EX 3.3). Therefore, the P-wave amplitude is largest on the Z component whereas for PP, which has a significantly larger incidence angle because of its shallower penetration into the mantle (Fig. 11.65), the amplitude on the R component is almost as large as on Z. For both P and PP no T component is recognizable above the noise. SKS is strong in R and has only a small T component (effect of anisotropy, Fig. 2.8). Depending on source depth and the v_P/v_S ratio the two phases PS and SP are more or less separated in time with the PS onset being SV polarized and SP as a P phase, both having a strong Z and R component. Love waves (LQ) appear as the first surface waves in T with very small amplitudes in R and Z. In contrast, Rayleigh waves (LR) are strongest in R and Z. SS in this example is also largest in R. From this one can conclude that the S waves generated by this earthquake and radiated into the direction of the recording station are almost purely of SV type. In other cases, however, it is only the difference in the R-T polarization which allows S to be distinguished from SKS (which is SV polarized; see below) in this distance range of around 80° where these two phases arrive closely to each other (Fig. 11.8 and Figure 11 in EX 11.2 where the E-W component agrees in fact with the R component because of the backazimuth of 269°).

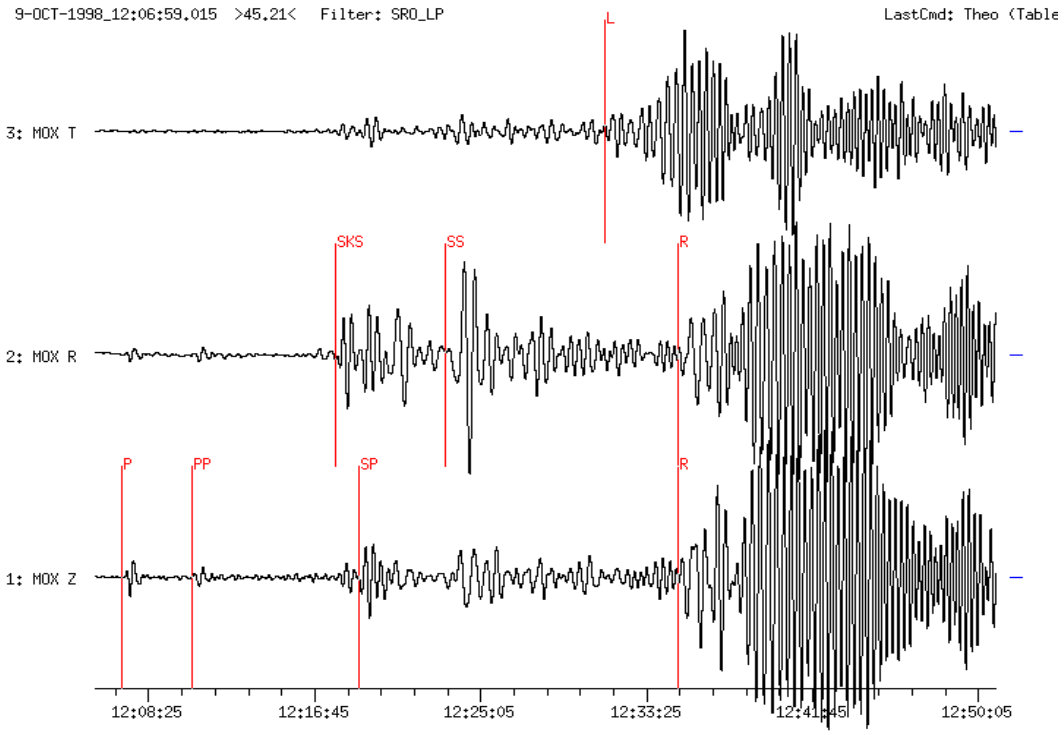

Fig. 11.17 Time-compressed long-period filtered three-component seismogram (SRO-LP simulation filter) of the October 9, 1998, Nicaragua earthquake recorded at station MOX (D = 86.5°). Horizontal components have been rotated (ZRT) with R (radial component) in source direction. The seismogram shows long-period phases P, PP, SKS, SP, SS and surface waves L (or LQ for Love wave) and R (or LR for Rayleigh wave).

Thus, when 3-component records are available, the particle motion of seismic waves in space can be reconstructed and used for the identification of seismic wave types (e.g., Vidale, 1986). However, usually the horizontal seismometers are oriented in geographic east (E) and north (N) direction. Then, first the backazimuth of the source has to be computed (see EX 11.2) and then the horizontal components have to be rotated into the horizontal R direction and the perpendicular T direction, respectively. This *axis rotation* is easily performed when digital 3-component data and suitable analysis software are available. It may even be carried one step further by rotating the R and Z component once more, R into the direction of the incident seismic ray (longitudinal L direction) and Z then being perpendicular to it in the Q direction of the SV component. The T component remains unchanged. Such a *ray-oriented co-ordinate system* separates and plots P, SH and SV waves in 3 different components L, T and Q, respectively (Fig. 11.18). These axes transformations are easily made given digital data from arbitrarily oriented orthogonal 3-component sensors such as the widely used triaxial sensors STS2 (Fig. 5.10 and DS 5.1). However, the principle types of polarization can often be quickly assessed even with manual measurement and elementary calculation of the backazimuth from the station to the source from analog 3-component records (see EX 11.2).

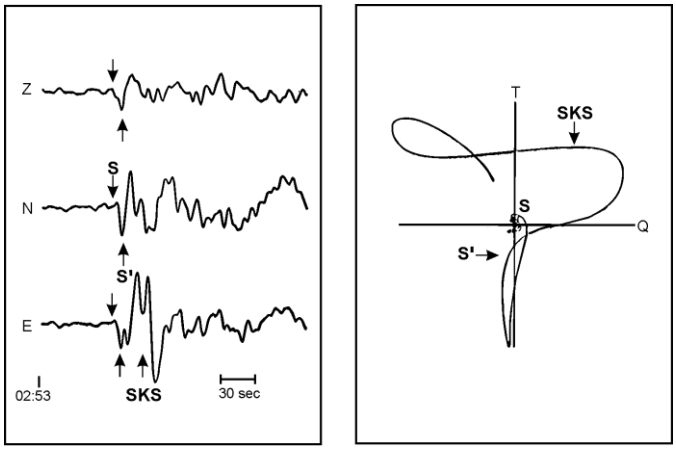

Fig. 11.18 Ray-oriented broadband records (left: Z-N-E components; right: particle motion in the Q-T plane) of the S and SKS wave group from a Hokkaido Ms = 6.5 earthquake on 21 March 1982, at station Kasperske Hory (KHC) at an epicentral distance of D = 78.5°.

According to the above, all direct, reflected and refracted P waves and their multiples such as

Pg, Pn, PnPn, …P, pP, PP, pPP, PPP,…PcP, PKP, PKIKP, PKKP, …PKPPKP(P'P'), …

as well as conversions from P to S and vice versa, such as

pS, sP, SP, PS, SPP, ScP, PKS, SKP, SKPPKP, SKKP, SKS, SKKS, …

have their dominant motion confined to, i.e., are polarized in the Z and R (or L and Q) plane. This applies to all core phases, also to SKS and its multiples, because no shear wave can travel through the liquid outer core and K stands for a longitudinal wave that has traveled through the Earth's outer core and I for a longitudinal wave that has traveled through the Earth's inner core. For ray paths of these waves see Fig. 11.65 and ray plots in IS 2.1.

In contrast, S waves may have both SV and SH energy. However, discontinuities along the propagation path of S waves may act as selective SV/SH filters. Therefore, when an S wave arrives at the free surface, part of its SV energy may be converted into P, thus forming an SP phase. Consequently, the energy reflected as S has a larger SH component as compared to the incoming S. Thus, the more often a mixed SH/SV type of S wave is reflected at the surface, the more it becomes of SH type. Accordingly, SSS, SSSS etc. will show up most clearly or even exclusively on the T component (e.g., Fig. 11.48) unless the primary S wave is dominantly of SV-type (e.g. in Fig. 11.17). As a matter of fact, Love waves are formed through constructive interference of repeated reflections of SH waves at the free surface as well as crustal and upper mantle discontinuities. Similarly, when an S wave hits the core-mantle boundary, part of its SV energy is converted into P which is either refracted into the core with phase name letter K or reflected back into the mantle as P, thus forming the ScP phase. Consequently, multiple ScS is also usually best developed on the T component.

The empirical travel-time curves in Fig. 2.61 (Astiz et al., 1996) summarize rather well, which phases are expected to dominate the vertical, radial or transverse motion in rotated three-component records. If we supplement the use of travel-time curves with seismic recordings in different frequency bands, and take into account systematic differences in

amplitude, frequency content and polarization for P, S and surface waves, and when we know the distances, where caustics and shadow zones occur, then the identification of later seismic wave arrivals is entertaining and like a detective inquiry into the seismic record. It would be regrettable if this art dies out in the age of minimalistic automatic record analysis.

11.2.4.4 Example for documenting and reporting of seismogram parameter readings

Fig. 11.19 shows a plot of the early part of a teleseismic earthquake recorded at stations of the GRSN. At all stations the first arriving P wave is clearly recognizable although the P-wave amplitudes vary strongly throughout the network. This is not a distance effect (the network aperture is less than 10% of the epicentral distance) but rather an effect of different local site conditions related to underground geology and crustal heterogeneity. As demonstrated with Figs. 4.37 and 4.38, the effect is not a constant for each station but depends both on azimuth and distance of the source. It is important to document this. Fig. 11.19 also shows for most stations a clear later arrival about 12 s after P. For the given epicentral distance, no other main phase such as PP, PPP or PcP can occur at such a time (see differential travel-time curves in Fig. 11.8). It is important to pick such later (so-called secondary) onsets which might be "depth phases" (see 11.2.5.1) as these allow a much better determination of source depth than from P-wave first arrivals alone (Figure 7 in IS 11.1).

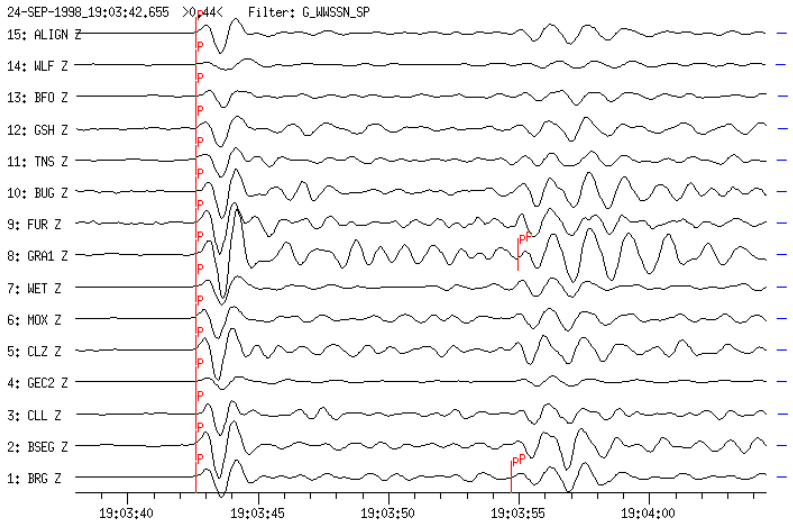

Fig. 11.19 WWSSN-SP filtered seismograms at 14 GRSN, GRF, GERES and GEOFON stations from an earthquake in Mongolia (24 Sept. 1998; depth (NEIC-QED) = 33 km; mb = 5.3, Ms = 5.4). Coherent traces have been time-shifted, aligned and sorted according to epicentral distance (D = 58.3° to BRG, 60.4° to GRA1 and 63.0° to WLF). Note the strong variation in P-wave signal amplitudes and clear depth phases pP arriving about 12 s after P.

Tab. 11.2 gives for the Mongolia earthquake shown in Fig. 11.19 the whole set of parameter readings made at the analysis center of the former Central Seismological Observatory Gräfenberg (SZGRF) in Erlangen, Germany [now: Seismological Central Observatory (SZO) of the BGR in Hannover]:

- first line: date, event identifier, analyst;
- second and following lines: station, onset time, onset character (e or i), phase name (P, S, etc.), direction of first particle motion (c or d), analyzed component, period [s], amplitude [nm], magnitude (mb or Ms), epicentral distance [°]; and
- last two lines: source parameters as determined by the SZGRF (origin time OT, epicentre, average values of mb and Ms, source depth and name of Flinn-Engdahl-region).

Generally, these parameters are stored in a database, used for data exchange and published in lists, bulletins and made available through the Internet (IS 11.2). As an example of station parameter reports grouped according IMS1.0 with ISF1.0 extensions see IS 10.2.The onset characters i (impulsive) should be used only if the time accuracy is better than a few tens of a second, otherwise the onset will be described as e (emergent). Also, when the signal-to-noise-ratio (SNR) of onsets is small and especially, when narrow-band filters are used, the first particle motion should not be given because it might be distorted or lost in the noise. Broadband records are better suited for polarity readings (Figs. 4.10 and 4.11). Their polarities, however, should be reported as u (for "up" = compression) and r (for "rarefaction" = dilatation) so as to differentiate them from short-period polarity readings (c and d, respectively).

Tab. 11.2 Parameter readings at the SZGRF analysis center for the Mongolia earthquake shown in Fig. 11.19 from records of the GRSN.

```
                                                ev_id 980924007     KLI
1998-09-24
    BRG   19:03:27.2  e P       Z  T 1.2  A 135.5   mb 5.9 D 58.3
    ALIGN 19:03:27.2  e P       Z  T 1.1  A 124.1   mb 5.8
    BSEG  19:03:28.2  e P       Z  T 1.1  A 198.3   mb 6.0 D 58.4
    CLL   19:03:28.6  e P       Z  T 0.9  A 98.9    mb 5.8 D 58.5
    GEC2  19:03:36.3  i P     c Z  T 1.2  A 46.9    mb 5.4 D 59.6
    CLZ   19:03:36.6  e P       Z  T 1.1  A 177.7   mb 6.0 D 59.6
    MOX   19:03:36.9  e P       Z  T 1.2  A 122.4   mb 5.8 D 59.6
    WET   19:03:38.5  e P       Z  T 1.2  A 107.2   mb 5.7 D 59.9
    BRG   19:03:39.3  e pP      Z
    GRA1  19:03:42.6  i P     c Z  T 1.1  A 286.5   mb 6.2 D 60.4
                                           b_slo 6.8 b_az  54
    BUG   19:03:48.5  e P       Z  T 1.1  A 162.4   mb 5.8 D 61.4
    FUR   19:03:48.6  e P       Z  T 1.1  A 174.3   mb 5.8 D 61.3
    TNS   19:03:49.9  e P       Z  T 1.1  A 103.0   mb 6.0 D 61.5
    GSH   19:03:54.5  e P       Z  T 1.3  A 132.3   mb 6.0 D 62.3
    GRA1  19:03:55.0  e pP      Z
    BFO   19:03:57.4  e P       Z  T 1.1  A 55.2    mb 5.6 D 62.8
    WLF   19:04:00.1  e P       Z  T 1.7  A 80.3    mb 5.6 D 63.0
    GRA1  19:11:52.2  e S       E                        D 60.4
    GEC2  19:30:36.0  e L       Z  T 19.9 A 3895.8  MS 5.5
    GRA1  19:31:03.6  e L       Z  T 20.6 A 3398.7  MS 5.5

SZGRF  OT 18:53:39.3  45.30N  106.84E    mb_av 5.8 MS_av 5.5
DEP  44km ▲ MONGOLIA
```

Note: For this event the international data center NEIC had "set" the source depth to 33 km because of the absence of reported depth phases. The depth-phase picks at the GRSN, however, with an average time difference of pP-P of about 12 s, give - in dependence of the velocity model in the source region - a focal depth of about 44 km. Also note in Tab. 11.2 the large differences in amplitudes (A) determined from the short-period records of individual stations. Accordingly, the station mb estimates vary between 5.4 and 6.2, which cannot be explained by the small differences in epicentral distance. These are mainly station site effects.

11.2.5 Criteria to be used in event identification and discrimination

11.2.5.1 Discrimination between shallow and deep earthquakes

Earthquakes are often classified on depth as: shallow focus (depth between 0 and 70 km), intermediate focus (depth between 70 and 300 km) and deep focus (depth between 300 and 700 km). However, the term "deep-focus earthquakes" is also often applied to all sub-crustal earthquakes deeper than 70 km. They are generally located in subducting slabs of the lithosphere which are subducted into the mantle. As noted above, the most obvious indication on a seismogram that a large earthquake has a deep focus is the small amplitude of the surface waves with respect to the body-wave amplitudes and the usually rather simple character of the P and S waveforms, which often have impulsive onsets (Fig. 4.15 and Fig. 11.20).

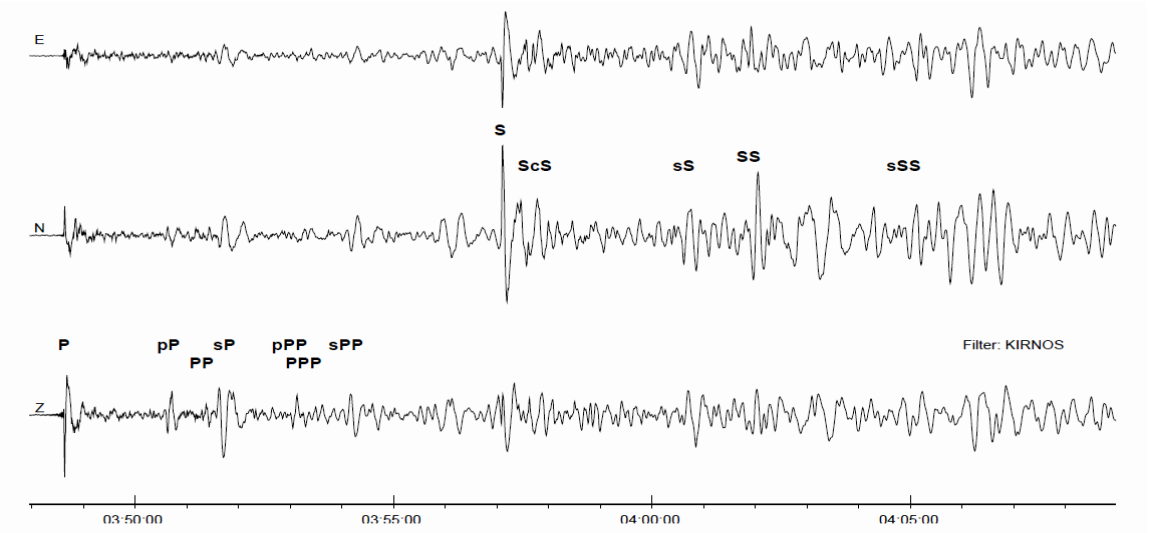

Fig. 11.20 3-component Kirnos SKD filtered record at station CLL (D = 70.6°) of the October 01, 2013 Mw = 6.7 deep earthquake (h = 592 km) underneath the Okhotsk Sea . Note the sharp impulsive body-wave onsets with well-developed depth phases.

In contrast to shallow-focus earthquakes, S phases from deep earthquakes may sometimes be recognizable even in teleseismic short-period records. The body-wave/surface-wave ratio and the type of generated surface waves are also key criteria for discriminating between local earthquakes, which mostly occur at depth larger than 5 km, and quarry blasts, underground explosions or rockbursts in mines, which occur at shallower depth (see 11.2.5.2).

A more precise determination of the depth h of a seismic source, however, requires either the availability of a seismic network with at least one station being very near to the source, e.g., at an epicentral distance D < h (because only in the near range the travel time t(D, h) of the direct P wave varies strongly with source depth h), or the identification of seismic *depth phases* in seismic records. The most accurate method of determining the focal depth of an earthquake in routine seismogram analysis, particularly when only single station or network records at teleseismic distances are available, is to identify and read the onset times of depth phases (Chapter 2, section 2.6.3). A depth phase is a characteristic phase of a wave reflected from the surface of the Earth at a point relatively near the hypocenter (Fig. 2.62). At distant seismograph stations, the depth phases pP or sP follow the direct P wave by a time interval

that changes only slowly with distance but rapidly with depth. The time difference between P and other primary seismic phases, however, such as PcP, PP, S, SS etc. changes much more with distance. When records of stations at different distances are available, the different travel-time behavior of primary and depth phases makes it easier to recognize and identify such phases. Because of the more or less fixed ratio between the velocities of P and S waves with $v_P/v_s \approx \sqrt{3}$ (Chapter 2, section 2.2.3), pP and sP follow P with a more or less fixed ratio of travel-time difference t(sP-P) ≈ 1.5 t(pP-P) (Figs. 11.20 and 11.21). Animations of seismic ray propagation and phase recordings from deep earthquakes are given in files 4, 6 and 9 of IS 11.3.

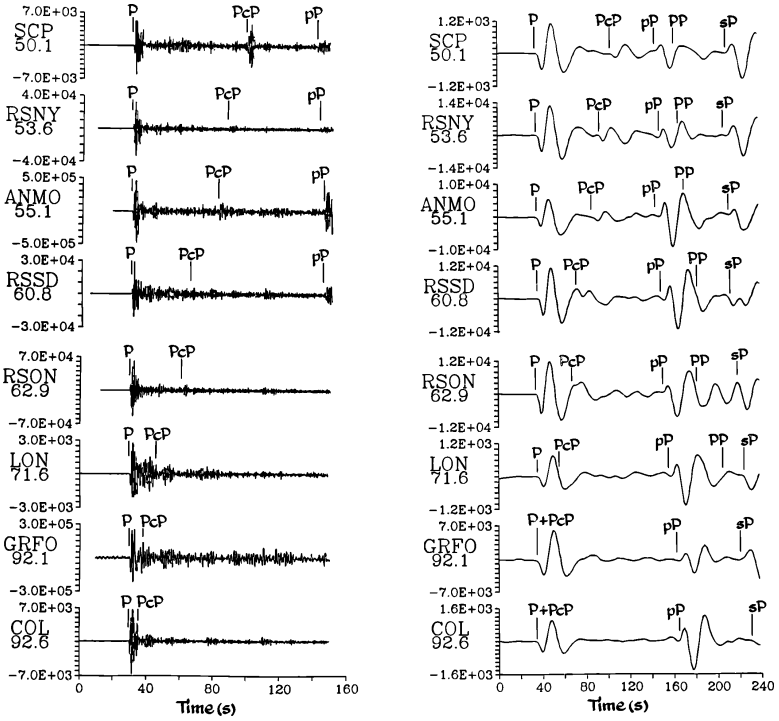

Fig. 11.21 Short-period (left) and long-period (right) seismograms from a deep-focus Peru-Brazil border region earthquake on May 1, 1986 (mb = 6.0, h = 600 km) recorded by stations in the distance range 50.1° to 92.2°. Note that the travel-time difference between P and its depth phases pP and sP, respectively, remains nearly unchanged. In contrast PcP comes closer to P with increasing distance and after merging with P on joint grazing incidence at the core-mantle boundary form the diffracted wave Pdif (reprinted from Anatomy of Seismograms, Kulhánek, Plate 41, p. 139-140; © 1990; with permission from Elsevier Science).

The time difference between pP and sP and other direct or multiple reflected P waves such as pPP, sPP, pPKP, sPKP, pPdif, sPdif, etc. are all roughly the same. S waves also generate depth phases, e.g., sS, sSKS, sSP etc. The time difference sS-S is slightly larger than sP-P (Figs. 1.10 and 11.20). The difference grows with distance to a maximum of 1.2 times the sP-P time. These additional depth phases may also be well recorded and can be used in a similar way for depth determination as pP and sP.

Given the rough distance between the epicenter and the station, the hypocenter depth (h) can be estimated within $\Delta h \approx \pm 10$ km from travel-time curves or determined by using time-

difference tables for depth-phases (e.g., from Δt(pP-P) or Δt(sP-P); see Kennett, 1991 or Table 1 in EX 11.2) or the "rule-of-thumb" in Eq. (11.4) in section 11.2.6.2. An example is given in Fig. 11.22. It depicts broadband records of the GRSN from a deep earthquake (h = 119 km) in the Volcano Islands, West Pacific. The distance range is 93° to 99°. The depth phases pP and pPP are marked. From the time difference pP-P of 31.5 s and an average distance of 96°, it follows from Table 1 in EX 11.2 that the source depth is 122 km. When using Eq. (11.4) instead, we get h = 120 km. This is very close to the source depth of h = 119 km determined by NEIC from data of the global network.

Note that on the records in Fig. 11.22 the depth phases pP and pPP have larger amplitudes than the primary P wave. This may be the case also for sP, sS etc., if the given source mechanism radiates more energy in the direction of the upgoing rays (p or s; Fig. 2.62) than in the direction of the downgoing rays for the related primary phases P, PP or S. Also, in Fig. 11.22, pP, PP and pPP have longer periods than P. Accordingly, they are more coherent throughout the network than the more short-period P waves. Fig. 11.48 shows for the same earthquake the LP-filtered and rotated 3-component record at station RUE, Germany, with all identified major later arrivals being marked on the record traces. This figure is an example of the search for and comprehensive analysis of secondary phases.

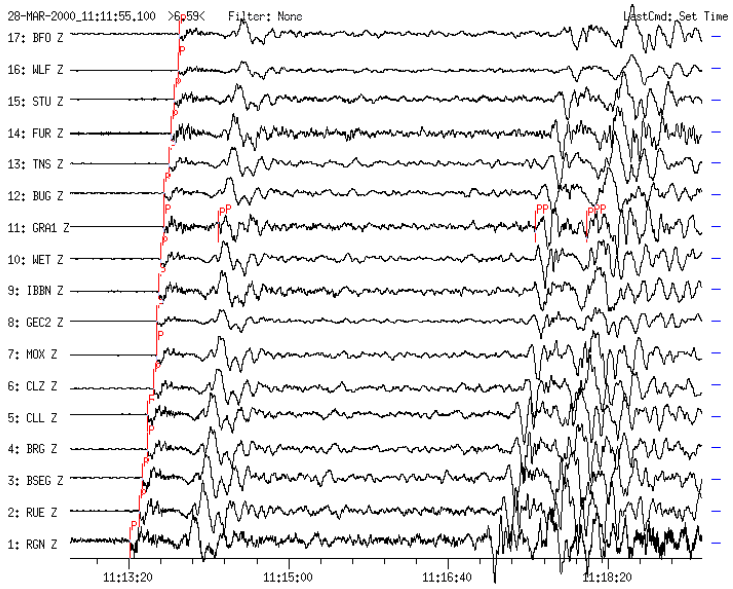

Fig. 11.22 Broadband vertical-component seismograms of a deep (h = 119 km) earthquake from Volcano Islands region recorded at 17 GRSN, GRF and GEOFON stations. (Source data by NEIC: 2000-03-28 OT 11:00:21.7 UT; 22.362°N, 143.680°E; depth 119 km; mb 6.8; D = 96.8° and BAZ = 43.5° from GRA1). Traces are sorted according to distance. Amplitudes of P are smaller than pP. Phases with longer periods PP, pP and pPP are much more coherent than P.

Crustal earthquakes usually have a source depth of less than 30 km, so the depth phases may follow their primary phases so closely that their waveforms overlap. Identification and onset-time picking of depth phases is then usually no longer possible by simple routine visual inspection of the record. Therefore, in the absence of depth phases reported by seismic stations, international data centers such as NEIC in its Monthly Listings of Preliminary (or

Quick) Determination of Epicenters often fix the source depth of (presumed) crustal events at 0 km, 10 km or 33 km, as has been the case for the event shown in Fig. 11.19. This is often further specified by adding the capital letter N (for "normal depth" = 33 km) or G (for depth fixed by a geophysicist/analyst). Waveform modeling, however (Fig. 2.85), may enable good depth estimates for shallow earthquakes to be obtained from the best fit of the observed waveforms to synthetic waveforms calculated for different source depth. Although this is not yet routine practice at individual stations, the NEIC has, since 1996, supplemented depth determinations from pP-P and sP-P by synthetic modeling of BB-seismograms. The depth determination is done simultaneously with the determination of fault-plane solutions. This has reduced significantly the number of earthquakes in the PDE listings with arbitrarily assigned source depth 10G or 33N.

Note, however, that often there is no clear evidence of near-source surface reflections in seismic records, or they show apparent pP and sP but with times that are inconsistent from station to station. Douglas et al. (1974 and 1984) have looked into these complexities, particularly in short-period records. Some of these difficulties are avoided in BB and LP recordings. Also, for shallow sources, surface-wave spectra may give the best indication of depth but this method is not easy to apply routinely. Notably, Engdahl et al. (1998) developed an automatic phase identification algorithm, termed EHB for short. It aims at significantly improved hypocenter relocations. EHB is applied to the phase group which immediately follows the P phase at teleseismic distances, including pP, pwP, sP and PcP and allows also the unambiguous identification of later phases such as S. The EHB bulletin is available at the ISC website http://www.isc.ac.uk/. The EHB bulletin covers the period 1960-2008 and represented a significant improvement in routine hypocenter determinations made by PDE and ISC before data year 2009, when the ISC implemented a new location algorithm (Bondár and Storchak, 2011). The new ISC location algorithms matches the quality of the EHB bulletin and attempts to obtain a free-depth solution if enough depth resolution is available. Therefore, the ISC would benefit from from reports of carefully picked depth phases.

In summary, observational seismologists should be aware that depth phases are vital for improving source locations and making progress in understanding earthquakes in relation to the rheological properties and stress conditions in the lithosphere and upper mantle. Therefore, they should do their utmost to recognize depth phases in seismograms despite the fact that they are not always present and that it may be difficult to identify them reliably. More examples of different kinds of depth phases are given in Figure 6b of DS 11.2 and Figures 1b, 2b, 5b and 7a+b in DS 11.3.

11.2.5.2 Discrimination between natural earthquakes and man-made seismic events

Quarry and mining blasts as well as controlled explosion charges may excite strong seismic waves. The largest of these events usually have local magnitudes in the range 2 to 4 and may be recorded over distances of several to several thousand kilometersFig. Rock bursts or collapses of large open galleries in underground mines may also generate seismic waves. The magnitude of these induced seismic events may range from around 2 to 5.5 and their waves may be recorded world-wide (as it was the case with the mining collapse shown in Fig. 11.11). In some countries with low to moderate natural seismicity but a lot of blasting and mining, anthropogenic (so-called "man-made" or "man-induced") events may form a major fraction of all recorded seismic sources and even outnumber recordings of earthquakes. Then a major seismological challenge is the reliable discrimination of different source types.

According to Figs. 2.38 in Chapter 2 and Figures 4 and 5 in DS 11.4 the amplitude ratio P/S for chemical or underground nuclear explosions is generally larger than for tectonic earthquakes that are dominantly shear fractures. Fig.11.23 shows a comparison of seismograms from: (a) a mining-induced seismic event; (b) a quarry blast; (c) a local earthquake; (d) a regional earthquake. According to (a) and (b) the high-frequency body-wave arrivals are followed, after Sg, by well-developed lower-frequency and clearly dispersed crustal Rayleigh surface waves (Rg, with strong vertical components). This is not the case for the two earthquake records (c) and (d) because earthquakes, which are usually more than a few kilometers deep, do not generate short-period fundamental Rayleigh waves of Rg type. For even deeper (sub-crustal) earthquakes (e.g., Fig. 2.50) only the two high-frequency P- and S- wave phases are recorded within a few hundred kilometers from the epicenter.

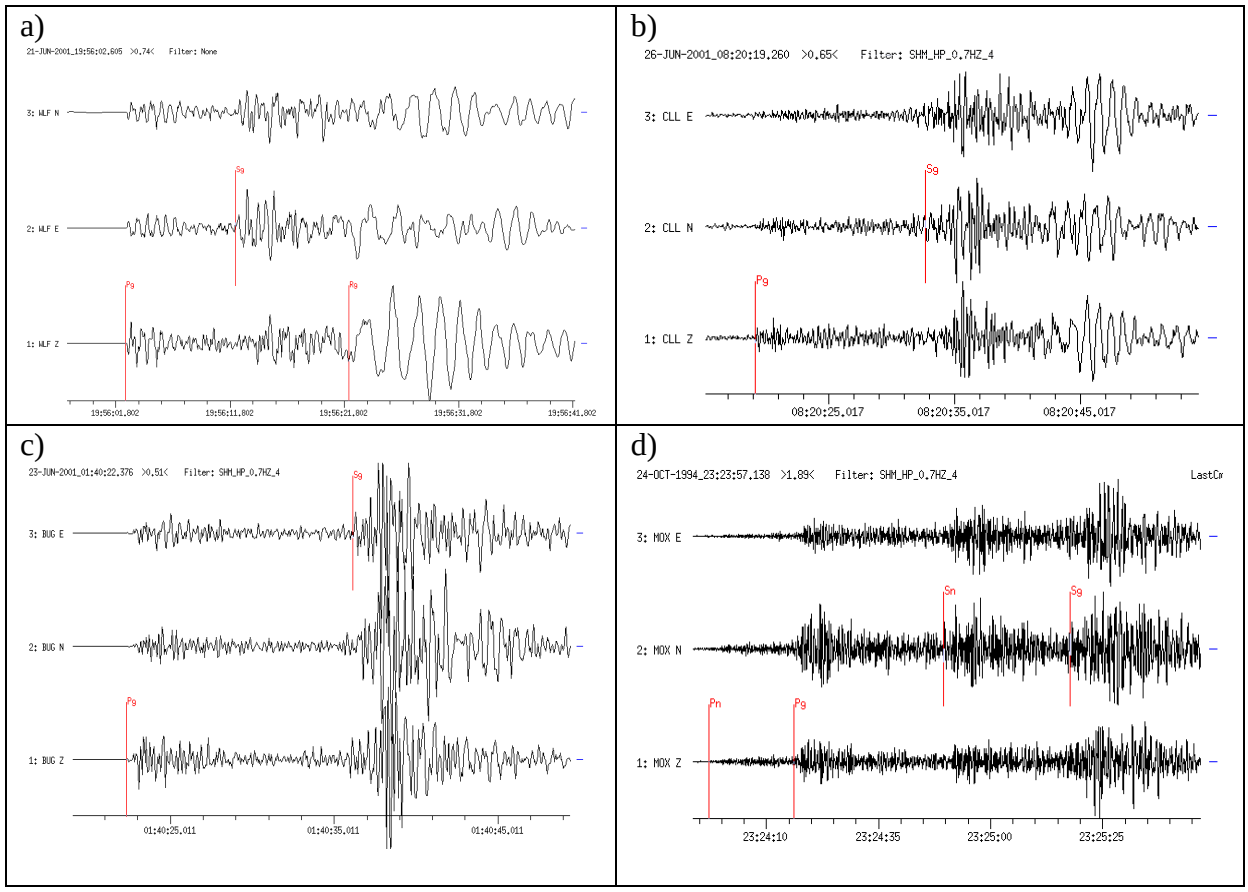

Fig. 11.23 Examples of 3-component seismograms recorded from a: a) mining-induced seismic event (D = 80 km); b) quarry blast explosion (D = 104 km); c) local earthquake (D = 110 km); d) regional earthquake (D = 504 km). Note the different time scales.

Some observatories that record many quarry blasts and mining events, such as the SZGRF, have developed automatic discrimination filters on the basis of such systematic differences in frequency content and polarization. They allow routine separation of such man-made or induced seismic events from tectonic earthquakes. Chernobay and Gabsatarova (1999) give references to many other algorithms for (semi-) automatic source classification. These authors tested the efficiency of the spectrogram and the Pg/Lg spectral ratio method for routine

discrimination between earthquakes in the Northern Caucasus area of Russia with magnitudes < 4.5 and chemical (quarry) explosions of comparable magnitudes. They showed that no single method can yet assure reliable discrimination between seismic signals from earthquakes and explosions in this region. However, by applying a self-training algorithm, based on hierarchical multi-parameter cluster analysis, almost 98% of the investigated events could be correctly classified and separated into 19 groups of different sources. However, local geology and topography as well as earthquake source mechanisms and applied explosion technologies may vary significantly from region to region. Therefore, there exists no straightforward and globally applicable set of criteria for reliable discrimination between man-made and natural earthquakes, thus requiring specific investigations for different regions.

In this context one should also discuss the discrimination between natural earthquakes (EQ) and underground nuclear explosions (UNE). The Comprehensive Nuclear-Test-Ban Treaty (CTBT) has been negotiated for decades as a matter of high political priority. A Preparatory Commission for the CTBT Organization (CTBTO) has been established with its headquarters in Vienna (http://ctbto.org) which is operating an International Monitoring System (IMS; Fig. 15.2 in Chapter 15). Agreement was reached only after many years of demonstrating the potential of seismic methods to discriminate underground explosions from earthquakes, down to rather small magnitudes mb ≈ 3.5 to 4. Thus, by complementing seismic event detection and monitoring with hydro-acoustic, infrasound and radionuclide measurements it is now highly probable that test ban violations can be detected and verified.

The source process of UNEs is simpler and much shorter than for earthquake shear ruptures. Accordingly, P waveforms from explosions are shorter, have higher predominant frequencies, are usually more impulse-like than for earthquakes and expected to have compressional first motions in all directions. Also, UNEs generate lower amplitude S and surface waves than earthquakes of the same body-wave magnitude (Figs. 11.24 and 11.25).

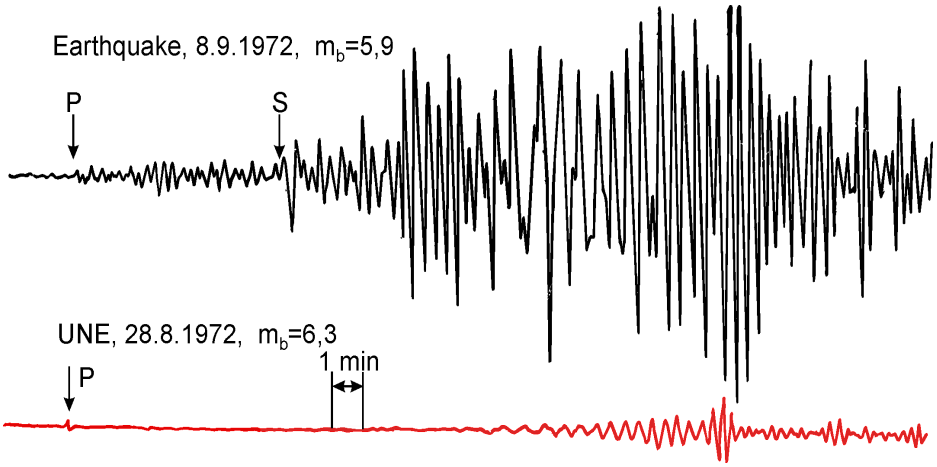

Fig. 11.24 Broadband displacement records at station Moxa (MOX), Germany of a Jan Mayen earthquake and a Semipalatinsk underground nuclear explosion (UNE) of comparable short-period body-wave magnitude mb and at nearly the same distance of about 40°.

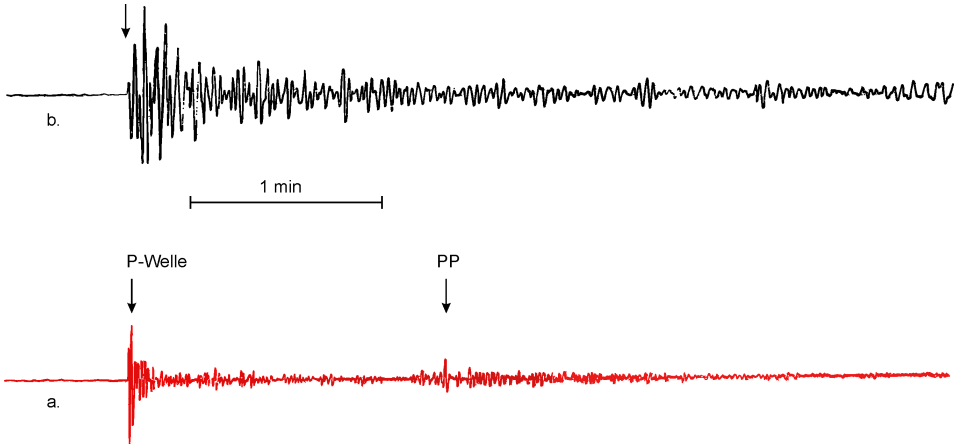

Fig. 11.25 Short-period records at station MOX a) of an underground nuclear explosion at the Semipalatinsk (SPT) test site in Kazakhstan (D = 41°) and b) of an earthquake in Afghanistan with comparable magnitude around 6 and at similar distance.

A powerful discriminant is the ratio between short-period P-wave magnitude mb and long-period surface-wave magnitude Ms. The former samples energy around 1 Hz while the latter samples long-period energy around 0.05 Hz. Accordingly, much smaller Ms/mb ratios are observed for explosions than for earthquakes (Fig. 11.26). Whereas for a global sample of EQs and UNEs the two populations overlap in an Ms/mb diagram, the separation is good when earthquakes and explosions in the same region are considered (e.g., Bormann, 1972c). Early studies have shown that with data of mb ≥ 5 from only one teleseismic station 100% of the observed UNEs with such magnitudes from the Semipalatinsk (SPT) test site could be separated from 95% of the EQs in Middle Asia (Fig. 11.26 left), whereas for the more distant test site in Nevada (D = 81°) 95% of the UNEs could be discriminated from 90% of the EQs in the Western USA and Middle America (Fig. 11.26 right).

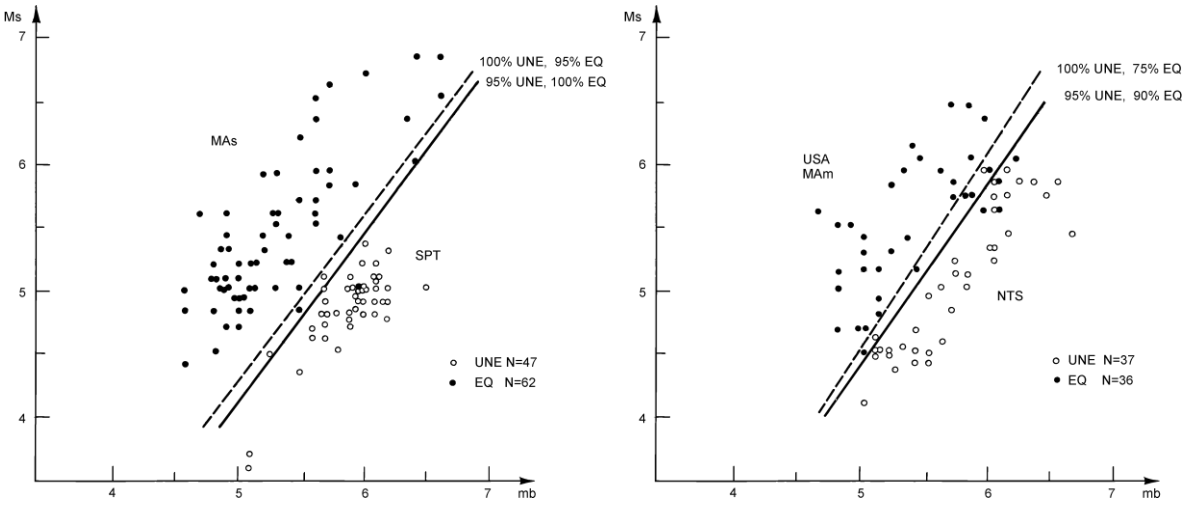

Fig. 11.26 Separation of EQs and UNEs by the Ms/mb criterion according to data collected at station MOX, Germany. **Left:** for Middle Asia and the test site in Semipalatinsk (SPT); **Right:** for USA/Middle America and the Nevada test site (NTS).

Bowers and Walter (2002) published a similar mb-Ms diagram for US earthquakes and UNE with an average offset of about 0.8 mb units at Ms = 5, which is comparable with Fig. 11.26 and corresponds to about 6 times larger P-wave amplitudes around 1 Hz for explosions than for earthquakes with the same surface wave magnitude.

Other potential discrimination criteria, such as the different azimuthal distribution of P-wave first-motion polarities expected from UNEs (always +) and EQs (mixed + and -), have not proved to be reliable. One reason is, that due to narrowband filtering, which is applied to reach the lowest possible detection threshold, the P waveform, and particularly the first half cycle, is often so much distorted, that the real first-motion polarity is no longer recognizable in the presence of noise (Figs. 4.10 and 4.11). Detailed investigations also revealed that simplified initial model assumptions about the difference between explosion and earthquake sources do not hold. Surprisingly, the explosion source is poorly understood and source dimensions around magnitude mb ≈ 4 seem to be about the same for earthquakes and explosions. Also, many explosions do not approximate to a point-like expansion source in a half-space: significant Love waves may be generated (e.g., by Novaya Zemlya tests in a terrain of rough topography or by triggered tectonic stress release) and many P-wave seismograms show arrivals that cannot be explained (see, e.g., Douglas and Rivers, 1988). Further, it has become clear that much of the differences observed between records of UNEs and EQs are not due to source differences but rather to differences in the geology, topography and seismotectonics of the wider area around the test sites, and that this necessitates the calibration of individual regions (e.g., Douglas et al., 1974).

In summary, one can say that the key criteria to separate EQs and explosions usually work well for large events, however, difficulties come with trying to identify every EQ down to magnitudes around mb = 4 with an average of about 8000 earthquakes of this size per year. It is beyond the scope of this section to go into more detail on this issue. For CTBTO goals and procedures see Chapter 15. State-of-the-art summaries have been published by Bowers and Selby (2009), CTBTO PrepComm, (2009; http://www.ctbto.org/verification-regime/), Dahlman et al. (2009), Richards (2002) and Richards and Wu (2011).

11.2.6 Quick event identification and location by means of single-station three-component recordings

Recognizing earthquakes in and locating them by means of seismic records, including also their size classification, are the most important tasks of observatory seismology. Increasingly seismograms are being analyzed at centers that receive the data in (near) real time from networks or arrays of seismometers (Chapters 8 and 9). The seismograms can then be analyzed jointly. This has clear advantages. Nevertheless, some seismic stations are still treated as single station for basic processing. Some of them still record with analog techniques. Yet much can be done even under these “old-fashioned” conditions by the station personnel, provided that at least some form of 3-component recording, either BB or both SP and LP, is available. If these records are in digital form, which is nowadays common, then modern software for digital seismogram analysis will make this task much easier and faster than in the “analog past”. But for most users of ready-made analysis software packages these tools are “black boxes”. Surely, to go through the various steps of analog and graphical location or other related seismological analysis procedures, is much more time consuming. This makes their application unacceptable in modern operational observatory practice. But the

classical analog procedures tell us much more about the underlying principles that are now implemented in algorithmic form in the analysis software. Therefore, those interested in the history of observatory practice but also students in undergraduate Earth science or "Seismology at Schools" courses should have taken note of and practized them oneself, at least once, to get the necessary "feeling". The same applies to the sections 11.2.7 on seismic network recordings and 11.2.8 on magnitude determinations, which also give reference to related basic exercises by hand. But all has to start with the single station seismogram analysis.

11.2.6.1 What to do with single station seismograms?

3-component records allow to quickly asses the source type and to roughly estimate the source location and event magnitude. Moreover, later seismic phases can be identified in quite some detail, even if rapid epicenter determinations by international data centers are not available. There would be advantages if, in future, such readings of secondary phases, especially of depth phases, will be reported as early as possible to regional and global data centers so as to enable better depth determinations. Indeed, only recently both NEIC and the ISC introduced more flexible and sophisticated algorithms and the AK135 travel-time model in order to make better use also of secondary phase readings for more reliable hypocenter locations. Locations derived in near real-time usually have not yet well constrained source depths since they are based only on first arriving P and (eventually) S.

It has also been realized that epicentral distances estimated from three-component broadband readings of secondary phases may significantly improve location estimates by small seismic array stations that are based on measurements of the P-wave vector slowness only. The reason is that the travel-time differences between P and later arriving phases, especially of S and SS, vary much more with distance than the first P-wave arrival-time and thus the first P-wave slowness differences at the various stations. Other procedures of modern multi-station (but usually single-component) data analysis are mentioned later *en passant*. Array analysis is discussed in detail in Chapter 9.

How one may proceed when analyzing interactively single station 3C-seismograms without having any prior information about the source and aiming at event location is outlined in EX 11.2 which may be suitable also for demonstration or a practical in "Seismology at Schools" sessions. Additionally, one might look for criteria discussed in sub-section 11.2.5.2 for discriminating between explosions and earthquakes.

If modern broadband digital records are available, which are usually proportional to ground velocity, it is recommended to filter them to produce simulated standard analog Wood-Anderson (WA), WWSSN-SP and -LP seismograms (for responses see Fig. 11.38). Because these types of records are required for proper estimation of the most frequently measured classical types of magnitudes (ML, mb and Ms_20) according to recently established IASPEI measurement standards (Chapter 3 and IS 3.3) and they may also ease phase identification by mutual inspection. One may also simulate Kirnos SKD BB-displacement and SRO-LP responses (Fig. 11.38) which are particularly suitable for later phase identification in the teleseismic range. This is documented in the following and in DS 11.2 and 11.3 with many record examples. The detailed seismogram analysis might then include phase identification, picking of onset times, amplitudes, periods and polarities, and, if required, also the application of special filters, such as the inverse Hilbert transformation, to phases that have been distorted

by traveling through internal caustics (Chapter 2, section 2.5.4.3), or for identifying phases on the basis of their different polarization.

Of course, in countries with many seismic events recorded every day it will not be possible, particularly for untrained analysts, to apply all these criteria to every recording. On the other hand, this kind of checking takes only a few seconds, minutes at most, for an experienced interpreter who has already trained himself/herself in recognizing immediately the different record patterns on seismograms from systems with standard responses. In addition, many data centers specialize in analyzing only seismograms from local, regional or teleseismic sources. Accordingly, either the number of questions to be asked to the record or the number of signals to be analyzed will be reduced significantly. Also, the task might be significantly eased at observatories or analysis centers which have advanced routines available for digital seismogram analysis such as SEISAN, Seismic Handler (SHM) or SeisComp3. Provided that first hypocenter estimates are already available from international data centers or from own automatic real-time analysis of array or network recordings (e.g., by using SeisComp3), these computer programs allow the theoretical onset times of expected seismic phases to be displayed on the seismogram. However, these theoretical times should not be followed blindly but considered only as assistance. The additional information on amplitudes, frequency content, and polarization has to be taken into account before giving a definite name to a recognizable onset (see 11.2.4 and 11.2.5).

On the other hand, it is meaningless to list more detailed and strict criteria and rules about the appearance and identification of seismic phases in different distance ranges, because they vary from event to event and from source region to source region. They also depend on the specific conditions along the wave-propagation paths and at the recording site. Therefore, every station operator or network analyst has to develop, through experience and systematic data analysis, his/her own criteria for improved seismogram analysis, phase and source identification, and source location. In any event, however, the general approach to record analysis given above should be followed in order to avoid the analysis becoming thoughtless, boring and routine, which would inevitably result in the reporting of inhomogeneous and incomplete low-quality data of little value for research or to the general user.

11.2.6.2 3-component hypocenter location

If well calibrated 3-component broadband and/or long-period recordings are available then it is possible to locate sufficiently strong local events (Ml > 3) and teleseismic sources (mb > 5) with an accuracy comparable to or even better than those for un-calibrated arrays or station networks, which, however, should nowadays no longer exist Yet, this could be demonstrated already some 40 years ago (Bormann, 1971a and b) by using standard film records of type A, B and C (for responses see Fig. 3.20). Amplitudes and onset times were at that time still measured by using an ordinary ruler or a sub-millimeter scaled magnification lens. Nevertheless, the mean square error of epicenters thus located within the distance range 20° < D < 145° was less than 300 km when compared with the epicenter coordinates published by the seismological World Data Centers A and B. This result compares well with the 4° cap location constraint achieved by the fully automatic multi-parameter processing procedure developed by Tong and Kennett (1996) for single 3-component broadband seismograms.

Fig. 11.27 shows the statistical distribution of errors in azimuth and distance based on several hundred 3-component event locations made between 1966 and 1968 at station MOX,

Germany. The errors in epicentral distance estimates, based on reading the S-P times in Kirnos BB records, were in the range 15° < D < 80° in 90% of the cases less than ±1° and in the range 80° < D < 120° also mostly less than about ±1° and rarely greater than ±2°. For 100° < D < 165°, when using in the core shadow of P time differences between other seismic phase arrivals, the errors are somewhat larger, but even then the mean errors seldom differed significantly from zero, and where they did this was usually related to specific source regions, respectively distance/azimuth ranges. This was better than for the automatic Tong and Kennett (2000) procedure for which the authors report that "…in most cases the estimated distances are within the error of 7%."

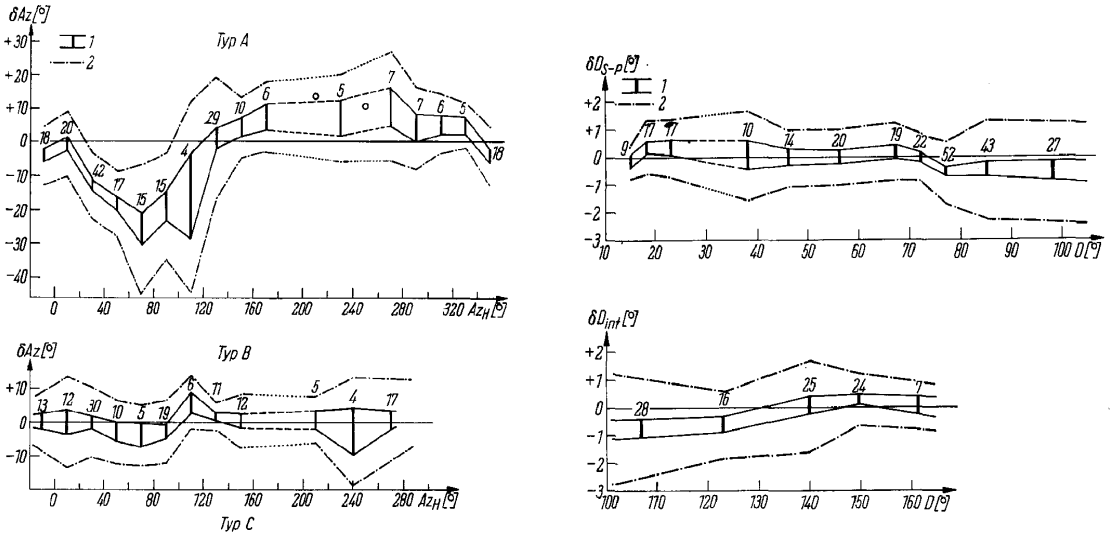

Fig. 11.27 Left: Errors in backazimuth Az (or BAZ) at station MOX estimated using 3-component records of type A (SP) and of type C (Kirnos SKD BB-displacement). **Right:** Errors in estimating the epicentral distance D at station MOX from records of type C using travel-time difference S-P in the distance range 10° < D < 100° or travel-time differences between other seismic phases for D > 100°. The solid lines give the 90% confidence interval for the mean error with number of the observations; the dash-dot lines are the 90% confidence interval for a single observation within different distance intervals. Figure according to Bormann (1971b)

When measuring BAZ on short-period records systematic errors may be rather large, reaching up to several tens of degrees (Fig. 11.27 upper left). In contrast, when BAZ is determined on LP or BB records (provided that the magnification of the horizontal components is identical or known with high accuracy) than the BAZ errors are much less, with about 90% probability within ±10° (Fig. 11.27 lower left). Here the Tong and Kennett (1996) results are better, at least for events at distances up to 100°, for which the estimated azimuths were within the error of 5° because of the superior polarization analysis possible with high resolution digital data. The reason for the much larger azimuth errors when using short-period data is obvious from Fig. 2.7 in Chapter 2. The particle motion is complicated in SP records and random due to wave scattering and diffraction by small-scale heterogeneities in the crust and by rough surface topography at or near the station site (see also Buchbinder and Haddon, 1990). In contrast, LP or BB records, which are dominated by longer wavelength signals, usually show simpler P waveforms with clearer first-motion polarity than do SP records.

Taking systematic distance and/or azimuth errors into account, the location accuracy can be improved. Nowadays many seismic arrays and networks use routinely multi-phase epicentral distance determinations for improving their slowness-based source locations. Some advanced software for seismogram analysis like SHM (section 11.4.2) and SEISAN (section 11.4.3 and section 6 in IS 11.6) include this complementary interactive analysis feature. EX 11.2 discusses in detail two examples based on earthquake records made at D ≈ 20° and ≈ 90°. Fig. 11.28 below gives an example for a Pakistan earthquake at D = 46.2°.

Rough estimates of hypocenter, respectively epicenter distance for shallow seismic sources can be made, however, even in the absence of travel-time tables or curves or related computer programs, when using the following simple "rules-of- thumb" (with 1° = 111.12 km):

hypocenter distance d [in km] ≈ Δt(Sg-Pg) [in s] × 8 (near range only) (11.1)

epicentral distance D [in km] ≈ Δt(Sn-Pn) [in s] × 10 (in Pn-Sn range < 15°) (11.2)

epicentral distance D [in °] ≈ {Δt(S-P) [in min] - 2} × 10 (for 20°< D <100°) (11.3)

For deep earthquakes one may use another "rule-of- thumb" for a rough estimate of source depth from the travel-time difference Δt(pP-P):

source depth h [in km] ≈ = Δt(pP-P)/2 [in s] × 7 (for h < 100 km) (11.4)
or × 8 (for 100 km < h < 300 km)
or × 9 (for h > 300 km)

The Pakistan earthquake was obviously shallow because it produced a well-developed surface-wave train with amplitudes much larger than the preceding body waves. Moreover, from the travel-time difference of 6.65 min between the identified P and S onset follows according to formula (11.3) D = 46.5°. This differs only about 0.3° or 33 km from D(CLL) = 46.2° calculated by GSR, corresponding to a distance deviation of only 0.065%.

When determining the backazimuth BAZ of the event with respect to the recording station from 3-component records in addition, it is possible to locate the event on a globe or on a suitable map projection. The determination of BAZ by using P-wave first-motion polarity readings has been described in detail in section 3.2 of EX 11.2 and in section 2 of IS 11.1. The insert in the upper right corner of Fig. 11.28 shows the magnified first motion direction of the long-period P-wave onset of the 2013 Pakistan earthquake. One clearly recognizes that the motion in the vertical component goes down, i.e., the ground motion shows in the direction towards the source, in the E-W component it moves with large amplitude up, i.e., the source is located in the East, and the N-S component goes weakly down, i.e., the ground moves also a bit southward. Measuring the correct ground amplitudes in the horizontal components one gets the ratio A_S/A_E = 0.262. This corresponds to an angle of 14.7° and thus a BAZ = 90° + 14.7° = 104.7°.

In contrast, the BAZ to station CLL, when calculated for the more precise epicenter determined on the basis of some hundred P-wave onset-time picks on global seismic network records is BAZ =101,1°, i.e., a deviation of only 3.7° from the 3-component BAZ(CLL). Comparing the two epicenter positions in Fig. 11.28 one can conclude that the location of this event in SE Pakistan has be correctly determined from a single station record more than 5000

km away with a total position difference of only 2.7° or 300 km with respect to the global network location. Thus this 3-component single station location agrees best with the conclusion by Tong and Kennett (1996) that for automatic multi-parameter 3-C broadband locations D estimates are mostly within the error of 7%, azimuths within 5° for D < 100°, and the locations within a 4° cap.

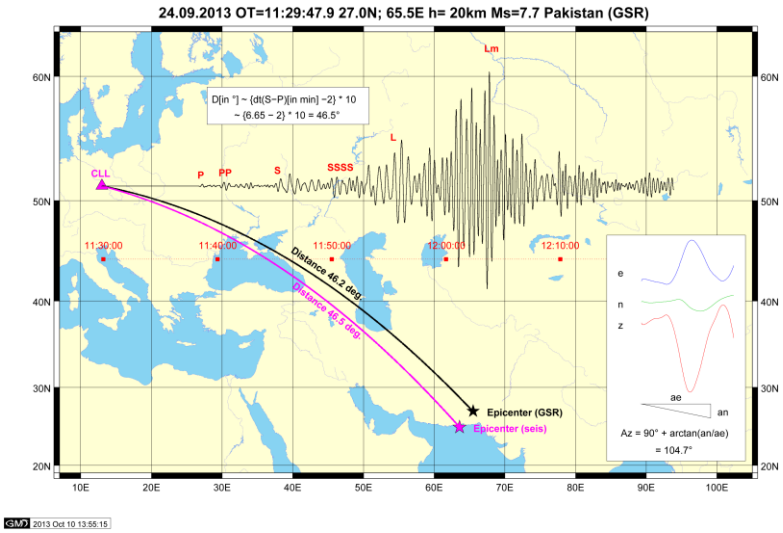

Fig. 11.28 Epicenter location of the Mw = 7.7 Pakistan earthquake on 24.09.2013 by the Obninsk data center GSR on the basis of global P-wave onset readings (black star) and by single station 3-component analysis at station CLL, Germany (cyan star), using the travel-time difference S-P for determining D and the long-period P-wave first-motion polarity in Z, E, and N component for determining BAZ = arctan (A_S/A_E) + 90°. Plotting single station locations on an epicenter map is a good check that the location is reasonable.

However, also global network epicenter positions may differ up to several 10 km from the true positions due to not accounting for velocity inhomogeneities in the real Earth along the travel paths to the stations (e.g., Engdahl et al., 1998) and also, that the earthquake location itself is not a sharp point but a rupture of finite length which is according to Eq. (3.188) in Chapter 3 for a magnitude M = 7.7 earthquake on average L ≈ 80 km.

Bormann (1971a) also showed that in the absence of a sufficiently strong P-wave arrival, the BAZ may also roughly be determined from horizontal components of any later seismic phase which is polarized in the vertical propagation plane, such as PP, PS, PKP or SKS. These phases are often much stronger in BB or LP records than P. However, because of phase shifts on internal caustics (PP, PS, SP, PKPab) the vertical component first motion direction of most of these phases cannot used reliably for resolving the 180° ambiguity of an azimuth determined from the ratio A_E/A_N only. However, by considering the inhomogeneous global distribution of earthquake belts, this problem can usually be solved.

In summary, simple 3-component event locations based solely on readings of onset times of identified phases, polarity of P-wave first motions and horizontal component amplitude ratio should proceed as follows:

- general event classification (near/far; shallow/deep; D < 100°/> 100° etc.);

- picking and identifying the most pronounced phases by comparing the 3-component record traces and related polarization characteristics (Fig. 11.29);
- determination of D by **a)** matching the identified body-wave phases with either overlays of differential travel-time curves of equal time scale (as in Fig. 11.8 or Figures 2 to 4 in EX 11.2), **b)** measuring their onset-time differences and comparing them with respective distance-dependent differential travel-time tables or by using rules of thumb [see formulas (11.1 to 11.4), **c)** computer calculation of D based on digital time picks for identified phases and local, regional and/or global travel-time models integrated into the analysis program;
- determination of source depth h on the basis of identified depth phases (see 11.2.5.1 and Figure 7 with related table in EX 11.2). When knowing h then correct D by using either travel-time curves, differential t-D tables or computer assisted time-picks and comparison with travel-time models;
- determination of the backazimuth (against North) from the station to the source from the first-motion directions in the original Z, N and E component records and from the amplitude ratio A_E/A_N. For details see Figure 1 and related explanations in EX 11.2;
- determination of the epicenter location and coordinates by using appropriate map projections with isolines of equal azimuth and distance from the station (Figures 5 and 6 in EX 11.2) or by means of suitable computer map projections.

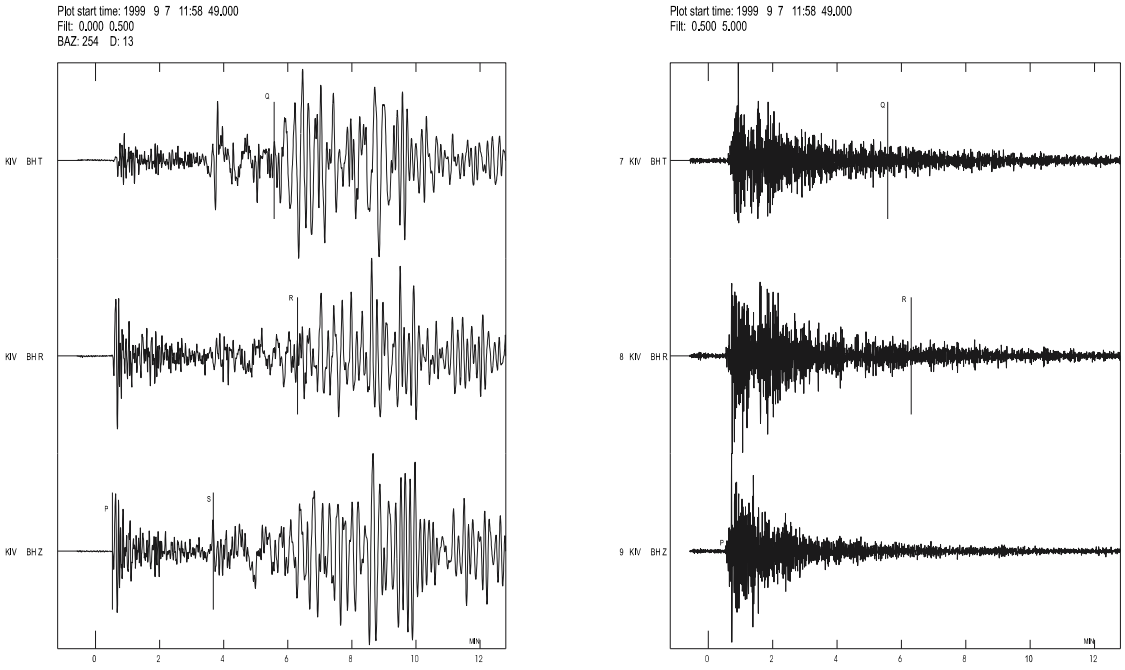

Fig. 11.29 Left: Low-pass filtered digital broadband record of the Global Seismograph Network (GSN) station KIV from the shallow (h = 10 km) Greece earthquake of 07 Sept. 1999 (mb = 5.8) at a distance of D = 13°. Note the clearly recognizable polarity of the first P-wave half-cycle! The record components have been rotated into the directions Z, R and T after determination of the backazimuth from first-motion polarities in Z, N and E (BAZ = 134°). Accordingly, P and Rayleigh waves are strongest in Z and R while S and Love (Q) wave are strongest in T. **Right:** The recordings after SP bandpass filtering (0.5-5.0 Hz). The SNR for the P-wave first-motion amplitude is much smaller and their polarity less clear. Also later arrivals required for distance determination are no longer recognizable (signal processing done with SEISAN; courtesy of L. Ottemöller).

Modern computer programs for seismogram analysis include subroutines that allow quick determination of both azimuth and incidence angle from particle motion analysis over the whole waveform of P or other appropriate phases. This is done by determining the direction of the principal components of the particle motion, using, as a measure of reliability of the calculated azimuth and incidence angle, the degree of particle motion linearity/ellipticity. Such an algorithm was available in the SEIS89 software (Baumbach†, 1999). Christoffersson et al. (1988) describe a maximum-likelihood estimator for analyzing the covariance matrix for a single three-component seismogram (see also Roberts and Christoffersson, 1990). The procedure allows joint estimation of the azimuth of approach, and for P and SV waves the apparent angle of incidence and, hence, information on apparent surface velocity and thus on epicentral distance. This has been implemented in the SEISAN software (Havskov and Ottemöller, 1999). Fig. 11.30 shows an example of the application of the software to a portion of the BB recording at Kongsberg (KONO) in Norway for the 12 November 1999, Turkey earthquake (Mw = 7.1). The program finds a high correlation (0.9) between the particle motions in the three components, gives the estimate of the backazimuth as 134°, an apparent velocity of 9.6 km/s and the corresponding location of this earthquake at 40.54°N and 30.86° E. This was only about 50 km off the epicenter located by the global network.

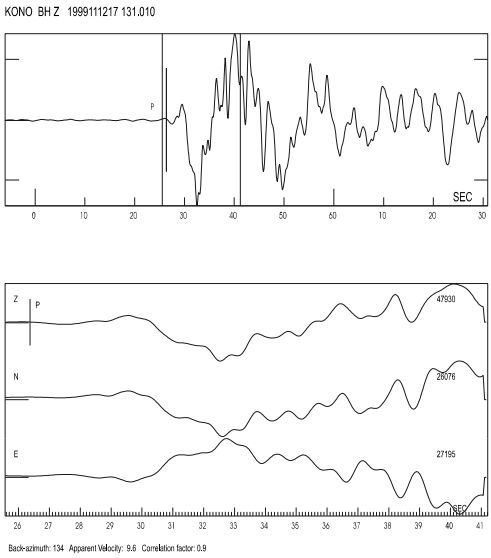

Fig. 11.30 Example of azimuth determination and epicenter location of the 12 Nov. 1999 Turkey earthquake by correlation analysis of three-component digital BB records at station KONO, Norway. Backazimuth, apparent velocity, and correlation factor are determined from the P-wave record section marked in the upper figure. For more details see text (signal processing done with SEISAN; courtesy of L. Ottemöller).

The TREMORS Algorithm by Talandier et al. (1991) determines automatically the epicenter of local, regional and teleseismic events based on the 3-component recordings of a single broad-band station. The program was originally developed for the fast tsunami warning in the French South Pacific Islands where network locations are not readily available. The Mantle magnitude Mm (Okal and Talandier, 1989) is used to characterize the size of the earthquake. An open version of the software was published by Dominique Reymond as part of his Seismic Tool Kit STK (Reymond (2002), http://seismic-toolkit.sourceforge.net/).

Applying another algorithms to digital 3-component data from short-period P waves recorded at regional distances, Walck and Chael (1991) show that more than 75% of the records yielded backazimuth within 20° of the correct values. They found, however, a strong dependence on the geological structure. Whereas stations located on Precambrian terrains produced accurate backazimuth for SNR > 5 dB, stations on sedimentary rocks with complicated structure had much larger errors. When excluding these stations, the RMS backazimuth error was only about 6° for recordings with SNR > 10 dB.

Ruud et al. (1988) found that 3-component BB locations for epicenters at distances up to about 1000 km seldom deviated at that time more than 50 km from network solutions, such deviations being mainly due to errors in azimuth estimates. For short-period teleseismic P waves, however, location errors occasionally exceeded 800 km, mainly because of poor distance estimates derived from incidence angles (slowness) alone. For stronger sources, using BB records and distance estimates based on travel-time differences, the location errors were reduced to about 1°.

These quantitative values may no longer be representative when comparing nowadays single station 3-component locations with improved modern network locations. However, the general message still holds, namely that already single station 3-component digital BB data allow reasonably good first location estimates when, for what reasons ever, faster and better network locations are not yet available for the interested user. The suitability of the combined use of seismic array and single 3-component locations had been discussed already by Cassidy et al. (1990).

11.2.7 Hypocenter location by means of network and array recordings

Hypocenter location and origin time determination require at least 4 stations if only first arrival times are read or three stations if independent distance estimates are available from travel-time differences between different phases. The more stations with good SNR (high weighting factor!) are available in local, regional or global networks and the more uniformly these stations are distributed around a seismic source in both azimuth and distance (the latter ranging from close-in to long range) and the more correctly identified and carefully measured seismic phase onsets are used for location, the lower is the uncertainty in these parameter estimates. The procedures in both manual and computer assisted multi-station hypocenter location are outlined in much more detail in IS 11.1, which gives the underlying algorithms and error calculations, as well as standard and advanced methods for both absolute and relative location. Also discussed are the influence of deviations from the assumed Earth models on the locations and the improvement of hypocenter relocations achievable with better Earth models.

Other special problems of seismic event location are dealt with in other information sheets. E.g., IS 7.4 looks into the detectability and earthquake location accuracy modeling of seismic networks, IS 8.5 outlines an authoritative operational location scheme for assessing the quality of automatic network locations, IS 8.6 focusses on the identification and collection of seismic events with accurately known locations (ground truth data) for network calibration and IS 8.7 offers and comments on a tutorial about theoretical and empirical approaches aimed at optimizing network configurations for different seismological tasks.

Array methods of event location are described in Chapter 9. They require that the distance of the source from the array/network is much larger than the array/network aperture (flat wave-front approach) and a high degree of waveform coherence/correlation between the station records. Although seismic arrays are very fashionable, mainly because of their potential for SNR improvement and direct slowness measurements (Fig. 11.45 and sections 11.3.3-11.3.5) there locations may not be superior at all as compared to those of well distributed seismic networks surrounding the source areas. The results may however be improved significantly by investigating and accounting for systematic array or network mislocations due to distance and azimuth dependent slowness anomalies (e.g., Bormann et al., 1992 and Fig. 11.31; Krüger and Weber, 1992; Schweitzer, 2002).

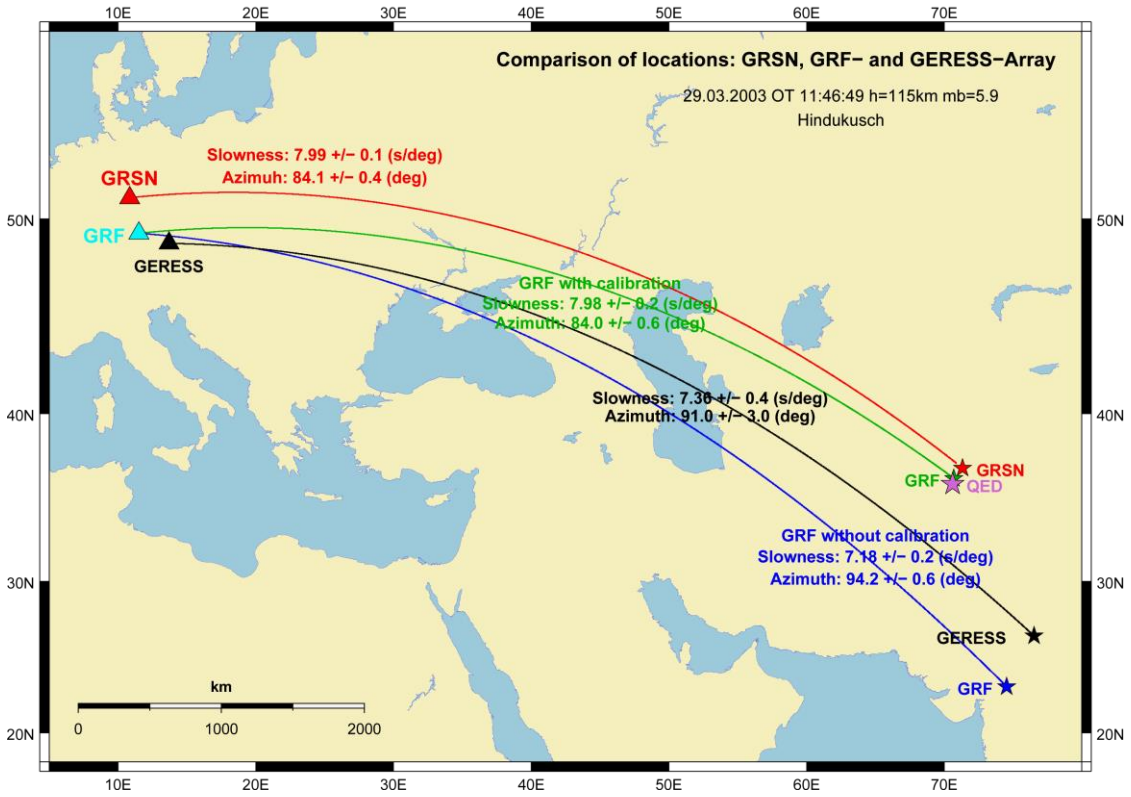

Fig. 11.31 Comparison of the epicenter locations determined by the GRSN and the Gräfenberg (GRF) and GERES seismic arrays in Germany for a Hindukush earthquake at intermediate depth. QED gives the position of the NEIC/USGS Quick Epicenter Determination based on global network records. The QED location and the epicenters determined by the GRSN with the largest aperture (about 590 km × 700 km), and by the calibrated GRF (aperture about 50 km × 120 km) agree very well (differences less than 100 km). This is not the case for uncalibrated locations of GRF and the very small GERES array (aperture only some 4 km). They are strongly affected by local site anomalies (velocity and/or topographic ones; for GERES see, e.g., Harjes et al., 1994; Bokelmann, 1995) and their locations are about 600-700 km off the QED solution.

In the following we outline for general understanding three basic graphical approaches to locate local seismic events. They all require a "flat Earth" or an "Earth flattening" pre-processing (Fig. 11.32):

1. The **circle and chord method** calculates for each station the hypocentral distance d, using a known or assumed travel-time model and the relationship $\mathbf{d = (t_S\text{-}t_P)\ \{(v_P \bullet v_S)\ /(v_P\text{-}v_S)}$. In a crust with mean P-wave velocity of about 5.9 km/s and $v_S = v_P/\sqrt{3}$ this can be approximated by **d** [in km] $\approx 8 \cdot \Delta t$ **(Sg-Pg)** [in s] [see "rule of thumb" (11.1)]. This method is rather insensitive to absolute variations of v_P and v_S as long as the ratio v_P/v_S remains constant.
2. The **circle method** uses only measured P-wave first arrival times at the stations and an assumed reasonable P-wave velocity **v**. Circles are drawn around the stations n-1 with radii equal to $\mathbf{v(t_n - t_1)}$, t_n being the P onset time at station n. The epicenter is then found in the center of the circle which runs through station 1 and touches also the other circles.
3. The **hyperbola method** uses only P-wave arrival time differences between selected station pairs. It requires no à priori knowledge of the P-wave velocity and yields rather good results. For a detailed description of the method and its benefits see Pujol (2004).

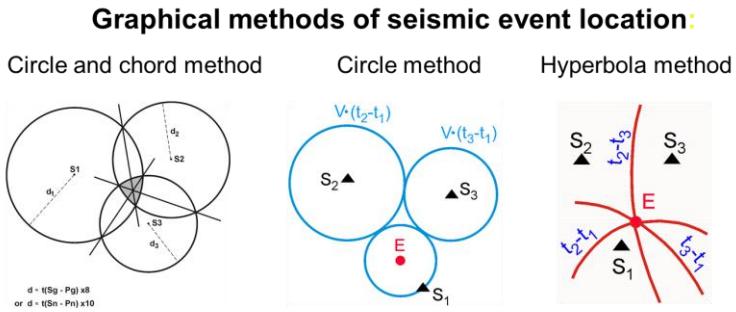

Fig. 11.32 Illustration of the main principles on which graphical location methods are based.

EX 11.1 in this Manual aims at epicenter location by the simple circle and chord method using records from seismic sources both within and outside of a local station network. It is suitable also as a practical for "Seismology at Schools". First one tries to identify the dominating seismic phase arrivals in the local records of each station by matching them best with the local travel-time curves of Pg, Sg, Pn and/or Sn for a surface focus (Fig. 11.33). This yields at the same time an estimate of the hypocentral distances from the travel-time differences Sg-Pg for each station and of the origin time OT if the assumption of h = 0 is correct (Fig. 11.34). However, when no local/regional travel-time curve is available one may also use as a first approximation the rules of thumb for Δt(Sg-Pg) or Δt(Sn-Pn) [see formulas (11.1-11.3)]. Then it is shown how one can estimate the likely epicenter position by drawing circles around the stations with the so determined station-hypocenter distances and by connecting the crossings of equal pairs of over-shouting circles with so-called straight-line chords (Fig. 11.35).

Finally, it is illustrated that the epicenter position, estimated from the "gravity" center of chord crossings, agrees rather well with the computer solution calculated with the common Geiger (1910 and 1912) algorithm and that additionally the source depth h can be estimated too by step-wise reduction of the circle radii until the circles all meet for the most likely assumed source depth h in the epicenter (Fig. 11.35). This iterative search for h with related modification of the depth-dependent local travel-time curve is also shown as a computer animation in IS 1.1.

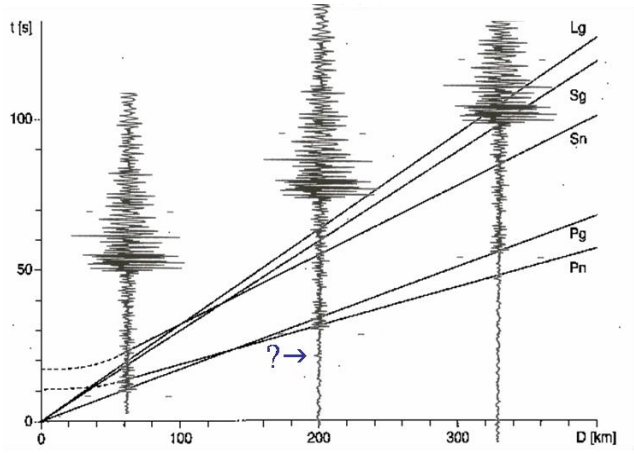

Fig. 11.33 Stepwise movement of a seismic record from left to right over a local travel-time curve for a surface focus until a best fit for three recognizable onsets (Pn, Pg, Sg) and the Lg wave group is achieved, here at a distance D ≈ 327 km.

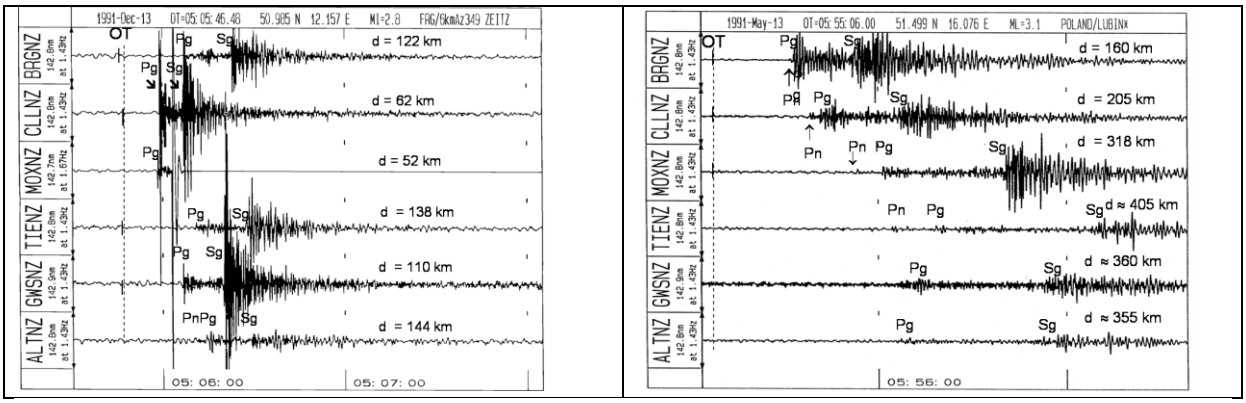

Fig. 11.34 **Left:** Identified local phases, estimated source origin time and station-source hypocenter distances for an earthquake in the distance range where Pg is the first arrival; **Right:** the same for another seismic event outside of the network in the distance range were Pn is the first arrival (d > about 150 km).

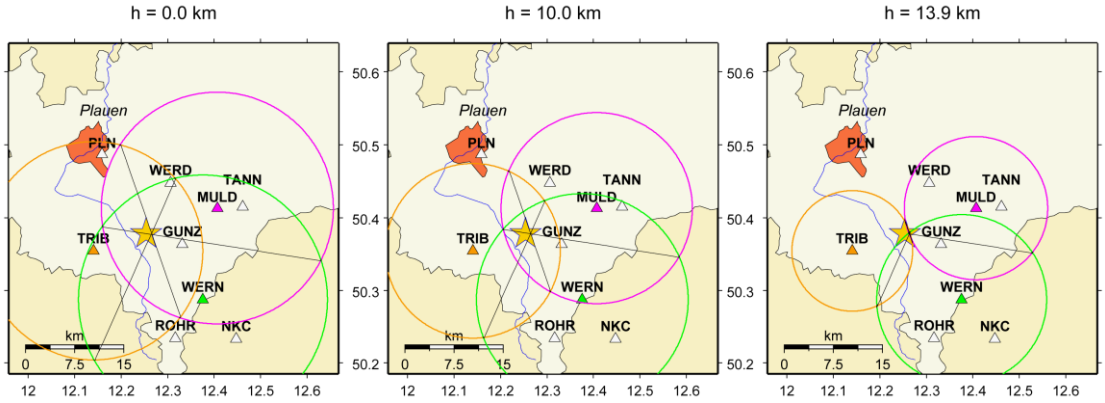

Fig. 11.35 Sequence of circle & chord plots for an earthquake in the Vogtland swarm earthquake region, Germany. Assumed are different source depths for fixed hypocentral distances d_i of the i stations as calculated from their S-P time differences. For h = 13.9 km the circles cross almost ideally in one point at the epicenter. For details see IS 1.1 and EX 11.1.

Although the results of graphical location principally compare reasonably well with computer assisted locations (see EX 11.3), with the general availability of computers it is nowadays only seldom used in the observatory practice of seismic networks. With digital multi-station data and advanced seismogram analysis software, source location calculation seems to become almost a trivial and very fast completed task. One just picks a sufficient number of first arrival times, activates the relevant location program for local, regional and/or teleseismic sources and gets the result of the iteration process in an instant. Nevertheless, in practice, large location errors or even completely wrong locations can be obtained if certain conditions of the seismic network configuration and the quality of the picked phases are not fulfilled for a certain seismic event. Moreover, up to now most or the location algorithms are run by assuming 1D velocity models. So calculated location errors are not a reliable measure of the true location accuracy. Velocity heterogeneities in real Earth may result in location errors up to several 10 km from the true source, respectively hypocenter location (e.g., Engdahl et al., 1998). These real location errors ar the larger the larger the azimuthal gaps are in the station distribution (e.g., Bormann, 1972a and IS 8.5). Reliable assessment of the actual location errors of seismic networks and their used procedures requires comparison with ground truth (GT) data of seismic events with precisely known locations and origin time, such as large chemical or nuclear explosions or precision located events by means of dense local networks with location errors less than about 5 to 10 km (see IS 8.6). For details on location with computer programs and related problems see IS 11.1 and for the program package HYPOSAT/HYPOMOD the PD 11.1.

The accuracy of location, particularly of the source depth, can be significantly improved when at least one of the stations is near to the epicenter at $D < h$ and/or by picking besides P-wave first arrivals also later arrivals which permit a much better distance and depth control than P-wave slowness data alone. Examples for both local and teleseismic event locations based on seismic network and array data are given in the following sections. IS 11.6 demonstrates the use of the SEISAN software for phase picking, event location and magnitude determination in the local, regional and teleseismic distance range based on seismic records from national and global seismic stations, as well as a 3-component earthquake location. Location using array data is described in Chapter 9, together with the underlying theory. Problems related to the optimization of network configuration aimed at best location results are discussed in detail in IS 8.7 and the PPT tutorial linked to this information sheet.

11.2.8 Magnitude determination

When epicentral distance and depth of a seismic source are (at least roughly) known the magnitude of the event can be estimated. The general procedures to be followed in magnitude determination based on the measurement of amplitudes, periods and/or record duration as well as the specifics of different magnitude scales to be used for local, regional or teleseismic recordings are dealt with in detail in section 3.2 of Chapter 3 on more than 100 pages, including also most recent, still experimental and not yet standardized scales. DS 3.1 presents various classical magnitude calibration functions as diagrams or tables together with other auxiliary material. Some of these classical procedures of magnitude determination can be learnt from EX 3.1, which also gives solutions for the different tasks.

In this context reference has to be made to the most recent

IASPEI resolution on magnitude standards (Fig. 11.36). It relates to classical short-period ML and mb, the traditional NEIC 20s surface-wave magnitude Ms and, most importantly, to the new velocity broadband body and surface-wave standards mB_B and Ms_BB. For calculating the moment magnitude Mw from seismic moment M_0 a standard formula has now been fixed too.

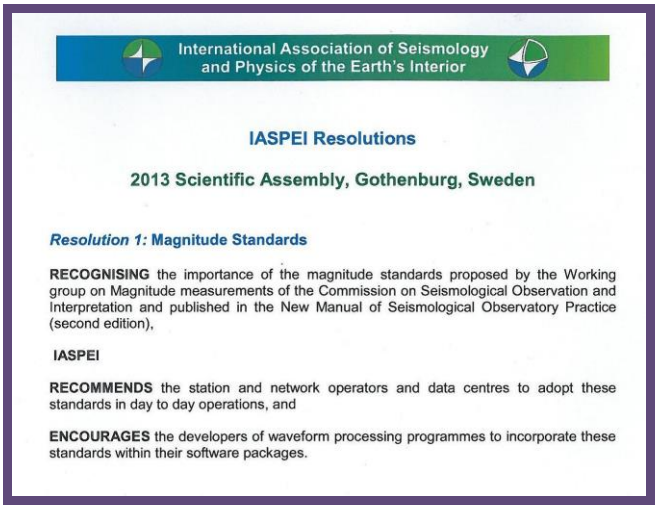
International Association of Seismology and Physics of the Earth's Interior

IASPEI Resolutions

2013 Scientific Assembly, Gothenburg, Sweden

Resolution 1: Magnitude Standards

RECOGNISING the importance of the magnitude standards proposed by the Working group on Magnitude measurements of the Commission on Seismological Observation and Interpretation and published in the New Manual of Seismological Observatory Practice (second edition),

IASPEI

RECOMMENDS the station and network operators and data centres to adopt these standards in day to day operations, and

ENCOURAGES the developers of waveform processing programmes to incorporate these standards within their software packages.

Fig. 11.36 IASPEI resolution 2013 on magnitude measurement standards.

The most recent short-version of the new IASPEI (2013) magnitude measurement standards and nomenclature, IASPEI (2013), can be read and downloaded from the IASPEI website via

http://www.iaspei.org/commissions/CSOI/Summary_WG_recommendations_20130327.pdf.

IS 3.3 elaborates in detail both on the standard procedures and their comparison with still common classical routines of magnitude determination and results. It also presents the partially modified nomenclature for standard magnitudes and related amplitude measurements and discusses admissible deviations in procedural details, especially in the filter responses to be applied for ML, mb and Ms_20 measurements, provided that the results for identical input data do not differ on absolute values average by more than 0.1 magnitude units.

Possible modifications of recommended standards of amplitude and period measurements in fully automatic procedures are discussed in section 3.2.3.2 of Chapter 3, showing their agreement with results of expert interactive magnitude determinations that strictly adhered to the recommended standards and discussing the reasons for partial disagreement and ways for improving currently available algorithms.

IS 3.4 provides a IASPEI standard magnitude reference data set together with guidelines how to use it for comparison and documentation of currently used magnitude procedures at seismological stations or network analysis centers with the new standards. In this context it is of great importance that all contributors of amplitude and period data for magnitude determination to international data centers, the International Seismological Centre (ISC) in particular, document and report to the ISC in detail their current, or, after they have already introduced the new standards, also their past procedures. This information is crucial for reliable assessment of procedural differences, related systematic biases or random error ranges, respectively of the achieved status of data compatibility and homogeneity and thus of a new level of reliability and representativeness of magnitude data for application and research. A related questionnaire, elaborated by the IASPEI Working on Magnitude Measurement, is attached as Annex 2 to IS 3.4.

Note that the widely used data analysis software packages SEISAN, SHM and SeisComp3 have by 2013 already implemented the related IASPEI recommended simulation filters as default or as auxiliary measurement routines.

11.3 Routine signal processing of digital seismograms

Standard analysis includes all data pre-processing and processing operations for the interpretation and inversion of broadband seismograms. Important time-domain processes are signal detection, signal filtering, restitution and simulation, phase picking, polarization analysis as well as beamforming and vespagram analysis for arrays. In the frequency domain the main procedures are frequency-wavenumber (f-k) and spectral analysis. Array-techniques as f-k and vespagram analysis, slowness and azimuth determination for plane waves, and beamforming are discussed in detail in Chapter 9 but a few examples are also shown below. Fourier spectral analysis can be applied to determine the frequency content of transient seismic waves, and power density spectral analysis for estimating the frequency content of seismic noise (Chapter 4 and section 7.2 of Chapter 7).

11.3.1 Signal detection

The first task of routine data analysis is the detection of a seismic signal. A signal is distinguishable from the seismic background noise either on the basis of its larger amplitudes or its differences in shape and frequency. Various methods are used for signal detection. Threshold detectors and frequency-wavenumber analysis are applied to the continuous stream of data. In practice, the threshold is not constant but varies with the season and the time of the day. For this reason, the threshold detectors determine the average signal power in two moving time windows: one long term (LTA) and one short term (STA). The ratio of the STA to LTA corresponds to the signal-to-noise-ratio (SNR). For details on the STA/LTA trigger and its optimal parameter setting see IS 8.1 and Chapter 9.

BB records are usually filtered before detectors are used although according to Douglas (1997) a detection algorithm is the better the less filtering is required. Useful filters are Butterworth high-pass filters with corner frequencies $f_c > 0.5$ Hz or standard band-pass types with center frequency f = 1 Hz for teleseismic P waves and high-pass filter with $f_c >$ 1-3 Hz for local sources. Fig. 11.37 demonstrates detection and onset-time measurement for a weak, short-period P wave. In the lowermost 30 s segment of a BB-velocity seismogram the oceanic microseisms dominate in the period band 4-7 s. The two other traces are short-period seismograms after narrow band-pass (BP) filtering with: (1) a filter to simulate a WWSSN-SP seismogram; and (2) a two-step Butterworth BP filter of 2^{nd}-order with cut-off frequencies of 0.7 and 2 Hz, respectively. The latter filter produces, for the noise conditions at the GRF-array, the best SNR for teleseismic signals. Seismic networks designed to detect mainly local seismic events may require other filter parameters that better account for the difference between local event and local noise frequencies. For optimal detection (see IS 8.1).

Generally, a seismic signal is declared when the STA/LTA exceeds a pre-set threshold. Various procedures, some analytical and some based on personal experience, are used to differentiate between natural earthquakes, mining-induced earthquakes and different kinds of

explosions. Usually, the detected signals are analyzed for routine parameter extraction and data exchange.

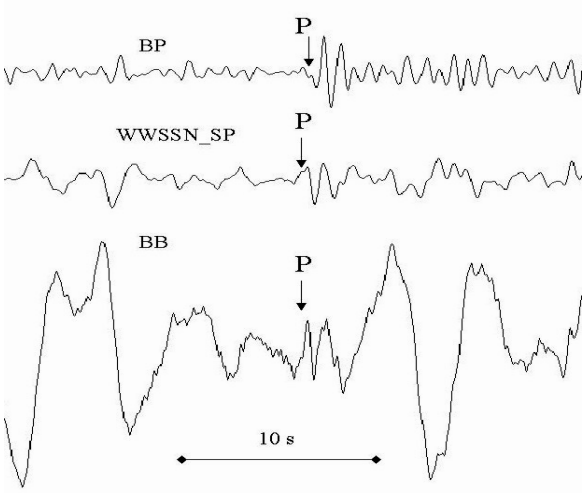

Fig. 11.37 Bandwidth and SNR: A small short-period P-wave arrival below the noise amplitude level on a BB-velocity record (lower trace) may still be recognized by an experienced record analyst because of its much shorter period but missed by a simple amplitude threshold STA/LTA detector. However, by applying a WWSSN-SP simulation filter (middle trace) or a Butterworth band-pass filter (BP; uppermost trace) the SNR can be significantly improved. While the amplitude-based SNR is 0.2 on the original BB record and about 1 on the WWSSN-SP filter it is about 2 on the BP-filtered trace. (Record of an earthquake in the Kurile Islands on 25 March 2002, 6:18:13 UT, recorded at station GRA1, Germany).

11.3.2 Signal filtering, restitution and simulation

Classical broadband seismographs, such as the Russian Kirnos SKD, record ground displacement with constant magnification over a bandwidth of 2.5 decades or about 8 octaves (Fig. 11.38 left). The IDA-system (International Deployment of Accelerometers), deployed in the 1970s, used originally LaCoste-Romberg gravimeters for recording long-period waves from strong earthquakes proportional to ground acceleration over the band from DC to about 0.1 Hz (nowadays replaced by STS1-VBB; Fig. 11.38 right). Modern strong-motion sensors such as the Kinemetrics Inc. Episensor ES-T have a flat response to ground acceleration in an even broader frequency band from DC to 200 Hz. In contrast, feedback-controlled BB sensors for recording weak-motion usually have a flat response proportional to the ground velocity (Fig. 11.38 right). Such BB recordings, however, are often not suitable for direct visual record analysis and parameter extraction in the time domain. Low-frequency signals and surface waves of weak earthquakes are not or only poorly seen. Therefore, BB data must be transformed by applying digital filters in a way that yields optimal seismograms for specific investigations and analysis.

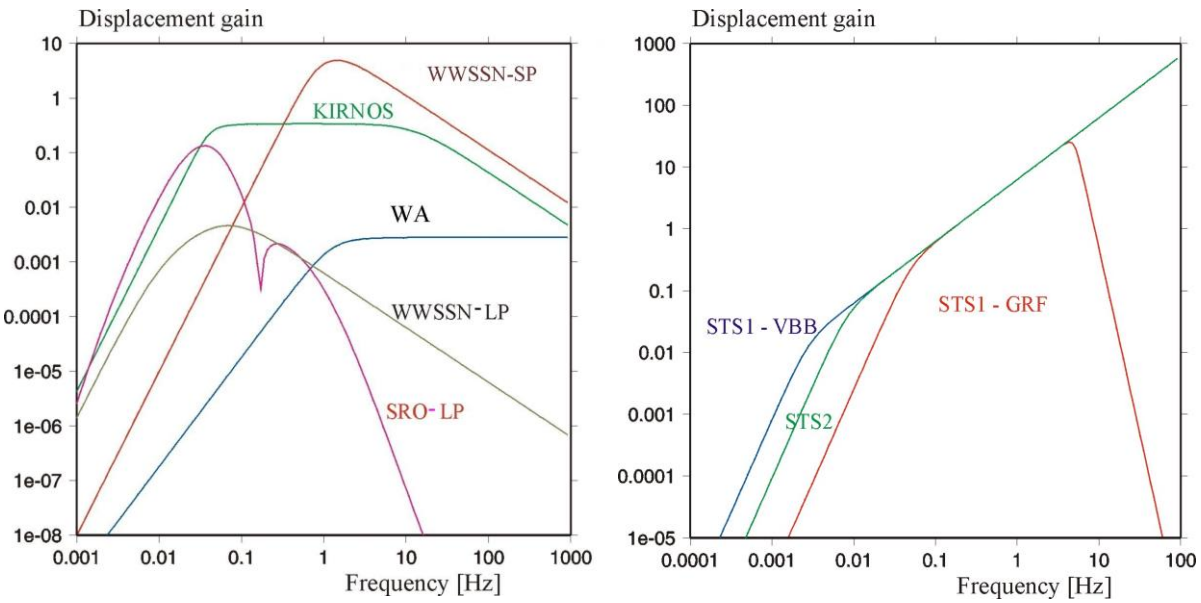

Fig. 11.38 Left: Displacement amplitude response characteristics of classical seismographs; **right:** The same for velocity broadband seismographs STS1(GRF) (old version as used at the Gräfenberg array), STS1 (VBB) (advanced version as used in the IRIS global network) and STS2. For STS1 (VBB) and STS2 the detailed response at higher frequencies is not shown (see comment below Tab. 11.4). The classical responses plotted on the left can be simulated with digital data from these broadband systems. Note the different scale of the vertical axes.

For some research tasks and ordinary routine analysis of BB seismograms the application of high-pass, low-pass and band-pass filters is usually sufficient. However, simultaneous multi-channel data processing or the determination of source parameters according to internationally agreed standards (such as body- and surface-wave magnitudes, which are defined on the basis of former analog band-limited recordings) often require simulation of a specific response, including those of classical analog seismograph systems (Seidl, 1980). Another special problem of simulation is "restitution". Restitution is the realization of a seismograph system whose transfer function is directly proportional to ground displacement, velocity or acceleration in the broadest possible frequency range. The restitution of the true ground displacement down to (near) zero frequencies is a precondition for seismic moment-tensor determinations both in the spectral and the time domain (e.g., signal moment; Fig. 11.6). It is achieved by extending the lowermost corner frequency of the seismometer computationally far beyond that of the physical sensor system. Both the simulation of arbitrary band-limited seismograph systems and the extreme broadband "restitution" of the true ground motion are necessary steps in pre-processing of digital BB data.

Simulation is the mapping of a given seismogram into the seismogram of another type of seismograph, e.g., those of classical analog recordings such as WWSSN-SP, WWSSN-LP, Kirnos SKD, SRO-LP, and Wood-Anderson (WA). Up to now, amplitudes and periods for the determination of body- and surface-wave magnitudes mb and Ms_20 are measured on simulated WWSSN-SP and WWSSN-LP or SRO-LP seismograms, respectively, and the maximum amplitude for the original local Richter magnitude is measured on Wood-Anderson simulated seismograms. Fig. 11.38 (left) depicts the displacement response of these classical seismographs with smaller bandwidth.

The possibility of carrying out these simulations with high accuracy and stability defines the characteristics that have to be met by modern digital broadband seismograph:

- large bandwidth;
- large dynamic range;
- high resolution;
- low instrumental seismometer self-noise (Chapter 4, section 4.3.2 and Chapter 5, section 5.6.2);
- low noise induced by variations in air pressure and temperature (Chapter 5, sections 5.3.4, 5.3.5, and 7.4.4: for seismometer shielding see IS 5.4);
- analytically exactly known transfer function (see 5.2).

Fig. 11.38 (right) depicts the displacement responses of a few common BB-velocity sensors such as:

- the original Wielandt-Streckeisen STS1 with a bandwidth of 2 decades between the 3-db roll-off points at frequencies of 0.05 Hz and 5 Hz (anti-aliasing filter). These seismographs were deployed in the world's first broadband array (GRF) around Gräfenberg/Erlangen in Germany (Fig. 11.3a);
- the advanced STS1 that is generally used at the global IRIS network of very broadband (VBB) stations (velocity bandwidth of about 3.3 decades between 5 Hz and 360 s; see also DS 5.1);
- the STS2 seismographs (see DS 5.1) that are usually operated in the frequency range between 0.00827 Hz and 40 Hz (velocity bandwidth of 3.7 decades or about 12 octaves, respectively). They are used at the stations of the GRSN (Fig. 11.3a), deployed world-wide at stations of the GFZ GEOFON network (see http://www.gfz-potsdam.de/geofon/) and at many other networks or single stations and have meanwhile also replaced the more narrowband original STS1 at the stations of the GRSN.

All these seismographs can be considered to be linear systems within the range of their usual operation. The transfer function H(s) of a linear system can be calculated from its poles and zeros by using the following general equation:

$$H(s) = N * \Pi (s - z_i) / \Pi (s - p_k) \qquad (11.5)$$

where N is the gain factor, $s = j\omega$ with $\omega = 2\pi f$ and j the complex number $\sqrt{-1}$, z_i are the zeros numbering from i = 1 to m and p_k the poles with k = 1 to n. Zeros are those values for which the numerator in Eq. (11.5) becomes zero while the poles are the values for which the denominator becomes zero.

Tab. 11.3 summarizes the poles and zeros of the classical standard responses WWSSN-SP, WWSSN-LP, WA (Wood-Anderson), Kirnos SKD and SRO-LP which control the shape of the response curves and Tab. 11.4 gives the poles and zeros for the three broadband responses shown in Fig. 11.38 on the right. Not given are the gain factors because they depend on the specific data acquisition system and its sensitivity.

Note: The poles and zeros in this tables are for WWSSN-SP, WWSSN-LP, WA (Wood-Anderson) close but not identical with those of the respective standard responses of these seismographs as now recommended by the IASPEI-CoSOI Working Group on Magnitude Measurements (Figure 1 and accompanying text in IS 3.3).

Tab. 11.3 Zeros and poles corresponding to the displacement transfer functions depicted in Fig. 11.38 left for the classical analog standard seismographs WWSSN-SP, WWSSN-LP, WA, Kirnos SKD and SRO-LP (according to K. Stammler, personal communication 2013).

Seismograph	Zeros	Poles
WWSSN-SP	(0.0, 0.0) (0.0, 0.0) (0.0, 0.0)	(-3.3678, -3.7315) (=p_1) (-3.3678, 3.7315) (=p_2) (-7.0372, -4.5456) (=p_3) (-7.0372, 4.5456) (=p_4)
WWSSN-LP	(0.0, 0.0) (0.0, 0.0) (0.0, 0.0)	(-0.4189, 0.0) (-0.4189, 0.0) (-6.2832E-02, 0.0) (-6.2832E-02, 0.0)
WA	(0.0, 0.0) (0.0, 0.0)	(-6.2832, -4.7124) (-6.2832, 4.7124)
Kirnos SKD	(0.0, 0.0) (0.0, 0.0) (0.0 0.0)	(-0.1257, -0.2177) (-0.1257, 0.2177) (-80.1093, 0.0) (-0.31540, 0.0)
SRO-LP	(0.0, 0.0) (0.0, 0.0) (0.0, 0.0) (-5.0100E+01, 0.0) (-0.0, 1.0500) (-0.0, -1.0500) (0.0, 0.0) (0.0, 0.0)	(-1.3000E-01, 0.0) (-6.0200, 0.0) (-8.6588, 0.0) (-3.5200E+01, 0.0) (-2.8200E-01, 0.0) (-3.9300, 0.0) (-2.0101E-01, 2.3999E-01) (-2.0101E-01, -2.3999E-01) (-1.3400E-01, 1.0022E-01) (-1.3400E-01, -1.0022E-01) (-2.5100E-02, 0.0) (-9.4200E-03, 0.0)

Tab. 11.4 Zeros and poles corresponding to the displacement transfer functions of the velocity-proportional broadband seismographs STS1(GRF), STS1-VBB(IRIS) and STS2 of generation 1 as depicted in Fig. 11.38 right. From their output data seismograms according to the classical analog standard seismographs WWSSN-SP, WWSSN-LP, WA, Kirnos SKD and SRO-LP are routinely simulated at the SZO in Hannover, Germany (Table and comment below according to K. Stammler, personal communication 2013).

Seismograph	Zeros	Poles
STS2 generation 1	(0.0,0.0) (0.0,0.0) (-15.15,0.0) (-318.6,401.2) (-318.6,-401.2)	(-3.674E-2, -3.674E-2) (-3.674E-2, 3.674E-2) (-15.99, 0.0) (-417.1, 0.0) (-100.9, 401.9) (-100.9, -401.9) (-7454.0, -7142.0) (-7454.0, 7142.0)
STS2 - approx	(0.0,0.0) (0.0,0.0) (0.0,0.0)	(-3.674E-2, -3.674E-2) (-3.674E-2, 3.674E-2)

STS1(GRF)	(0.0, 0.0) (0.0, 0.0) (0.0, 0.0)	(-0.2221, -0.2222) (-0.2221, 0.2222) (-31.416, 0.0) (-19.572, 4.574) (-19.572, -24.574) (-7.006, 30.625) (-7.006, -30.625) (-28.306, 13.629) (-28.306, -13.629)
STS1(VBB))	(0.0, 0.0) (0.0, 0.0) (0.0, 0.0)	(-1.2341E-02, 1.2341E-02) (-1.2341E-02, -1.2341E-02)

Comment: The detailed characteristics of the STS2 at high-frequencies depends on the production date. There are three different generations available, shown here is the first generation of STS2. In most cases high frequencies of 40 Hz or more are not relevant. Then a simple approximation of the STS2 transfer function, as STS2-approx in Tab. 11.4, is sufficient. When high frequencies are important and are close to the Nyquist frequency (e.g. for 100 Hz sampled data the Nyquist frequency would be 50 Hz) then also the characteristics of the digitizer has to be taken into account. In order to prevent aliasing digitizers one should apply steep low-pass filters just below the Nyquist frequency, usually represented as cascades of FIR filters with dozens of FIR coefficients per stage. Details on FIR filters can be found in Scherbaum and Bouin (2007).

Using the data given in these tables, the exact responses of the respective seismographs can be easily found. As an example, we calculate the response curve of the WWSSN-SP. According to Tab. 11.3 it has three zeros and four poles. Thus we can write Eq. (11.5) as

$$H(s) = N * s^3 / (s-p_1)(s-p_2)(s-p_3)(s-p_4) \qquad (11.6)$$

with

$p_1 = -3.3678 - 3.7315j$
$p_2 = -3.3678 + 3.7315j$
$p_3 = -7.0372 - 4.5456j$
$p_4 = -7.0372 + 4.5456j.$

The squared lower angular corner frequency of the response (that is in the given case the eigenfrequency of the WWSSN-SP seismometer) is $\omega_l^2 = p_1 \cdot p_2$ whereas the squared upper angular eigenfrequency (which used to be in the classical SP records that of the galvanometer) is $\omega_u^2 = p_3 \cdot p_4$. Since the product of conjugate complex numbers $(a + bj)(a - bj) = a^2 + b^2$ it follows for the poles:

$\omega_l^2 = 25.27$ with $f_l = 0.80$ Hz and
$\omega_u^2 = 70.18$ with $f_u = 1.33$ Hz.

When comparing these values for the corner frequencies of the displacement response of WWSSN-SP in Fig. 11.38 (left) one recognizes that the maximum displacement magnification (slope approximately zero) lies indeed between these two values. Further, as outlined in EX 5.6, a conjugate pair of poles such as p_1 and p_2 or p_3 and p_4 correspond to a second order corner of the amplitude response, i.e., to a change in the slope of the asymptote to the response curve by 2 orders. Moreover, the number of zeros controls the slope of the response curve at the low-frequency end, which is three in the case of the WWSSN-SP (see Eq. (11.6) and Tab. 11.3). Thus, at its low-frequency end, the WWSSN-SP response has according to its three zeros a slope of 3. This changes at the first pair of poles, i.e., at $f_l = 0.8$

Hz, by 2 orders from 3 to 1 (i.e., to velocity proportional), and again at f_u = 1.33 Hz by two orders from 1 to –1. This is clearly seen in Fig. 11.38.

In the same manner, the general shape of all the responses given in that figure can be assessed or precisely calculated according to Eq. (11.5) by using the values for the poles and zeros given in Tabs. 11.3 and 11.4. Doing the same with the values given in Tab. 11.3 for WWSSN-LP one gets for f_l = 0.06667 Hz, corresponding to the 15 s seismometer and f_u = 0.009998 Hz corresponding to the 100 s galvanometer, used in original WWSS-LP seismographs. The aim of the exercise in EX 5.5 is to calculate and construct with the method shown above the responses of seismographs operating at several seismic stations of the global network from the data given in their SEED header information and EX 5.6 outlines this in detail for the calculation of the response of WWSSN-LP.

When comparing poles and zeros in Tab. 11.3 for WWSSN-SP with those given in Table 1 of IS 3.3 for the respective IASPEI standard response than one realizes that the former has besides the 3 zeros two conjugate poles whereas the latter has two conjugate and three single poles. Single poles mean, however, that at their respective frequency the response slope changes not by two but only by one order. But since the standard WWSSN-SP has three single poles instead of the second conjugate pole, the standard response (Figure 1 in IS 3.3) decays steeper towards higher frequencies than the WWSSN-SP response in Fig. 11.38 left. But the response slope towards longer periods, which is of third order and controlled by the number of zeros, is identical in both cases. The slight difference in response shape, however, results in a slight difference of amplitude-period measurements, which make mb(IASPEI) on average 0.033 m.u. smaller than mb(BGR) (Figure 11 in section 5.1.2 of IS 3.3). This is still acceptable within the IASPEI magnitude standard requirements as long as the absolute average differences for magnitudes of the same type but measured with different procedures is < 0.1 m.u.).

Note that the poles and zeros given in Tabs. 11.3 and 11.4 are valid only if the input signal to the considered seismographs is ground displacement (amplitude A_d). Consequently, the values in Tab. 11.3 are not suitable for simulating the responses of the classical seismographs if the input signal to the filter is not displacement. From the output of the STS2, any simulation filter gets as an input a signal, which is approximately velocity-proportional within the frequency range between 0.00827 Hz and 40 Hz. In this range its amplitude is $A_v = \omega A_d$. Accordingly, the transfer function of the simulation filter $H_{fs}(s)$ has to be the convolution product of the inverse of the transfer function $H_r(s)$ of the recording instrument and the transfer function $H_s(s)$ of the seismograph that is to be simulated:

$$H_{fs}(s) = H_r^{-1}(s) * H_s(s). \qquad (11.7)$$

Thus, even for the same $H_s(s)$ to be simulated, the poles and zeros of the simulation filter differ depending on those of the recording seismograph. Tab. 11.5 gives, as an example from the SZ0, the poles and zeros of the displacement filters for simulating the responses shown in Fig. 11.38 (left), and the poles and zeros given in Tab. 11.4, from output data of the STS2-approx.

Tab. 11.5 Poles and zeros of the simulation filters required for simulating standard seismograms of WWSSN-SP, WWSSN-LP, WA, Kirnos SKD and SRO-LP, respectively, from the SZO STS2-approx BB-velocity records (according to K. Stammler, personal communication 2013).

Simulation filter	Zeros	Poles
WWSSN-SP	(-3.6743E-02, -3.6754E-02) (-3.6743E-02, 3.6754E-02)	(-3.3678, -3.7316) (-3.3678, 3.7315) (-7.0372, -4.5456) (-7.0372, 4.5456)
WWSSN-LP	(-3.6743E-02, -3.6754E-02) (-3.6743E-02, 3.6754E-02)	(-0.4189, 0.0) (-0.4189, 0.0) (-6.2832E-02, 0.0) (-6.2832E-02, 0.0)
WA	(-3.6743E-02, -3.6754E-02) (-3.6743E-02, 3.6754E-02)	(-6.2832, -4.7124) (-6.2832, 4.7124) (0.0, 0.0)
Kirnos SKD	(-3.6743E-02, -3.6754E-02) (-3.6743E-02, 3.6754E-02)	(-0.12566, -0.2177) (-0.1257, 0.2177) (-80.1094, 0.0) (-0.3154, 0.0)
SRO-LP	(-3.6744E-02, -3.6754E-02) (-3.6743E-02, 3.6754e-02) (-5.0100E+01, 0) (-0, 1.0500) (-0, -1.0500) (0.0, 0.0) (0.0, 0.0)	(-1.3000E-01, 0.0) (-6.0200, 0.0 (-8.6588, 0.0) (-3.5200E+01, 0.0) (-2.8200E-01, 0.0) (-3.9301E+00, 0.0) (-2.0101E-01, 2.3999E-01) (-2.0101E-01, -2.3999E-01) (-1.3400E-01, 1.0022E-01) (-1.3400E-01, -1.0022E-01) (-2.5100E-02,0.0) (-9.4200E-03,0.0)

If one wishes, however, to simulate accurately the WWSSN-SP response in Fig. 11.38 left only in the frequency range of interest for this type of seismograph, namely about 0.1 to 10 Hz in which the STS seismographs yield a perfect velocity-proportional output signal, then the simulation filter would just require one zero less but the same two conjugate poles as in Tab. 11.3.

Fig. 11.39 shows a comparison of the original three-component BB-velocity record of an STS2 at station WET from a local earthquake in Germany with the respective seismograms of a simulated Wood-Anderson (WA) seismograph. For a teleseismic earthquake Fig. 11.40 gives the STS2 BB-velocity record together with the respective simulated records for WWSSN-SP and LP. Figs. 11.41 and 11.42 give two more examples of both record simulation and the restitution of very broadband (VBB) true ground displacement. VBB restitution of ground displacement is achieved by convolving the given displacement response of the recording seismometer with its own inverse, i.e.,:

$$H_{rest}(s) = H_s^{-1}(s) * H_s(s). \qquad (11.8)$$

However, Eq. (11.8) works well only for frequencies smaller than the upper corner frequency (anti-alias filter!) and for signal amplitudes that are well above the level of ambient, internal (instrumental), and digitization noise.

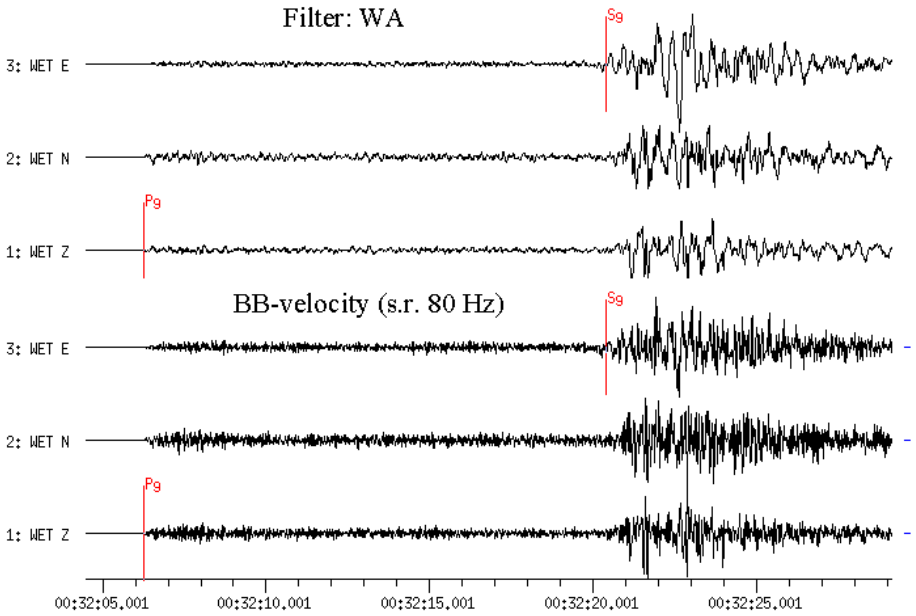

Fig. 11.39 3-component recordings at station WET (Wettzell) of a local earthquake at an epicentral distance of D = 116 km. Lower traces: original STS2 records with sampling rate of 80 Hz; upper traces: simulated Wood-Anderson (WA) recordings. Note that the displacement-proportional WA record contains less high frequency oscillations than the velocity-proportional STS2 record (compare responses shown in Fig. 11.38).

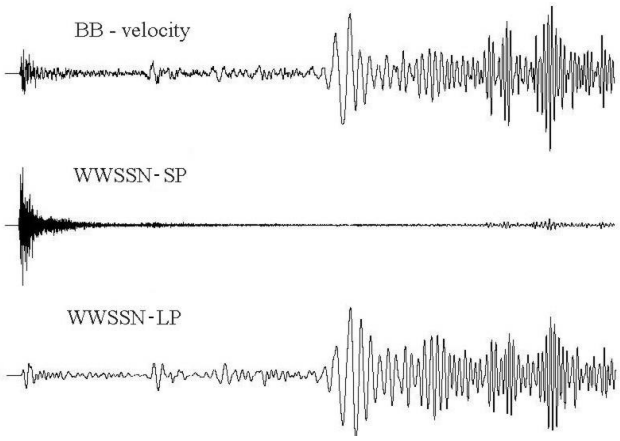

Fig. 11.40 BB-velocity seismogram (top) and simulated WWSSN-SP (middle) and WWSSN-LP seismograms (bottom). Note the strong dependence of waveforms and seismogram shape on the bandwidth of the simulated seismographs.

Both Fig.11.39 and 11.40 clearly show the strong influence of differences in bandwidth and center frequencies of the seismometer responses on both the individual waveforms and the general shape of the seismogram. This is particularly obvious in the simulated teleseismic records of Fig. 11.41 showing the teleseismic P-wave group of an earthquake in California on 16 Sept. 1999. In the BB-velocity seismogram one recognizes clearly the superposition of a

low-frequency signal and a high-frequency wave group. The latter is clearly seen in the WWSSN-SP record but is completely absent in the SRO-LP simulation. From this comparison it is obvious that both the BB-velocity and the SP seismograms enhance short-period signal amplitudes. Therefore, only the former recordings are well suited for studying the fine structure of the Earth and determining the onset time and amplitude of short-period P waves. In contrast, BB-displacement seismograms and LP- filtered seismograms suppress the high-frequencies in the signals. Generally they are more suited to routine practice for surface-wave magnitude estimation and for the identification of most (but not all!) later phases (Figs. 11.16, 11.17, 11.48 and Fig. 2.52).

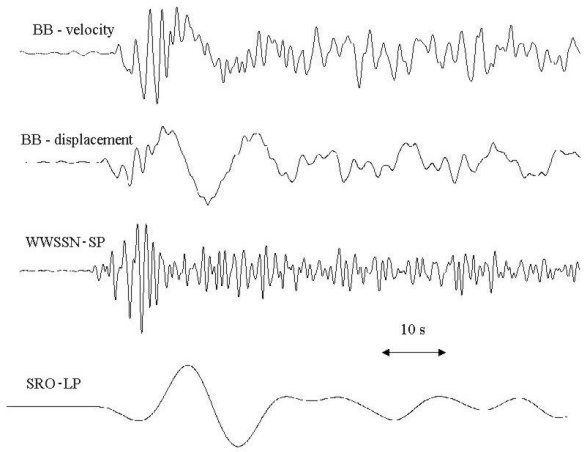

Fig. 11.41 From top to bottom: The original BB-velocity seismogram recorded at station GRFO; the BB-displacement record derived by restitution; the simulated WWSSN-SP; and the simulated SRO-LP seismograms of the P-wave group from an earthquake in California (16 Sept. 1999; D = 84.1°; Ms = 7.4).

Fig. 11.42 shows 10-days of a VBB record from an STS1 vertical-component seismograph (corner period T_c = 360s) at station MOX and simulated WWSSN-SP and SRO-LP seismograms for a short (40 min) time segment of this VBB record.

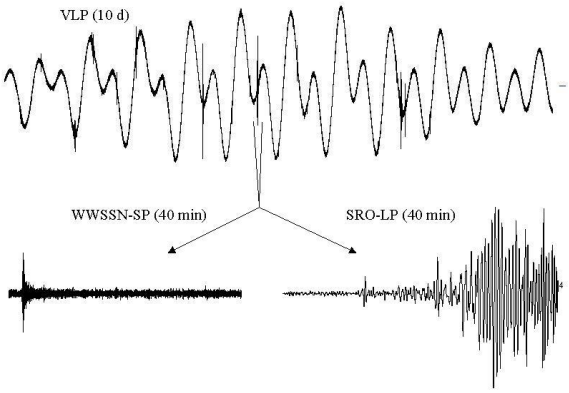

Fig. 11.42 STS1 (T_c = 360s) vertical-component seismogram with a length of 10 days (upper trace) as recorded at MOX station, Germany. In the seismogram we recognize Earth's tides and different earthquakes as spikes. For one of these earthquakes a WWSSN-SP and SRO-LP simulation filter was applied (lower traces). The length of the filtered records is 40 minutes.

Figs. 11.43a-d demonstrate, with examples from the GRSN , the restitution of ("true") displacement signals from BB-velocity records as well as the simulation of WWSSN-SP, Kirnos BB-displacement and SRO-LP records. All traces are time-shifted for the P-wave group and summed (they are aligned on trace 16). The summation trace forms a reference seismogram for the determination of signal form variations. Generally, this trace is used for the beam (see 11.3.5 below). The different records clearly demonstrate the frequency dependence of the spatial coherence of the signal. Whereas high-frequency signals are incoherent over the dimension of this regional network (aperture about 500 to 800 km) this is not so for the long-period records which are nearly identical at all recording sites.

The following features are shown in Figs. 11.43a-d:

a) Time shifted BB-displacement (traces 16-30) and BB-velocity seismograms (traces 1-15) with a duration of 145 s of the P-wave group from an earthquake in Peru on 23 June 2001 (Ms = 8.1) as recorded at 15 stations of the GRSN. The BB-displacement seismogram suppresses the high-frequencies, which are clearly shown on the BB-velocity record.

b) WWSSN-SP simulations for the same stations as in Figure 11.43a. The high-frequency signals are relatively enhanced by the short-period bandpass but the shape and amplitudes of the waveforms are shown to vary considerably within the network, i.e., the coherence is low.

c) Kirnos SKD BB-displacement and d) SRO-LP simulations for the same stations as in Fig.11.43a. The high-frequency signals are masked. All traces show coherent waveforms.

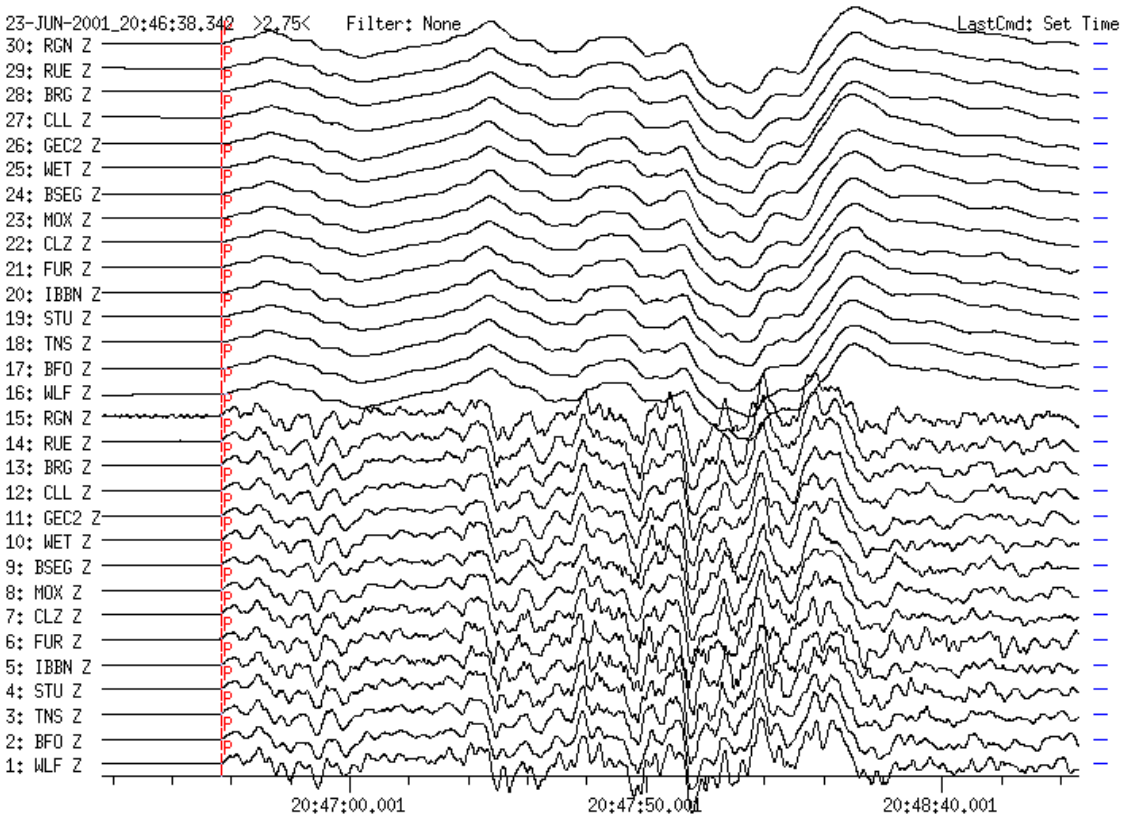

Fig. 11.43a (for explanation see preceeding text)

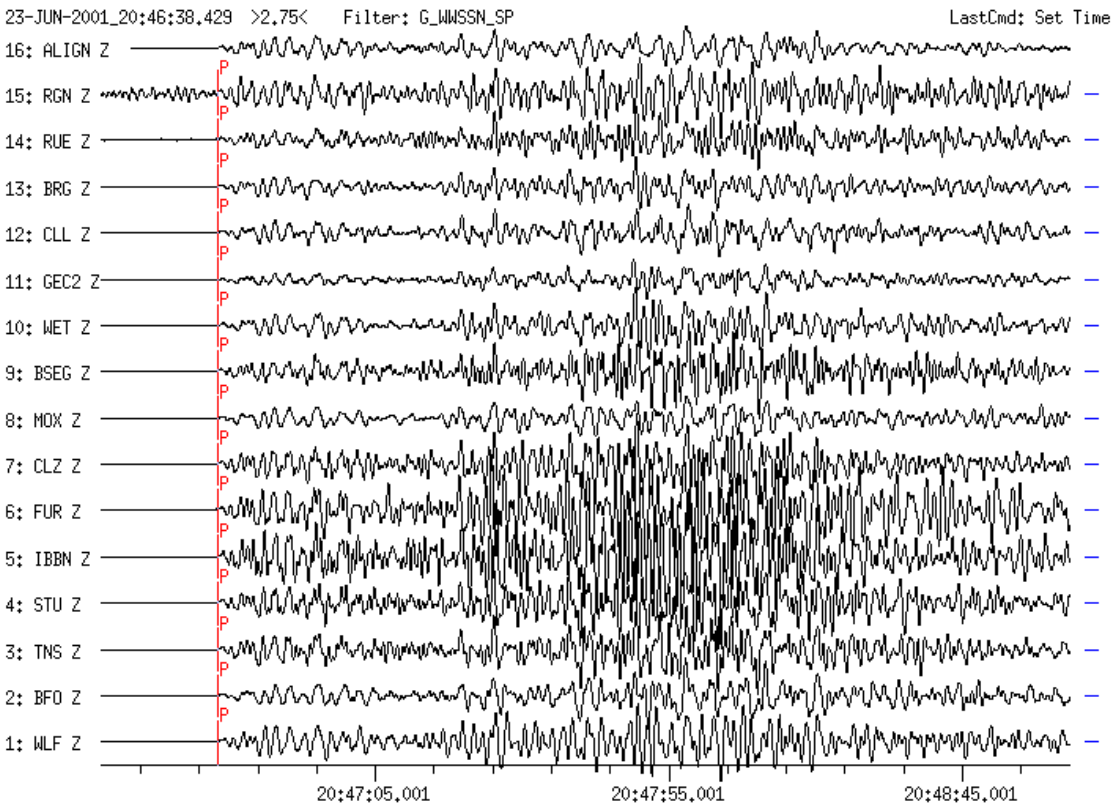

Fig. 11.43b As Fig. 11.43a however with short-period WWSSN-SP simulation.

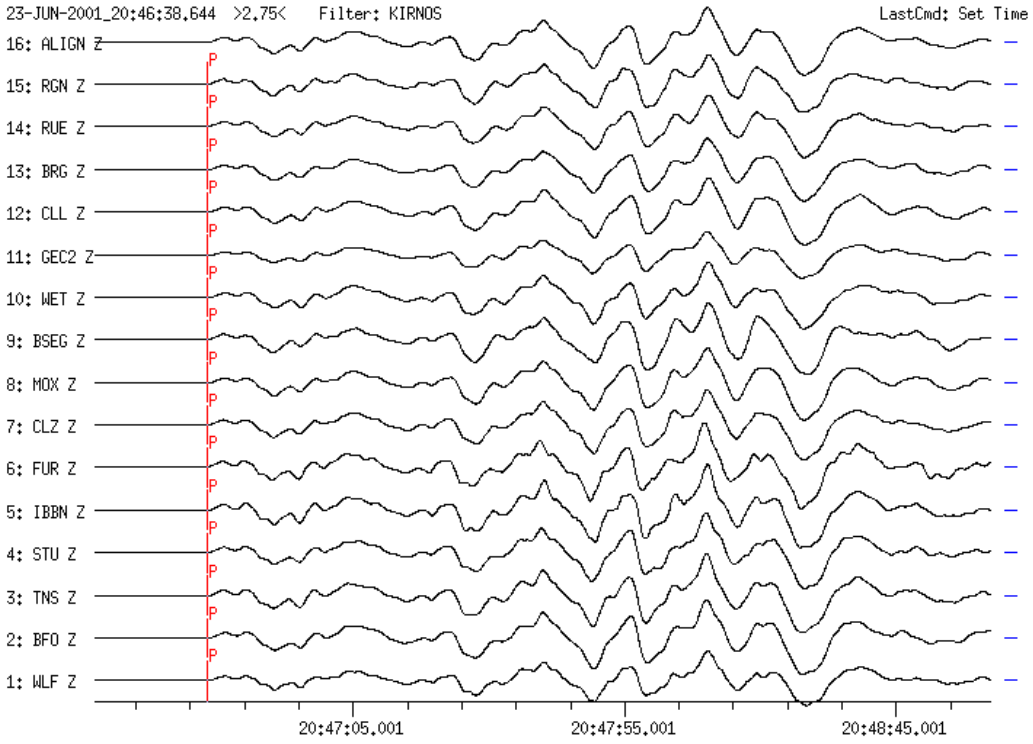

Fig 11.43c As Fig. 11.43a but for displacement-proportional Kirnos SKD simulation.

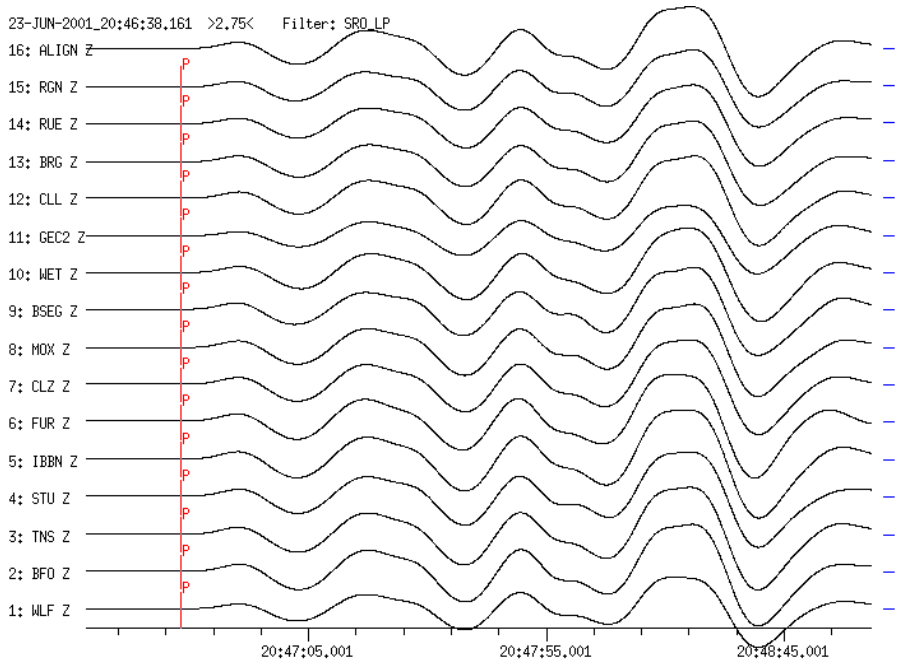

Fig. 11.43d As Fig. 11.43a but for long-period SRO-LP simulation.

Fig. 11.43a-d Restitution, simulation and coherency of seismograms demonstrated with records of the GRSN from an earthquake in Peru (23 June 2001, Ms = 8.1) in the epicentral distance range from 96° to 100°; for explanation see text).

11.3.3 Signal coherency at networks and arrays

Heterogeneous crustal structure and the array aperture limit the period band of spatially coherent signals. The larger the aperture of an array the more rapidly the signal coherence falls off with frequency. At short periods the array behaves like a network of single stations whereas at long periods the array behaves like a sensitive single station. For the GRF-array (aperture about 50 to 120 km) for instance, the signals are coherent for periods between about 1 and 50 s. For the GRSN the band of coherent signals is at longer periods than for the small aperture detection arrays like GERES in Germany or NORES in Norway (aperture 4 and 3 km, respectively) where signals are coherent at periods shorter than 1 s. In the coherency band itself, waveforms vary depending on their dominant frequency, apparent horizontal velocity and azimuth of approach. For instance, coherent waveforms are observed from the GRSN for BB-displacement records, Kirnos SKD simulation and all long-period simulated seismograms (Figs. 11.43a-d) whereas for simulated WWSSN-SP seismograms the waveforms have low coherence or are incoherent.

Figs. 11.44a and b show a comparison of the first 14 s of a P-wave group recorded by the GRSN and the GRF-array. The coherence is clearly higher in the short-period range for the recordings at the smaller GRF-array than for the GRSN. The GRSN works as an array for periods longer than about 10 s but it is a network for shorter periods where the GRF-array works as an array down to periods of about 1 s. This discussion is valid for teleseismic signals only, where the epicentral distance is larger than the aperture of the station network or array.

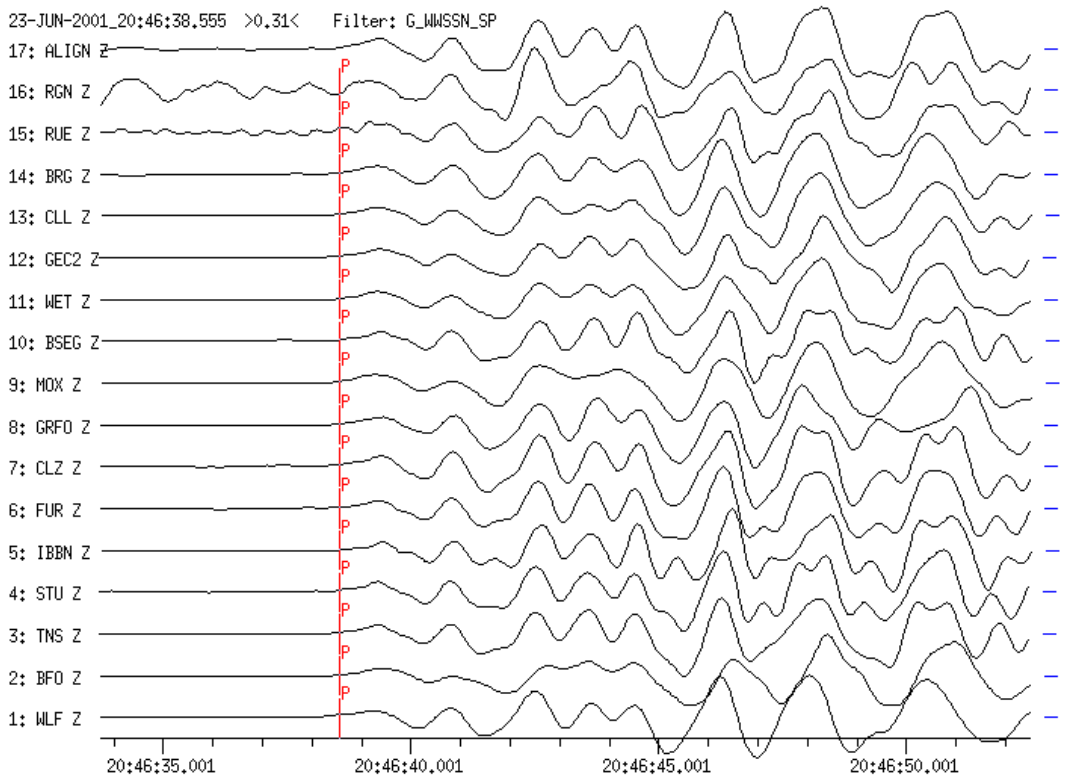

Fig. 11.44a (Figure caption below)

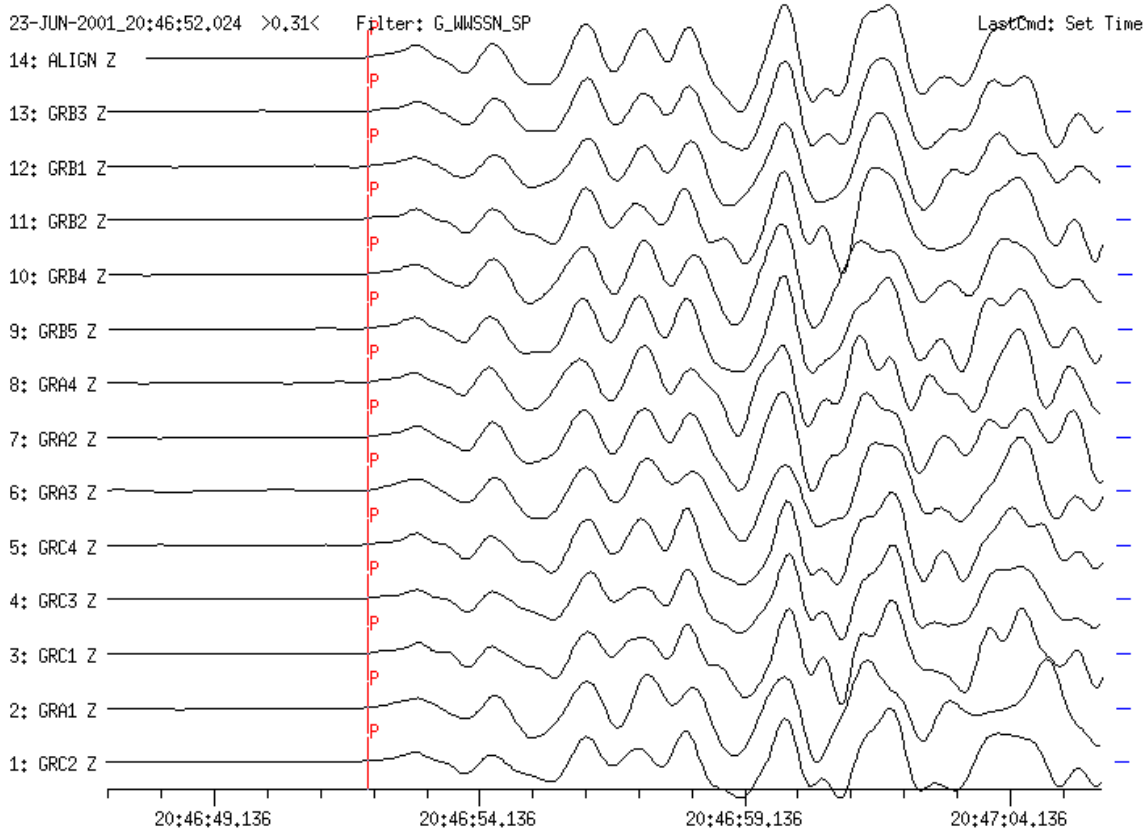

Fig. 11.44b (Figure caption below)

Fig. 11.44 WWSSN-SP simulations of the first 14 s after the P-wave onset from the same Peru earthquake as in Fig. 11.43. **a)** Recordings at the GRSN. **b)** Recordings at the GRF array. Note the lower coherence of the waveforms recorded at the stations of the regional network, which has an aperture much larger than the GRF-array (Fig. 11.3a). The summation traces 17 and 14, respectively, are reference seismograms for the determination of signal waveform variations.

11.3.4 Beamforming

Beamforming improves the SNR of a seismic signal by summing the coherent signals from array stations (see 9.4.5). Signals at each station are time shifted by the delay time relative to some reference point or station. The delay time depends on ray slowness and azimuth and can be determined by trial and error or by f-k analysis (see 11.3.5). The delayed signals are summed "in phase" to produce the beam. In delay-and-sum beamforming with N stations the SNR improves by a factor $\sqrt{N}$ if the noise is uncorrelated between the seismometers. In the summation the increase in amplitude of the coherent signal is proportional to N. For incoherent waves (random seismic noise in particular), it is only proportional to $\sqrt{N}$. Thus, beamforming and f-k analysis are helpful for routine analysis if very weak signals have to be detected and analyzed. Fig. 11.45 shows an example. The signal on the beam trace is the PKP wave of an underground nuclear explosion at Mururoa Atoll. The onset time and signal amplitude of a weak seismic signal can only be read on the beam. The peak-to-peak amplitude is only about 2 nm with a period around 1 s.

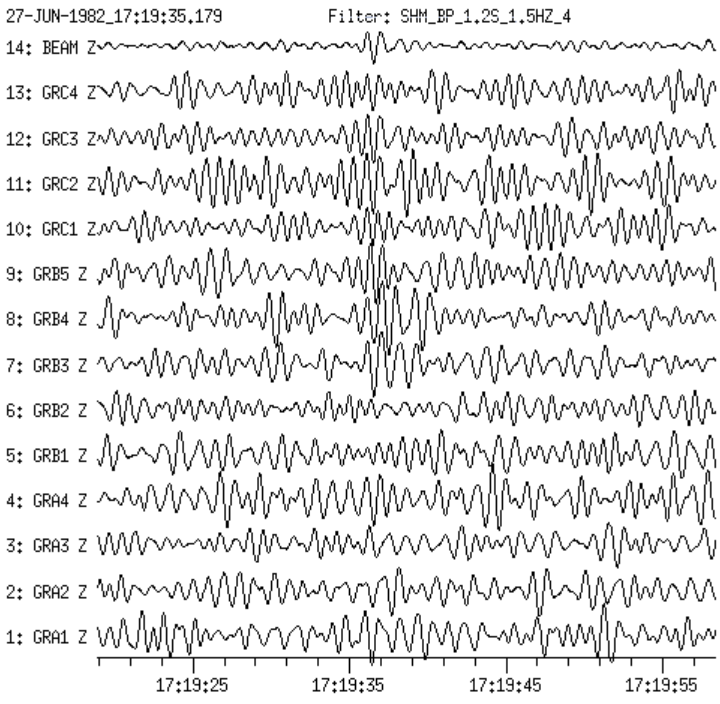

Fig. 11.45 Detection of the PKP wave of a nuclear explosion at Mururoa Atoll on 27 June 1982 at the Gräfenberg array using the delay-and-sum-method and a very narrowband Butterworth bandpass filter (BP) centered around 1 Hz. The event occurred at an epicentral distance of 146° and the explosion yield was approximately 1 kt TNT.

11.3.5 f-k and vespagram analysis

Array-techniques such as f-k and vespagram analysis (Chapter 9) should be applied only to records with coherent waveforms. Vespagram analysis or the velocity spectrum analysis is a method for separating signals propagating with different apparent horizontal velocities. The seismic energy reaching an array from a defined backazimuth with different slownesses is plotted along the time axis. This allows identification of later phases based on their specific slowness values. The best fitting slowness is that for which a considered phase has the largest amplitude in the vespagram. Fig. 11.46 shows the original records from the GRSN (top) and the related vespagram (bottom). More vespagrams are given in Figures 12e–g of DS 11.2.

Note: The original vespagram or VESPA process was defined for plotting the observed energy from a specific azimuth for different apparent velocities as isolines versus time (Davies et al., 1971) and not beam traces with maximum amplitudes for maximum energy from a specific azimuth for different apparent velocities (or slowness) as here and in DS 11.2. For "true" vespagrams see Chapter 9, e.g., Fig. 9.30). But we feel that the trace beam presentation with different maximum amplitudes instead of the energy isolines eases the phase identification.

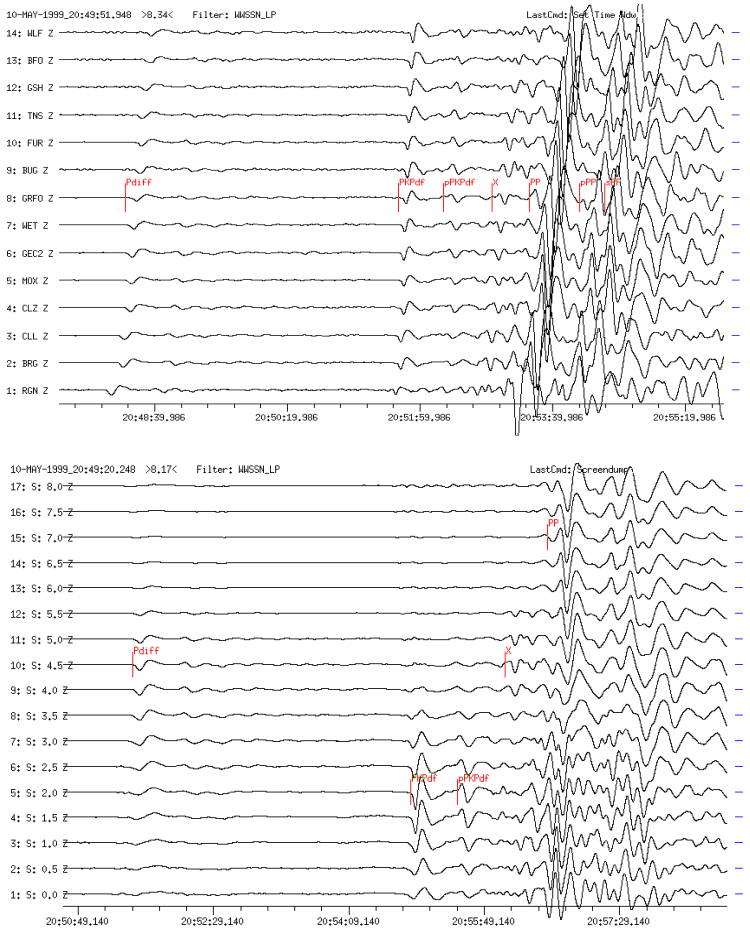

Fig. 11.46 **Top:** Simulated vertical-component WWSSN-LP seismograms from an earthquake in the region of Papua New Guinea. Source data NEIC-QED: 10 May 1999; depth 137 km; mb = 6.5; D = 124° to GRF, BAZ = 51°. The phases Pdif (old Pdiff), PKPdf, pPKPdf, PP, pPP, sPP and an unidentified phase X have been marked. **Bottom:** Vespagram of the upper record section. The analysis yields slowness values of 4.5s/° for Pdif, 2.0s/° for PKPdf and pPKPdf, 7.0s/° for PP, and a value that corresponds to the slowness for Pdif for the unknown phase X.

The f-k analysis is used to determine slowness and backazimuth of coherent teleseismic wave groups recorded at an array. Fig. 11.47 shows an example. The epicentral distance must be much larger than the aperture of the recording array. The f-k analysis transforms the combined traces within a current time window (Fig. 11.47a) into the frequency-wavenumber domain. The result in the f-k domain is displayed in a separate window (Fig. 11.47b) with amplitudes (corresponding to wave energy) coded in color. A good result is achieved when there is a single, prominent color in the maximum (yellow in Fig. 11.47b). This maximum denotes slowness and backazimuth of the investigated phase and is helpful for source parameter determination and phase identification. The example was recorded at the GRF-array from an earthquake in East of Severnaya Zemlya. Slowness and backazimuth (BAZ) values are 7.39 s/° and 12.3°, respectively. These values have been used for producing the beam.

Figs. 11. 47a-b (below) Illustration of the procedure of frequency-wavenumber (f-k) analysis: a) coherent P-wave signals recorded at the GRF-array stations from an earthquake on 19 April 1997 (the box marks the time window selected for the f-k-analysis); b) energy (coded in colors) in the frequency range 0.39-2.97 Hz as a function of wavenumber k. A good result is achieved because the single, prominent maximum (in yellow) shows the presence of a coherent signal. The estimated slowness and BAZ values are 7.39 s/° and 12.3°, respectively.

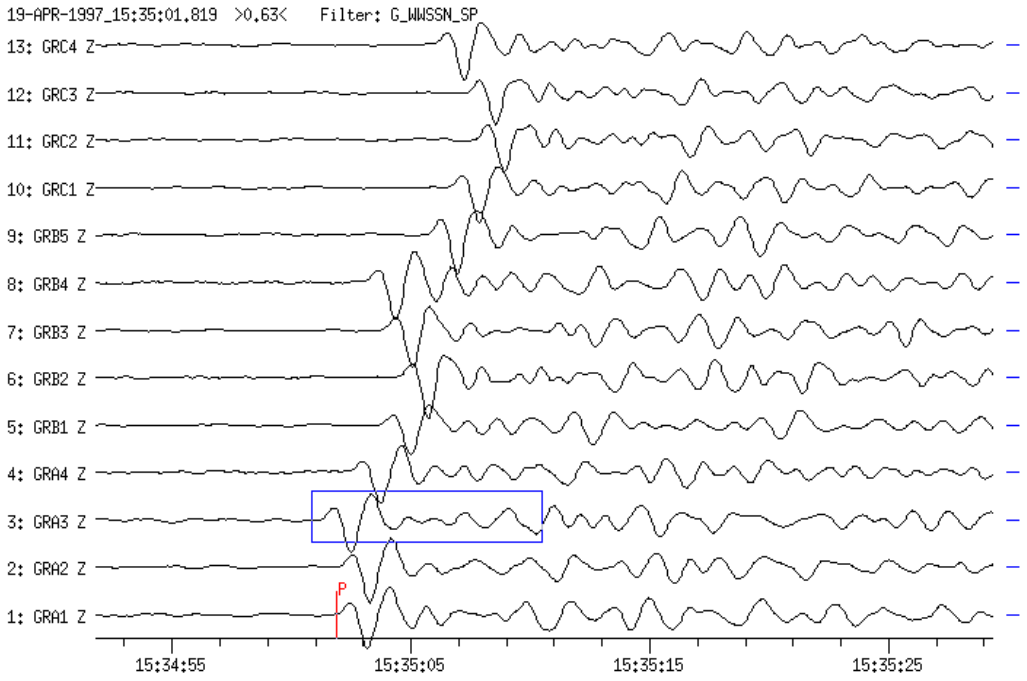

Fig. 11.47a

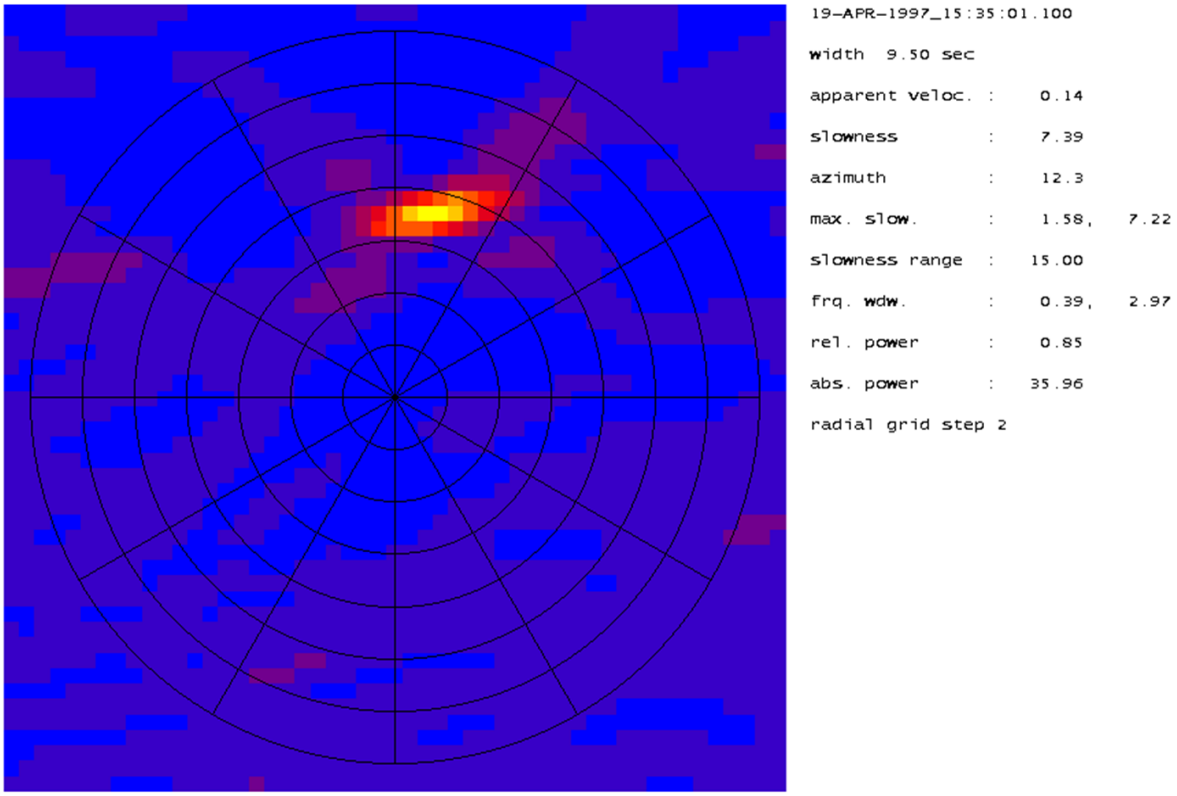

Fig. 11.47b

11.3.6 Polarization analysis

The task of polarization analysis is the transformation of recorded three component seismograms into the ray-oriented co-ordinate systems. For linearly polarized and single pulse P waves in a lateral homogeneous Earth, this task is simple, at least for signals with a high SNR; the direction of the polarization vector of the P wave clearly determines the orientation of the wave co-ordinate system. However, when propagating through heterogeneous and anisotropic media, the seismic waves have three-dimensional and frequency-dependent particle motions and the measured ray-directions may scatter by ten degrees and more about the great circle path from the epicenter to the station (Figs . 2.7 and 2.8 in Chapter 2). Accordingly, one may also describe the wave polarization by its attributes *rectiliniarity*, *planarity* and/or the *largest eigenvalue* (e.g., Wagner and Owens, 1996). If the three main axes of particle motion in space are λ_1, λ_2 and λ_3 than the rectilinearity is *rect* = $1 - (\lambda_2 + \lambda_3)/2\lambda_1$ and the planarity *plane* = $1 - 2\lambda_3/(\lambda_1 + \lambda_2)$ (Flinn, 1965). Their values may vary between 1 (ideal linearity or planarity) and 0.

Determination of particle motion is included in most of the analysis software. For identification of wave polarization and investigation of shear-wave splitting, the rotation of the traditional components N, E, and Z into either a ray-oriented co-ordinate systems (L, Q, T) or in the directions R (radial, i.e., towards the epicenter) and T (transverse, i.e., perpendicular to the epicenter direction) is particularly suitable for the identification of secondary later phases. An example for the comprehensive interpretation of such phases in a teleseismic record is given in Fig. 11.48.

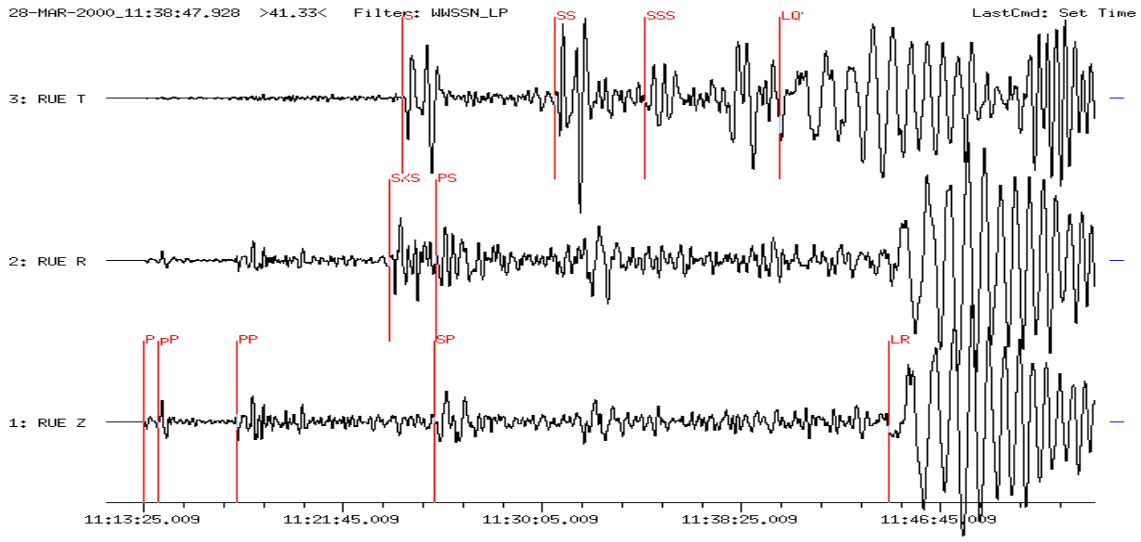

Fig. 11.48 Simulation of three-component WWSSN-LP seismograms of the Volcano Islands earthquake of 28 March 2000, recorded at station RUE in Germany (D = 94°, h = 119 km). The horizontal components N and E are rotated into R and T components. The phases P, pP, SP and the beginning of the dispersed surface Rayleigh wave train LR are marked on the vertical-component seismogram, SKS, PS on the radial component (R) and S, SS, SSS and the beginning of the Love waves LQ on the transverse component (T), respectively. Not marked (but clearly recognizable) are the depth phases sS behind S, sSS behind SS, and SSSS+sSSSS in the T component before LQ. The plotted record length is 41min.

11.4 Software for routine analysis

11.4.1 Brief overview and software library links

There are many different software packages available for automatic and manual processing of earthquake recordings. Some are mainly suited for scientific analysis of the data, others permit the fast routine processing, which includes the generation of reports and maps as needed for the information to the authorities and the public about relevant seismic activity. The companies which sell seismic networks provide commercial software for these tasks. A well-known software of this type is *Antelope* (www.brtt.com). For a briefing Chapter 8, section 8.4.2.2. Other programs were created by university groups or seismological institutions to improve their work such as SHM, SEISAN, SeisComp3 and Earthworm. They were published under free or partially free licencing schemes and applied by other seismologists with so good results that they were later adopted by many observatories and network centers. For more details sections 11.4.2 to 11.4.5. Most of the analysis examples shown in this Chapter have been processed interactively by using the SHM and SEISAN software which belong to the latter type of software. Several software packages combine the fully automatic on-line and seismic data acquisition, archiving, integration, processing and interactive reprocessing such as the commercial SeisComP. Olivieri and Clinton (2012) published a detailed comparison of the features and performance of Earthworm and SeisComp3.

The ORFEUS Software Library (http://orfeus.knmi.nl/) presents a comprehensive list and links to available software in seismology, both for routine seismogram analysis and different research tasks. The focus is on shareware, but some relevant commercial sites are also included. Links to the USGS (http://earthquake.usgs.gov/research/software/) and the IRIS software libraries (http://www.iris.edu/manuals/) are included as well. The latter provides also detailed information about the Seismic Analysis Code (SAC; Goldstein et al, 2003; Goldstein and Snoke, 2005). SAC2000 is used by more than 400 institutions worldwide on a diversity of platforms. Its signal processing capabilities include data inspection, signal correction, and quality control; travel-time analysis and magnitude estimation; spectral analysis and spectrograms, array and three-component analysis. These features are widely used not only in earthquake, explosion and volcanic source studies and the investigation of Earth structure, wave path and site effects but also in the analysis of other geophysical data related to electromagnetic and hydroacoustic phenomena.

Available at the Orfeus ftp site is also the program *PREPROC* for preprocessing (filtering, restitution, simulation etc.) of seismic traces, seismograph calibration, and fast ray synthetic seismograms for body waves (Authors: Axel Plesinger, Miroslav Zmeskal and Jan Zednik).

An older, widely used interactive analysis program, *PCEQ*, for IBM compatible PCs, had been written by C. M. Valdés. It was published as Volume 1 of the IASPEI Software Library (Lee, 1995) and works with the location program HYPO71 for local events. Its principal features are: picking P- and S-wave arrivals; filtering the seismogram for better P- and S-wave picks, and computing the spectra of selected seismogram sections. Quite many analysis examples presented in this Manual, e.g., on event location, spectral and polarization analysis, had been processed with the rather comfortable and appealing software *SEIS89* (Baumbach †, 1999) which is, regrettably, no longer maintained because of the death of the author.

Andrey Petrovich Akimov wrote the program *WSG* (in English AWP: Automated workplace of seismologists). It works in an environment of Windows 95/98/NT and is used at single stations and seismic networks for estimating parameters from local, regional and teleseismic sources. The program converts different seismic data formats such as XDATA, PCC-1, CSS 2.8 and 3.0, DASS, CM6 GSE2 and can import via the TCP/IP protocol data from NRTS and LISS systems (miniSEED). Program and documentation in Russian for version 4.5 are available via http://www.ceme.gsras.ru/engl/stations/wsg_arm.htm.

Another relevant complementary software, named *Geotool*, has been developed at the CTBTO (Chapter 15) for interactively displaying and processing seismoacoustic data from the International Monitoring /system (IMS). A Software User Tutorial provides a set of exercises that cover the full range of functionality of the software system. It is available via http://www.ctbto.org/fileadmin/user_upload/procurement/2013/Ap_D_Part1.pdf, The tutorial covers, amongst others, filter procedures, display and aligning of waveforms, measurement and review of signal arrivals and amplitudes, particle motion analysis and component rotation, waveform analysis (Fourier Transform and spektrograms), f-k and cepstrum analysis, signal correlation, event location, production of bulletins, maps and map overlays.

The wide variety of computer platforms, file formats, and methods to access seismological data often requires considerable effort in preprocessing such data. Although pre-processing work-flows are usually very similar, few software standards exist to accomplish this task. *ObsPy* offers solutions to this problem (section 11.4.6).

11.4.2 SHM

The Seismic Handler Motiv, SHM, is a powerful program for analyzing local, regional and teleseismic recordings with station networks or arrays. It has been developed at the BGR (Federal Institute for Geosciences and Natural Resources) originally for the analysis of data from the Gräfenberg (GRF) array and the German Regional Seismic Network (GRSN) (author: Klaus Stammler; recent developments by Marcus Walther). Program and descriptions are available via http://www.seismic-handler.org. A screen display of SHM is shown in Fig. 11.49.

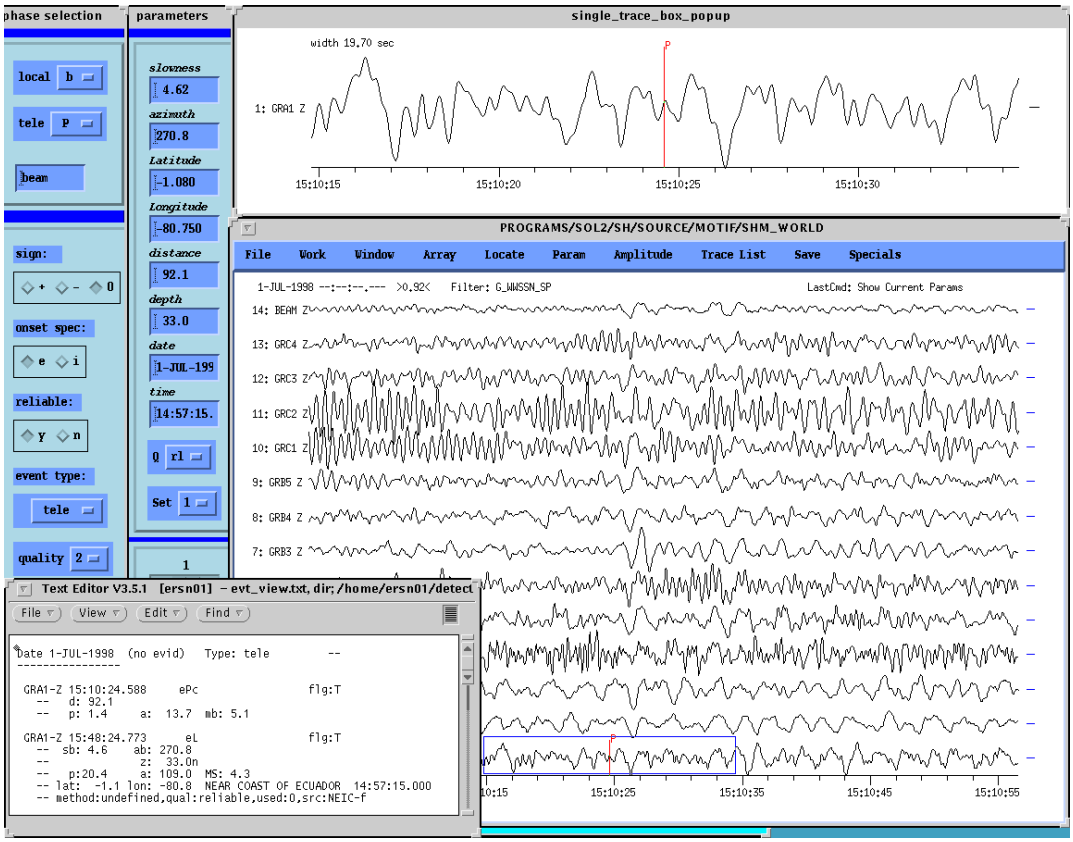

Fig. 11.49 Screen display of the seismic analysis program SHM. Different windows display a number of station recordings (large window), a zoomed single-station window, two seismogram and source parameter windows (left side) and an output window for the results of

Main features of SHM are:

- application of array procedures to a set of stations (slowness- and backazimuth determination by means of beamforming and f-k analysis);
- location algorithms (teleseismic locations using travel-time tables and empirical correction vectors, local and regional locations via external programs, e.g., LocSAT).

The basic program has some (more or less) standardized options, e.g.:

- manual and automatic phase picking (Figs. 11.5 and 11.6);
- trace filtering with simulation and bandpass filters (Figs. 11.37 to 11.40);
- determination of amplitudes, periods and magnitudes (Fig. 11.4);
- display of theoretical travel times on the traces (Fig. 11.48 and 11.52).

Furthermore, the following tasks are implemented:

- rotation of horizontal components (Figs. 11.17, 11.18 and 11.48);
- particle motion diagrams (Fig. 2.7);
- trace amplitude spectrum (Fig. 11.60);
- vespagram trace display (Fig. 11.46);
- determination of signal/noise ratio (Fig. 11.60); and
- trace editing functions.

In 2012 an optional plugin for the magnitude determinations following the IASPEI standards has been implemented, as an alternative to the slightly differing traditional magnitude routines and filter parameters of the Gräfenberg observatory (mb, MS, ml). All resulting parameters are stored in an easily readable and extendable text file format. Different waveform data formats are supported, however the preferred data format is continuous MiniSEED. SHM is supported on a number of Linux distributions (see web page).

11.4.3 SEISAN

Another widely used seismic analysis system is SEISAN developed at University of Bergen, Norway (Ottemöller, Voss, and Havskov, J. (Eds.) (2013). It contains a complete set of programs and a simple database for analyzing digital recordings. SEISAN can be used, amongst other things, for phase picking, spectral analysis, azimuth determination, and plotting seismograms. SEISAN is supported by DOS, Windows95, SunOS, Solaris and Linux and contains conversion programs for the most common data formats. The program, together with a detailed Manual, is available via http://www.ifjf.uib.no/seismo/software/seisan/seisan.html and can also be downloaded from the Manual front page via the link *Download programs and files*. IS 11.6 gives examples of record and parameter presentation, the picking of phase onset times, amplitudes and periods, event location and magnitude determination in the local, regional and teleseismic distance range and the determination of source mechanisms by using either first motion polarities or S/P amplitude ratios. Since its version 8.3 SEISAN is so far the only widely used interactive analysis software (besides the NEIC Hydra software) that has implemented as default the IASPEI recommended filters for determining the standard magnitudes. On the records, where the respective amplitudes and periods are measured, the cursors are annotated with the related unique standard amplitude phase names (Table 4 in IS 3.3 and Fig. 11.50). However, as of now (October 2013), neither SEISAN nor any other currently operating analysis software, with the exception of the NEIC Hydra system, presents the standard magnitudes, with the exception of mb and ML, also in their standard nomenclature (e.g., mB_BB, Ms_20, Ms_BB). Therefore, with its resolution No. 1 of 2013 (Fig. 11.36) IASPEI encourages developers of waveform processing programs to incorporate these standards into their software and the station and network operators as well as data centers to adopt these magnitude and amplitude standards in their day to day operations.

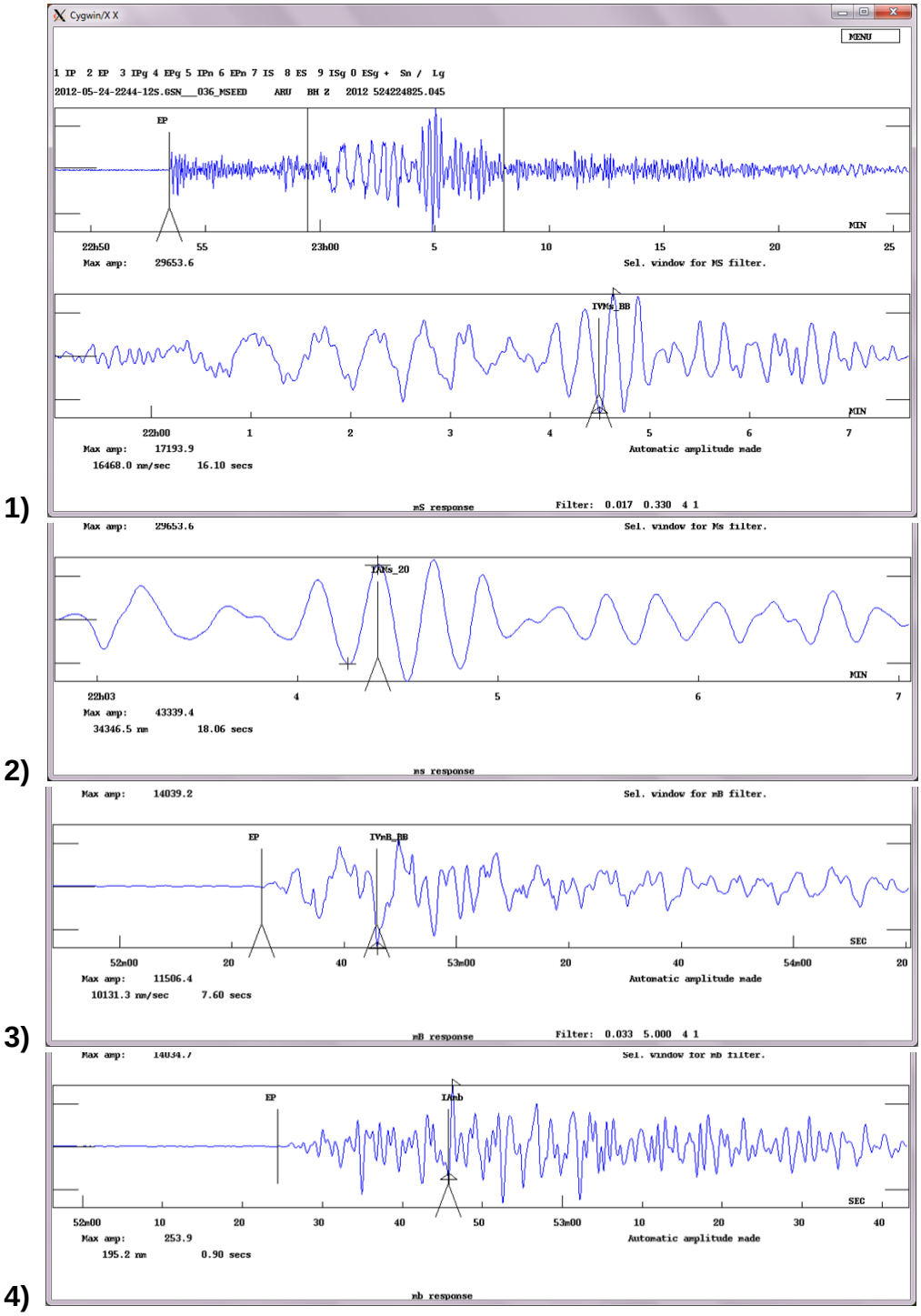

Fig. 11.50 Compiled from SEISAN analysis example 3 in IS 11.6. **1) Uppermost trace:** Velocity broadband record at station ARU (D = 26.2°) of the 24 May 2012 Mw6.2 Mohns Ridge earthquake, offshore northern Norway. **Lower trace:** broadband velocity surface wave window with the marked position for Ms_BB amplitude measurement, annotated with the standard amplitude phase name IVMs_BB. **2) to 4)** Filtered traces for Ms_20, mB_BB and mb amplitude measurements according to IASPEI standards with marked positions annotated with the respective standard amplitude phase names IAMs_20, IVmB_BB and IAmb. I stands for IASPEI standard, A for displacement amplitude and V for velocity amplitude.

Since the beginning of the 1990s, SEISAN was installed in many developing countries in Central and South America, the Caribbean, Asia and Africa by the seismological institutions University of Bergen and NORSAR within Norwegian technical assistance projects on seismic hazard and risk mitigation. The package served very well the needs of the seismological observatories of these countries, was improved and developed taking into account the variable environments and user inputs. The package unites routine seismic processing, reporting, and programs for scientific analysis, for crustal structure, seismic hazard estimation and other topics. The program had always a companion program named SEISLOG for data acquisition and event detection. A new module RTQUAKE is in development which includes also automatic event location. A combination of RTQUAKE and SEISAN could be a good alternative for seismologists at small networks who fear the difficulties to install Earthworm or SeisComP which have a rather steep learning curve.

11.4.4 SeisComP3

SeisComP (Seismological Communication Processor; Hanka et al., 2000 and 2010; http://www.seiscomp3.org) is the most commonly used software in Europe within the scope of real-time earthquake monitoring and increasingly also on a global scale with meanwhile about 300 installations/licenses granted world-wide. It had originally been developed in conjunction with the GEOFON network (Hanka and Kind, 1994; see also Chapter 8, Fig. 8.5) and the GEOFON earthquake information system operated at GFZ (German Research Centre for Geosciences in Potsdam) (see http://geofon.gfz-potsdam.de/). All stations in the global GEOFON network send their data in real time to the GFZ.

A major breakthrough has been the development of the SeedLink protocol for data acquisition and transfer (Hanka et al., 2000) as part of the GEOFON´s SeisComP concept. It permits the connection of digitizers and data loggers from all major manufacturers and all major acquisition systems, the conversion of the native data formats to MiniSEED (for formats Chapter 10) and the uniform transmission, acquisition and archival of heterogeneous network data (Hanka et al., 2010). Automatic real-time data processing became part of SeisComP in 2003. The early GFZ prototype earthquake monitoring system was upgraded with SeisComP3 (for short SC3) which forms a powerful system able to issue within a few minutes automatic but nevertheless rather reliable global and regional earthquake parameter information. Moreover, SC3 allows later interactive refinement and distribution of revised solutions. This system provides now the backbone for the German Indonesian Tsunami Early Warning System (GITEWS; http://www.gitews.org/index.php?id=6), for other tsunami warning centers in the Indian Ocean and the NEAMTWS (Northeastern Atlantic and Mediterranean Tsunami Warning System) area as well as for the GEOFON Extended Virtual Network (GEVN) which presently comprises more than 900 stations world-wide (Hanka et al., 2010).

Besides reliable near real-time automatic data processing SC3 allows very rapid visualization of the results, quick graphical review, and interaction of seismic experts in the warning centers at any time in order to improve the automatic results. This was a precondition under the GITEWS time constraints to issue tsunami warnings already within 5 min after origin time. According to Hanka et al. (2010) the basic automatic system of SC3 consists of modules for:

- quality control
- picking
- event location

- amplitude and magnitude calculation
- waveform quality assessment and
- event and station parameter management.

The interactive part of the system provides according to Hanka et al. (2010):

- graphical user interfaces for visualizing in a map the overall situation regarding earthquake location and station status (Fig. 11.51)
- real-time trace and event summary display
- toolkits for analyzing the earthquake epicenter, source depth and magnitude
- manual picker optimized for rapid verification of pre-calculated picks from strong earthquakes
- automatic loading of newly acquired real-time data with picks associated to the ongoing event
- automatic amplitude scaling and trace alignment
- conventional off-line event analysis, also of small and moderate earthquakes that have not been processed by the automatic system.

The latter point allows for more detailed and accurate seismic phase and magnitude measurements for the final station and/or network parameter bulletins and thus also for making valuable contributions to final regional and global seismological parameter bulletins, e,g., of the EMSC and the ISC, in agreement with IASPEI recommended measurement standards. Making full use of the off-line data processing and analysis potential offered by SC3 reduces procedure dependent data scatter and systematic biases. This assures best representativeness, long-term compatibility and accuracy of its final data products also on a global scale, thus improving the usefulness of international parameter data bases for earthquake statistics, hazard assessment and other research tasks.

Although SC3 measures in its automatic mode, besides several other magnitudes, in principle already two of the four IASPEI recommended teleseismic standard magnitudes, namely mb and mB_BB, the stringent time limit set for early warning applications requires to measure mb already within the first 30 s and mB within the first 60 s of the event record traces. For the greatest or very slow strong earthquakes this means, however, that the largest amplitude in the P-wave train may still be missed by such a pre-set measurement time window, more frequently for mb but occasionally also for mB (see, e.g., Figs. 3.6, 3.13, 3.46, 3.62 and 3.65 in Chapter 3). Then these two body-wave magnitudes but also the Mw proxy estimate Mw(mB) (see Bormann and Saul, 2008) may be underestimated, up to about 0.3 magnitude units (m.u.) This can be corrected easily by later off-line analysis, when the whole wave train is available. Then also the very important complementary broadband surface-wave magnitude standard Ms_BB (Chapter 3, section 3.2.5), can be measured without any restrictions set by the rapid automatic processing mode when applied to large global sets of waveform data for early warning purposes. For smaller networks, however, it is said to be practicable already even in the automatic mode.

Originally developed for tsunami early warning, SC3 evolved also to be a very powerful system for local earthquake monitoring including off-line analysis, providing typically needed functionality as customizing and applying filters to the records, project theoretical phase onset times on the records, allow axes rotations to ease phase detection and identification and provide a first motion analysis to determine source mechanisms.

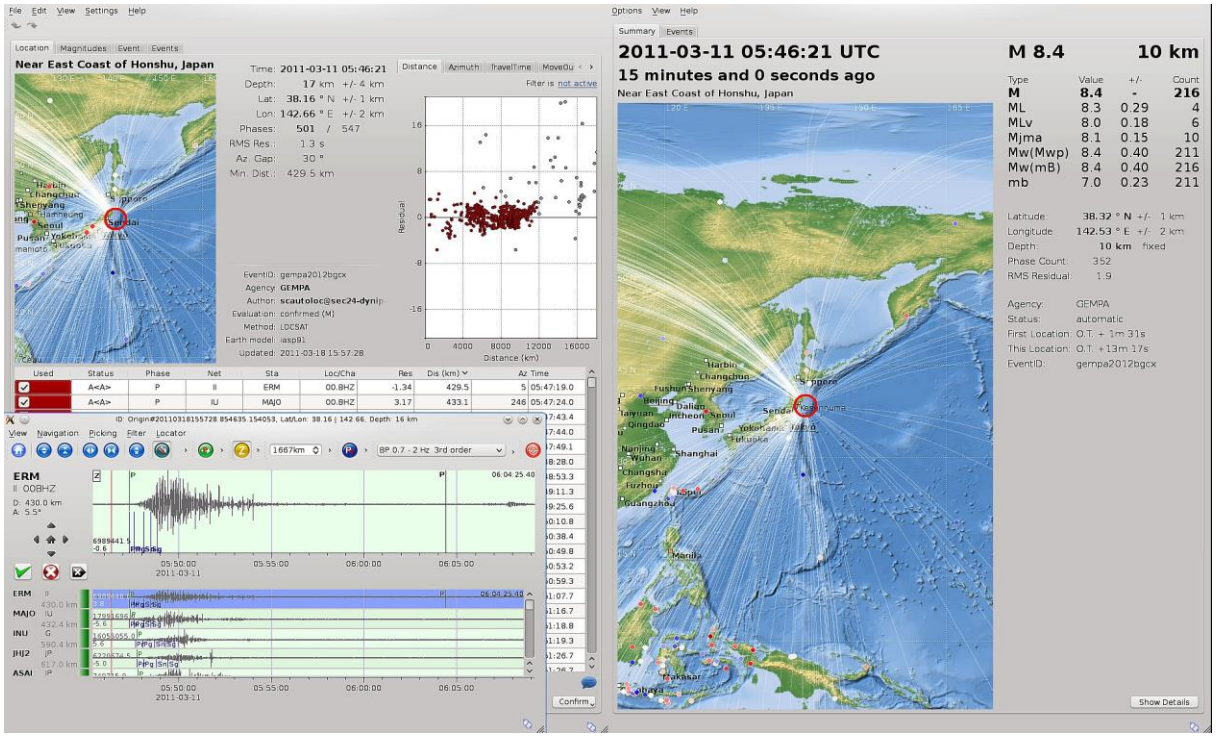

Fig. 11.51 SeisComP3 screenshots of an authentic playback from the Tohoku earthquake on March 11, 2011. **Left** side: Screenshot from the SC3 module to review/revise hypocenter solutions; **right side** shows the event summary view (Figure by courtesy of B. Weber).

11.4.5 Earthworm

Earthworm is a non-commercial seismological software package (Johnson et al., 1995; http://folkworm.ceri.memphis.edu/ew-doc/ and http://www.earthwormcentral.org/). On its web page it is described as follows:

"Earthworm is an open architecture, open source public software for data acquisition, processing, archival and distribution. It was originally developed by the United States Geological Survey. Earthworm binaries and source files are freely available to everyone. Development and maintenance are now carried out by the Earthworm User Community, ISTI (Instrumental Software Technologies, Inc., New York, USA) and CERI (Center for Earthquake Research and Information, University of Memphis, USA)."

The software is written in C and can be compiled for Windows, Linux, Solaris and Mac OS X operating systems. Precompiled binaries can be downloaded from the Earthworm websites. Earthworm seismic data acquisition and processing software can be used for single stations as well as local, regional and global seismic networks. The development of the package started in 1993. Nowadays, over 150 institutions have registered installations of Earthworm. Many more "Earthworms" run on the office computers or Laptops of seismologists, geophysicists, and hobbyists without formal registration as the software is completely free. In addition to seismology, Earthworm's data acquisition and management capabilities are used for other waveform data, including Infra-sound, Geomagnetic, and Atmospheric measurements.

Earthworm is very structured and consists of around 130 modules which the user can configure according to his needs and combine them for executing a specified task. This task can be so simple as to acquire the data of a single component and write its data to disk. The script which controls the execution would contain only a few lines and an experienced user would edit it in some minutes. The task can also be rather complicated as to acquire, in real time, the data of a network of several hundred stations, perform band pass filtering and phase picking for all the traces, event definition, automatic localization and magnitude determination. To control such a demanding task necessitates, however, a rather large script which might require many weeks or months of development and testing to get it working properly. Simpler Earthworm configurations can run on very cheap and small computers such as the Raspberry Pi. For a small or medium seismic network a low cost PC with two cores could be sufficient. Larger networks of several hundred stations require more powerful computers. Different tasks could even been distributed to several servers in the seismic data center.

There are around 30 data acquisition modules suited for many of the A-D-cards and digital seismographs on the market, even for some cheap A-D-cards used mainly by hobbyists. Earthworm systems can communicate with each other as with other data acquisition and processing systems (e.g. SeisComP) by using special modules. For instance, an Earthworm installed on a simple computer with an A-D card could acquire data at a seismic station and transmit them in real time to another Earthworm or SeisComP which is running in a server of the seismic data center and performs the automatic earthquake detection and processing. Earthworm has also modules for sending out email messages triggered by seismic event detection but Earthworm lacks sophisticated visualization tools for seismogram.

“Glowworm” is a special suite of Earthworm modules that has been developed at the USGS in the late 1990s. It contains data archiving and processing methods and visualization tools typical for volcano monitoring. Nowadays, Glowworm seems to be outdated as several of its modules were not adapted to structural changes of the main stream of Earthworm. Nevertheless, it is still in use in many volcano observatories. The most important processing modules of original Glowworm, e.g. for the continuous calculation of RSAM (*Real-time Seismic-Amplitude Measurement*, which represents the overall signal size over periods of 10 minutes) and SSAM (*Seismic Spectral-Amplitude Measurement*, which shows the relative signal size in different frequency bands) were ported to the standard Earthworm.

Standard Earthworm is dedicated only to automatic data acquisition and routine processing. Therefore it has no own interactive processing modules. But it contains modules which permit the generation of event files in data formats needed by other seismological data processing programs, for instance SEISAN or SAC. These packages can then be used for interactive routine processing or for scientific research. A widely used combination at seismological observatories with smaller networks and lack of personnel experienced in computing and programming is to use Earthworm for data acquisition, event detection and generation of event files; and SEISAN for the interactive routine processing of the events. This avoids the automatic location and magnitude determination which is not easy to configure. Based on Earthworm the Alaska Tsunami Warning Center (ATWC) developed the *Early Bird* package (Luckett et al., 2008) for the detection, automatic location and magnitude determination of local, regional and teleseismic events, especially for tsunami warning. It contains also modules for seismogram visualization and interactive processing, phase picking and generation of epicenter maps.

11.4.6 ObsPy

ObsPy is an open-source project (Beyreuther et al. 2010; Megies et al., 2011) aimed at facilitating rapid application developments for seismology. It provides a toolbox using *Python* language (http://www.python.org/ and http://en.wikipedia.org/wiki/Python) and simplifies the usage of Python programming for seismologists. It provides parsers for common file formats, clients to access data centers and seismological signal processing routines that allow the manipulation of seismological time series. Good starters are ObsPy Gallery and Tutorial (http://docs.obspy.org/index.html). ObsPy is currently running and tested on Linux, Windows XP/Vista/7/8 and Mac OS X.

In ObsPy the following essential seismological processing routines are implemented and ready to use:

- reading and writing data only SEED/MiniSEED and Dataless SEED (http://www.iris.edu/manuals/SEEDManual_V2.4.pdf);
- XML-SEED (Tsuboi et al. 2004);
- GSE2 (http://www.seismo.ethz.ch/autodrm/downloads/provisional_GSE2.1.pdf) and
- SAC (http://www.iris.edu/manuals/sac/manual.html), as well as filtering, instrument simulation, triggering, and plotting.
- Modules to read SEISAN data files (Havskov and Ottemöller 1999) and to retrieve data with the IRIS/FISSURES data handling interface (DHI) protocol (Malone 1997);
- Support to retrieve data from ArcLink (a distributed data request protocol for accessing archived waveform data, see Hanka and Kind 1994) or a SeisHub database (Barsch 2009).

While Python gives the user all the features of a full-fledged programming language including a large collection of scientific open-source modules, ObsPy extends Python by providing direct access to the actual time series, thus allowing the use of powerful numerical array-programming modules like NumPy (http://numpy.scipy.org) or SciPy (http://scipy.org) and the visualization of the results. This is an advantage over SAC, SEISAN, and SeismicHandler which do not provide methods for general numerical array manipulation.

11.5 Examples of seismogram analysis

11.5.1 Introductory remarks

The character of a seismogram depends on the source mechanism and size, the source depth, the signal-to-noise ratio (SNR) and whether the epicenter of the source is at local, regional or teleseismic distances. Many seismic phases of different origin and character may occur in these different ranges. For explanations of their phase names and origin see IS 2.1. In the following we deliberately show mostly records with good SNR because we wish to illustrate what types of seismic phases, also relatively week ones with respect to the strongest phases, may occur at which distances and what their basic features such as relative travel-time, period, amplitude and polarity are with respect to other phases. However, most seismic events are relatively weak and therefore the SNR is low and most signal phases are buried in the noise, especially in broadband records. Then filter procedures have to be applied in order to improve the SNR. But what types of filters are suitable depends on the frequency, wave number and polarization properties of the signal and of the noise. These problems, including

those of bandwidth-dependent waveform distortion due to filtering, are outlined in detail in Chapter 4. There also many examples are presented on SNR-improvement by applying different types of filters and their pros and cons are discussed. For array-specific methods of SNR improvement see also Chapter 9 and in the Data Sheets DS 11.1-11.3 more examples are given that show the different record appearance depending on the applied filter and time resolution. There are no straightforward standardized receipts for optimal filtering. Which filter procedure and parameters are best suited also depends on which parameters (such as onset time, amplitude, period, slowness or polarization) have to be determined best in which frequency range and of what type of seismic phase. Only rich own interactive and task-dependent experience can help to develop the proper "feeling" for it. Who only uses and relies on some basic default parameter settings of automated procedures will never get a deeper understanding of it and learn to discriminate between real signal improvements, distortions or even filter-induced artifacts.

Seismograms of small local earthquakes are characterized by short duration of the record from a few seconds to 1-2 minutes, higher frequencies, and a characteristic shape of the wave envelope, usually an exponential decay of amplitudes after the amplitude maximum, termed "coda" (Figure 1b in DS 11.1 and Figure 2in EX 11.1). However, records of large earthquakes with longer rupture duration and thus radiating dominatingly longer periods may look differently in the local distance range. At teleseismic distances records show generally lower frequencies (because high-frequency energy has already been reduced by anelastic attenuation and scattering), and much longer duration from say fifteen minutes to several hours (e.g., Figs. 1.6, 2.20, 2.21 and 11.52).

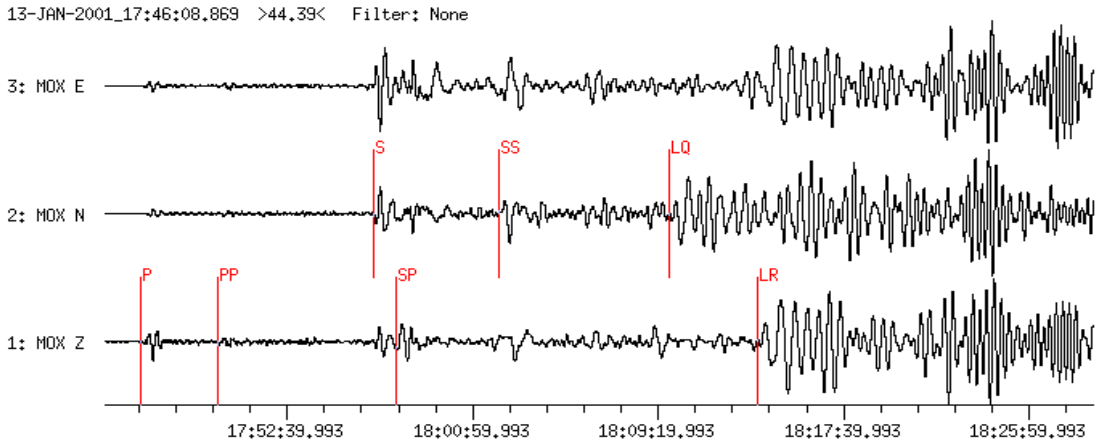

Fig. 11.52 Example of 3-component broadband velocity seismograms of a teleseismic Mw = 7.7 earthquake in El Salvador recorded at station MOX, Germany (D = 86.5°).

Records of regional events at distances of several hundred kilometers have intermediate features, and are - as local events - characterized by still high frequency content and only a few distinct phase onsets with much signal-generated noise in between due to scattering at crustal heterogeneities. This hardly allows to recognize and pick for sure the onsets of weaker but theoretically expected phases such as Pb, Sb, and Sn (Figs. 11.53 and 11.54 in section 11.5.1).

The various wave groups above the noise level, arriving at a station over different paths, are called seismic phases. They have to be recognized, identified and their parameters determined (onset time, amplitude, period, polarization, etc.). Phase symbols should be assigned according to the IASPEI recommended standard nomenclature of seismic phases. For phase names, their definition and ray paths see IS 2.1. Types and characteristics of seismic phases vary with distance, depending also on the source type and depth. These characteristics will be discussed in more detail in the following sections.

There is no unique standard definition yet for the distance ranges termed "near" or "local" and "regional" (near to far regional), or "distant" ("teleseismic"; sometimes subdivided into "distant" and "very distant"). Regional variations of crustal and upper-mantle structure make it impossible to define a single distance at which propagation of local or regional phases stops and only teleseismic phases will be observed. In the following we consider a source as local if the direct crustal phases Pg and Sg arrive as first P- and S-wave onsets, respectively. In contrast, the phases Pn and Sn, which have their "bottoming" (or starting) point in the uppermost mantle, are the first arriving P and S waves in the regional distance range. However, as discussed in Chapter 2, section 2.6.1 and shown in Fig. 2.47, the distance at which Pn takes over as first arrival depends on the crustal thickness, average wave speed and the dip of the crustal base. The "cross-over" distance x_{co} between Pn and Pg is - according to Eq. (6) in IS 11.1 for shallow (near surface) sources - roughly $x_{co} \approx 5 \times z_m$ where z_m is the Moho depth. Note, however, that as focal depth increases within the crust, x_{co} decreases, down to about $3 \times z_m$. Accordingly, the local distance range may vary from region to regions and range between about 100 km and 250 km. The CTBTO Technical Instructions (see IDC Documentation, 1998) considers epicentral distances between 0° to 2°, where Pg appears as the primary phase, as local distance range.

The Willmore (1979) Manual defines as near earthquakes those which are observed up to about 1000 km (or 10°) of the epicenter, and P and S phases observed beyond 10° as usually being teleseismic phases. However, regional phases such as Pn, Sn and Lg, will generally propagate further in stable continental regions than in tectonic or oceanic regions. According to the Earth model IASP91, Pn may be the first arrival up to 18°. The rules published in the IDC Documentation (1998) allow a transitional region between 17° and 20° in which phases may be identified as either regional or teleseismic, depending on the frequency content and other waveform characteristics. Accordingly, one might roughly define seismic sources as local, regional and teleseismic if their epicenters are less than 2°, between 2° and 20°, or more than 20° away from the station. Sometimes, the regional range is further subdivided into 2°-6°, where also the phase Rg may be well developed (Fig. 11.23), and 6°-20° where only Sn and Lg are strong secondary phases.

On the other hand, the calibration curve for the local magnitude Ml according to Richter (1935) has originally been given for distances up to 600 km and has been extended now for some regions far beyond (up to 1500 km, Table 2 in DS 3.1) making Ml an even far regional magnitude. On the other hand, the new IASPEI standards for teleseismic magnitudes mb and Ms(20) are measured between 20° and 100°, respectively 20° and 160°, whereas the broadband surface-wave magnitude Ms(BB), measured between 2° and 160°, is in fact both a regional and a teleseismic magnitude.

At distances beyond 15° Pn and Sn amplitudes become too small (except in some shield regions). The first arriving P and S phases have then already taken travel paths through deeper parts of the upper mantle, thus being affected by the pronounced velocity increases at the

bottom of the upper mantle (410 km discontinuity) and at the bottom of the transition zone to the lower mantle (660 km discontinuity) (Chapter 2, Figs. 2.77 and 2.79). This gives rise to the development of two triplications of the P- and S-wave travel-time curves with prograde and retrograde branches,.the second one reaching up to about 28° epicentral distance. In some distance ranges the related P and S onsets follow closely to each other (Figs. 2.32 and 2.76), thus forming rather long and complex waveforms (Fig. 11.53). The largest amplitudes occur in the range of the left-side cusp of the 660 km discontinuity triplication (P660P) between about 18° and 21° (termed "20°-discontinuity"; see also the amplitude-distance curves in Fig. 11.10) but with weaker P-wave first arrivals some 5 to 10 s earlier. Accordingly, small differences in epicentral distance can lead to large differences in the amplitude of the body-wave groups in seismic records (see also Figure 2b in DS 11.2.

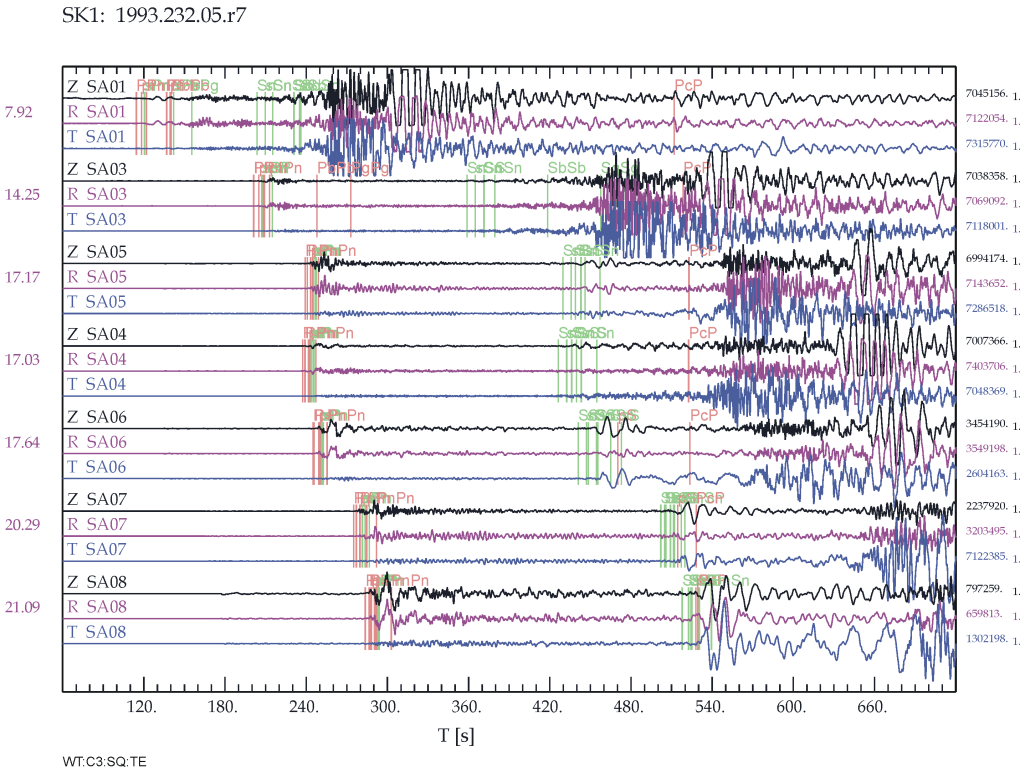

Fig. 11.53 3-component records in the distance range between 7.9° and 21.1° by a regional network of portable broadband instruments deployed in Queensland, Australia (seismometers CMG3ESP; unfiltered velocity response). The event occurred in Papua New Guinea at 15 km depth. The predicted phase arrival times for the AK135 model are depicted. Primary, depth and other secondary arrivals (such as PnPn in the P-wave group and SbSb as well as SgSg in the S-wave group) superpose to complex wavelets. Also note that several of the theoretically expected phases have such weak energy that they cannot be recognized on the records at the marked predicted arrival times above the noise level or the signal level of other phases (e.g., PcP) (courtesy of B. Kennett).

These complications and different pros and cons for various definitions notwithstanding we present, slightly different from NMSOP-1 and DS 11.2, in the following the examples from near to regional sources up to about 20°, in the teleseismic range between about 20° and 100°, and in the far teleseismic "core shadow" range beyond 100°,

11.5.2 Seismograms from near and regional sources (0° < D <≈20°)

Seismograms recorded in this distance range are dominated by P and S waves that have traveled along different paths through the crust and the upper mantle of the Earth. They are identified by special symbols for "crustal phases" (see IS 2.1). Pg and Sg, for example, travel directly from a source in the upper or middle crust to the station whereas the phases PmP and SmS have been reflected from, and the phases Pn and Sn critically refracted along or "dived beneath" the Moho discontinuity (Fig. 11.53). Empirical travel-time curves are given in Exercise EX 11.1 (Figure 4) and a synthetic record section of these phases in Fig. 2.82. In some continental regions, phases are observed which have been critically refracted from a mid-crustal discontinuity or have their turning point in the lower crust. They are termed Pb (or P*) for P waves and Sb (or S*), for S waves, respectively. For shallow sources, crustal "channel-waves" Lg (for definition see IS 2.1) and surface waves Rg are observed after Sg-waves. Rg is a short-period Rayleigh wave (T ≈ 2 s) which travels in the upper crust and is usually well developed in records out to about 300 km of near-surface sources such as quarry blasts or mining induced events and thus suitable for discriminating such events from local tectonic earthquakes (Figs. 11.23a-d).

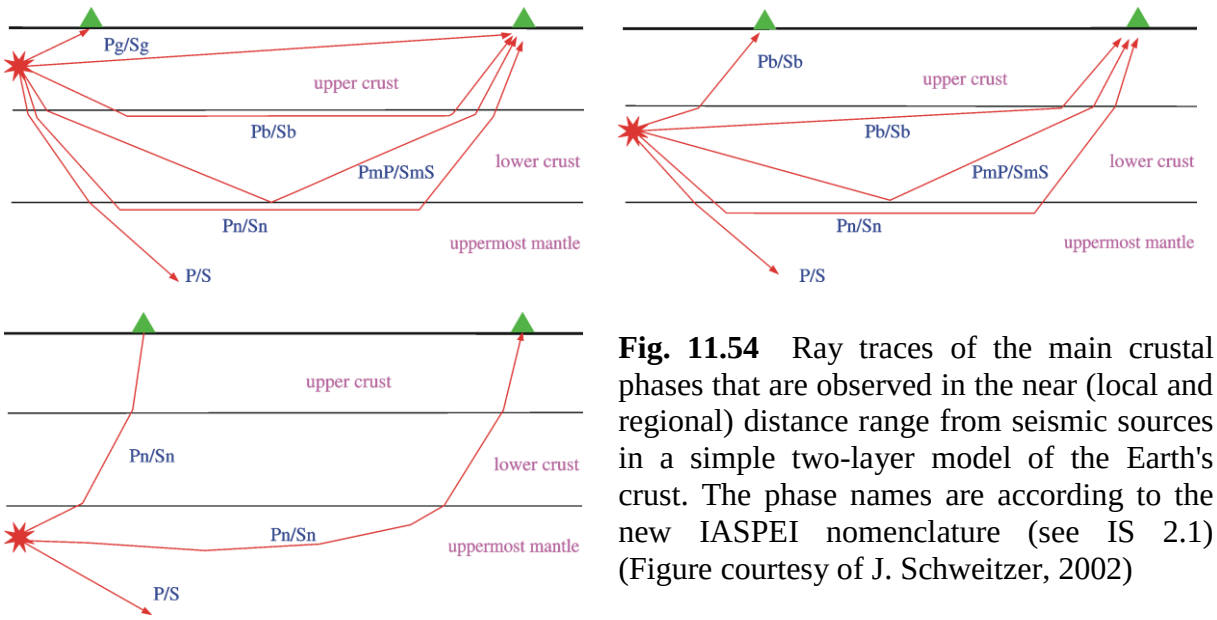

Fig. 11.54 Ray traces of the main crustal phases that are observed in the near (local and regional) distance range from seismic sources in a simple two-layer model of the Earth's crust. The phase names are according to the new IASPEI nomenclature (see IS 2.1) (Figure courtesy of J. Schweitzer, 2002)

.

Usually, Sg and SmS (the supercritical reflection, which often follows Sg closely at distances beyond the critical point; Fig. 2.43) are the strongest body wave onsets in records of near seismic events whereas Pg and PmP (beyond the critical point) have the largest amplitudes in the early part of the seismograms, at least up to 200 – 400 km. Note that for sub-crustal earthquakes no reflected or critically refracted crustal phases exist. However, according to the new IASPEI nomenclature, P and S waves from sub-crustal earthquakes with rays traveling from there either directly or via a turning point in the uppermost mantle back to the surface are still termed Pn and Sn (Fig. 11.54, lower left). At larger distances such rays arrive at the surface with apparent "sub-Moho" P and S velocities (see below).

Typical propagation velocities of Pg and Sg in continental areas are 5.5-6.2 km/s and 3.2-3.7 km/s, respectively. Note, that Pg and Sg are direct waves only to about 2° to 3°. At larger distances the Pg-wave group may be formed by superposition of multiple P-wave reverberations inside the whole crust (with an average group velocity around 5.8 km/s) and the Sg-wave group by superposition of S-wave reverberations and SV to P and/or P to SV conversions inside the whole crust. According to the new IASPEI phase nomenclature the definitions given for Lg waves and Sg at larger distances are identical, with the addition that the maximum energy of an Lg crustal "channel" wave travels with a group velocity around 3.5 km/s. According to the definition of the IASPEI mb_Lg standard magnitude (see IS 3.3) the amplitude of Lg is measured as the *"...third largest amplitude in the time window corresponding to group velocities of 3.6 to 3.2 km/s, in the period (T) range 0.7 s to 1.3 s*".

In routine analysis, usually only the first onsets of these wave groups are picked without noting the change in character at larger distances. According to the Technical Instructions of the IDC Documentation (1998), stations of the CTBTO International Monitoring System (IMS) generally tend to name the strongest transverse arrival Lg and not Sg. A reliable discrimination is still a subject of research and not yet one of routine analysis and data reporting. Therefore, no simple and unique criteria for discrimination, which also depend on source type and propagation path, can be given here. They may be added to this Manual at a later time.

Lg waves may travel in continental shield regions over large distances (Fig. 2.15), even beyond 20° whereas Rg waves, which show clear dispersion and longer periods than Lg (Fig. 11.23a and b), are more strongly attenuated and generally not observed beyond 6°. The apparent velocities of Pn and Sn are controlled by the P- and S-wave velocities in the upper mantle immediately below the Moho and typically range between 7.5 - 8.3 km/s and 4.4 - 4.9 km/s, respectively.

Note: Seismograms from local and regional seismic sources are strongly influenced by the local crustal structure which differs from region to region and even between local stations. This may give rise to the appearance of other onsets (which may be strong) between the mentioned main crustal phases. These "unexpected" phases cannot simply be explained as direct or refracted/reflected waves radiated from a near-surface source in a single or two-layer crustal model. Some of these phases may relate to converted waves and/or depth phases such as sPmP (e.g., Bock et al., 1996). Also, at larger distances, up to about 30°, multiples such as PgPg, PbPb, PnPn, PmPPmP etc. and their related S phases, are expected to follow each other closely within the P and S-wave group according to the AK135 travel-time model (Fig. 11.53).

However, usually these details cannot be handled in routine data analysis and epicenter location and require specialized study. For routine purposes, as a first approximation, the IASP91 or AK135 global models (see DS 2.1) can be used for the analysis and location of near events based on the main crustal phases. However, one should be aware that crustal structure and velocities may differ significantly from region to region. Therefore, the event location can be significantly improved when local travel-time curves or crustal models are available (e.g., IS 11.1, Figures 11 and 12).

Fig. 11.55 shows seismograms of a shallow local earthquake from the Vogtland/NW Bohemia region in Central Europe, recorded at seven GRSN stations in the epicentral distance

range 10 km (WERN) to 180 km (GEC2). Stations up to D = 110 km (BRG) show only the direct crustal phases Pg, Sg, except GRFO, which in addition shows PmP. At GEC2 Pn arrives ahead of Pg with significantly smaller amplitude. The onset times of phases Pg, Sg and Pn were used to locate the epicenter of this event with a precision of about 2 km. If more stations close to the epicenter are included (e.g., Fig. 11.56; D = 6 – 30 km), the precision of the hypocenter location may be in the order of a few hundred meters.

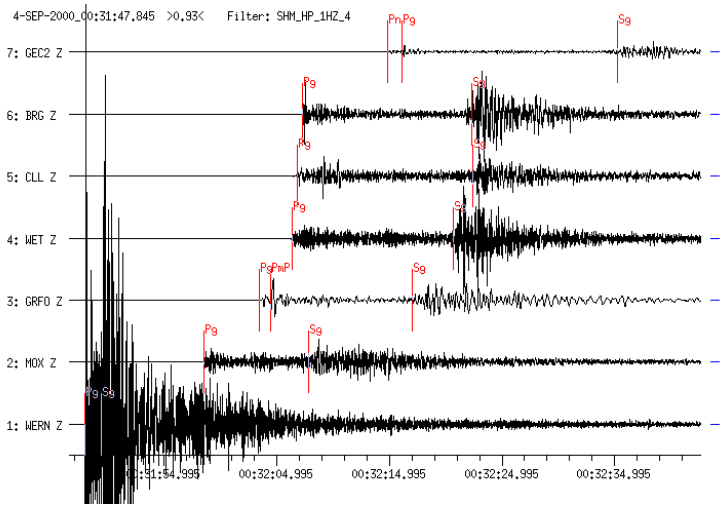

Fig. 11.55 Filtered short-period vertical component seismograms (4th order Butterworth high-pass filter, f = 1 Hz) from a local earthquake in the Vogtland region, 04 Sept. 2000 (50.27°N, 12.42°E; h = 8 km, Ml = 3.3). Sampling rates at the stations differ: 80 Hz for MOX, WET, CLL, and BRG, 100 Hz for WERN and 20 Hz for GRFO and GEC2. Traces are sorted according to epicentral distance (from 10 to 180 km). The local phases have been marked (Pg and Sg at all stations, PmP at GRFO and Pn at the most distant station GEC2 (D = 180 km).

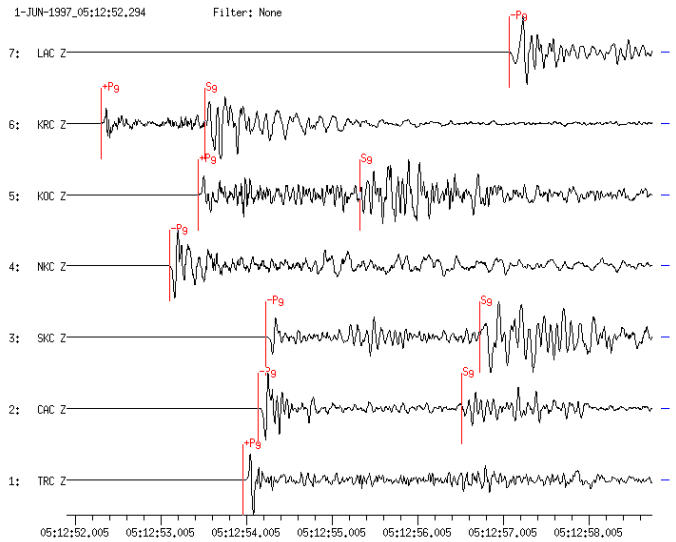

Fig. 11.56 Short-period recordings from stations of the local network of the Czech Academy of Sciences in Prague from a small (Ml = 3.3) local earthquake in the German/Czech border region on June 1, 1997. The epicentral distance range is 6 km and 30 km. Such local networks allow hypocenters to be located to better than a few hundred meters.

From these figures and the animation file 1 in IS 11.3 the following conclusions can be drawn:

- at some stations the arrival times are in good agreement with the times predicted from an average crustal model for the considered region, at other stations they are not. This implies lateral and/or distance-dependent variations in crustal velocities;

- the amplitude ratio Pg/Sg varies strongly with azimuth because of the different radiation patterns for P and S waves. This can be used to derive the fault-plane solution of the earthquake (Figs. 3.100 - 3.103 in section 3.4.1 of Chapter 3).

Fig. 11.57 shows recordings from an earthquake in the Netherlands (Ml = 4.0) in the distance range 112 km to 600 km, and Fig. 11.58 those from a mining-induced earthquake in France (Ml = 3.7) in the range 80 km to 500 km. These records again show obvious variations in the relative amplitudes of Pn, Pg and Sg. The relative amplitudes depend on both distance and azimuth of the stations relative to the radiation pattern of the source, and particularly with respect to the differences in take-off angles of the rays for the direct and the critically refracted waves (Fig. 11.54). The source depth with respect to the major crustal discontinuities may also influence the relative amplitude ratio between these various phases.

As in Figs. 11.23a and b, also the record of station WLF in Fig. 11.58 of this shallow mining induced event shows well developed longer-period Rg waves that follow Sg. Rg is usually not present in records of tectonic earthquakes (Figs. 11.55-11.57).

For near-surface sources and distances smaller than about 400 km, Pn is usually much smaller than Pg (see also Fig. 11.34 and Figures 3a and 3c in Datasheet 11.1). But for larger distances the relative amplitudes of Pn and Sn may grow so that these phases may even become the dominating first arriving the P and S waves (Fig. 2.17 and the uppermost traces in Figs. 11.57 and 11.58). This is not only because of the stronger attenuation of the direct waves that travel mostly through the uppermost heterogeneous crust, but also because P and S near the critical angle of refraction at the Moho form so-called “diving” phases which are not critically refracted into the Moho but rather travel within the uppermost mantle with sub-Moho velocity. Such diving phases have much larger amplitudes then the ones to be expected by theory for critically refracted inhomogeneous waves. The sub“diving” Pn and Sn at distance beyond 600-800 km becoming the dominating first arriving P and S onsets, usually have longer periods than Pn and Sn at shorter distances.

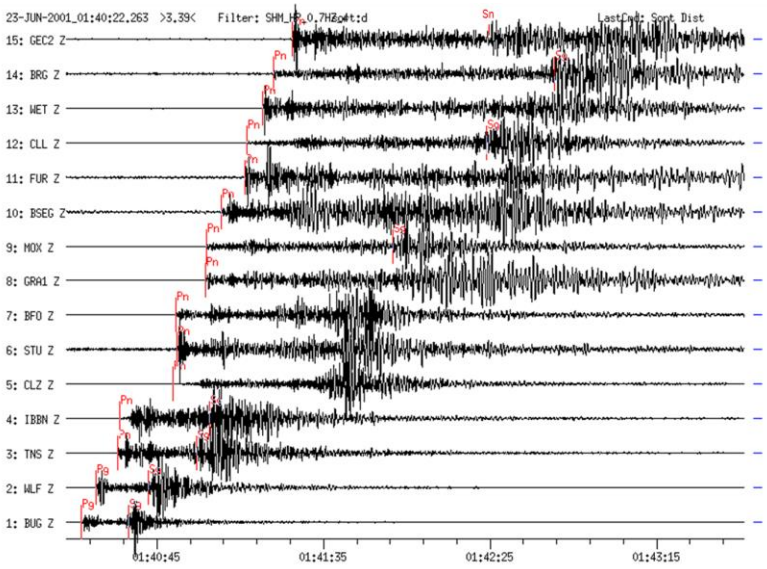

Fig. 11.57 Vertical-component short-period filtered broadband seismograms (4th order Butterworth high-pass filter, f = 0.7 Hz; normalized amplitudes) from a local earthquake at Kerkrade, Netherlands, recorded at 15 GRSN, GRF, GERES and GEOFON stations. Ml = 4.0; epicentral distances between 112 km (BUG) and 600 km (GEC2). The time difference Sn-Pn of 60 s in the GEC2 records yields also with the "rule of thumb" in Eq. (1.2) the calculated epicentral distance for this station. Note the variability of waveforms and relative phase amplitudes of local/regional earthquakes in network recordings in different azimuths and epicentral distances. The suitability of filters for determination of local phase onsets has to be tested. Local magnitudes are measured on a Wood-Anderson record simulation.

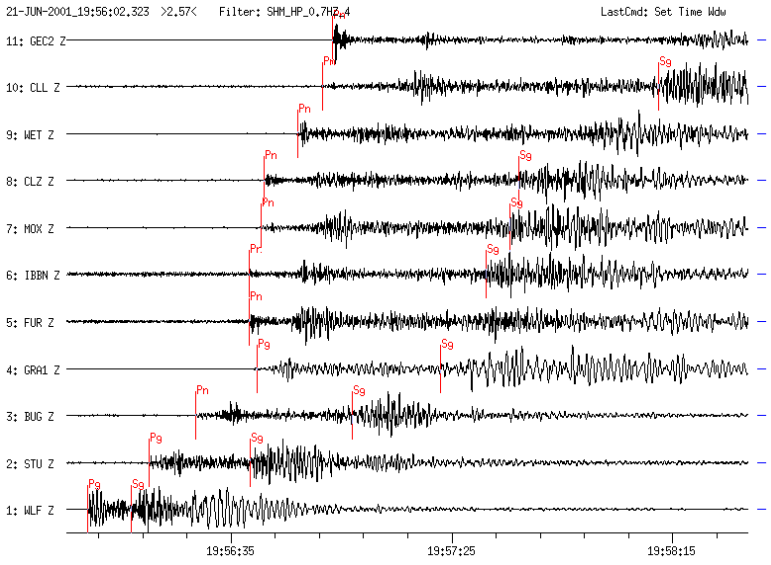

Fig. 11.58 Vertical-component short-period filtered BB seismograms (4th order Butterworth high-pass filter, f = 0.7 Hz, normalized amplitudes) from a local mining-induced earthquake at the French-German border recorded at 11 GRSN, GERES and GEOFON stations (Ml = 3.7; D between 80 km (WLF) and 501 km (GEC2). Note the well developed more long-period and dispersive Rg group following Sg in the record of WLF. Usually one does not find this phase in records of deeper tectonic earthquakes (e.g., Figs. 11.55-11.57).

But Fig. 11.59 shows the great variability in the appearance of waveforms and relative amplitudes in near-earthquake recordings, which often deviate from such average rules. Even seismic records at the same station from two different sources at nearly the same distance and with similar azimuth may look very different. This may be because the waves from the two earthquakes travel along slightly different paths through the highly heterogeneous Alpine mountain range. However, the fault-plane orientation and related energy radiation with respect to the different take-off angle of Pn and Pg may also have been different for these two earthquakes.

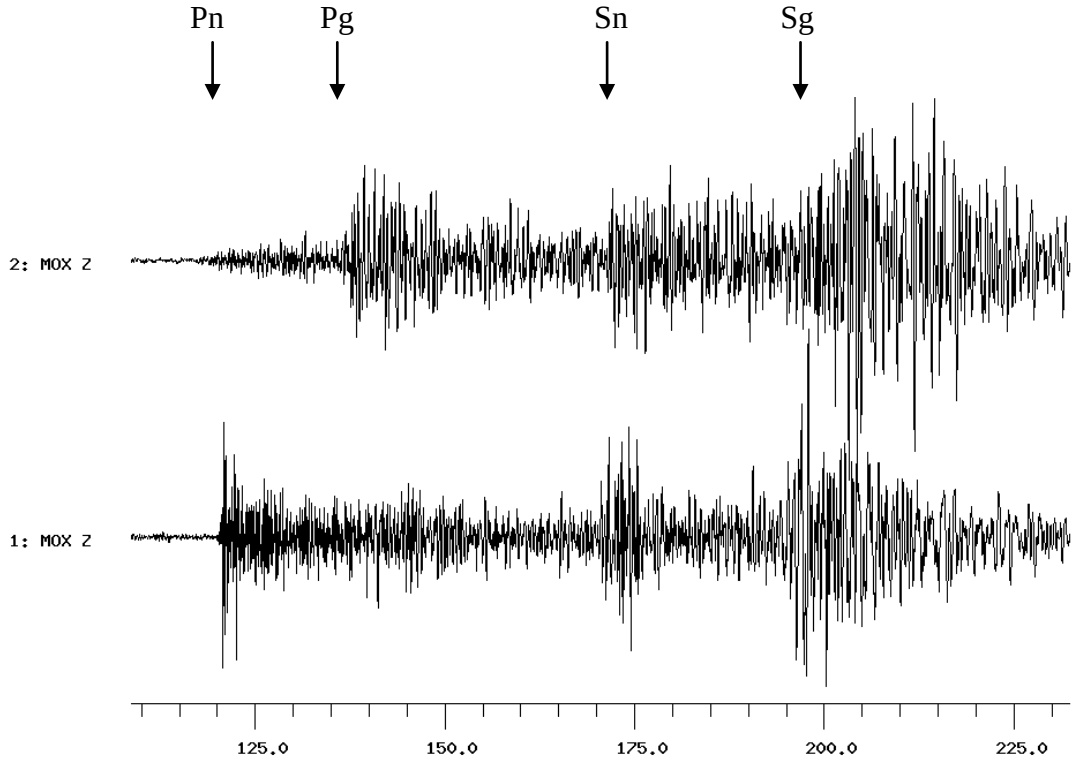

Fig. 11.59 Comparison of Z-component short-period filtered records at station MOX, Germany, of two earthquakes in Northern Italy (trace 1: 28 May 1998; trace 2: 24 Oct. 1994) at about the same epicentral distance (D = 505 km and 506 km, respectively) and with only slightly different backazimuth (BAZ = 171° and 189°, respectively). Note the very different relative amplitudes between Pn and Pg, due to either crustal heterogeneities along the ray paths or differences in rupture orientation with respect to the different take-off angles of Pn and Pg rays.

The recognition and differentiation of the various crustal phases and the precision of onset-time picking can be significantly improved by stretching the time scale in digital records (compare, e.g., Figures 3a and 3c in DS 11.1). But local and regional earthquakes do not only appear in short-period recordings. Stronger near events with magnitudes above 4 usually generate already strong long-period waves (e.g., Figs. 11.11 and 11.13). In BB records of shallow earthquakes Pn and Sn will then be followed by well-developed surface-wave trains of even much larger amplitudes. Figure 6a in DS 11.1 shows a typical 3-component BB-velocity record at station GRA1, Germany (D = 10.3°) of such an earthquake in Italy. Figure 6c shows the respective BB records at 10 stations of the GRSN (D = 8°- 12°). Pg and Sg are no longer recognizable.

With the exception of the P- and S-wave triplications and thus complicated and elongated P- and S-wave groups at distances beyond 15° the records in the far regional range look rather simple. Usually, only P, S, and surface waves are clearly developed (Fig. 11.53 and Figures 2b and 4c in DS 11.2). The surface waves of shallow earthquakes are strong, clearly separated from the S waves and very useful for surface wave magnitude estimation, with Ms(BB) even down into the near regional range. In the case of deep earthquakes and thus negligible surface waves the the core reflection PcP may sometimes also be observed in the far regional distance range (6°-20°+) in short-period seismograms of stronger events (Ml > 4). PcP, which gives a good control of source depth, can be identified in array recordings because of its very small slowness (e.g., Fig. 9.14 in Chapter 9).

In general, regional stations and local networks complement each other in the analysis of smaller sources at local distances. Additionally, source processes and source parameters can be estimated using local station data. For this purpose, first motion polarities (compression c or +, dilatation d or -) for phases Pg, Pn, Sg and amplitude ratios (P/SV) should be measured for fault plane solution and moment tensor inversion (see 3.4 and 3.5). In regions with poor azimuthal and distance coverage by stations, the mean precision of location may be several kilometers and source depths may then only be estimated via depth phase modeling and fitting (Fig. 2.85).

An important aspect to consider in digital recordings and data analysis of local and regional seismograms is the sampling rate. Sampling with more than 80 s.p.s. is generally suitable for near seismic events. With lower sampling rate some of the most essential information about the seismic source process such as the corner frequency of the spectrum and its high-frequency decay, may be lost. Fig. 11.60 gives an example, which shows that only the 80 Hz data stream with a Nyquist frequency of 40 Hz allows the corner frequency near 20 Hz to be determined. In some regions, however, or when studying small local earthquakes, still higher frequencies have to be analyzed. This may require sampling rates between 100 and 250 Hz.

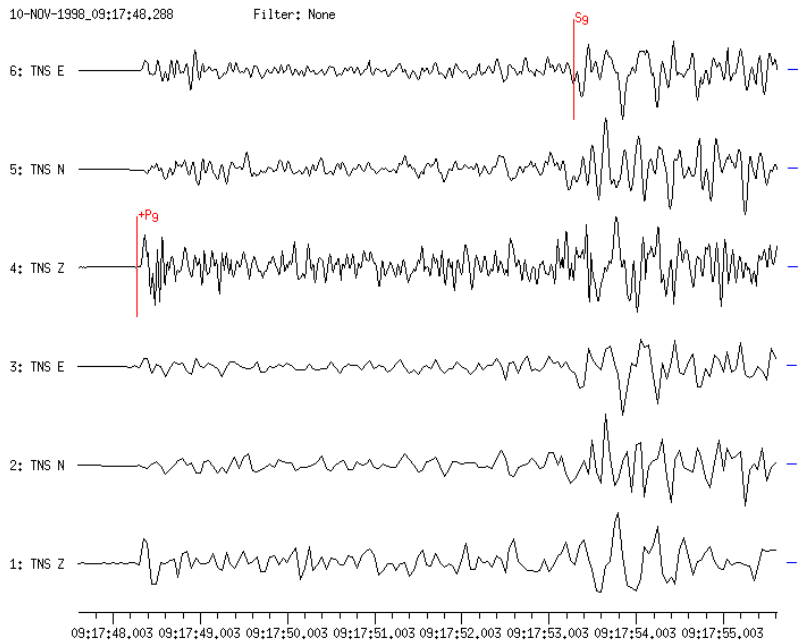

a)

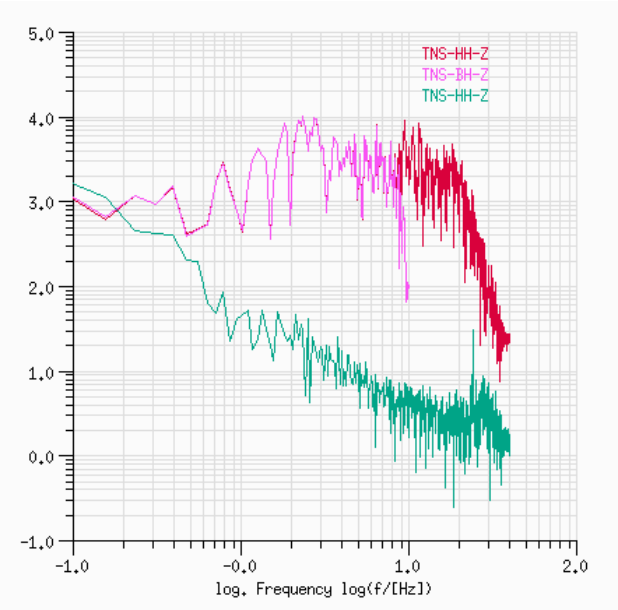

b)

Fig. 11.60 a): BB-velocity seismogram from a local earthquake near Bad Ems, Germany (11 Oct. 1998; Ml = 3.2) recorded at the GRSN station TNS (D = 40 km). Different sampling rates were used for data acquisition. Traces 1 – 3 were sampled at 20 Hz and traces 4 – 6 at 80 Hz. In the records with the higher sampling rate, the waveforms are much more complex and contain higher frequencies. The high frequency content is suppressed with the lower sampling rate. **b):** Fourier spectrum of traces 1 (sampling rate 20 Hz – pink) and 4 (sampling rate 80 Hz – red). The lower sampling rate cuts off the high-frequency components of the seismic signal. Thus the corner frequency of the signal at about 20 Hz and the high-frequency decay could not be determined from the pink spectrum. The green spectrum represents the seismic noise.

Note that besides the crustal phases so far mentioned a very different type of seismic wave, the so-called T-phase, may appear in records of oceanic earthquakes at near coastal stations. The T-phase forms a rather long envelope-shaped wave train with a faint onset and ending and follows well behind the crustal phase wave train. For records and more explanations about the origin of these phases Chapter 2, section 2.6.5, Figs. 2.71 and 2.72.

In Box 1 a summary is given of essential features that can be observed in records of local and regional seismograms. For more records in this distance range see DS 11.1.

BOX 1: General rules for local and regional events

- The frequency content of local events (D < 2°) is usually high (f ≈ 0.2 - 100 Hz). Therefore they are best recorded on SP or SP-filtered BB instruments with sampling rates f ≥ 80 Hz. The overall duration of short-period local and regional (D < 20^{o}) seismograms ranges between a few seconds and several minutes.
- Stronger local/regional sources radiate long-period energy too and are well recorded by BB and LP seismographs. In the far regional range the record duration may exceed half an hour (Chapter 1, Fig. 1.2).

- Important seismic phases in seismograms of local sources are Pg, Sg, Lg and Rg and in seismograms of regional sources additionally Pn and Sn, which arrive beyond 1.3°-2° as the first P- and S-wave onsets. The P waves are usually best recorded on vertical and the S waves on horizontal components.
- Note that Pg is not generally seen in records from sources in the oceanic crust. Also, deep (sub-crustal) earthquakes lack local and regional crustal phases.
- For rough estimates of the epicentral distance D [km] of local sources, multiply the time difference Sg-Pg [s] by 8, and in the case of regional sources the time difference Sn-Pn [s] by 10. For more accurate estimates of D use local and regional travel-time curves or tables or calculations based on more appropriate local/regional crustal models.
- The largest amplitudes in records of local and regional events are usually the crustal channel waves Lg (sometimes even beyond 15° in continental platform areas), and for near-surface sources the short-period fundamental Rayleigh mode Rg. For near-surface explosions or mining-induced earthquakes, Rg, with longer periods than Sg, may dominate the record, however usually not beyond 4°.
- In records of oceanic earthquakes at near coastal stations occasionally T phases may be observed.
- For routine analysis the following station/network readings should be made: (1) the onset time and polarity of observed first motion phases; (2) onset times of secondary local and regional phases; (3) local magnitude based either on maximum amplitude or duration. If local/regional calibration functions, properly scaled to the original magnitude definition by Richter (1935) or the IASPEI standard formula, are not available it is recommended to use the original Richter equation and calibration function, together with local station corrections.

11.5.3 Teleseismic earthquakes (20°< D < 180°)

11.5.3.1 Distance range 20° < D ≤ 100°

The main arrivals at this distance range up to about 80° have traveled through the lower mantle and may include reflections from the core-mantle boundary (CMB) (Figs 11.61, 11.62 and 11.64). The lower mantle is more homogeneous than the upper mantle (Fig. 2.79). Accordingly, P and S waves and their multiples form rather simple long-period seismograms (Figs. 11.12 and 11.63; see also files 5 and 6 in IS 11.3). Between 30° and 55°**,** the waves reflected from the core (e.g., PcP, ScP etc.) are also often recorded as sharp pulses on short-period records, particularly on records of deep earthquakes where depth phases appear well after the core reflections (Fig. 11.21). At around 40°, the travel-time curve of PcP intersects those of PP and PPP (Figs. 11.8 and 11.64) and in horizontal components PcS intersects S, and ScS intersects SS and SSS (Fig. 11.8). This complicates proper phase separation, at least for the later phases on long-period records, where SS and SSS may be strong. ScP, however, may also be rather strong on short-period vertical components (Fig. 11.64). The amplitudes of the core reflections decrease for larger distances but they may be observed up to epicentral distance of about 80° (ScP and ScS) or 90° (PcP), respectively, beyond which ScS merges with the travel-time curves of SKS and S and PcP with that of P (see Figs. 11.8, 11.20, 11.21 and 11.66). Note that PP, PS, SP and SS are Hilbert-transformed (see 2.5.4.3). Their onset and amplitude picks can be improved by inverse Hilbert transformation, which is part of modern analysis software such as Seismic Handler (SH and SHM).

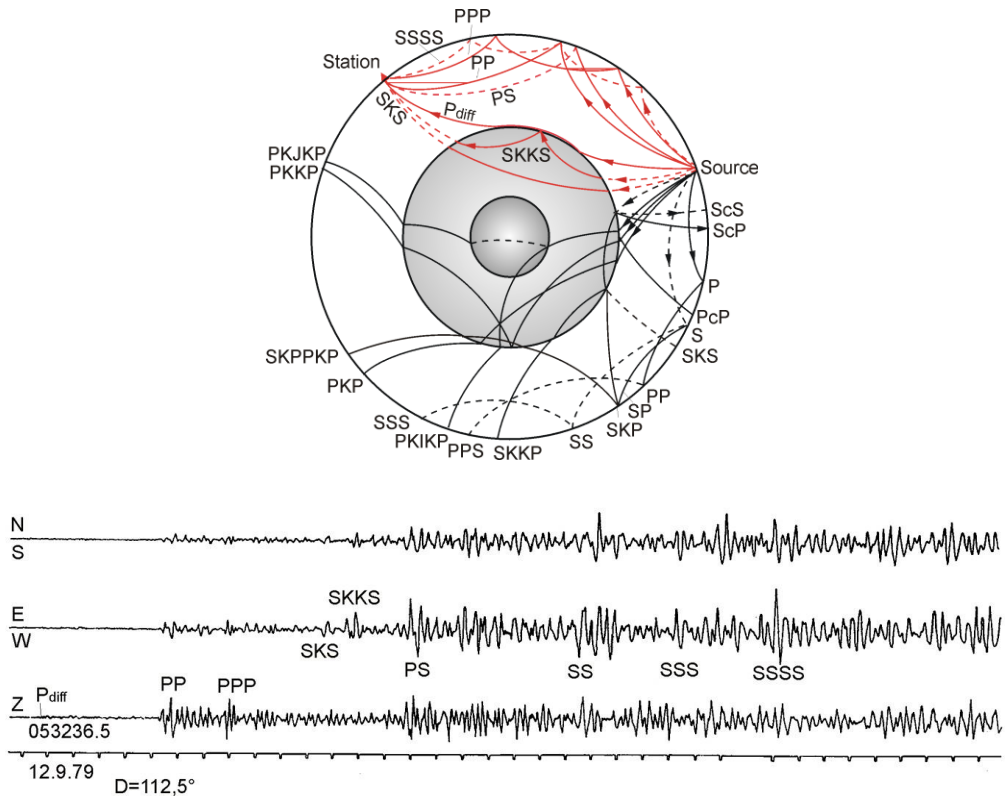

Fig. 11.61 Seismic ray paths through the mantle and core of the Earth with the respective phase names according to the international nomenclature (Chapter 2, Figs. 2.58 and 2.60, and IS 2.1 for phase names and their definition). The red rays relate to body wave onsets in the 3-component analog Kirnos SKD BB-displacement record below from an earthquake at D = 112.5° at station MOX, Germany.

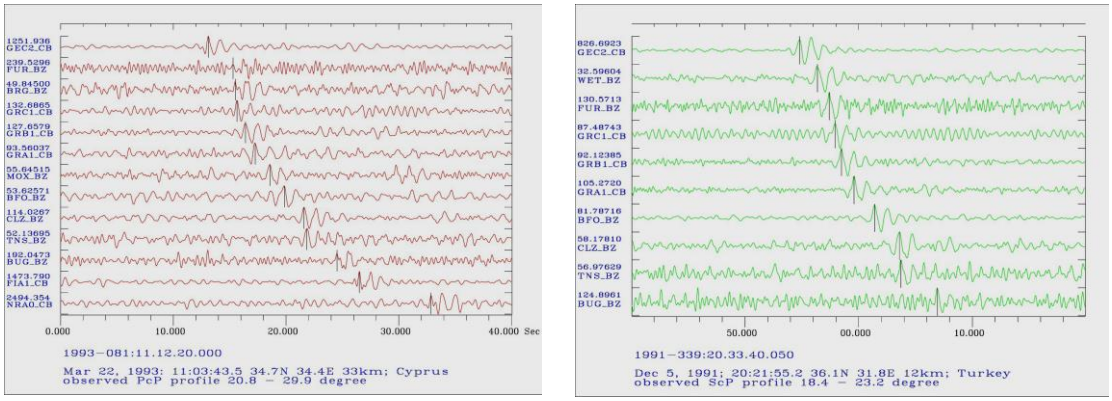

Fig. 11.62 Left: Array and single station observations of PcP for an mb = 5,3 and h = 29.7 km deep Cyprus earthquake on 1993 March 22. The beam traces of the arrays are named by their reference stations GEC2 (GERES), GRA1, GRB1, GRC1 (Gräfenberg), FIA1 (FINES), and NRA0 (NORES), respectively. All data are bandpass filtered between 0.8 and 3 Hz. The un-restituted, velocity proportional traces are scaled to their maximum amplitude, which is given in digital counts. **Right:** The same for ScP observations of an mb = 5.0 and h = 106.6 km deep earthquake in Turkey on 1991 December 5 The beam traces of the arrays are named by their reference stations GEC2 (GERES), GRA1, GRB1, and GRC1 (Gräfenberg), respectively. Color versions of Figures 2 and 3 of Schweitzer (2002); © Geophys. J. Int.

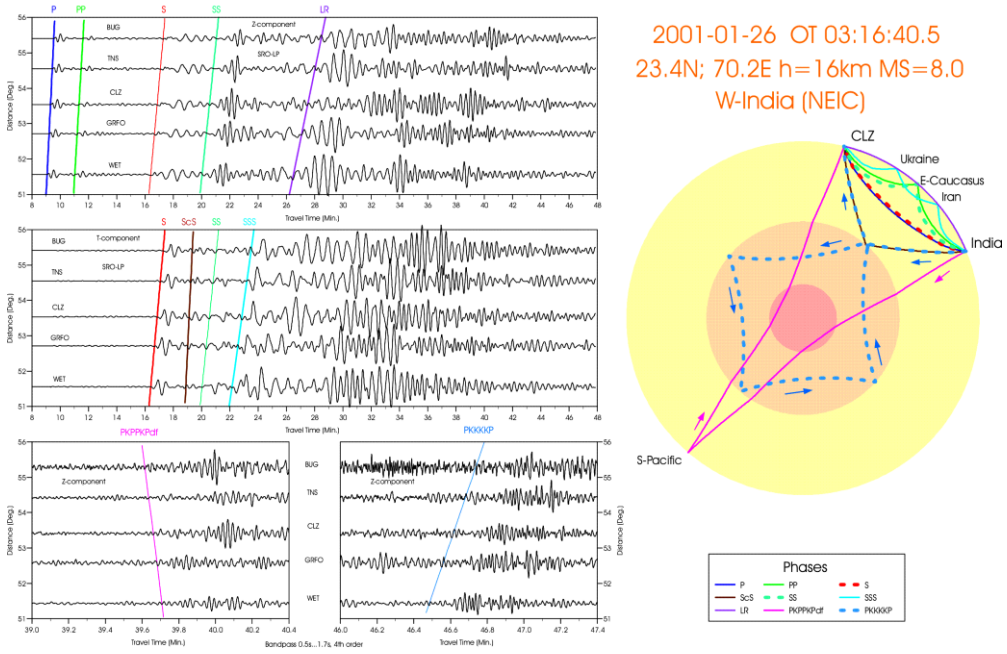

Fig. 11.63 Long-period Z- (top record section) and T-component seismograms (middle record section) of a shallow earthquake in western India recorded in the distance range 51° to 56° at stations of the GRSN. The two cut-out vertical component short-period record sections at the bottom left and middle show the in the later part of the surface waves arriving multiple core phases PKPPKPdf (= P'P') and P4KP. For all phases identified in these records the related ray paths are depicted on the right side diagram (for animation see file 5 in IS 11.3).

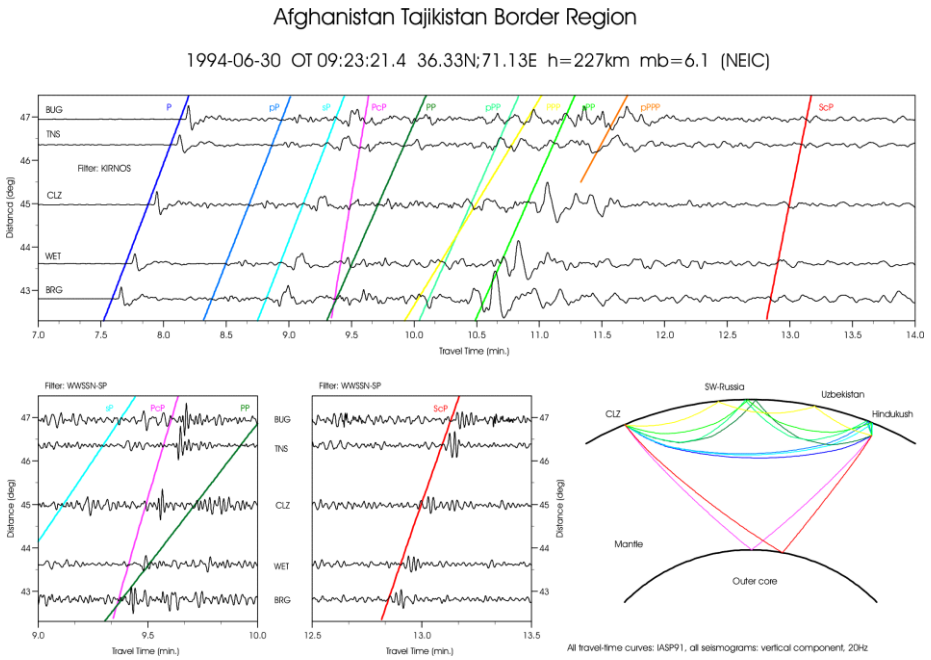

Fig. 11.64 Vertical-component Kirnos SKD BB-displacement (top record section) and WWSSN-SP seismograms (lower left two record sections) from an intermediate depth (h = 227 km) earthquake in the Afghanistan-Tajikistan border region recorded at stations of the GRSN. Besides P the depth phases pP, sP, pPP, sPP and pPPP the core reflections PcP and ScP are clearly visible, particularly on the short-period records. The ray traces of these phases are shown in the lower right diagram (see also file 4 in IS 11.3 and related animation).

Remark: For many of the above and following record sections with accompanying ray diagrams one finds in DS 11.2 and 11.3 more clear records with better time resolution.

Fig. 11.65 shows the ray paths for S, ScS and SKS and their related travel-time curves according to the IASP91 model for the distance range from 60° to 180° and Fig. 11.66 both short- and long-period records of these waves between 50° and 80°.

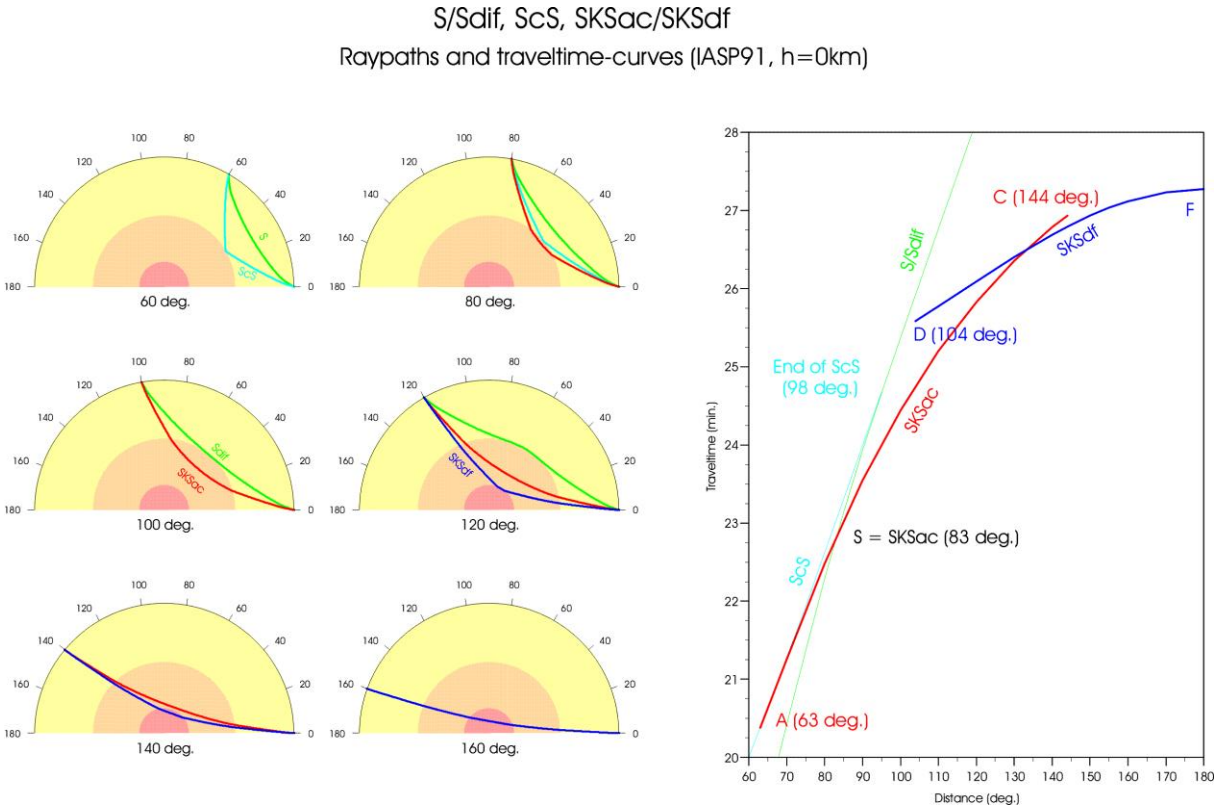

Fig. 11.65 Ray paths for S, ScS and SKS and their related travel-time curves according to the IASP91 model for the distance range from 60° to 180°.

Arrays and network records, which also allow f-k and vespagram analysis, are very useful for identifying the core reflections PcP, ScP and ScS because their slownesses differ significantly from those of P, S and their multiple reflections (Fig. 11.62 and Figures 6a and b and 7b in DS 11.2). Surface reflections PP, PPP, SS and SSS are well developed in this distance range in long-period filtered records and converted waves PS/SP at distances above 40°. Sometimes the surface reflections are the strongest body-wave onsets at large distances (Figures 10c and 11b in DS 11.2). Their identification can be made easier when network records are available so vespagram analysis can be used (e.g., Figure 11c in DS 11.2). In short-period filtered network records it is sometimes possible to correlate in this distance range multiple reflected core phases such as PKPPKP (or P'P'), SKPPKP and SKPPKPPKP (Chapter 1, Fig. 1.10)

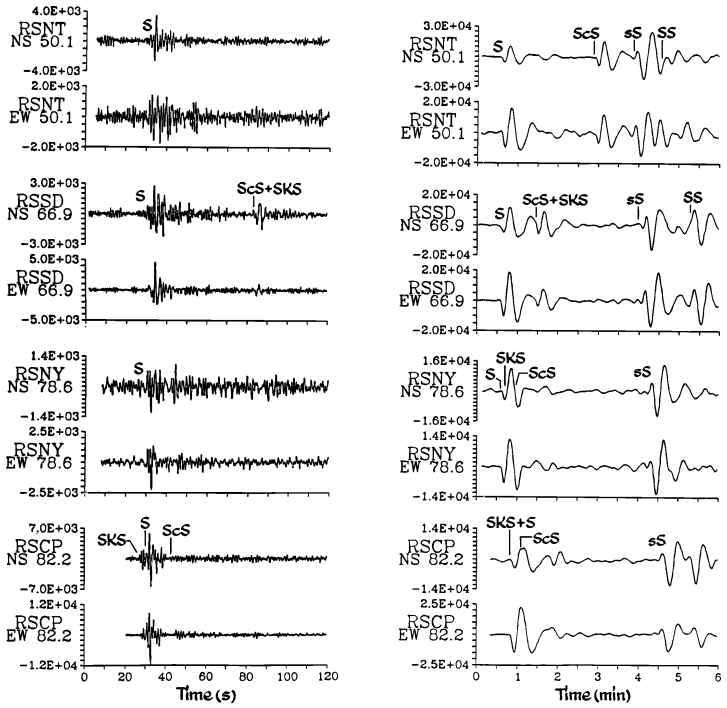

Fig. 11.66 SP (left) and LP (right) horizontal-component seismograms from a deep-focus earthquake in the Sea of Okhotsk (20 April 1984, mb = 5.9, h = 588 km) recorded at stations in the distance range 50.1° to 82.2°. Note the different amplitude scaling. Accordingly, the amplitudes of various transverse phases are 2 to 10 times larger in long-period records when compared with short-period records. Four distinct phases are identified: S, ScS, sS and SS. SKS, however, which emerges at distances larger than 60°, overlaps with ScS between about 65° and 75°. S, ScS and SKS start to coalesce as distance increases toward 82°. Beyond this distance SKS arrives before S, SKKS and ScS (reprinted from Anatomy of Seismograms, Kulhánek, Plate 40, p.137-138; © 1990; with permission from Elsevier Science).

Beyond 83° SKS arrives for near surface sources - but earlier already for deeper earthquakes - ahead of S and its amplitude relative to S increases with distance. Network and array analysis yields different slowness values for S and SKS because of their diverging travel-time curves (Fig. 11.65). This helps to identify these phases correctly. Note that the differential travel time SKS-P increases only slowly with distance (Fig. 11.8). Misinterpretation of SKS as S may therefore result in an underestimation of D by up to 20°! Since SKS is polarized in the vertical plane it can be observed and separated well from S in radial and vertical components of rotated seismograms (Fig. 11.67 and Figures 10c, 13e, 14e, and 15b in DS 11.2). This also applies to PcS and ScP that are polarized in the vertical propagation plane as well (Fig. 11.64).

In the distance range between about 30° and 105° multiple reflected core phases P'N or between about 10° < D° < 130° the phases PNKP, with N-1 reflections either at the free surface (P'N) or from the inner side of the core-mantle boundary (PNKP), respectively, may appear in short-period records some 13 min to 80 min after P. An example for PKPPKP (P'P') and PKKKKP (P4KP) is given in Fig. 11.63. These phases are particularly strong near caustics, e.g., P'P' (Fig. 11.77) and P'P'P' (P'3) near 70° and PKKP near 100° (Fig. 11.78) but they are not necessarily observable at all theoretically allowed distances. Figures 9 and 10 in EX 11.3, however, document the rather wide distance range of real observations of these

phases at station CLL (for P'P' between 40° and 105° and for PKKP between 80° and 126°). Note the different, sometimes negative slowness of these phases. More record examples, together with the ray paths of these waves, are presented in a special section on late core phases (11.5.4). For differential travel-time curves of PKKP-P and PKPPKP-P Figures 9 and 10 in EX 11.3. Also PKiKP, a weak core phase reflected from the surface of the inner core (ICB), may be found in short-period array recordings throughout the whole distance range, about 4.5 to 12 min after P. Its slowness is less than 2s/°. Beyond 95°, P waves show regionally variable, fluctuating amplitudes. Their short-period amplitudes decay rapidly (Fig. 11.10) because of the influence of the core (core-shadow) while long-period P waves may be diffracted around the curved core-mantle boundary (Pdif, Figs. 11.70and 11.74 as well as Figures 1, 2, 4b and 6c and b in DS 11.3).

In any case, comprehensive seismogram analysis should be carried out for strong earthquakes which produce many secondary phases. Unknown phase arrivals should also be reported for further investigations into the structure of the Earth. When reporting both identified and unknown phases to international data centers the IASPEI-proposed international nomenclature should strictly be observed (see IS 2.1).

11.5.3.2 Distance range 100° < D ≤ 144°

Within this distance range, the ray paths of the P waves pass through the core of the Earth. Due to the large reduction of the P-wave velocity at the core-mantle boundary (CMB) from about 13.7 km/s to 8.0 km/s (Fig. 2.79 in Chapter 2) seismic rays are strongly refracted into the core (i.e., towards the normal at this discontinuity). This causes the formation of a "core shadow". This "shadow zone" commences at an epicentral distance around 100°. The shadow edge is sharper for short-period P and S waves than for long-period P and S waves that are diffracted much further around the curved CMB (compare Figures 6b and c as well as 7a and b in DS 11.3). For strong earthquakes Pdif and Sdif may be observed out to distances of more than 150° (Figs. 11.67, 11.68, 11.70 and 11.74).

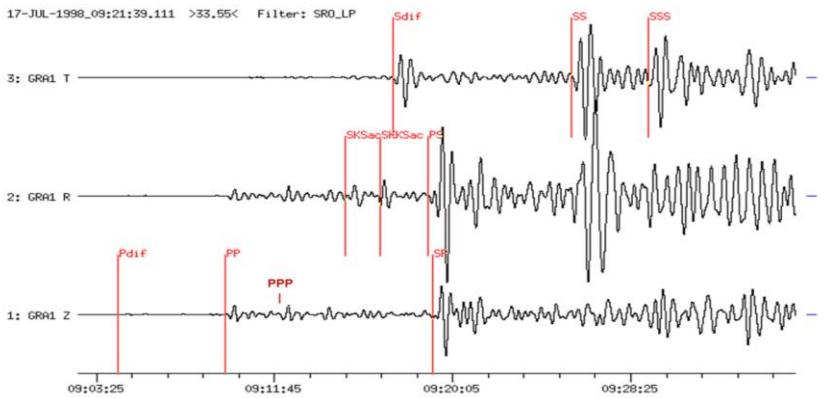

Fig. 11.67 SRO-LP filtered 3-component seismograms at station GRA1, Germany, in D = 117.5° from an earthquake in Papua New Guinea (17 July 1998, Ms = 7.0). The N and E components have been rotated into the R and T directions. Phases Pdif, PP, PPP and a strong PS and SP are visible on the vertical component, whereas the phases SKS, SKKS and PS, which are polarized in the vertical propagation plane, are strong on the radial (R) component (as are PP and PPP). In contrast, Sdif, SS and SSS are strong on the transverse (T) component.

Fig. 11.68 shows rotated (R-T) horizontal component SRO-LP recordings at GRSN stations from two intermediate deep events in the Chile-Bolivia border region and in the Mariana Islands, respectively. The related ray paths are depicted in the upper part. The records cover the transition from the P-wave range into the P-wave core shadow. Magnified cut-outs, also of the related Z-component records, are presented for both earthquakes in Figures 1 and 2 of DS 11.3. They show more clearly the first arriving longitudinal waves and their depth phases. The following conclusions can be drawn from a comparison of these figures:

- Pdif arrives about 4 minutes (at larger distance up to 6 min; Fig. 11.74) earlier than the stronger PP;
- The largest phases (Figs 11.68 and . 11.71) are usually PP, PPP, PS, SP, Sdif, SKS, SKKS, SS and SSS;
- SKS is the first arriving shear wave, followed by SKKS, SP or PS (and the related depth phases), all on the R component;
- S/Sdiff and SS may be strong(est) in T or R, or even in both components, depending on the SV/SH ratio of shear-wave energy radiated by the source.

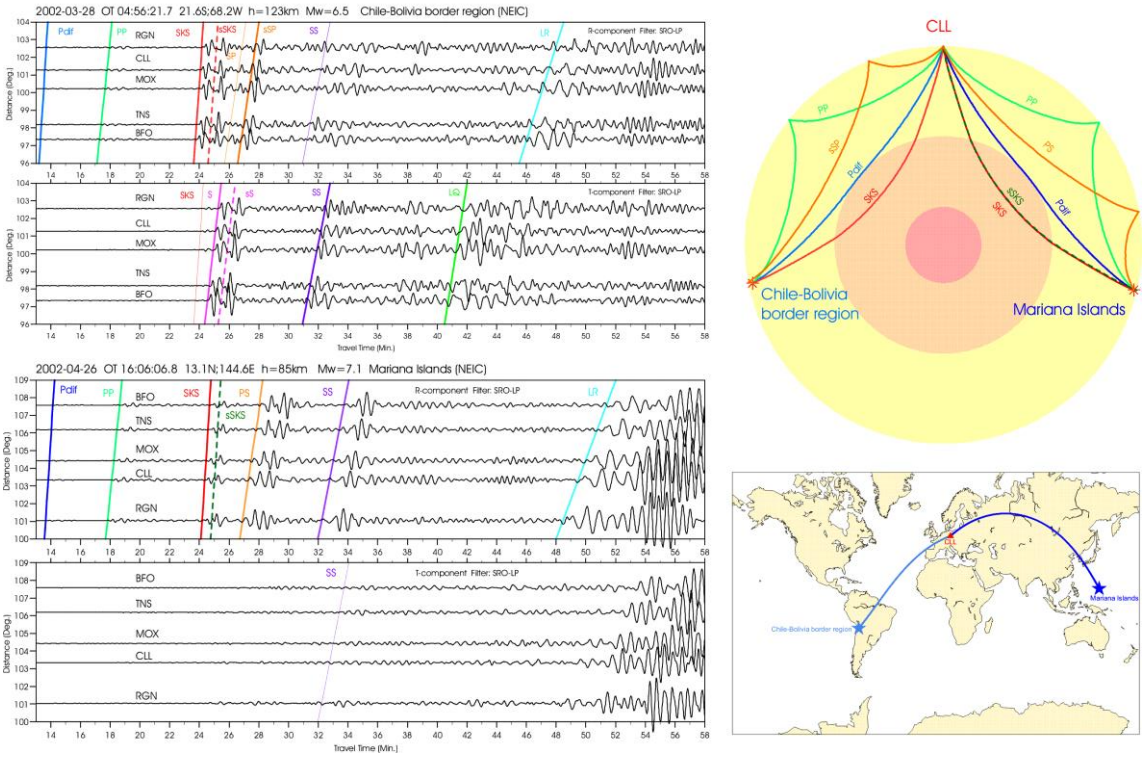

Fig. 11.68 SRO-LP filtered records of GRSN stations on R and T components in the distance range between 96° and 109° from two earthquakes on opposite backazimuth (Chile-Bolivia Border region and Mariana Islands, respectively; source data according to the NEIC).

If no Pdif is observed, PKiKP is the first arrival in short-period records up to 113° (Figure 3b in DS 11.3). For distances beyond 114° PKiKP follows closely after PKPdf (alternatively termed PKIKP). The latter has traveled through the outer and inner core and arrives as first onset for D ≥ 113°. PKPdf is well recorded in short-period seismograms but usually with emergent onsets and, up to about 135° distance, still with weaker amplitudes than PKiKP. Fig. 11.69 shows theoretical amplitude-distance relationship between PKiKP, PKPdf and the other

direct core phases PKPab and PKPbc, which appear with largest amplitudes beyond 143°. Fig. 11.70 depicts the ray paths and travel-time curves of Pdif, PKiKP, PKPdf, PKPab and PKPbc (for more complete ray paths see IS 2.1). Also PKKP (with its branches ab and bc) is often clearly recorded between 110° and 125° (Figures 3c and d in DS11.3).

Fig. 11.71 presents records of GRSN stations in the distance range 121° to 127° from an earthquake at intermediate depth (h = 138 km) in the region of New Britain (see file 8 in IS 11.3 and animation CD). They show the PKPdf arrivals about 3.5 min after Pdif together with the dominant phases in this range, namely PP, PPP, PS, PPS and the Rayleigh-wave arrival LR in the Z component and the SS, SSS and the Love-wave arrival LQ in the T component. Also shown, together with the ray paths, is the core phase P4KPbc, which has been reflected 3 times at the surface of the Earth, and which is recognizable only on the short-period filtered vertical component. Between about 128° and 144° some incoherent waves, probably scattered energy from "bumps" or heterogeneities at the CMB or in the D″ layer above it (Chapter 2, Fig. 2.79), may arrive as weak forerunners up to a few seconds before PKPdf. They are termed PKPpre (old PKhKP). PKPdf is followed by clear PP, after about 2 to 3 minutes, with SKP or PKS arriving about another minute later (Fig. 11.72).

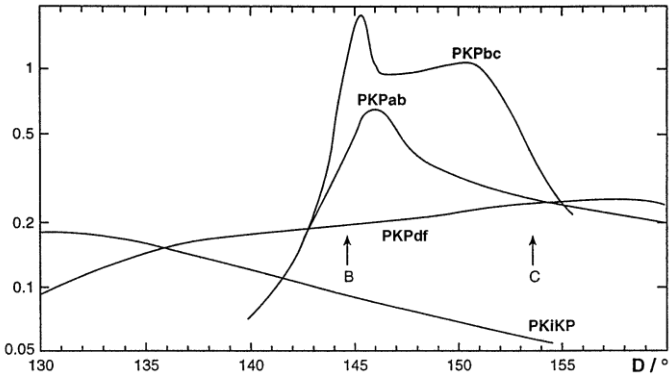

Fig. 11.69 Theoretical smoothed amplitude-distance relationships for the core phases PKiKP, PKPdf, PKPab and PKPbc as calculated for the model 1066B in the distance range 130° to 160° (modified from Houard et al., 1993, Bull. Seism. Soc. Am., Vol. 83, No. 6, Fig. 4, p. 1840, © with permission Seism. Soc. Am.).

SKP/PKS have their caustics at about 132° and thus, near that distance, usually have rather large amplitudes in the early part of short-period seismograms (Fig. 11.72). For medium-sized earthquakes these phases may even be the first ones to be recognized in the record and be mistaken for PKP. Note that for near-surface events SKP and PKS have the same travel time, but with the former having relatively larger amplitudes in the Z component whereas PKS is larger in the R component. For earthquakes at depth, PKS and SKP separate, with the latter arriving the earlier the deeper the source (Fig. 11.72). Beyond 135° there are usually no clear phases between SKP and SS. Misinterpretation (when Pdif is weak or missing) of PP and SKS or PS waves as P and S may in this distance range result in strong underestimation of D (up to 70°). This can be avoided by looking for multiple S arrivals (SS, SSS) and for surface waves which follow more than 40 min later (Table 5 in DS 3.1). For more records see DS 11.3, examples 1 to 7.

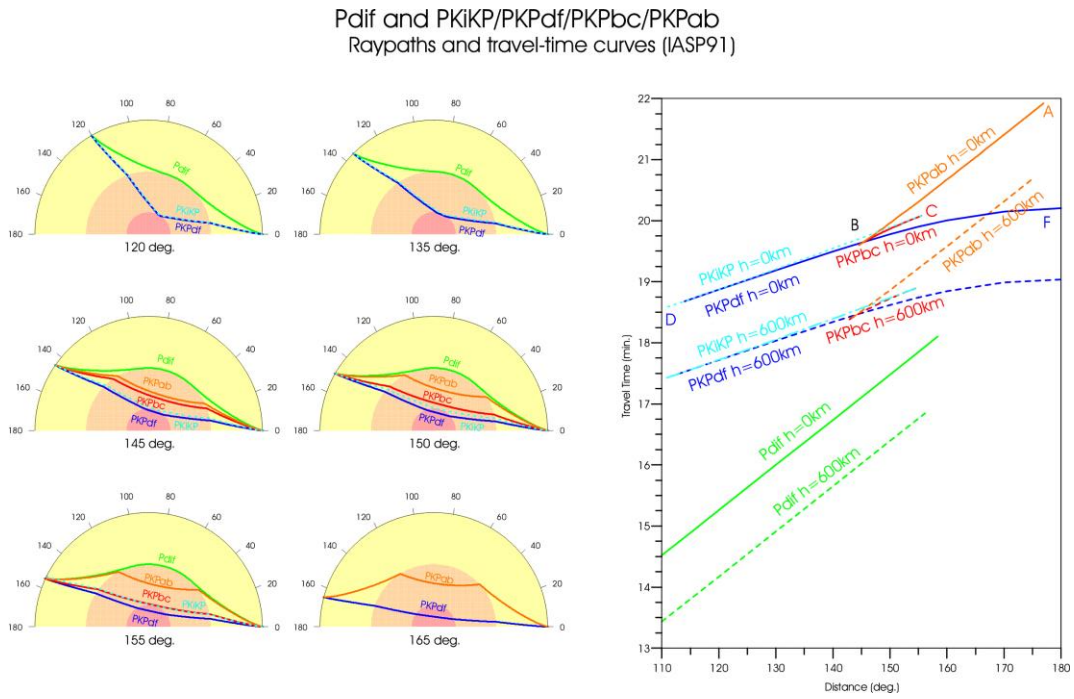

Fig. 11.70 Ray paths of Pdif, PKPdf, PKPab and PKPbc and their travel-time curves for surface focus and deep focus (h = 600 km) events.

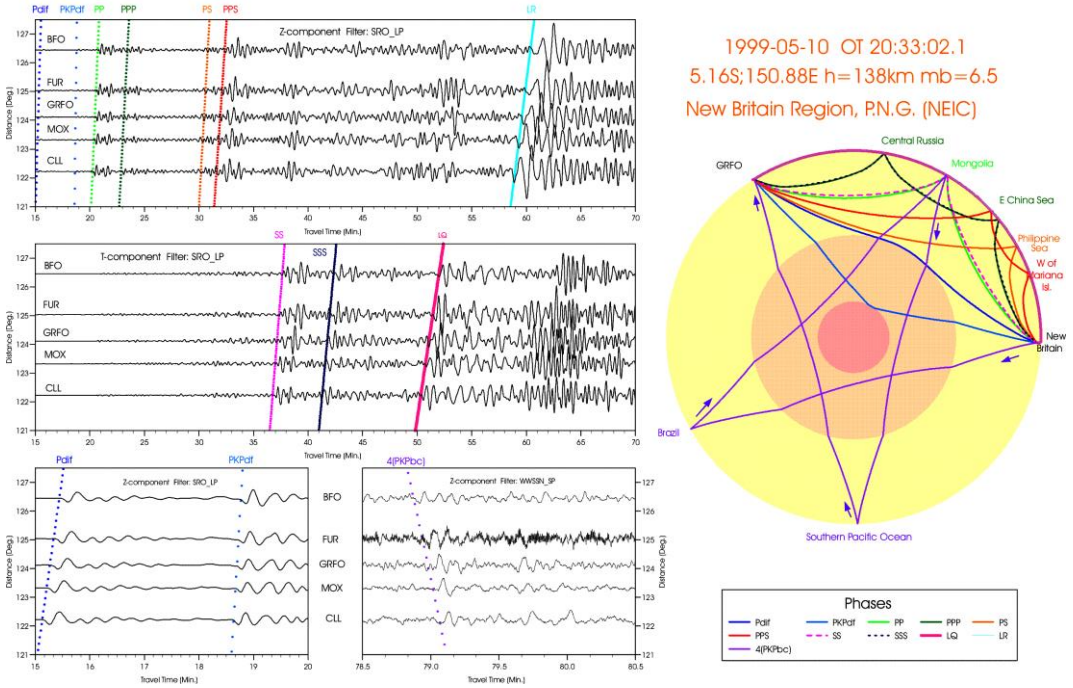

Fig. 11.71 Main seismic phases in the distance range 121° to 127° on records made at GRSN stations and related ray traces. Top and middle left: SRO-LP filtered Z and T component, respectively. Bottom left: SRO-LP enlarged Z-component records of the first 5 minutes; bottom middle: WWSSN-SP Z-componentrecord 1 hour after the first onset with the onset of the 3 times reflected 4(PKPab). Right side: Ray traces of all phases shown (see also animation file 8 in IS 11.3).

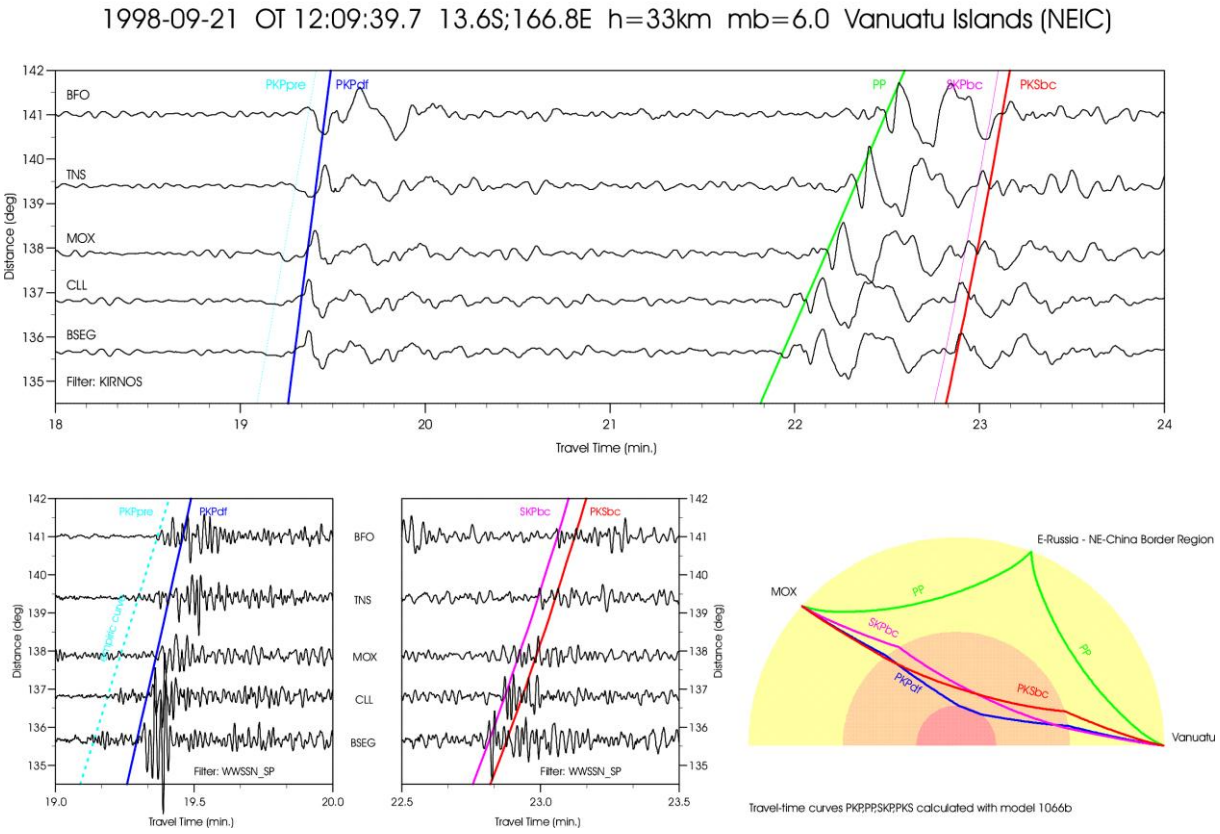

Fig. 11.72 Vertical-component seismograms at GRSN stations recorded in the distance range 135° to 141°. **Top:** Kirnos SKD BB-displacement; **Bottom:** from left to right - WWSSN-SP filtered records showing the onsets of PKPpre, PKPdf, SKPbc and PKSbc as well as the ray paths of the plotted phases.

11.5.3.3 Core distance range beyond 144°

Between 130° and 143° the first onsets of longitudinal core phases are relatively weak and complex in short-period records, but their amplitudes increase strongly towards the caustic around 144°. At this epicentral distance three PKP waves, which have traveled along different ray paths through the outer and inner core, namely PKPdf, PKPbc (old PKP1) and PKPab (old PKP2) arrive approximately at the same time (Fig. 11.70 above) so their energies superimpose to give a strong arrival with amplitudes comparable to those of direct P waves at epicentral distances around 40° (compare with Fig. 11.10). Beyond the caustic the travel-time curves of these three PKP waves split into the branches AB (or ab), BC (or bc) and DF (or df) (Fig. 11.70). Accordingly, the various arrivals can be identified uniquely by attaching to the PKP symbol for a direct longitudinal core phase the respective branch symbol (IS 2.1 and Figs. 11.70 and 11.73). Note that the PKPbc branch shown in Figs. 11.70 between the point B and C is ray-theoretically not defined beyond 155°. However, in real seismograms one often observes weak onsets between PKPdf and PKPab up to about 160° or even slightly beyond in the continuation of the PKPbc travel-time curve. This phase is a PKP wave diffracted around the inner core boundary (ICB) and named PKPdif (IS 2.1 and Fig. 11.76 and 11.77).

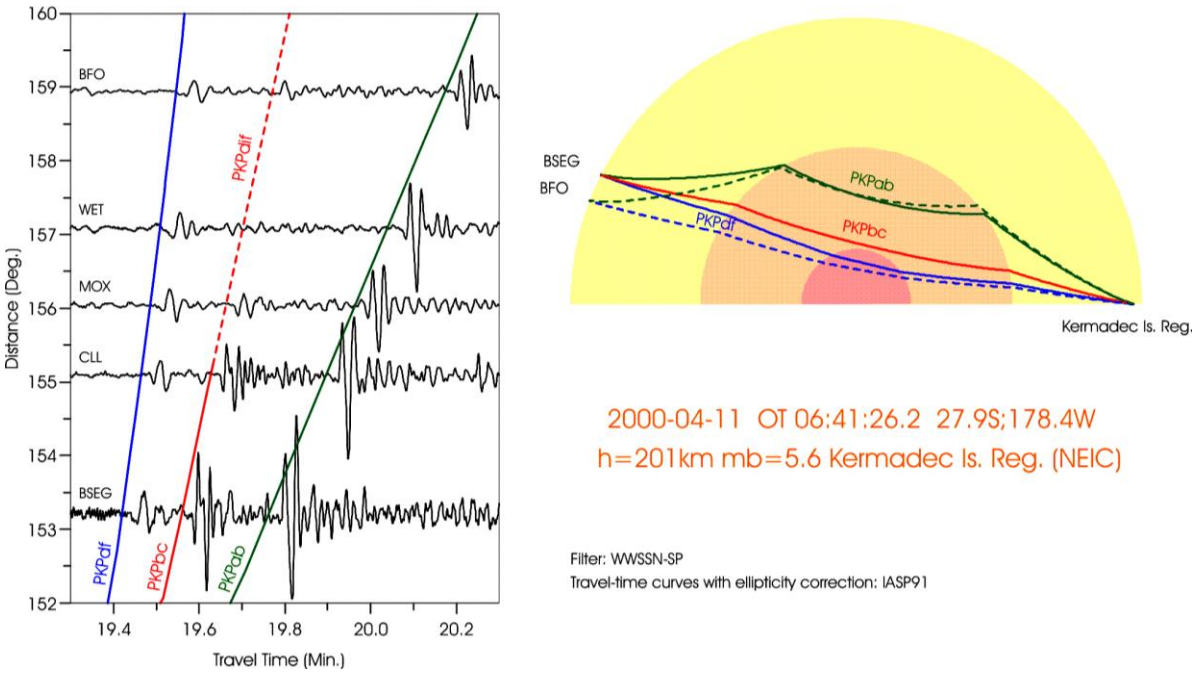

Fig. 11.73 Left: Records of the direct core phases PKPdf, PKPbc and PKPab as well as of the diffracted phase PKPdif from a Kermadec Island earthquake at stations of the GRSN in the distance range between 153° and 159°; **right:** PKP ray paths through the Earth.

The relative amplitudes between the three direct longitudinal core phases change with distance. In SP records these three phases are well separated beyond 146°, and PKPbc is the dominant one up to about 153° though the separation between these three phases is not clear within this range in LP records (Fig. 11.74 right and Figures 9a-c in DS 11.3).

On short-period records the phases PKPdf, PKPbc and PKPab are easy to identify on the basis of their typical amplitude and travel-time pattern. D can be determined with a precision better than 1.5° by using differential travel-time curves for the different PKP branches (see EX 11.3). On records of weaker sources, PKPbc is often the first visible onset because the PKPdf, which precedes the PKPbc, is then too weak to be observed above noise. On long-period records the different superimposed onsets may be recognizable only at distances larger than 153°. Then PKPab begins to dominate the PKP-wave group on short-period records (compare Figs. 11.74). Towards the antipode, however, PKPdf (PKIKP) becomes dominating again whereas PKPab disappears beyond 176°.

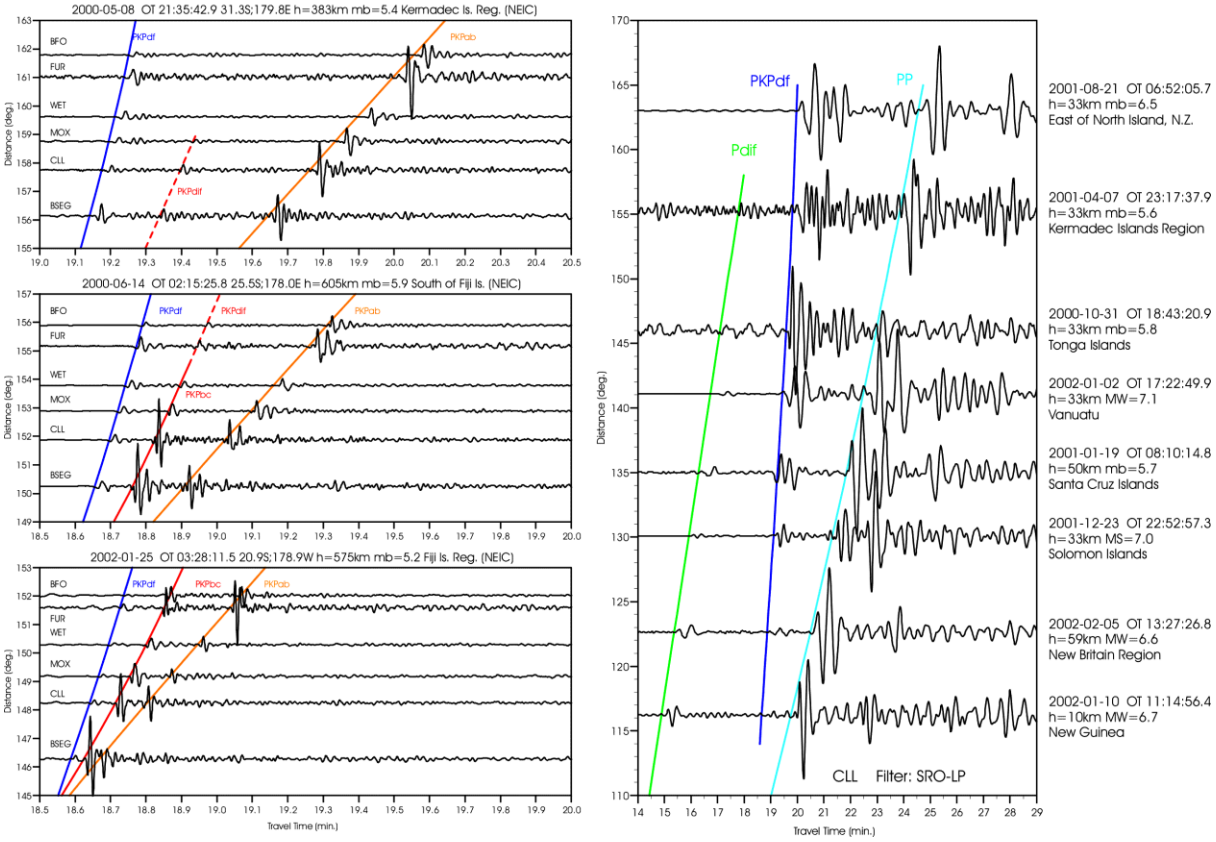

Fig. 11.74 Short-period (left side) and long-period (SRO-LP; right side) filtered broadband records of PKP phases at GRSN stations in the distance range 116° to 163°. In the LP records additionally the onsets of Pdif and PP have been correlated with their travel-time curves.

On LP and BB records the dominant phases on vertical and radial components are PKP, PP, PPP and PPS while on the transverse component SS and SSS are dominant. For deep sources, their depth phases sSS and sSSS may be strongest (Fig. 11.75). Besides PP, which has traveled along the minor arc (epicentral distance D) the phase PP2, which has taken the longer arc to the station (360° - D), may be observable, as well as phases such as PcPPKP and others (Fig. 11.76 as well as the animation file 10 in IS 11.3). SKKS, SKKKS, SKSP etc. may still be well developed on radial component records (Chapter 2, Figs. 2.60 and 2.61). The whole length of BB or LP seismograms in this distance range between the first onsets and the surface wave maximum is more than an hour (Tab. 5 in DS 3.1).

11.5.4 Late and very late core phases

For large magnitude sources, core phases reflected at the Earth's surface or at the core-mantle-boundary (CMB) may be observed in addition to the direct ones, sometimes with up to 4 (or even more) repeated reflections. These phases may be observed at practically all teleseismic distances with delays behind the first arriving P or PKP onsets ranging from about 10 minutes up to about 80 minutes, depending on the number of multiple reflections (for travel-time curves Chapter 2, Fig. 2.59). These phases are clearly discernible only in high-magnifying SP (or appropriately filtered BB) records (Fig. 2.57). Most frequently observable are the single surface

reflection P'P' (also termed PKPPKP), and the single reflection from the inner side of the core-mantle boundary, PKKP. As for the direct core phases, these multiple reflections develop different travel-time branches according to their different penetration depth into the outer core (see also ray tracing figures in IS 2.1). Figs. 11.77 and 11.78 show the ray paths for P'P' and PKKP waves, respectively, together with their related IASP91 travel-time curves (Kennett and Engdahl, 1991) for sources at depth h = 0 km and h = 600 km. Where there is more than one reflection the respective phases are often written P'N or PNKP, respectively, with the number of reflections being N-1. Ray paths and short-period record examples for P'N with N = 2 to 4 are shown in Figs. 11. 79 to 11.81 and for PNKP with N = 2 to 5 in Figs. 11.81 and 82. Fig. 11.75 shows a P5KP (PKKKKKP), which has been four times reflected from the inner side of the CMB. It is observed nearly 37 min after PKP. The phase P7KP has been found in a record at Jamestown, USA, of an underground nuclear explosion on Novaya Zemlya in 1970. Complete ray diagrams of many direct, converted and multiply reflected core phases have been presented in IS 2.1.

Additionally, the figures presented below show that these late arrivals may still have a significant SNR. Since they appear very late and thus isolated in short-period records, station operators may wrongly interpret them as being P or PKP first arrivals from independent events. This may give rise to wrong phase associations and event locations, which, particularly in a region of low seismicity, may give a seriously distorted picture of its seismicity. This was demonstrated by Ambraseys and Adams (1986) for West Africa.

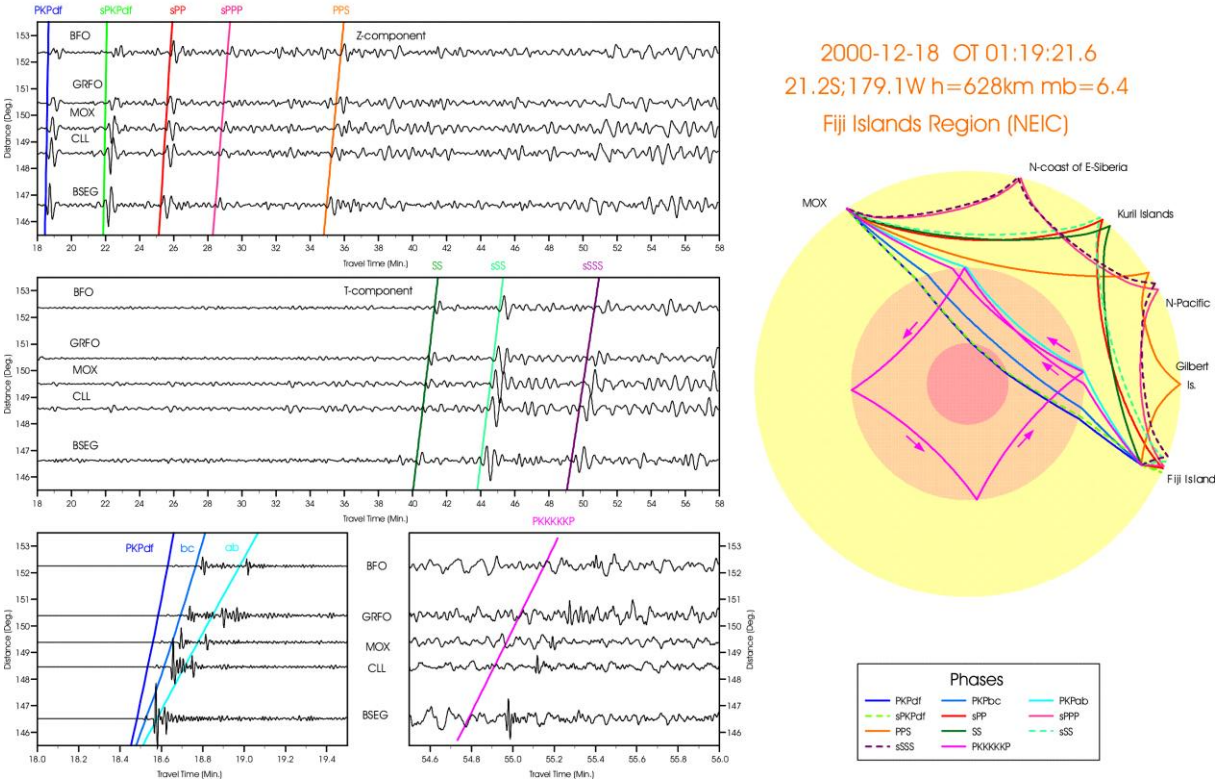

Fig. 11.75 Records of GRSN stations of a deep earthquake in the Fiji Island region. **Right**: ray paths and source data; **Left:** Records on the Z component (LP top left and SP lower left) and T component (LP middle left) (see also animation file 9 in IS 11.3).

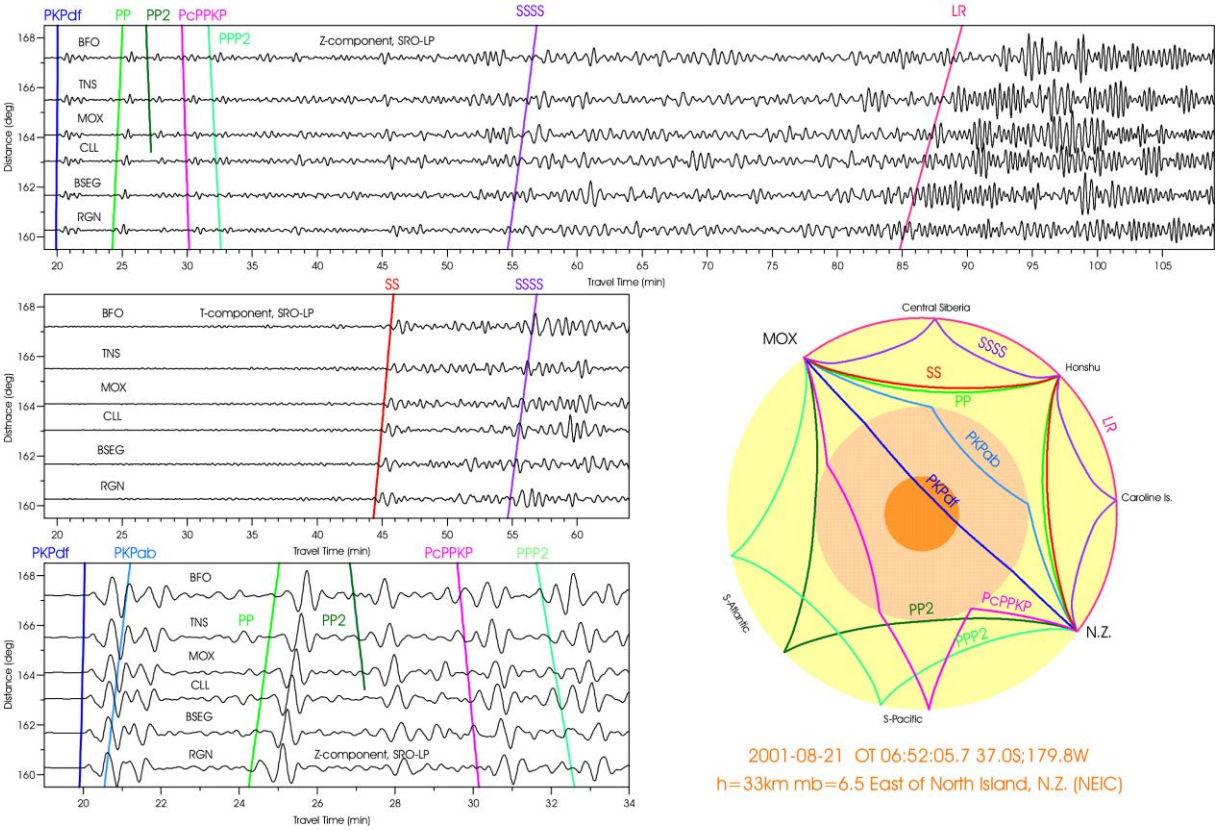

Fig. 11.76 Records of GRSN stations of a shallow (crustal) earthquake east of the North Island of New Zealand. **Lower right:** ray paths to station MOX in Germany and source data; **Top and middle left**: Records on SRO-LP components Z and T). **Lower left:** The first 14 min of the SRO-LP Z-component P-wave record. For animation see file 10 in IS 11.3).

In Figs. 11.73 to 11.82 the theoretical travel-time curves, respectively arrival times for core phases have been plotted. For consistency, they are based on the travel-time model IASP91 (Kennett and Engdahl, 1991), as in all earlier record sections shown for the teleseismic distance range. An exception is Fig. 11.79, which shows additionally the theoretical travel-time curve for the JB model (Jeffreys and Bullen, 1940) as in the lower middle record segment too for P5KP. One recognizes that the model IASP91 yields onset times for core phases that tend to be up to several seconds earlier than the real onsets in the seismograms (see also Fig. 9b and c in DS 11.3). This applies to both direct and multiple reflected core phases. The agreement between real and theoretical onsets of core phases is better when using the JB model. Also S onsets arrive with respect to the IASP91 model a bit too late. The more recent model AK135 (Kennett et al., 1995) is more appropriate than IASP91. The JB model has regularly been used until recently for the location of teleseismic sources at the international data centers in Boulder (NEIC), Thatcham (ISC) and Moscow whereas the IDC of the CTBTO uses IASP91. AK135 is now the default model used by the ISC and the NEIC.

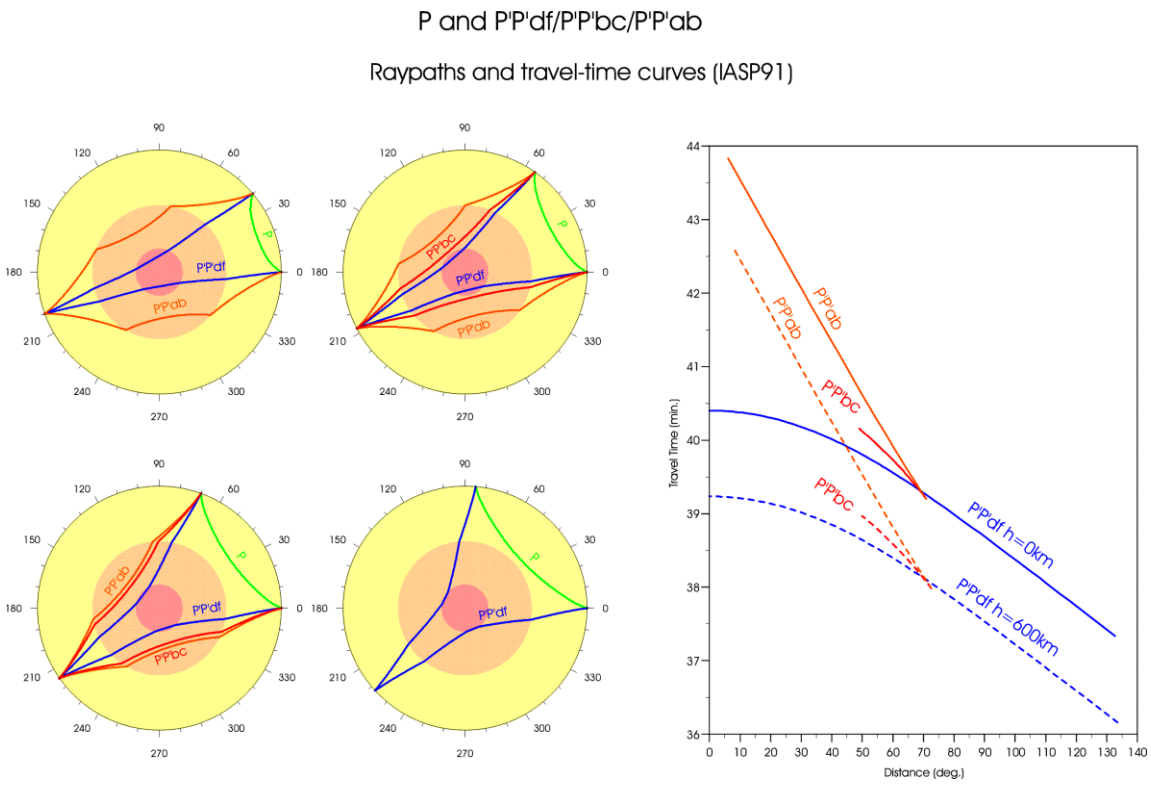

Fig. 11.77 Ray paths and travel-time curves for P'P' according to the Earth model IASP91 (Kennett and Engdahl, 1991).

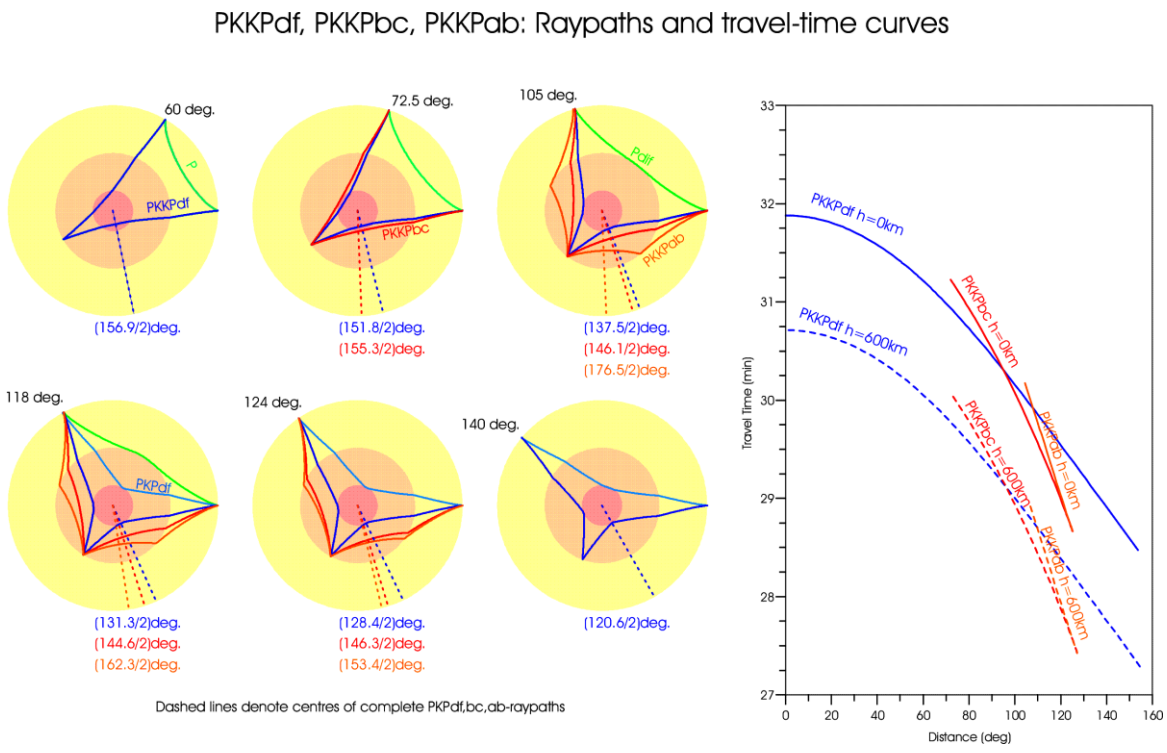

Fig. 11.78 Ray path and travel-time curves for PKKP according to the Earth model IASP91 for epicentral distances of the source between 60^o and 140^o.

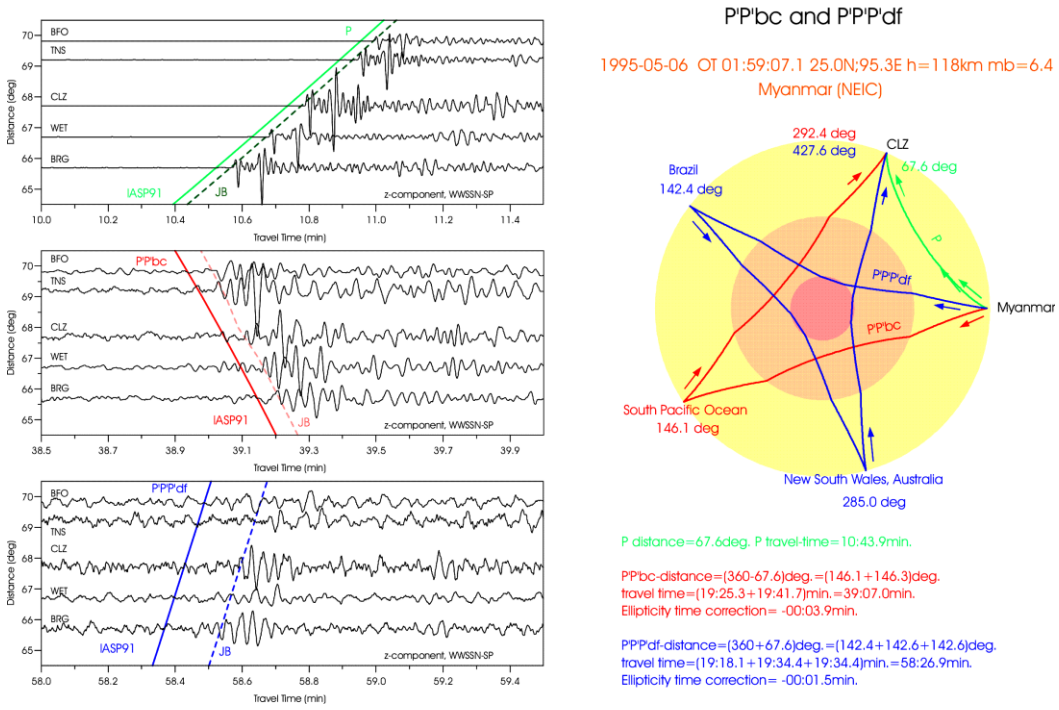

Fig. 11.79 **Right:** Source data of the Myanmar earthquake and ray paths to station CLZ in Germany. **Left:** Short-period Z-component record segments of GRSN stations with P, P'P' and P'3 arrivals at 65° < D < 70° together with their theoretically expected arrival times according to the IASP91 and JB tables. Note the much better fit with the JB times.

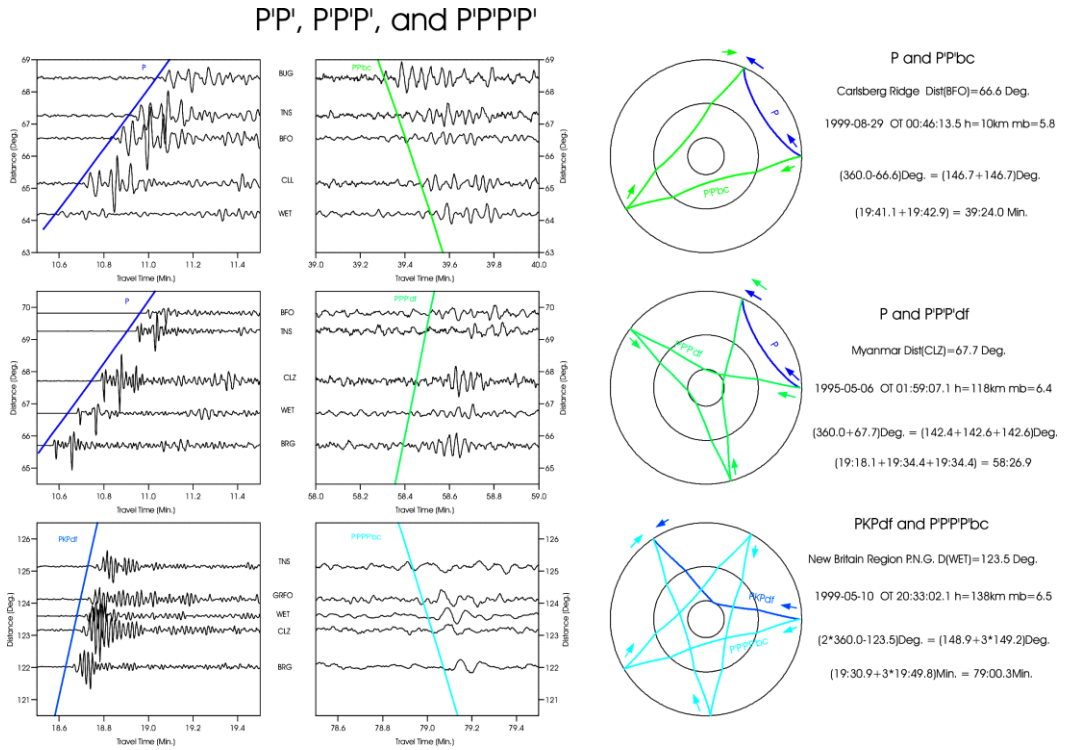

Fig. 11.80 **Left:** 1 min long SP record segments showing P and PKPdf (outer left) together with P'2, P'3 and P'4 (middle left) at GRSN stations. **Right:** Related ray paths and source data. Note the negative slowness for P'2 and P'4. The travel-time curves relate to IASP91.

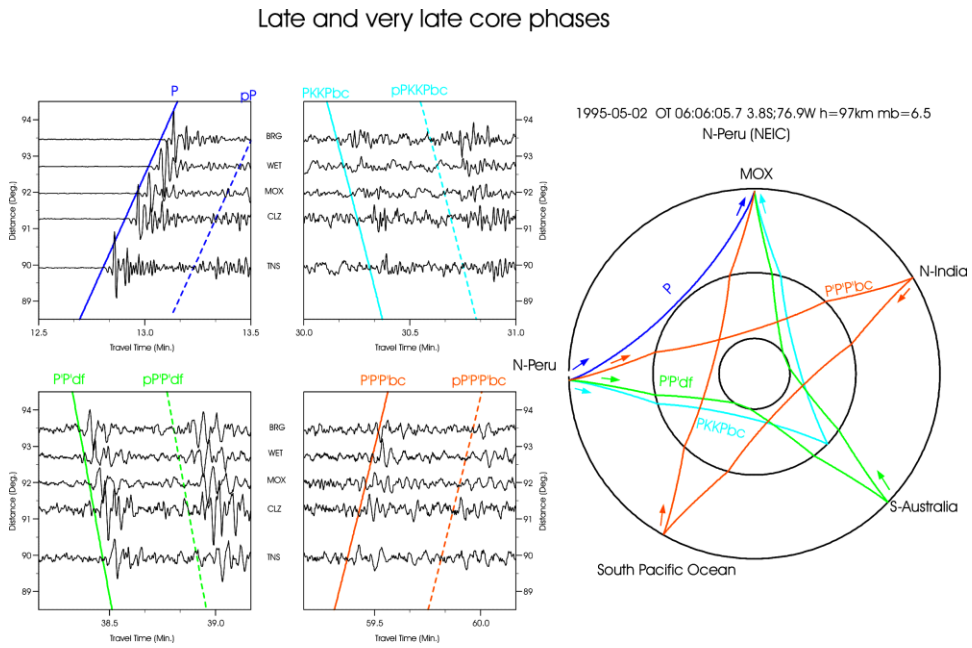

Fig. 11.81 Late and very late multiple core phases PKKP, P'2 and P'3, respectively, together with their depth phases in short-period filtered record segments of GRSN stations from an earthquake in Northern Peru at epicentral distances around 92°. For an animation of ray propagation and seismogram formation from this source see file 6 in IS 11.3.

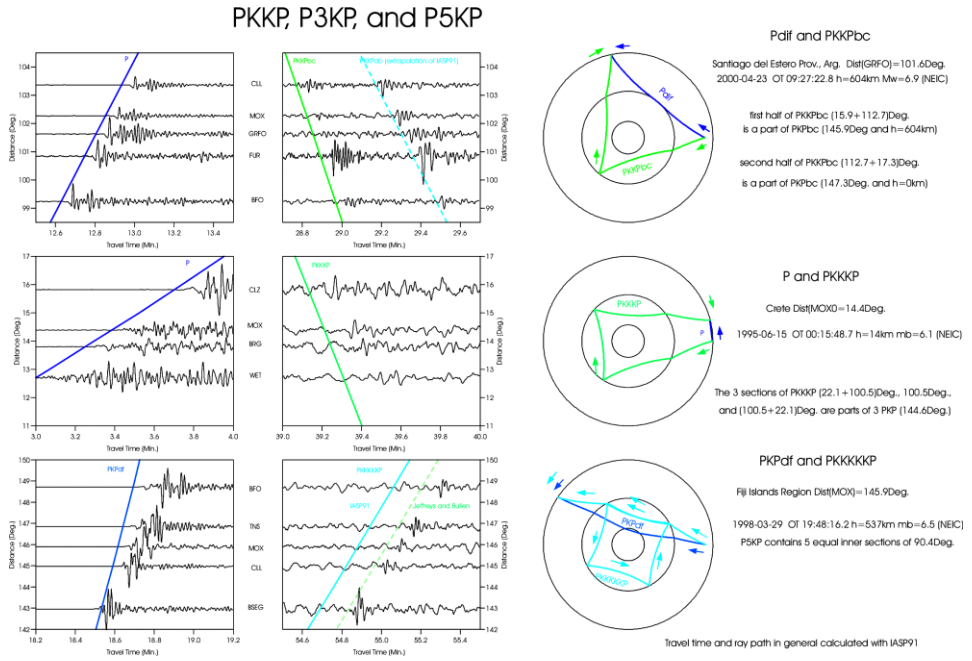

Fig. 11.82 **Left:** Short-period 1 min record segments of P and PKPdf (outer left) together with those of PKKP, P3KP and P5KP (middle left) at GRSN stations. Note in the upper middle segment the excellent fit of the second onset with the extrapolation of the IASP91 PKKPab branch and the much better fit of the P5KP onset in the lower middle segment with the JB-times **Right:** Related source data and ray paths. Note the negative slowness for PKKP and P3KP. The other theoretical travel-time curves relate to IASP91.

Note that the difference between the azimuth of the P wave and that of P'P' and PKKP, respectively, is 180° (Figs. 11.77 and 11.78). The related angular difference of the surface projections of their ray paths is 360°–D where D is the epicentral distance. Accordingly, the slowness of P'P' as well as of any even number P'N is negative, i.e. their travel time decreases with D. This also applies to PKKP and P3KP, as can be seen from Fig. 11.82. The surface projection of the travel paths of P'3 is 360° + D and that of P'4 is 2 × 360°–D. PKPPKP (= P'P') is well observed between about 40° < D ≤ 105°. In this range the phase follows the onset of P by 33 to 24 min (Figure 10 in EX 11.3 with observed data). The existence of P'N is not limited to PKPbc. Fig. 11.79 shows an example of P'3df, recorded at a distance of about 67°. P'4 is sometimes observed in the distance range 112° to 136°. An example is given in Fig. 11.80.

Similar ray paths can be constructed for PNKP, the phase with (N-1) reflections from the inner side of the core-mantle boundary (Fig. 11.82). Figure 9 in EX 11.3 gives the differential travel-time curves for PKKP to the first arrivals P or PKP, respectively, in the distance range between 80° and 130° together with the observed data. In this range PKKP arrives 13 to 19 min behind P or 9.5 to 12 min behind PKPdf. Higher multiple reflections from the inner side of the CMB such as P3KP, P4KP and P5KP are observed, if at all, at 37 ± 1 min after the first arriving wave. The latter is true for P3KP following P at around 10°, for P4KP following P between 45° < D < 75° and for P5KP following the onset of PKPdf between about 130° < D < 150° (called "37- min" rule- of- thumb).

The travel-time difference of multiple reflected core phases to the first arriving P and PKP does not change much with source depth. Therefore, you may try it just for fun although there is no more *need* for it in the present time world of near real-time global network locations and data dissemination, but the identification of these phases and knowing their travel-time curves, allows rather good distance estimates to be made even from single station records, irrespective of whether you know the source depth or not. Because of the inverse differential travel-time curves of PKPPKP and PKKP with respect to P and PKP their identification can be facilitated by comparing the onset times at neighboring stations (e.g., upper left two panels in Fig. 11.81).

The polarization of both the first arrival and the possible PKKP or PKPPKP onset, determined from 3-component records, can also aid identification because their azimuths should be opposite to that of P or PKIKP, respectively. Sometimes, also converted core reflections such as SKPPKP or SKKP can be observed in short-period recordings. However, direct or reflected core phases, which have traveled along the two ray segments through the mantel as S waves (such as SKS, SKKS, etc.) are mostly observed in broadband or long-period records.

11.5.5 Final remarks on the recording and analysis of teleseismic events

Box 2 summarizes the key criteria that should be taken into account when recording and analyzing seismograms from sources at teleseismic distances (see also 11.2.6.1).

Box 2: General rules for recording and analyzing teleseismic events

- The overall duration of teleseismic records at epicentral distances larger than 15^{o} (or 20°) ranges from tens of minutes to several hours. It increases both with epicentral distance and the magnitude of the source.
- High frequencies, of S waves in particular, are more strongly attenuated with distance. Therefore recordings at teleseismic distances are usually of lower ($f \approx 0.01$ - 1 Hz) frequency than local or regional recordings although for some events frequencies up to about 10 Hz have also been observed in P and PKP waveforms.
- Usually only longitudinal waves, both direct or multiple reflected P and PKP phases, which are much less attenuated than S waves, are well recorded by short-period, narrow-band seismographs (or their simulated equivalents) with high magnification of frequencies around 1 Hz. However, S waves from deep earthquakes may sometimes be found also in SP teleseismic records.
- Because of the specific polarization properties of teleseismic body and surface waves, polarization analysis is an important tool for identifying the different types of wave arrivals.
- According to the above, teleseismic events are best recorded by high-resolution 3-component broadband seismographs with large dynamic range and with sampling rates f = 20-40 Hz.
- The main types of seismic phases from teleseismic sources are (depending on distance range) the longitudinal waves P, Pdif, PKP, PcP, ScP, PP, and PPP and the shear waves S, Sdif, SKS, ScS, PS, SS, and SSS. The longitudinal waves are best recorded on vertical and radial components whereas the shear waves appear best on transverse and/or radial components.
- Multiple reflected core phases such as P'N and PNKP, which appear on SP records as isolated wavelets, well separated from P or PKP, may easily be misinterpreted as P or PKP arrivals from independent seismic sources if no slowness data from arrays or networks are available. Their proper identification and careful analysis helps to avoid wrong source association, improves epicenter location and provides useful data for the investigation of the physical properties of the deeper interior of the Earth.
- Several body wave phases such as PP, PS, SP, SS, PKPab, SKKSac, SKKSdf, PKPPKPab, SKSSKSab and their depth phases undergo phase shifts and wavelet distortions at internal caustics (see 2.5.4.3). This reduces the accuracy of their time and amplitude picks and their suitability for improving source location by waveform matching with undistorted phases. Therefore it is recommended that seismological observatories correct these phase shifts prior to parameter readings by applying the inverse Hilbert-transformation, which is available in modern software for seismogram analysis.
- Surface waves of shallow events have by far the largest amplitudes but surface wave amplitudes from deep earthquakes and large (nuclear) explosions are small at teleseismic distances.
- At seismic stations or network centers the following parameter readings should be obligatory during routine analysis: onset time, SNR, and, if possible, polarity of the first arriving phase; maximum P amplitude A [nm],

period T [s] and/or ground velocity V [nm/s]; onset time of secondary phases; and, if existing, additionally also for surface waves the maximum amplitude A [nm], period T [s] and/or V [nm/s], irrespective of source depth.

- P-wave amplitudes A_{max} for the determination of the short-period body-wave magnitude mb have to be measured on standard short-period (WWSSN-SP simulated) records at periods<3 s < T <3 s and for broadband mB_BB V_{max} in the period range between 0.2 s and 30 s, whereas the surface-wave amplitudes A_{max} for the determination of the surface-wave magnitude Ms_20 have to be measured on standard long-period filtered (WWSSN-LP or SRO-LP simulated) records, typically in the period range between 18 and 22 s, whereas V_{max} for broadband Ms_BB has should be measured between 3 s and 60 s period.
- For more guidance on magnitude determination, using also other phases and records/filters, consult Chapter 3 and IS 3.3 in particular.
- Networks and arrays should additionally measure and report slownesses and azimuths for analysed onsets.
- For improved determination of epicentre distance and source depth the measurement and reporting of onset time readings for secondary onsets such as S, depth phases (pP, sP, sS, etc.) and of core reflections (PcP, ScP, etc.) in particular, are very important.
- Picking and reporting of onset-times, amplitudes and periods of other significant phases, including those not identified, are encouraged by IASPEI within the technical and personnel facilities available at observatories and analysis centers as being a useful contribution to global research. These extended possibilities for parameter reporting are now well supported by the recently adopted IASPEI Seismic Format (ISF), which is much more flexible and comprehensive than the traditional Telegraphic Format (see 10.2 as well as IS 10.1 and 10.2), or by QuakeML (see IS 3.2, section 2).
- For reporting of seismic phases (including onsets not identified) one should exclusively use the new IASPEI phase names. For the definition of seismic phases and their ray paths see IS 2.1. Amplitude data should be reported according to the agreed IASPEI nomenclature for standard magnitudes (IS 3.3) and also other non-standard amplitude measurements (see IS 2.1).

11.6 Is fully automatic seismogram analysis, event location and classification already possible and feasible?

11.6.1 Introduction

Despite the potential benefits which digital data and interactive analysis software nowadays offer it is a matter of fact that digital records are increasingly less frequently read manually in a comprehensive way by seismologically trained experienced people. As outlined in Chapter 1, one main reason for this development is the tremendous increase in the number of high-gain seismic stations and networks deployed now all over the world for a steadily growing number of tasks which nowadays go even far beyond classical earthquake monitoring. They include volcano- seismology (Chapter 13 and Hammer et al., 2012); monitoring of induced seismicity (e.g., McGarr et al., 2002; Beyreuther et al., 2012) related to industrial activities such as the exploitation of geothermal, gas and oil reservoirs, mining activities (e.g., Kwiatek

et a., 2010), waste water disposal, impoundment and level-changes of huge water reservoirs (e.g., Gupta and Rastogi, 1976), or mass movements in mountain areas (e.g., Hammer et al., 2013). Accordingly, the amount of data to be analyzed has grown in recent decades by several orders of magnitude as compared to the times of classical analog earthquake seismology. Another reason is the increasing unwillingness of decision makers and funding institutions to pay fair salaries for a much larger number of well-educated people required to do all these jobs. Pressing demands for reducing labor cost both in the public sector and in industry and the often non-realistic believe that in the computer age automated procedures could do the job already not only faster but even better than well trained and experienced human beings are dominating nowadays.

The latter is surely not yet true. Nevertheless, we are now in a rapidly advancing process of increasingly better modeling of human intelligence, pattern recognition, and knowledge-based decision making. Machine-learning methods for the automatic classification and analysis of seismic waveforms gain momentum (e.g., Riggelsen and Ohrnheimer, 2012). Automatic algorithms, advanced or not yet advanced, have the advantage of being objective. Their results are fully reproducible, but not the analysis results of a group of human analysts (see IS 11.5). This even makes it difficult to correctly assess, in a unique manner, the performance of automatic algorithms as compared to human seismic data analysis. An example for such a comparison see is section 3.2.3.2 in Chapter 3. Moreover, both the acceptable ratio between missed events and false alarms on the one hand and between the timeliness and required accuracy/completeness of the data and derived information on the other hand are task-dependent. This also applies to the proper balance to be found between automatic and human analysis of seismological data.

Of greatest importance is in this context the fact of rapid population growth and urbanization since the mid 20^{th} century, combined with a dramatic increase of the vulnerability and related human and material losses due to earthquakes and volcanic eruptions. This necessitate the development of earthquake, tsunami and volcanic eruption early warning systems (EEWS; TEWS; VEEWS) for enabling fastest possible appropriate automatic or human controlled response aimed at mitigating the disastrous consequences of such events. Highest priority has the timeliness of sufficiently accurate information for triggering and guiding response actions. This can only be realized with fully or highly automated systems of seismological data analysis and is clearly different from the need for most complete and precise/accurate information required for related future basic research.

Early efforts of automatic seismological detection and classification techniques were based on attributes of specific seismic phases. However, when monitoring volcano-induced seismicity, due to the rather different source processes and complex propagation conditions of the mostly high-frequency waves in a highly heterogeneous medium, a clear identification of individual seismic phases may not be possible. Therefore methods that make use of the whole seismogram are required for event type classification. The majority of algorithms applied to event-based data sets have been based so far on artificial neural networks (ANN). These algorithms, however, are “black boxes”, as are support vector machines that focus on the output only and do not allow any insight into the physical processes which control the relationship between input and output parameters. Alternatives approaches will be sketched below. Good summaries with many references one finds, e.g., in Hammer et al. (2012).

A state-of-the-art overview of concepts, theory and approaches to automated seismic event and phase identification gives Chapter 16. Already operational or still experimental tsunami

or earthquake early warning systems such as the Pacific Tsunami Warning System (PTWC; http://ptwc.weather.gov/), GITEWS (http://www.gitews.org/index.php?id=6), and similar ones in Alaska, Japan, Mexico, Taiwan, Turkey and elsewhere (see Gasperini et al., 2007; Allen et al., 2009; Fleming et al., 2009) are examples of how far developments have already gone this way. In the following we add a few more case studies published in recent years that illustrate the different approaches chosen and the progress made in the automation of seismogram analysis and the classification of seismic events.

11.6.2 Amplitude/energy event triggers, phase identification and event location

Allen (1978, 1982) has been the first to propose an automatic P-wave picker for earthquake recognition and timing from short-period narrow-band single trace seismic records. The trigger is based on the long-term/short-term average amplitude, respectively energy ratio STA/LTA (Fig. 11.86; for details Chapter 16 and IS 8.1). It is still the most common and widely applied event trigger algorithm which has to be tuned to the specific signal and noise conditions.

Still most common is the application of the STA/LTA trigger in seismic network recordings. A seismic event is then declared if at least 4 stations have coincident observations in time of trace amplitudes above the set detection threshold that are consistent with seismic wave propagation models. Then, assuming that all these signal detections above noise relate to the first P-wave onset, they can be associated with each other to calculate the 4 unknowns of the hypocenter coordinates and origin time. Various such automatic association programs have been developed, e.g., by Engdahl and Gunst (1966), Slunga (1980), and a knowledge-based system by Bache et al. (1993) to produce automatically teleseismic event bulletins. However, as emphasized by Tong and Kennett (1996), most association programs use only P and S (including also Pn, Pg, Sn, Sg and Lg) as identifying phases. Other frequently observed phases such as PcP, ScS, PKP, PKiPK, PP, PS, SS, SKS, SKP, depth phases and multiple core phases (Fig. 11.16 and Figs. 2.57-2.61 in Chapter 2) are usually not taken into account. Withers et al. (1998a) compared selected trigger algorithms for onset time picking both in the time and frequency domain and also for particle motion and adaptive processing while Withers et al. (1998b) described an automated local and regional seismic event detection and location system using waveform correlation. All of these algorithms require a multi-station network, as do small aperture seismic arrays used for event detection and location of regional events (Chapter 9).

If, however, the number of available stations is small and/or the SNR at many sites is low then signals may be missed on the single station level and as a consequence probably a significant number of weak events will not appear in the automatic draft event bulletins. But then there will also be no visual inspection of records concerned and those weak events remain undetected. On the other hand, when lowering the detection threshold too much then noise fluctuations may cause a great number of spurious detections, *false alarms*, not related to true seismic events or even being wrongly associated to *fake events*, which all have to be reviewed in the interactive visual control step, thus increasing again the analyst workload.

An alternative approach for event detection and location is to rely not only on the automatically picked single component first onset time readings, i.e., just measuring one

parameter at many stations. Rather one should improve also the accuracy and completeness of waveform attributes measured at 3-component broadband records of single stations for many seismic phases,. Such differences may relate to polarization, amplitude ratios, frequency differences and others. Such comprehensive automatic real-time single-station record analysis may yield rather good starting locations for a subsequent iterative location refinement. This particularly holds for short-period seismic arrays because of the inferior distance control of P-wave slowness data as compared to distance estimates based on differential travel times between P and later phases with rather different slowness. But it will also apply when network data are available only from stations with rather bad azimuthal and distance coverage. The latter is often the case for near coastal events because of lacking or insufficient stations in the ocean environment or for seismic events in areas with no co-operation and data exchange between neighboring countries at all. Because of the globally rapidly growing number of stations with free data excess and exchange via Internet this will, however, in future increasingly less be the case. On the other hand, there exist but no near real-time data exchange with others, such as. In such cases the larger information content of 3C BB stations has necessarily to be exploited. Also the International Monitoring System (IMS) of the CTBTO with its rather autonomous global network of a relatively limited number of high quality stations has shown great interest in the performance of 3C-station based automatic event detection, classification and location schemes (Riggelsen and Ohrnberger, 2012).

Saari (1981) described an algorithm for automatic event location by using single-site, 3C seismograms from near earthquakes (D < 100 km) and Cichowicz (1993) an automatic S-wave picker. Earle and Shearer (1994) extended the STA/LTA trigger concept to 3C broadband velocity records and their bandpass-filtered versions in all distance ranges. Astiz et al. (1996) additionally used axes rotated records from the NEIC data base and the Global Seismic Network (GSN) in order to take into account also the different polarization properties of the various seismic phases that appear in different frequency bands and distances ranges. These authors took the STA/LTA along an envelope function generated from the seismogram, thus adapting the trigger parameters to the variable amplitude-frequency content of seismic noise and signal in the band-pass filtered records. The algorithm returns arrival times and related pick qualities which can then be associated in plots of travel-time versus distance easily with theoretically expected travel-time curves. Some of the travel-time-period-polarization-distance plots of these authors have been reproduced as Figs. 2.57, 2.58 and 2.61, together with the related IASP91 theoretical travel-time curve for short-period and long-period phases in Figs. 2.59 and 2.60.

With this automatic procedure it has been possible to pick practically all seismic phases which could be expected according to the 1D global travel-time model and which an experienced analyst would be able to recognize and identify with different relative frequency according to their different average SNR in seismic records of different type and in different components (see, e.g., Fig. 11.16). Picks made from LP records are less precise but good enough to reveal the discrepancy in SV and SH travel-times due to upper mantle anisotropy, being larger for SS than for S. Moreover, the travel-time residuals from the short-period automatic picks were comparable with those reported to the ISC from mostly human analysis. This indicates that human picking errors are not the main reason for the observed data scatter but rather travel-time inhomogeneities due to local site effects and velocity heterogeneities along the travel paths as compared to the 1D Earth model used in the computations.

Trabant et al., (2012) developed the Astiz et al. (1996) procedure further for real-time applications to all events with magnitude ≥ 6.0. Their “Global Body-Wave Envelope Stacks”

are generated by stacking of envelope functions in 1°-distance bins. The envelopes have the mean pre-P-wave noise re- moved, and the square roots of the amplitudes are then summed. The stacks are nonlinearly weighted by the number of contributing seismograms to enhance visualization of the wave field. They are among the about 70 different automatically generated "Event Plots" published by the IRIS Data Management Center (DMC) about 2 hours after origin time, including, amongst others, also global surface- and body-wave record sections, virtual array P-waves and vespagrams and P-wave coda stacks (see http://www.iris.edu/spud/eventplot). An example of a body-wave envelope stack plot for the 2013 Mw(GCMT)8.3 deep Sea of Okhotsk earthquake is given in Fig. 11.83.

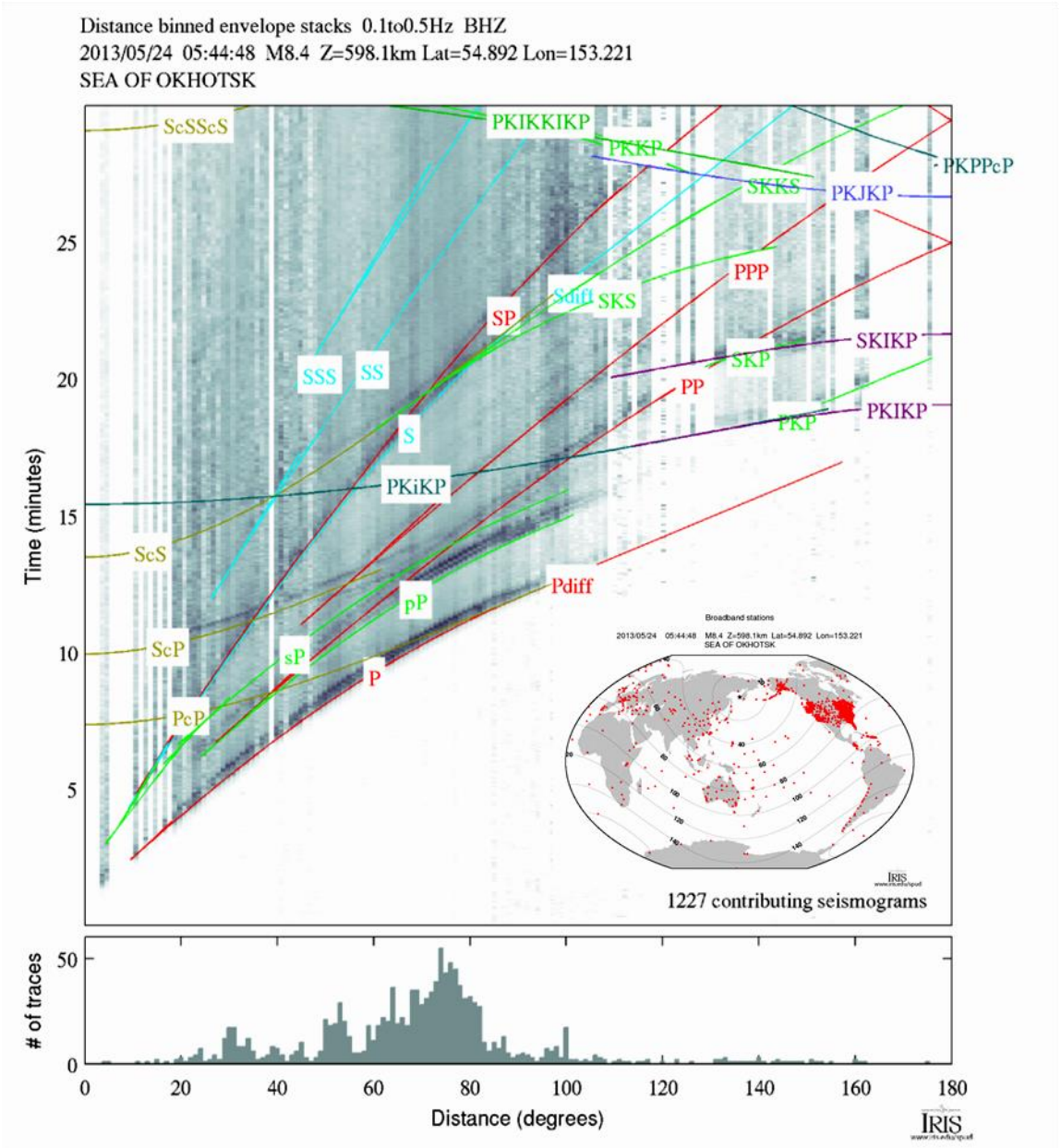

Fig. 11.83 IRIS DMC global body-wave envelope stacks for the May 24, 2013, Mw(GCMT)8.3 Sea of Okhotsk deep earthquake (h = 598 km) with inserted station distribution map and superposed theoretical AK 135 body-wave travel-time curves. Courtesy of A. Hutko, 2014.

For the same event we presented in Fig. 11.15 an unfiltered STS2 broadband record of the German station RUE at D = 67.9°. However, for the envelop travel-time stack a 0.1-0.5 Hz bandpass filter had been applied, as compared to the unfiltered 0.0083-20 Hz STS2 record in Fig. 11.15. Therefore, in the DMC vertical component plot the more long-period and usually also more horizontal component phases SS, sSS, as well as the inversely dispersed mantle surface waves are not present. Also the usually distinct core phases PKP, SKP and SKS are underrepresented do to the lack of stations at D > 100° for this specific event (see inserted map of station distribution). In any event, such near real-time plots allow a quick assessment of data availability and quality for almost all sufficiently large and thus hazardous earthquakes. Moreover, similar to vespagrams, these plots are especially useful for quickly scanning events to determine whether in the considered bandwidth range specific phases are visible in the data or not.

Fig. 11.84 compares long-term Astiz et al. (1996) STA/LTA stacks with the respective new global IRIS stacks based on about 20-times more data. The improvement is obvious.

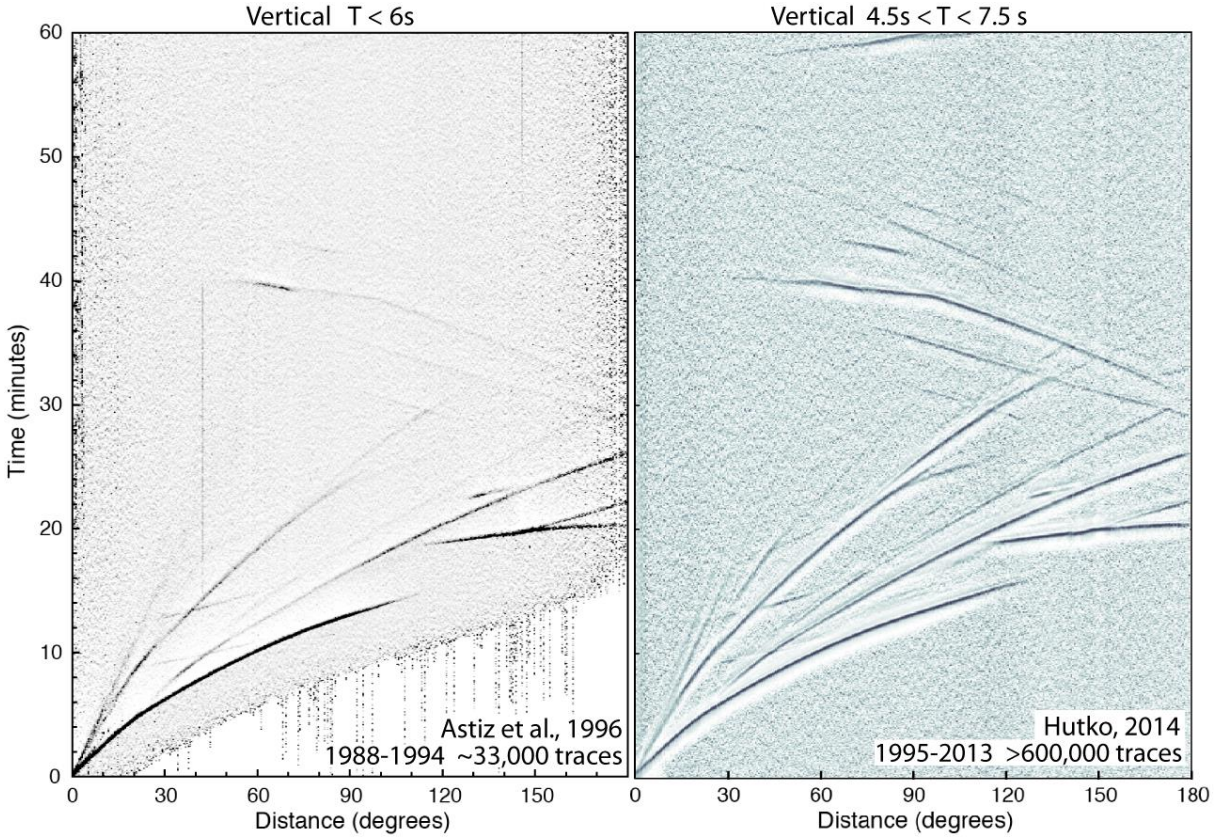

Fig. 11.84 Comparison of the long-term Astiz et al. (1996) vertical component STA/LTA stacks for T < 6 s with the respective new global IRIS stacks in the period range 4.5 s < T < 7.5 s, based on more than 600,000 event records. For more and updated information see http://www.iris.edu/dms/products/globalstacks. Compiled by courtesy of A. Hutko, 2014.

Chapter 16 gives many more examples on automatic event detection, phase picking and phase identification based on single component, 3-component-, network and array records. Amongst these examples the authors brief also on essentials of the rather sophisticated 3C algorithms developed by Tong and Kennett (1995, 1996) and Bai and Kennett (2000). These algorithms

combine automated detection and phase association for first and later arrivals and have been implemented in an experimental expert systems for automatic later phase identification and event location by means of single station 3-component broadband records. One key element was the introduction of a complexity measure for better discrimination between seismic signals and noise. It mimics the performance of the human eye, which uses the local change in frequency as a key criterion for a phase arrival. Also polarization analysis proved to be quite successful in distinguishing body waves from background noise. Assessing the performance of this robust and near real-time automatic event-recognition and classification system for teleseismic earthquakes Tong and Kennett (1996) conclude that "…the more phases detected and identified when recognizing a seismic event, the better discrimination between the possible solutions …". In most cases their estimated event distances were within 7% and the related azimuths within 5°, thus constraining the location within 4° caps. This compares well with what also an experienced analyst could achieve off-line with some more time delay even with simple analog 3C data analysis (section 11.2.6.2 and EX 11.2), or even better and more comfortably nowadays interactively with modern PC-assisted analysis programs (see example 6 in IS 11.6). Surely, no single station location cannot compete at all with modern seismic network locations and are not thought to be propagated here as being a viable alternative for the latter. But they illustrate what would be achieved already with competent comprehensive data analysis in near real-time with just one good 3C-BB station in the case that network locations are not timely available, for what reason ever. And for "Seismology at Schools", undergraduate geoscience courses or public demonstrations on how seismology works (concept Education and Outreach) such on-the-spot single-station performance demonstrations are much more attractive and convincing than the reference to the near real-time communication about a seismic event by the agency processing the data of an anonymous regional or global network consisting of dozens to hundreds of stations.

In a follow-up paper Bai and Kennett (2000) proposed for arrival recognition and detection of a variety of P and S type phases a combination of three different techniques with different sensitivity to noise. They may be applied with different weightings to account for specific station site effects such as temporal/seasonal variations in the nature and power of seismic noise. The authors applied this method to unfiltered records in a wide range of epicentral distances from far-regional to teleseismic. Thus they followed the precept of Douglas (1997): "…the less filtering, the better the algorithm." The procedure works successful even when noise is quite low and weak phases are buried in the coda of earlier events. For the used set of windows and thresholds they achieved an effective precision of onset-time picking of about 1 s, thus constraining the differential time between P and S to within 2 s. This corresponds to about 0.3° in the distance range between 20° and 60°. Once a phase detection has been made even more sophisticated picking algorithms may be applied ubsequent filtering can help to clarify the nature of phases. such as the tensor AR method by Leonard and Kennett (1999). S

While the above approach focusses on the comprehensive picking and interpretation of later phase onsets in 3C-records at single stations VanDecar and Crosson (1990) aimed at the determination of teleseismic relative phase arrival times using multi-channel regional network records, their cross-correlation and least squares. They found for quality records of the Washington Regional Seismograph network that the rms uncertainty in arrival time estimates was of the order of the sampling interval of 0.01 s. Also the reproducibility of delay anomalies was excellent for events from the same geographic location, even if their waveform character differed significantly.

Outlining further the details of these methods would go, however, well beyond the scope of the Manual. Here the original literature needs to be consulted. The same applies to the machine learning approaches by Ohrnberger and his team (e.g., Riggelsen et al., 2007; Riggelsen and Ohrnberger (2012); Hammer et al., 2012). Therefore, we will introduce them only briefly in the next and last section.

11.6.3 Machine learning approaches for improving event detection and classification at single 3-component seismic stations

Ohrnberger (2001) was the first who applied Hidden Markov Model (HMM) based speech recognition techniques to parameters deduced from the continuous analysis of seismic data recorded at the Mt. Merapi volcano (Chapter 13; also: Hidden Markov Model Toolkit HMT, http://htk.eng.cam.ac.uk/; Python toolbox ObsPy, http://www.python.org/ and http://docs.obspy.org/index.html). Riggelsen et al. (2007) introduced the method of Dynamic Bayesian networks (DBNs) to supervised learning in seismology. One of the key elements in their detection procedures is the adaptation to drifts in the noise characteristics. This results in distinct improvement of performance.

In order to cope with the situation of sparse networks, e.g., at volcanos and in particular also during volcanic crises, Beyreuther et al. (2012) designed an earthquake detector with a probabilistic architecture. It is based on the generation of characteristic functions and the derivation of a multi-dimensional feature vector via principal component analysis and inverse weighting. It performs already well when applied to just a single station. In contrast to the analysis of teleseismic earthquake records, where the emphasis lies on the detection and identification of as many as possible phase onsets for a given event, the main task in volcano seismology is to detect and discriminate/classify different types of volcano-seismic events of different origin such as volcano-tectonic event (VT), Hybrids (HY) with characteristics of both “high-frequency” and “long-period” earthquakes, or rock falls (GU). In periods of reactivation or ongoing eruption of a volcano they may occur in dense and mixed sequences in different relative proportions. The relative frequency and strength of occurrence of these different types of events have both predictive power and assessment quality for the formulation of a likely pending volcanic threat or the objective characterization and documentation of an ongoing activity. Applying the procedure to almost 4 months of continuous data sampling during the activity period of Mt. Merapi, Indonesia, in 1998, the authors concluded that even single channel single station multi-parameter HMM triggers work well, provided that they have been well-trained with a sufficient number of representative training events for the various classes. In terms of objectivity and reproducibility of the classification results the procedure may be equivalent or even outperform those of an experienced volcanologist who bases his decisions on the waveforms recorded at many more sensors.

However, often training set data are not available and their compilation and testing is a tedious process which takes quite some time. Therefore, Hammer et al. (2012) took a HMM *learning-while-recording* approach for volcano monitoring. In a first step the algorithm converts the seismic waveforms into a sequence of n-dimensional parameter vectors. This compressed signal representation increases the robustness of the procedure. After creation of the draft model for each particular event type, the classification process can be started on an unknown data stream and begin to retrain the original classification model as more and more

data become available. Moreover, new event type classes can be created if incoming data segments cannot be associated with any of the previously specified classes. The procedure has been applied to the detection and classification of volcano-tectonic events, hybrids and rockfalls in records at Soufrière Hills volcano, Montserrat (Fig. 11.85). The initial recognition accuracy of 84% could be increased to 97% by retraining the system on newly detected events.

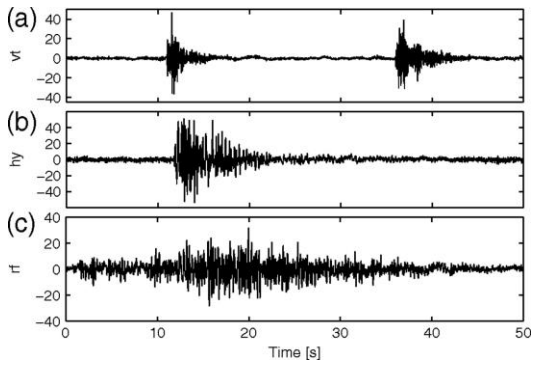

Signal type	Domin. Freq.	Duration	Waveform characteristics
VT	> 5 Hz	< 10 s	Impulsive P and S waves
HY	0.4-4 Hz	several s to tens of s	High-frequency impulsive onset no separate P and S, LP coda
GU	1-10 Hz	up to several tens of s	Cigar-shaped emergent signal, no separate P and S waves

Fig. 11.85 Left: Typical examples of VT, HY and GU events recorded at Soufrière Hills volcano, Montserrat. Right: Characteristics of these three considered signal classes. Compiled from Figure 6 and Table 2 in Hammer et al. (2012), BSSA, **102**(3), pp. 954 and 955; © Seismological Society of America.

The same algorithm has been applied by Hammer et al. (2013) to small earthquakes with magnitudes Ml < 2.5 and source depth ≤ 20 km and thus record durations less than 20 s in an area of 2700 km^2 in Switzerland. They had to be detected and discriminated from quite many quarry blasts and rare rockfalls in records of the only seismic station, FUSIO, in this area. Over the 9 years of the Swiss Earthquake Survey (SED) event catalog analyzed for the small area under investigation with the continuously re-trained self-learning algorithm, 97% of all events (earthquakes, quarry blasts and rockfalls) have been detected and none of the earthquakes or quarry blasts been misclassified as rockfall. But there is disagreement between the automatic and human classification for about 11 % of the detected events whether these are earthquakes or explosions.

These examples give an idea of the development of theoretical concepts and procedures for automatic detection and classification of seismic events. They show, as of now, what can be achieved with them and what not. But the various discussions in this section and in Chapter 11 as a whole also reveal what still remains to be the permanent duty of well-educated and practically trained seismologists who work with compassion and zeal over many years in the field of comprehensive seismogram and event analysis. Without their expertise also the automation of seismological data analysis procedures will not progress in the right direction, may result in too many uncontrolled and by users not well understood “black box”-procedures and data products whose completeness and accuracy may not satisfy the requirements for long-term fundamental and applied seismological research.

Acknowledgments

The authors are very grateful to A. Douglas and R. D. Adams for their careful reviews which helped to significantly improve the original draft of the first edition. Thanks go also to staff members of the Geophysical Survey of the Russian Academy of Science in Obninsk who shared in reviewing the various sections of this Chapter (Ye. A. Babkova, L. S. Čepkunas, I. P. Gabsatarova, M. B. Kolomiyez, S. G. Poygina and V. D. Theophylaktov). Many of their valuable suggestions and references to Russian experience in seismogram analysis were taken into account. Thanks go to M. Ohrnberger and his team for making their recent publications available. We are greatful also to K. Stammler, for useful information and clarifications with respect to the procedures of the SZO Hannover and the analysis program SHM as well as to B. Weber and J. Saul for the same with respect to SeisComP3. Our greatest thanks, however, go to the four reviewers of the largely new and amended Chapter 11, L. Ottemöller, D. DiGiacomo, J. Schweitzer and W. Strauch. Their comments helped greatly to clarify several issues and to streamline and shorten the first draft. W. Strauch additionally contributed the subsection on Earthworm and A. Hutko from IRIS the Figs. 11.83 and 11.84 together with related references and links.

Recommended overview readings

Bowers and Selby (2002)
Dahlmann et al. (2009)
Gasperini et al. (2007)
Havskov and Ottemöller (2010)
Kennett (2002)
Kulhanek (1990 and 2002)
Payo (1986)
Richards and Wu (2011)
Richter (1958)
Richards (2002)
Richards and Wu (2011)
Scherbaum (2001 and 2002)
Simon (1981)
Willmore (1979)

References

Allen, R. V. (1978). Automatic earthquake recognition and timing from single traces. *Bull. Seism. Soc. Am.*, **68**, 1521-1532.

Allen, R. V. (1982). Automatic phase pickers: Their present and future prospects. *Bull. Seism. Soc. Am.*, **72,** 225-242.

Allen, Q. M., Gasperini, P., Kamigaichi, O., and Böse, M. (2009). The status of earthquake early warning around the world. An introductory overview. *Seism. Res. Lett.*, **80**, 682-693; doi: 10.1785/gssrl.80.5.682.

Ambraseys, N. N., and Adams, R. D. (1986). Seismicity of West Africa. *Annales Geophysicae*, **86**, 6, 679-702.

Astiz, L., Earle, P., and Shearer, P. (1996). Global stacking of broadband seismograms. *Seism. Res. Lett.*, **67**, 8-18.

Barsch, R. (2009). *Web-based technology for storage and processing of multi-component data in seismology*. PhD thesis, LudwigMaximilians Universität München, Munich, Germany.

Baumbach(†), M. (1999). SEIS89 - A PC tool for seismogram analysis. In: Bormann (Ed.) International Training Course 1999 on Seismology, Seismic Hazard Assessment and Risk Mitigation, Lecture and exercise notes, Vol. 1, *GeoForschungsZentrum Potsdam, Scientific Technical Reports* **STR99/13**, 423-452.

Bache, T., Bratt, W. R., Swanger, H. J., Beall, G. W., and Dashiell, F. K. (1993). Knowledge-based interpretation of seismic data in the Intelligent Monitoring System. *Bull. Seism. Soc. Am.*, **83**, 1521-1532.

Bai, C. Y., and Kennett, B. L. N. (2000). Automatic phase-detection and identification by full use of a single three-component broadband seismogram. *Bull. Seism. Soc. Am.*, **90**, 187-198.

Beyreuther, M., Barsch, R. Krischer, L., Megies, T., Behr,Y. and Wassermann, J. (2010). ObsPy: A Python toolbox for seismology. *Seism. Res. Lett*., **81**(3); doi:10.1785/gssrl.81.3. 530.

Beyreuther, M., Hammer, C., Wassermann, J., Ohrnberger, M., and Megies, T. (2012). Constructing a Hidden Markov Model based earthquake detector: application to induced seismicity. *Geophys. J. Int.*, **189**(1), 602-610; doi: 10.1111/j.1365-246X.2012.05361.x.

Bisztricsany, E. (1958). *A new method for the determination of the magnitude of earthquake*. *Geofiz. Kozl*., **7**, 69-96 (in Hungarian with English abstract).

Bock, G., Grünthal, G., and Wylegalla, K. (1996). The 1985/86 Western Bohemia earthquakes: Modelling source parameters with synthetic seismograms. *Tectonophysics*, **261**, 139-146.

Bokelmann, G. (1995). Azimuth and slowness deviations from the GERESS regional array. *Bull. Seism. Soc. Am.*, **85**, 5, 1456-1463.

Bondár, I. and D. Storchak. (2011). Improved location procedures at the International Seismological Centre. *Geophys. J. Int.*, **186**, 1220-1244, doi:10.1111/j.1365-246X2011.05107.x

Bormann, P. (1971a). Statistische Untersuchungen zur Ortung teleseismischer Ereignisse aus Raumwellenregistrierungen der Station Moxa. *Veröff. Zentralinstitut für Physik der Erde* **9**(1971), 103 pp.

Bormann, P. (1971b). Location of teleseismic events by means of body-wave records at station Moxa (in German: Ortung teleseismischer Ereignisse aus Raumwellenregistrierungen der Station Moxa), *Monatsberichte der ADW*, **13**, 10-12, 847-852.

Bormann, P. (1972a). A study of travel-time residuals with respect to the location of teleseismic events from body-wave records at Moxa station. *Gerl. Beitr. Geophys*., **81**, 117-124.

Bormann, P. (1972b). A study of relative frequencies of body-wave onsets in seismic registrations of the station Moxa. In: Seismological Bulletin 1967, Station Moxa (MOX). *Akademie-Verlag*, Berlin 1972, 379-397

Bormann, P. (1972c). Identification of teleseismic events in the records of Moxa station. *Gerl. Beitr. Geophys.*, **81**, ½, 105-116.

Bormann, P., Wylegalla, K., Strauch, W. and Baumbach, M. **(**1992). Potsdam seismological station network: processing facilities, noise conditions, detection threshold and localization accuracy. *Physics Earth Planet. Int.*, **69**, 311-321.

Bowers, D., and Walter, W. R. (2002). Discriminating between large mine collapses and explosions using teleseismic P Waves. *Pure and Applied Geophysics*, **159**, 803–830.

Bowers, D., and Selby, N. D. (2009). Forensic Seismology and the Comprehensive Nuclear-Test-Ban Treaty. *Annual Reviews of Earth and Planetary Sciences*, **37**, 209–236.

Buchbinder, G. R., and Haddon, R. A. W. (1990). Azimuthal anomalies of short-period P-wave arrivals from Nahanni aftershocks, Northwest territories, Canad, and effects of surface topography. *Bull. Seism. Soc. Am.*, **80**,5, 1272-1283.

Cassidy, F., Christoffersson, A., Husebye, E. S., and Ruud, B. O. (1990). Robust and reliable techniques for epicentre location using time and slowness observations. *Bull. Seism. Soc. Am.*, **80**, 1, 140-149.

Chernobay, I. P., and Gabsatarova, I. P. (1999). Source classification in the Northern Caucasus. *Phys. Earth Planet. Int.*, **113**, 183-201.

Chernobay, I. P., and Gabsatarova, I. P. (1999). Source classification in the Northern Caucasus. *Phys. Earth Planet. Int.*, **113**, 183-201.

Chernobay, I. P., and Gabsatarova, I. P. (1999). Source classification in the Northern Caucasus. *Phys. Earth Planet. Int.*, **113**, 183-201.

Christoffersson, A., Husebye, E. S., and Ingate, S. F. (1988). Wavefield decomposition using ML-probabilities in modeling single-site 3-component records. *Geophys. Journal*, **93**, 197-213.

Cichowicz. A. (1993). An automatic S-wave picker. *Bull. Seism. Soc. Am.*,**83**, 180-189.

Dahlman, O., Mykkeltveit, S., and Haak, H. (2009). *Nuclear Test Ban: Converting Political Visions to Reality*. Berlin: Springer.

Davies, D., Kelly, E. J., and Filson, J. R. (1971). The VESPA process for the analysis of seismic signals. *Nature*, **232**, 8-13.

Douglas, A., and Rivers, D. W. (1988). An explosion that looks like an earthquake. Bull. Seism. Soc. Am., **78**, 2, 1011-1019.

Douglas, A. (1997). Bandpass filtering to reduce noise on seismograms: is there a better way? . *Bull. Seism. Soc. Am.*,**87**, 770-777.

Douglas, A., Hudson, J. A., Marshall, P. D., and Young, J. B. (1974). Earthquakes that look like explosions. *Geophys. J. R. astr. Soc*., **36**, 227-233.

Douglas, A., Stewart, R. C., and Richardson, L. (1984). Comments on "Analysis of broadband seismograms from the Chile-Peru area" by R. Kind, and D. Seidl. *Bull. Seism. Soc. Am.*, **74**, 2, 773-777.

Douglas, A., and Rivers, D. W. (1988). An explosion that looks like an earthquake. Bull. Seism. Soc. Am., **78**, 2, 1011-1019.

Douglas, A., Bowers, D., and Young, J. B. (1997). On the onset of P seismograms. *Geophys. J. Int.*, **129**, 681-690.

Earle, P. S., and Shearer, P. M. (1994). Characterization of global seismograms using an automatic-picking algorithm. *Bull. Seism. Soc. Am.*, **84**, 366-376.

Engdahl, E. R., and Gunst, R. H. (1966). Use of a high speed computer for the preliminary determination of earthquake hypocenters. *Bull. Seism. Soc. Am.*, **56**, 325-336.

Engdahl, E. R., Van der Hilst, R. D., and Buland, R. P. (1998). Global teleseismic earthquake relocation with improved travel times and procedures for depth determination. *Bull. Seism. Soc. Am.*, **88**, 722-743.

Fleming, K., Picozzi, M., Milkereit, C., Kühnlenz, F., Lichtblau, B., Fischer, J., Zulfikar, C., Özel, O., and the SAFER and EDIM working groups (2009). The self-organizing seismic early warning information network (SOSEWIN). *Seismol. Res. Lett.*, **80**(5), 755-771; doi: 10.1785/gssrl.80.5.755,

Flinn, E. (1965). *Signal analysis using rectilinearity and direction of particle motion.* Proc. IEEE, **53**,1874-1876.

Gasperini, P., Manfredi, G, and Zschau, J. (2007). *Earthquake early warning systems*. Springer Berlin-Heidelberg, 349 pp.

Geiger, L. (1910). Herdbestimmung bei Erdbeben aus den Ankunftszeiten. *Nachrichten von der Königlichen Gesellschaft der Wissenschaften zu Göttingen*, Mathematisch-Physikalische Klasse, 331-349. (In 1912 translated to English by Peebles, F. W. L., and Corey, A. H.: see Geiger, L. (1912).

Geiger, L. (1912). Probability method for the determination of earthquake epicenters from the arrival time only (translation of the 1911 article). *Bull. St. Louis Univ*., **8**, 60-71.

Goldstein, P., and Snoke, A. (2005). SAC Availability for the IRIS Community. Incorporated Institutions for Seismology Data Management Center Electronic Newsletter. http://www.iris.edu/dms/newsletter/vol7/no1/sac-availability-for-the-iris-community/

Goldstein, P., Dodge, D., Firpo, M., Lee, M. (2003). 85.5 SAC2000: Signal processing and analysis tools for seismologists and engineers. In: W.H. K Lee, H. Kanamori, P.C. Jennings, and C. Kisslinger (Eds.). International Handbook of Earthquake and Engineering Seismology, Vol. 81, Part B. 1613-1614: Academic Press, London. DOI: 10.1016/S0074-6142(03)80284-X

Gupta, H. K., and Rastogi, B. K. (1976). *Dams and earthquakes*. Elsevier.

Gutenberg, B., and Richter. C. F. (1956a). Magnitude and energy of earthquakes. *Annali di Geofisica*, **9**, 1-15.

Hammer, C., Beyreuther, M., and Ohrnberger, M. (2012). A seismic-event spotting system for volcano fast-response systems. *Bull. Seism. Soc. Am.*, **102**(3), 948-960; doi: 10.1785/0120110167..

Hammer, C., Ohrnberger, M., and Fäh, D. (2013). Classifying seismic waveforms from scratch: a case study in the alpine environment. *Geophys. J. Int.*, **192**(1), 425-439; doi: 10.1093/gji/ggs036.

Hanka, W., and R. Kind (1994). The GEOFON program. *Annali di Geofisica*, **37** (5), 1,060-1,065.

Hanka, W., Heinloo, A., and Jäckel, K.-H. (2000). Networked seismographs: GEOFON real-time data distribution. *ORFEUS Electronic Newsletter*, **2**, 3, http://www.orfeus-eu.org.

Hanka, W., Saul, J., Weber, B., Becker, J., Harjadi, P., Fauzi, and GITEWS Seismology Group (2010). Real-time earthquake monitoring for tsunami warning in the Indian Ocean and beyond. *Nat. Hazards Earth Syst. Sci.*, **10**, 2611-2622; doi: 10.5194/nhess-10-2611-2010.

Harjes, H.-P., Jost, M. L., and Schweitzer, J. (1994). Preliminary Calibration of Candidate Alpha Stations in the GSETT-3 Network. *Annali di Geofisica*, **37**, 382-396.

Havskov, J. (Ed.) (1996). The SEISAN earthquake analysis software for the IBM PC and SUN, Version 5.2. *Institute of Solid Earth Physics, Univ. of Bergen*, August 1996.

Havskov, J., and Ottemöller, L. (1999). Electronic Seismologist - SeisAn Earthquake Analysis Software. *Seism. Res. Lett*., **70**, 532-534.

Havskov J., and Ottemoller, L. (2010). Routine Data Processing in Earthquake Seismology: With Sample Data, Exercises and Software, Springer (May 25, 2010), ISBN-10: 904818696X, ISBN-13: 978-9048186969

Herrin, E. (1968). Introduction to "1968 Seismological Tables for P phases". *Bill. Seism. Soc. Am.*, **58**(44), 1193-1195.

Houard, S., Plantet, J. L., Massot, J. P., and Nataf, H. C. (1993). Amplitudes of core waves near the PKP caustic, from nuclear explosions in the South Pacific recorded at the "Laboratoire de Detection et Geophysique" network in France. *Bull. Seism. Soc. Am*., **83**, 6, 1835-1854.

Hwang, L. J., and Clayton, R. W. (1991). A station catalog of ISC arrivals: Seismic station histories and station residuals. *U.S. Geological Service Open-File Report* 91-295.

IASPEI (2013). Summary of Magnitude Working Group recommendations on standard procedures for determining earthquake magnitudes from digital data.

http://www.iaspei.org/commissions/CSOI/Summary_WG_recommendations_20130327.pdf

IDC Documentation (May 1998). Technical Instructions: Analyst instructions for seismic, hydroacoustic, and infrozonic data, 103pp.

Jeffreys, H., and Bullen, K. E. (1940, 1948, 1958, 1967, and 1970). Seismological Tables. British Association for the Advancement of Science, *Gray Milne Trust*, London, 50 pp.

Johnson, C. E., Bittenbinder, A., Bogaert, B., Dietz, L., and Kohler, W. (1995). Earthworm: A flexible approach to seismic network process- ing, *IRIS Newsletter* **14**, 2, 1–4.

Kennett, B. L. N. (Ed.) (1991). IASPEI 1991 Seismological Tables. Research School of Earth Sciences, Australian National University, 167 pp.Kennett, B. L. N. (2002). The seismic wavefield. Volume II: Interpretation of seismograms on regional and global scales. *Cambridge University Press*, Cambridge, x + 534 pp, ISBN 0-521-00665-1, 163-170.

Kennett, B. L. N., and Engdahl, E. R. (1991). Traveltimes for global earthquake location and phase identification. *Geophys. J. Int*., **105**, 429-465.

Kennett, B. L. N., Engdahl, E. R., and Buland, R. (1995). Constraints on seismic velocities in the Earth from traveltimes. *Geophys. J. Int*., **122**, 108-124.

Kim, W.-Y., Simpson, D. W., and Richards, P. G. (1993). Discrimination of earthquakes and explosions in the Eastern United States using regional high-frequency data. *Geophysical Research Letters*, **20**, 1507–1510.

Kulhánek, O. (1990). *Anatomy* of seismograms. Developments in Solid Earth Geophysics **18**, Elsevier, Amsterdam,78 pp.

Kulhanek, O. (2002). The structure and interpretation of seismograms. In: Lee, W. H. K., Kanamori, H., Jennings, P. C., and Kisslinger, C. (Eds.) (2002). International Handbook of Earthquake and Engineering Seismology, Part A. *Academic Press, Amsterdam*, 333-348.

Kwiatek, G., Plenkers, K., Nakatani, M., Yabe, Y., Dresen, G., and JAGUARS-Group (2010). Frequency-magnitude characteristics down to magnitude -.4.4 for induced seismicity recorded at Mponeng gold mine, South Africa. *Bull. Seism. Soc. Am.*, **100**(3), 1165-1173 ; doi: 10.1785/0120090277.

Lee, W. H. K. (1995). Realtime seismic data acquisition and processing. *IASPEI Software Vol.1*, 2nd Edition.

Leonard, M., and Kennett, B. L. N. (1999). Multi-component autoregressive techniques for the analysis of seismograms. *Phys. Earth Planet Int.*, **113**, 247-263.

Luckett, R., Ottemöller, L., and Whitmore, P. (2008). A Tsunami Warning System for the Northewast Atlantic. *ORFEUS Newsletter*, **8**, 1; http://www.orfeus-eu.org.

McGarr, A., Simpson, D., and Seeber, L. (2002). Case histories of induced and triggered seismicity. In: Lee, W. H. K., Kanamori, H., Jennings, P. C., and Kisslinger, C. (Eds.) (2002). *International Handbook of Earthquake and Engineering Seismology*, Part A. Academic Press, Amsterdam, 647-661.

Megies, T., Beyreuther, M., Barsch, R., Krischer, L., Wassermann, J. (2011). ObsPy – What can it do for data centers and observatories? *Ann. Geophys.*,**54**, 1; doi: 10.4401/ag-4838.

Mykkeltveit, S., and Bungum, H. (1984). Processing of regional seismic events using data from small aperture arrays. Bull. Seism. Soc. Am., **74**, 2313-2333.

Ohrnberger, M. (2001). Continuous automatic classification of seismic signals of volcanic origin at Mt. Merapi, Java, Indonesia, *Dissertation, Institute of Geosciences, University of Potsdam*.

Okal E.A. and Taladier, J. (1989) Mm: A Variable-Period Mantle Magnitude, Journal of Geophysical Research, Vol. 94, No B4, p.4169-4193, April 10, 1989

Olivieri, M., and Clinton, J. (2012). An almost fair comparison between earthworm and SeisComp3. *Seismol. Res. Lett.*, 83 (4), 720-727

Ottemöller, L., Voss, P., and Havskov, J. (Eds.) (2013). *SEISAN earthquake analysis software for Windows, Solaris, Linux and Macosx Version 10.0.* Institute of Solid Earth Physics, Univ. of Bergen, July 2013, http://seis.geus.net/software/seisan/seisan.html.

Payo, G. (1986). Introduccion al analisis de sismogramas. Instituto Geográfico Nacional, Madrid, 125 pp.

Plenkers, K., Kwiatek, G., Nakatani, M., Dresen, D., and the JAGUARS group (2010). Observation of seismic events with frequencies f > 25 Hz at Mponeng deep gold mine, South Africa. *Seism. Res. Lett.*, **81**, 467-479.; doi: 10.1785/gssrl.81.3.467.

Pujol, J. (2004). Earthquake location tutorial: graphical approach and approximate epicentral location techniques. *Seism. Res. Lett.*, **75**, 63-74.

Reymond, D. (2002). Seismic Tool Kit STK. http://seismic-toolkit.sourceforge.net/

Richards, P. G. (2002). Seismological methods of monitoring compliance with the Comprehensive Nuclear Test-Ban Treaty. In: Lee, W. H. K., Kanamori, H., Jennings, P. C., and Kisslinger, C. (Eds.) (2002). *International Handbook of Earthquake and Engineering Seismology*, Part A. Academic Press, Amsterdam, 369-382.

Richards, P., and Wu, Z. (2011). Seismic monitoring of nuclear explosions. In: Gupta, H. (Ed.) (2011): *Encyclopedia of Solid Earth Geophysics*. Springer, Dordrecht, Vol. 1144-1156.

Richter, C. F. (1958). *Elementary seismology.* W. H. Freeman and Company, San Francisco and London, viii + 768 pp.

Riggelsen, C., Ohrnberger, M., and Scherbaum, F. (2007). Dynamic Bayesian networks for real-time classification of seismic signals. In Kok, J., Koronacki, J., Lopez de Mantaras, R., Matwin, S., Mladenic, D., and Skowron, A. (Editors). *Knowledge Discovery in*

Databases: PKDD 2007, Lecture Notes in Computer Science, Springer, Berlin/Heidelberg, **4702**, 565–572.

Riggelsen, C., and Ohrnberger, M. (2012). A machine learning approach for improving the detection capabilities at 3C seismic stations. *Pure App. Geophys.*, 17pp.; doi: 10.1007/s00024-012-0592-3.

Roberts, R. G., and Christoffersson, A. (1990). Decomposition of complex single-station three-component seismograms. *Geophys. J. Int.*, **103**, 55-74.

Ruud, B. O., Husebye, E. S., Ingate, S. F., and Christoffersson, A. (1988). Event location at any distance using seismic data from a single, three-component station. Bull. Seism. Soc. Am., **78**, 308-325.

Saari, J. (1991). Automated phase picker and source location algorithm for local distances using a single three-component seismic station. *Tectonophysics*, **189**, 307-315.

Scherbaum, F. (1996). *Of poles and zeros; Fundamentals of Digital Seismometry*, Kluwer Academic Publishers, Boston, 256 pp.

Scherbaum, F. (2001). *Of poles and zeros: Fundamentals of digital seismology. Modern Approaches in Geophysics*, Kluwer Academic Publishers, 2nd edition, 265 pp. (including an CD-ROM by Schmidtke, E., and Scherbaum, F. with examples written in Java).

Scherbaum, F. (2007). *Of poles and zeros; Fundamentals of Digital Seismometry*. 3rd revised edition, *Springer Verlag*, Berlin und Heidelberg.

Scherbaum, F., and Johnson, J. (1992). Programmable Interactive Toolbox for Seismological Analysis (PITSA). IASPEI Software Library Volume 5, Seismological Society of America, El Cerrito.

Scherbaum, F., and Bouin (2007). FIR filter effects and nucleation phases. *Geophys. J. Int.*, **130**(3), 661-668; doi: 10.1111/j.1365-246X.1997.tb01860.x

Schweitzer, J. (2002). Slowness corrections – one way to improve IDC products. *Pure & Appl. Geophys.*, **158**, 375-396.

Schweitzer, J. (2002). Simultaneous inversion of steep-angle observations of PcP and ScP in Europe – what can we learn about the core-mantle boundary? *J. Geophys, Res.*,**151**, 209-220.

Seidl, D. (1980). The simulation problem for broad-band seismograms. *J. Geophys*., **48**, 84-93.

Seidl, D., and Berckhemer, H. (1982). Determination of source moment and radiated seismic energy from broadband recordings. *Phys. Earth Planet. Inter*., **30**, 209-213.

Seidl, D., and Stammler, W. (1984). Restoration of broad-band seismograms (part I). *J. Geophys.*, **54**, 114-122.

Seidl, D., and Hellweg, M. (1988). Restoration of broad-band seismograms (part II): Signal moment determination. *J. Geophysics*, **62**, 158-162.

Simon, R. B. (1981). *Earthquake interpretations: A manual of reading seismograms*. William Kaufmann Inc., Los Alto, CA, 150 pp.

Slunga, R. (1980). International Seismological Data Center. An algorithm for associating reported arrivals to a global seismic network into groups of defining seismic events. FOA Report, C20386-T1.

Takanami, T., and Kitagawa, G. (1988). A new efficient procedure for estimation of onset times of seismic waves. *J. Phys. Earth*, **36**, 267-290.

Takanami, T., and Kitagawa, G. (1991). Estimation of the arrival times of seismic waves by multivariate time series model. *Ann. Inst. Stat. Math.*, **43**, 407--433.

Takanami, T., and Kitagawa, G. (1993). Multivariate time-series models to estimate the arrival times of S waves. *Computers and Geosciences*, **36**, 295-301.

Tong, C. (1995). Characterization of seismic phases – an automatic analyser for seismograms. *Geophys. J Int.*, **123**, 937/947.

Tong, C., and Kennett, B. L. N. (1995). Towards the identification of later seismic phases. *Geophys. J. Int.*, **123**, 948-958.

Tong, C., and Kennett, B. L. N. (1996). Automatic seismic event rcognition and later phase identification for broadband seismograms. *Bull. Seism. Soc. Am.*,**86**, 6, 1896-109.

Trabant, C, Hutko. A. R., Bahavar, M., Karstens, R., Ahern, T. and Aster, R. (2012). Data products at the IRIS DMC: stepping-stones for research and other applications. *Seismol. Res. Lett.*, **83**(6), 846-854. doi: 10.1785/0220120032.

Vidale, J. D. (1986). Complex polarization analysis of particle motion. *Bull. Seism. Soc. Am.*,**76**, 1393-1405.

Wagner, G., and Owens, T. (1996). Signal detection using multi-channel seismic data. *Bull. Seism.Soc. Am.*, **86**(1), Part A, 221-231.

Walck, M. C., and Chael, E. P. (1991). Optimal backazimuth estimation for three-component recordings of regional seismic events. *Bull. Seism. Soc. Am.*, **81**, 2, 643-666.

Willmore, P. L. (Ed.) (1979). Manual of Seismological Observatory Practice. *World Data Center A for Solid Earth Geophysics*, Report **SE-20**, September 1979, Boulder, Colorado, 165 pp.

Withers, M. M., Aster, R. C., and Young, Ch., Beiriger, J., Harris, M., Moore, S., and Trujillo, J. (1998a). A comparison of selected trigger algorithms for automated global seismic phase and event location. *Bull. Seism. Soc. Am.*, **88**, 3, 95-106.

Withers, M. M., Aster, R. C., and Young, Ch. (1998b). An automated local and regional seismic event detection and location system using waveform correlation. *Bull. Seism. Soc. Am.*, **88**, 3, 657-669.